

LARGE TRANSVERSE MOMENTUM
 π^0 MESON PRODUCTION BY 0.5 TeV/c
 p , π^+ AND K^+ INCIDENT ON BERYLLIUM

A Dissertation
presented to
the Faculty of the Graduate School
University of Missouri-Columbia

In Partial Fulfillment
of the Requirements for the Degree

Doctor of Philosophy

by
DAVID STRILEY

Professor Guy Schupp, Dissertation Supervisor

AUGUST 1996

The undersigned, appointed by the Dean of the Graduate School, have examined the dissertation entitled

LARGE TRANSVERSE MOMENTUM
 π^0 MESON PRODUCTION BY 0.5 TeV/c
p, π^+ AND K^+ INCIDENT ON BERYLLIUM

Presented by David Striley

A candidate for the degree of Doctor of Philosophy
and hereby certify that in their opinion it is worthy of acceptance.

<u>Guy Schupp</u>	<u>✓</u>
<u>Justin C. Hwang</u>	<u>✓</u>
<u>David Hardick</u>	<u>✓</u>
<u>David L. Cunn</u>	<u>✓</u>
<u>Brian deJorio</u>	<u>✓</u>
<u>Carmen Chicone</u>	<u>✓</u>

ACKNOWLEDGEMENTS

No project of this magnitude is accomplished without the assistance of many individuals. While space does not permit me to thank everyone by name, I wish to acknowledge several individuals who have had an outstanding impact on the course of events which led to the completion of my dissertation research.

First and foremost, I wish to thank my parents, Fred and Kathryn Striley not only for bringing me into this world, but for providing a loving and nurturing environment which served as the seed from which my insatiable curiosity and love of knowledge evolved. I am eternally grateful for their undying support and patience through the years. Thanks to my brother Fred for inspiring me to become a physicist and to his family for allowing me to crash on their couch when I needed a place to stay. Special thanks also to my other brothers, Mike and Steve, for their unfailing encouragement and support. I am grateful to Cindy for her support through the years. Thanks also to Maxwell Edison and Samantha my (former) cats whom I will miss and to Titanium and Leia who have helped to fill the gap.

I am grateful to Matt and Grant for their excellent friendship for the past 23 years and to my musical friends who have provide me with tremendous support over the past year. It's been a lot of fun.

My sincere gratitude goes to Vice Provost Marvin Querry of the University of Missouri - Kansas City (UMKC), my former M.S. thesis advisor, for leading me into my first research lab and for encouraging me to work towards a Ph.D. in

physics. Thanks to Professor Richard Murphy, also of UMKC, for teaching me to solve problems with more creativity than a "well trained monkey". I am grateful to Elgin Community College for the opportunity to teach and to Professors Loren Weaver and Lavois Banks for their support.

The University of Missouri - Columbia directors of doctoral studies, Vik Sturges, Louise Lawson and Jenny Mummert, have my gratitude for their efforts and for approving the numerous changes to my program over the years. A special thanks to Louise for her assistance in the final weeks of preparation.

Special praise has been earned by the secretaries Cora, Debbie, Vicky, Lisa, Donna, Liz and Priscilla for their patient assistance. I am also grateful to people at the Fermilab library and Audio-Visual for their kind help.

Turning to the others at Fermilab, thanks to Dan Ruggiero, the glue holding E706 together. We'd all be flipping hamburgers if it weren't for Dan's many versatile contributions. Also, thanks to Jim Tweed for his many contributions to the Čerenkov hardware. I am grateful to the Mechanical and Electrical Engineering and Machine Shop people who did a commendable job producing the many detector components and to Dave Anderson for the optical spectra.

I wish to express my sincere appreciation to the beamline experts, Roger Tokarek, Dave Carey, Anthony Malensek and Win Baker for their patience with my persistent questions about TURTLE and to Ioanis Kourbanis for providing me with a starting point for my analysis. I am deeply grateful to Carol Johnstone, the designer of the MWEST Čerenkov detector, for bringing me up to speed working on the God forsaken beast (though I had fun) and to herself and her father, Jerry Harvey, for providing me with an affordable place to stay during the past year.

I am grateful to the entire E706 crew for making it all possible. To Lee Sorrell, thanks for befriending me in my early days on the experiment. I enjoyed the dinners and conversations. Thanks also for carefully timing the Čerenkov detector. It

certainly paid off. Thanks to John Bacigalupi for the support when things looked really bleak and for teaching me that “pain is good”. I am grateful to Michael Begel for the effort he put into fussing over the Čerenkov DA. I hope the tags are useful to you. Sorry, no \bar{p} , though. Thanks also for all the chocolate. I think the coma is starting to wear off. Many thanks to Lucyna (Lucy) deBarbaro and George Osborne for the dinners during the past year. It has helped to make things a bit more bearable. I have certainly enjoyed sharing with your families. Thanks to Wieslaw Dhugosz for the all too brief companionship. Best wishes. Finally, thanks to the other graduate students and post-docs of the collaboration including, but not limited to, Marek Zieliński, Dane Skow, Jim Dunlea, Chris Lirakis, William (Bill) DeSoi, George Fanourakis, John Mansour, Vijay Kapoor, Jan Ftacnik, Carlos Yosef, Keith (Casey) Hartman, Brajesh Choudhary, Sudhindra Mani, David Brown, Dhammika Weerasundara, Nikos Varelas, Rob Roser, Paoti Chang, Woohyun Chung, Steve Blusk, André Maul, Vishnu Zutshi, Lenny Apanasevich and John Kuehler. I am also grateful to Professors Tom Ferbel, Carl Bromberg and Gene Engels for the encouragement to continue. Also thanks to Ed Pothier and to the folks on E672. It’s been a pleasure working with you all.

I am sincerely grateful to our spokesperson Professor Paul Slattery whose encouragement and “behind the scenes” labors have helped to keep both myself and the whole experiment afloat. I am deeply indebted to Senior Research Associate Dr. George Ginther, the real motivating force behind E706, for directly overseeing my research project and for his efforts in all areas of the experimental operations. He has spent more time overseeing my project than it probably deserved for which he has earned my undying gratitude. I believe that I have sharpened my analytical skills under his guidance and hope that this experience will serve as a learning experience for us both.

I wish to give special thanks to Professor David Garelick, my advisor from

Northeastern University. He has supported and encouraged me through all hardships, extending himself beyond normal expectations to help find support for me. I have learned a lot about professors and human beings. He has demonstrated a special ability to fill both roles simultaneously. I also wish to express my gratitude to Professor Guy Schupp, my advisor from the University of Missouri - Columbia for his continued support. Thanks also to the members of my doctoral committees: Professors DeFacio, Huang, Urani, Cowan, Chicone and Retzloff.

Thanks to the University of Rochester, the National Science Foundation and the Department of Energy for their partial financial support. I also wish to acknowledge Northeastern University for their support. I wish to thank the several individuals who have anonymously provided partial financial support during the past few months in order to help me complete the dissertation. You have my sincere gratitude.

Finally, thanks to Lauren for your patience and support and for sharing many very special moments with me. I sincerely hope that we may continue to grow together.

LARGE TRANSVERSE MOMENTUM
 π^0 MESON PRODUCTION BY 0.5 TeV/c
 p , π^+ AND K^+ INCIDENT ON BERYLLIUM

David Striley

Professor Guy Schupp, Dissertation Supervisor

ABSTRACT

Results are presented on the production of high transverse momentum π^0 mesons from hard scattering collisions of hadrons incident on a nuclear target. The inclusive π^0 production cross-sections were measured as a function of p_T for p , π^+ and K^+ incident on beryllium targets. These data were recorded by Fermilab experiment E706 during the 1991 data acquisition period. The π^0 mesons were detected as pairs of high p_T photons which produced electromagnetic showers in a finely segmented lead-liquid argon calorimeter. The unseparated incident beam particles were identified using the Meson West beamline Čerenkov detector. The measured cross-sections are presented for π^0 mesons in the rapidity range $-0.75 < y < 0.75$ and with $p_T > 3.5$ GeV/c for the various incident particle types. The cross-sections are compared to the results of next-to-leading logarithm QCD calculations.

Table of Contents

ACKNOWLEDGEMENTS	ii
ABSTRACT	vi
LIST OF TABLES	xii
LIST OF ILLUSTRATIONS	xiv
1 Introduction	1
1.1 The Standard Model	1
1.2 Motivation	9
2 The Meson West Spectrometer	11
2.1 The Meson West Beamline	11
2.1.1 Beam Structure and Spill Cycle	12
2.1.2 Production of Secondary Beam Particles	14
2.1.3 Beam Transport	16
2.2 The Meson West Beamline Čerenkov Detector	21
2.2.1 The Theory of Čerenkov Radiation	21
2.2.2 Čerenkov Hardware	25
2.2.3 Čerenkov Optics	27
2.2.4 Gas System	41

2.3	The Meson West Spectrometer	44
2.3.1	Hadron Shield	44
2.3.2	Veto Walls	46
2.3.3	Beam Hodoscope and Hole Counters	46
2.3.4	Interaction Counters	48
2.3.5	Targets	48
2.3.6	Charged Particle Tracking	48
2.3.7	Liquid Argon Calorimeter	53
2.3.8	Forward Calorimeter	60
3	E706 Data Acquisition System and Triggers	62
3.1	Čerenkov Data Acquisition System	64
3.1.1	Čerenkov Pressure and Temperature Monitoring	64
3.1.2	Čerenkov Phototube Signal Readout	65
3.2	EMLAC Data Acquisition	69
3.3	The E706 Trigger	70
3.3.1	The Beam and Interaction Requirements	70
3.3.2	p_T Measurement	71
3.3.3	The Pretrigger Requirements	71
3.3.4	The Local Triggers	72
3.3.5	Lower Bias Triggers	73
4	Event Reconstruction	74
4.1	MAGIC	74
4.2	Discrete Logic Reconstructor	75
4.3	Planes Reconstructor	76
4.3.1	Beam Tracks	76
4.3.2	PWC Tracks	76

4.3.3	Straw Tracks	77
4.3.4	SSD Tracks	77
4.3.5	Linking	78
4.3.6	Vertex Reconstruction	78
4.4	Tracking System Momentum Scale Calibration	79
4.5	Electromagnetic Shower Reconstructor	79
4.5.1	Conversion of ADC Counts to Energy	81
4.5.2	Groups and Peaks	81
4.5.3	GAMMAs	82
4.6	Calibration of the EMLAC	82
4.6.1	Time Dependence Correction	83
4.6.2	Octant Corrections	83
4.6.3	Energy Loss Correction	86
4.6.4	Boundary Corrections	87
4.6.5	Radial Position Corrections	87
4.6.6	π^0 and η Mesons in the $\gamma\gamma$ Mode	87
4.6.7	ω Mesons in the $\pi^0\gamma$ Mode	87
4.6.8	Zero Mass Pairs	90
5	Identification of Incident Beam Particles	95
5.1	Particle Tags	95
5.2	Čerenkov Pressure Curves	96
5.3	Overview of Čerenkov Analysis Methods	101
5.4	Monte Carlo Simulations	104
5.4.1	TURTLE Simulation of the +530 GeV/c and -516 GeV/c Beams	105
5.4.2	Čerenkov Monte Carlo Simulation	113

5.5	Composition of the Incident Beam and Tags	132
5.5.1	Muon Contamination	132
5.5.2	+530 GeV/c Pressure Curves and Beam Composition	139
5.5.3	+530 GeV/c Pressure Curves and Tag Compositions	145
5.5.4	Fraction of Incident Beam Tagged	151
5.6	Ratio of the π^+ and p Absorption Cross-Sections	152
5.7	Čerenkov Data Selection	159
5.7.1	Collimation Effects	159
5.7.2	Stability of Magnet Currents	161
5.7.3	Pressure Stability	161
6	Cross-Section Analysis	164
6.1	E706 Monte Carlo	164
6.2	Data Selection and Corrections	165
6.2.1	Tag Selection	165
6.2.2	Vertex Selection	165
6.2.3	Photon Conversion Correction	167
6.2.4	Fiducial Requirement	167
6.2.5	Energy Asymmetry Requirement	167
6.2.6	Hadron Rejection	169
6.2.7	Muon Rejection	173
6.2.8	Trigger Selection	176
6.2.9	Octant Correction	176
6.2.10	Rapidity Requirement	178
6.2.11	Signal Definition	178
6.2.12	Reconstruction Efficiencies	179
6.2.13	Branching Ratios	179

6.2.14	Beam Normalization	179
6.3	Production Cross-Section Measurements	180
6.4	Čerenkov Contamination Corrections	180
7	Results and Conclusions	183
7.1	Inclusive π^0 Cross-Section Results	183
7.1.1	Inclusive π^0 Cross-Section for Incident -515 GeV/c Beam .	183
7.1.2	Inclusive π^0 Cross-Section for Incident $+530$ GeV/c Beam .	183
7.1.3	Tagged Versus Untagged Inclusive π^0 Cross-Sections for In- cident $+530$ GeV/c Beam Particles	185
7.1.4	Cross-Section Sensitivity to Operating Pressure	190
7.1.5	Inclusive π^0 Cross-Sections for Incident $+530$ GeV/c p , K^+ and π^+	190
7.1.6	Comparison of Cross-Sections from Different Incident Parti- cle Types	196
7.1.7	Comparison of Cross-Sections with QCD Calculations	196
7.2	Conclusions	196
	BIBLIOGRAPHY	205
	VITA	213

List of Tables

1.1	The fundamental particles along with their corresponding quantum numbers.	3
1.2	Valence quark compositions and masses of several hadrons. The proton and neutron are examples of baryons while the other particles listed are mesons.	4
2.1	Majority beam particle yields at the primary production target required to generate $\approx 2 \times 10^8$ particles on the experiment target. Data given for each mode of operation.	15
2.2	Meson West magnet currents for the transport of secondary beam with a nominal momentum of +530 GeV/c. The magnet polarities are reversed for the transport of -516 GeV/c beam, but the field magnitudes vary by not more than a few percent relative to the +530 GeV/c values.	19
2.3	Lengths of the E706 targets.	48
3.1	Summary of the total statistics accumulated by E706 for each mode of operation.	64
5.1	Production model parameters from fits to the absorption cross-section measurements.	107

5.2	Muon population fractions in the Meson West beamline as measured using the FCAL.	139
5.3	Fractional particle type composition of the +530 GeV/c beam incident on the MWEST Čerenkov detector as determined from an analysis of the $K4\pi2p2$ and $K3\pi2p2$ pressure curves.	151
5.4	Fraction of all +530 GeV/c incident particles satisfying the BEAM1 *BH requirement which were tagged by the specified tag logic. Particle type composition of each particle type for each tag logic requirement. Boxed values represent the particle type which the tag logic was used to identify. All data acquired at an operating pressure of 6.24 psia. Errors are statistical only.	153
5.5	Fraction of all +530 GeV/c incident particles satisfying the BEAM1 *BH requirement which were tagged by the specified tag logic requirement. Particle type composition of each particle type for each tag logic requirement. Boxed values represent the particle type which the tag logic was used to identify. All data acquired at an operating pressure of 6.31 psia. Errors are statistical only.	154
5.6	Uncorrected absorption cross-section compared to interpolated lower energy results based on measurement by Carroll et al.	156

List of Illustrations

1.1	Feynman diagrams showing the "Compton" and annihilation processes which contribute to first-order direct photon production. . . .	8
2.1	Meson West beam transport elements. The lines marked "Horiz." and "Vert." represent the relative angular skewing of the beam with respect to the beam direction in the $x - z$ and $y - z$ planes respectively. Note that the trajectories are parallel throughout the Čerenkov detector.	13
2.2	Schematic diagram of the beam spill structure. The small dark circle represents a beam particle confined to a time period of about 1 ns. .	14
2.3	Calibration curves for (a) 4-2-240 dipole magnet (points represent actual data while the solid curve represents a fit to the data) and (b) 3Q120 quadrupole magnet (only linear fit shown).	18
2.4	Longitudinal and transverse profiles of the Meson West Čerenkov detector. Only two rings of phototubes are shown in the longitudinal profile. Phototube mounting arrangement is shown in the transverse profile. Each ring of phototubes is labeled according to the particle which it was designed to tag.	26

2.5	Transverse profile of raytrace of Čerenkov photon from point of emission to interception by lenses.	27
2.6	Design specifications for the p lenses.	31
2.7	Design specifications for the K lenses.	31
2.8	Design specifications for the πK lenses.	32
2.9	Design specifications for the π lenses.	32
2.10	Transmittance curve for the Čerenkov lenses.	34
2.11	Design specifications for the lens mount plate.	35
2.12	Design specifications for the innermost cylinder (#1).	35
2.13	Design specifications for the middle cylinder (#3).	37
2.14	Design specifications for the outermost cylinder (#4).	37
2.15	Schematic diagram of raytrace of Čerenkov radiation from the lenses to the phototubes. The effect of the laser mirrors in separating the overlapping light from incident kaons and pions is illustrated.	39
2.16	Transmittance and reflectance curves for the dichroic laser mirrors.	40
2.17	Design specifications for laser mirror mount.	40
2.18	Schematic diagram of the Čerenkov gas system.	42
2.19	Schematic layout of the detectors in the Meson West spectrometer.	45
2.20	Schematic layout of the E706 targets and Silicon Strip Detectors (SSDs).	45
2.21	Schematic diagram of the Meson West hodoscope showing the X-view scintillator strips only. The dashed circle represents the nominal edge of the hole counter.	47
2.22	Schematic layout of the proportional wire chambers (PWCs).	51
2.23	Schematic diagram of a straw tube bundle.	53
2.24	Schematic diagram of the liquid argon calorimeter (LAC).	54
2.25	Schematic diagram of an electromagnetic calorimeter (EMLAC) cell.	57

2.26	Schematic diagram of an hadron calorimeter cell showing the triangular readout pads.	59
2.27	Schematic diagram of the forward calorimeter (FCAL).	60
3.1	Schematic diagram of the data acquisition system.	63
3.2	Time history of the status of phototube $K2$ around the in-time bucket (bucket 7) for an individual run. The in-time bucket is enhanced due to the trigger requirement.	68
4.1	Mass distributions for (a) $K_S^0 \rightarrow \pi^+ \pi^-$ and (b) $J/\psi \rightarrow \mu^+ \mu^-$ as reconstructed from tracking data. Here m and σ represent the mean and width of a gaussian fit to the data with a linear background. The measured masses compare well with the accepted nominal values of $M_{J/\psi} = 3.097 \text{ GeV}/c^2$ and $M_{K_S^0} = 0.498 \text{ GeV}/c^2$	80
4.2	Sensitivity of the measured $\pi^0 p_T$ spectrum to the uncertainty in the calibration of the EMLAC energy response for π^0 mesons produced in $\pi^- N$ interactions at 515 GeV/c.	84
4.3	Time dependence of the energy response of the EMLAC plotted as a function of beam days. The vertical axis represents the ratio of the reconstructed meson masses to their accepted nominal values. The mass ratio for the reconstructed 50 GeV/c electron's used to calibrate the EMLAC is also shown.	85
4.4	Distributions for energy lost by electrons (dashed) and photons (solid) in the material upstream of the EMLAC as a function of the reconstructed energy. Data were generated using the E706 Monte Carlo program.	86

4.5	Radial dependence of the energy scale for π^0 and η mesons. Data are plotted as a ratio of the meson mass to the accepted nominal value. For the ZMP sample, data are plotted as the ratio of E/P. The time dependence correction has already been applied to the data in this plot. Results are from the 1991 data sample.	88
4.6	Invariant mass distributions showing the π^0 and η signals in the $\gamma\gamma$ mode. $\pi^0\gamma$ invariant mass distribution showing the ω signal. Here m and σ represent the mean and width of a gaussian fit to the data with a linear background. The values compare well with the accepted nominal values of 134.98 MeV/c ² , 547.5 MeV/c ² and 781.9 MeV/c ² in order. Results are from the 1991 data sample.	89
4.7	Two photon invariant mass where one photon converts into a ZMP in the target region for $p_T > 3.0$ GeV/c.	92
4.8	Ratio of the γe^+e^- mass to the accepted π^0 value as a function of reconstructed photon energy and as a function of target radiation length compared with the reconstructed π^0 mass when neither photon converts. The decrease in the γe^+e^- mass with target length is clearly consistent with the bremsstrahlung theory and satisfactorily explains the reduction in the reconstructed π^0 mass. • - $p_T > 0.8$ GeV/c. ○ - $p_T > 3.0$ GeV/c. Results are from the 1991 data sample.	93
4.9	The $e^+e^-e^+e^-$ invariant mass distribution for electrons resulting from the conversion of $\gamma\gamma$ pairs in the material upstream of the EMLAC. Data are representative of the 1990 π^- sample with $p_T > 0.5$ GeV/c. The π^0 signal is evident.	94

5.1	Pressure curve for the $K4\pi2p2$ tag logic (kaon tag) with incident +530 GeV/c beam. Peaks are labeled by particle type. Note that the plot is on a semi-logarithmic scale.	97
5.2	Pressure curves for pion, kaon and proton tags with incident +530 GeV/c beam. Each curve is labeled by tag logic. Peaks/plateaus are labeled by the associated particle type. Plot is on a semi-logarithmic scale. The solid vertical line represents a typical operating pressure. The line clearly passes through the desired peaks for tagging each particle type with the appropriate coincidence logic.	99
5.3	Overlapping single particle pressure curves which contribute to the $K4\pi2p2$ coincidence with incident +530 GeV/c beam. The curves are labeled according to the type of particle producing the curve. The curves are taken from a Monte Carlo simulation. The actual pressure curve would correspond to a superposition of all contributing single particle pressure curves. Each generated single particle pressure curve was weighted to account for the relative particle fractions in the beam. Weights were taken from the following analysis. Data were acquired during runs 14896-14898.	100
5.4	Pressure curve taken with 800 GeV/c incident protons illustrating asymmetry in the $K4\pi2p2$ coincidence. Data acquired online using scalers are represented by the solid points. The solid line represents a gaussian fit to the data.	102

5.5	Pressure curve taken with incident +530 GeV/c beam illustrating the shape differences for peaks produced by different incident particle types. The solid points represent data acquired online using scalers. The solid line represents the fit of 3 gaussian curves plus a flat background to the data. The π curve is clearly narrower than the p and K curves.	103
5.6	Secondary particle yields for 800 GeV/c protons incident on beryllium calculated from the production model. Yields are shown in particles per 5×10^{12} protons incident on the Meson West production target. The production angles for each polarity are listed. . . .	106
5.7	Conventional beamline coordinates showing the central trajectory and magnetic midplane.	109
5.8	Comparisons of SWIC and TURTLE distributions for (a) the x -distribution of beam particles and (b) the y -distribution of beam particles at the entrance to the Čerenkov detector for incident +530 GeV/c beam. • - TURTLE simulation for incident protons. o - SWIC data.	111
5.9	Comparisons of SWIC and TURTLE distributions for (a) the x -distribution of beam particles and (b) the y -distribution of beam particles at the entrance to the Čerenkov detector for incident -516 GeV/c beam. • - TURTLE simulation for incident protons. o - SWIC data.	112
5.10	Comparison of the x distributions for each type of +530 GeV/c beam particle at the entrance to the Čerenkov counter as produced by the TURTLE simulation. The plots are normalized to the same number of generated particles for 100% population of each particle type in the beam.	114

5.11	Comparison of the y distributions for each type of +530 GeV/c beam particle at the entrance to the Čerenkov counter as produced by the TURTLE simulation. The plots are normalized to the same number of generated particles for 100% population of each particle type in the beam.	115
5.12	Comparison of the x' distributions for each type of +530 GeV/c beam particle at the entrance to the Čerenkov counter as produced by the TURTLE simulation. The plots are normalized to the same number of generated particles for 100% population of each particle type in the beam.	116
5.13	Comparison of the y' distributions for each type of +530 GeV/c beam particle at the entrance to the Čerenkov counter as produced by the TURTLE simulation. The plots are normalized to the same number of generated particles for 100% population of each particle type in the beam.	117
5.14	Comparison of the $\Delta p/p$ distributions for each type of +530 GeV/c beam particle at the entrance to the Čerenkov counter as produced by the TURTLE simulation. The plots are normalized to the same number of generated particles for 100% population of each particle type in the beam.	118
5.15	Čerenkov Monte Carlo results showing the wavelength distribution for emitted photons integrated over all relevant pressures for incident 800 GeV/c protons.	120

5.16	Čerenkov Monte Carlo results showing uniform distributions for (a) longitudinal position of the incident beam particle at the point of photon emission (relative to the upstream end of the Čerenkov counter) and (b) azimuthal angle of Čerenkov photon emissions with respect to the direction of particle propagation.	121
5.17	Monte carlo simulation of the two dimensional photon position distributions transverse to the Čerenkov counter axis at various points in the counter for incident +800 GeV/c protons and an operating pressure of 6.21 psia. The distributions are summed over all relevant wavelengths. Locations are at the (a) Spherical mirror. The circle represents the edge of the mirror. (b) Lenses. Only first sextant lenses are shown. The arcs represent lens edges. Photons are incident on the thin πK lens. (c) Laser mirror assembly. The smaller box represents the laser mirror. The larger box represents the flat aluminum mirror. (d) Phototubes. Photons are incident on both the K and p phototubes. The p (middle) phototube has been artificially rotated to place it along the same radius with the other phototubes resulting in the overlapping circles.	123
5.18	Quantum efficiency for the Philips XP2020Q phototubes. The solid curve is a digitization taken from the Philips manual. The histogram represents the curve generated by the Čerenkov Monte Carlo simulation.	124
5.19	Laser mirror reflectance and transmittance curves for the s - and p -polarization states as reproduced by the transfer matrix model.	126
5.20	Comparison of single phototube pressure curves in the K channel for unpolarized (\bullet) versus polarized (\circ). All results are from the Čerenkov Monte Carlo simulation.	129

5.21	Comparison of single phototube pressure curves in the π channel for unpolarized (\bullet) versus polarized (\circ). All results are from the Čerenkov Monte Carlo simulation.	130
5.22	(a) SWIC x -distribution and (b) SWIC y -distribution for beam particles at the upstream entrance to the Čerenkov detector for incident 800 GeV/c beam. The histograms represent digitizations of actual SWIC profiles as read out by EPICURE for a single spill. The smooth curves are gaussian fits.	133
5.23	(a) SWIC x -distribution and (b) SWIC y -distribution of beam particles at the downstream entrance to the Čerenkov detector for incident 800 GeV/c beam. The histograms represent digitizations of actual SWIC profiles as read out by EPICURE for a single spill. The smooth curves are gaussian fits.	134
5.24	Single phototube pressure curves for the p phototubes with incident 800 GeV/c proton beam. \square - Minnesota latch data. \bullet - Čerenkov Monte Carlo simulation. Error bars are statistical.	135
5.25	Single phototube pressure curves for the K phototubes with incident 800 GeV/c proton beam. \square - Minnesota latch data. \bullet - Čerenkov Monte Carlo simulation. Error bars are statistical.	136
5.26	Single phototube pressure curves for the π phototubes with incident 800 GeV/c proton beam. \square - Minnesota latch data. \bullet - Čerenkov Monte Carlo simulation. Error bars are statistical.	137
5.27	Monte Carlo fits to 800 GeV/c coincidence pressure curves for several tag requirements. \triangle - pressure curves from actual scaler data. \bullet - Čerenkov Monte Carlo simulation. Errors are statistical only. Note that the plots are semi-logarithmic.	138

5.28	Comparison of single phototube pressure curves in the π -ring of phototubes for incident pions (\bullet) and incident muons (\square).	140
5.29	Single phototube pressure curves for the p phototubes with incident +530 GeV/c beam. \square – Minnesota latch data. \bullet – Čerenkov Monte Carlo simulation. Error bars are statistical only.	142
5.30	Single phototube pressure curves for the K phototubes with incident +530 GeV/c beam. \square – Minnesota latch data. \bullet – Čerenkov Monte Carlo simulation. Error bars are statistical only.	143
5.31	Single phototube pressure curves for the π phototubes with incident +530 GeV/c beam. \square – Minnesota latch data. \bullet – Čerenkov Monte Carlo simulation. Error bars are statistical only.	144
5.32	Monte Carlo simulation of the +530 GeV/c $K4\overline{\pi}2p2$ coincidence pressure curve. Open triangles represent actual pressure curves. Dark circles with error bars represent the results of the Monte Carlo simulation with statistical errors only. Actual pressure curves are from data acquired during runs 14211-14212. Note that the plots are semi-logarithmic.	146
5.33	Monte Carlo simulation of the +530 GeV/c $K3\overline{\pi}2p2$ coincidence pressure curve. Open triangles represent actual pressure curves. Dark circles with error bars represent the results of the Monte Carlo simulation with statistical errors only. Actual pressure curves are from data acquired during runs 14211-14212. Note that the plots are semi-logarithmic.	147

5.34	Monte Carlo simulation of the +530 GeV/c $\pi 3\overline{p}2$ coincidence pressure curve. Open triangles represent actual pressure curves. Dark circles with error bars represent the results of the Monte Carlo simulation with statistical errors only. Actual pressure curves are from data acquired during runs 14211-14212. Note that the plots are semi-logarithmic.	148
5.35	Monte Carlo simulation of the +530 GeV/c $\pi 2\overline{p}2$ coincidence pressure curve. Open triangles represent actual pressure curves. Dark circles with error bars represent the results of the Monte Carlo simulation with statistical errors only. Actual pressure curves are from data acquired during runs 14211-14212. Note that the plots are semi-logarithmic.	149
5.36	Monte Carlo simulation of the +530 GeV/c $p 2\overline{K} 3\overline{\pi} 2$ coincidence pressure curve. Open triangles represent actual pressure curves. Dark circles with error bars represent the results of the Monte Carlo simulation with statistical errors only. Actual pressure curves are from data acquired during runs 14211-14212. Note that the plots are semi-logarithmic.	150
5.37	Distribution in the transverse plane of all beam particles incident on the beryllium target for a $p 2\overline{\pi} 2\overline{K} 2$ tag. The circle represents the target fiducial region.	155
5.38	Absorption cross-section ratio, σ_{π}/σ_p , as a function of coincidence level for an operating pressure of 6.31 psia. Errors are statistical. The mean value obtained by Carroll is represented by the horizontal line.	157

5.39	Absorption cross-section ratio, σ_{π}/σ_p , as a function of coincidence level for an operating pressure of 6.24 psia. Errors are statistical. The mean value obtained by Carroll is represented by the horizontal line.	158
5.40	Collimator half-aperture size as a function of run number for incident +530 GeV/c beam for (a) horizontal and (b) vertical collimators. The solid vertical line represents the division between the HIGH and LOW pressure Čerenkov data samples. The dashed vertical lines bound the range of runs for the -516 GeV/c data acquisition period. Each error bar represents the RMS deviation taken over all spills in the run.	160
5.41	Dipole magnet currents as a function of run number for incident +530 GeV/c beam for (a) MW7W1 and (b) MW7W2. The solid vertical line represents the division between the HIGH and LOW pressure Čerenkov data samples. The dashed vertical lines bound the range of runs for the -516 GeV/c data acquisition period. Each error bar represents the RMS deviation taken over all spills in the run.	162
5.42	Operating pressure as a function of run number. The solid vertical line represents the division between the HIGH and LOW pressure Čerenkov data samples. The horizontal lines represent the two fiducial operating pressures at 6.24 and 6.31 psia. The dashed vertical lines bound the range of runs for the -516 GeV/c data acquisition period. Each error bar represents the RMS deviation taken over all spills in the run.	163

6.1	Distribution of vertices reconstructed from the E706 tracking data in the target region for π^0 candidates. The targets are labeled by material type. Data are corrected for beam absorption and photon conversions in the target materials. Data are taken from the LOW Čerenkov pressure sample only. No Čerenkov tag selections have been applied at this stage.	166
6.2	Top: Schematic diagram of the definition of energy asymmetry. Bottom: Energy Asymmetry distribution for photons from π^0 decays.	168
6.3	Comparison of E706 Monte Carlo generated asymmetry distribution with reconstructed data.	170
6.4	E_{front}/E_{total} distributions for all particles showering in the EMLAC and for only electrons showering in the EMLAC. Hadrons deposit most their energy in the back section of the EMLAC.	171
6.5	Comparison of the E_{front}/E_{total} distributions produced by the E706 Monte Carlo simulation with reconstructed EMLAC data. Data are presented in several photon energy ranges.	172
6.6	p_T^b/p_T (bapt/pt), Directionality (direction) and χ^2/E (chisq/energy) distributions for both muons and photons producing showers in the EMLAC.	174
6.7	Sample trigger p_T turn-on efficiency curves for the SLH and SLL triggers for both the inner and outer sections of the EMLAC.	177
7.1	Inclusive cross-section as a function of $\pi^0 p_T$ for the production of π^0 mesons by π^- mesons incident on the beryllium target. This cross-section is untagged and uncorrected for the negligible K^- and \bar{p} contamination. Data are plotted on a semi-logarithmic scale. Data were acquired during the 1990 data acquisition period.	184

7.2	Inclusive cross-section as a function of $\pi^0 p_T$ for the production of π^0 mesons by the unseparated and untagged +530 GeV/c beam particles incident on the beryllium target. Data represent the HIGH Čerenkov pressure sample only. Data are plotted on a semi-logarithmic scale.	186
7.3	Ratio of the inclusive π^0 production cross-section for +530 GeV/c beam particles incident on the beryllium target which satisfy a $p2\overline{K3\pi2}$ tag to the corresponding untagged cross-section as a function of $\pi^0 p_T$. The tagged data are uncorrected for particle contaminations. Data are from the HIGH Čerenkov pressure sample only.	187
7.4	Ratio of the inclusive π^0 production cross-section for +530 GeV/c beam particles incident on the beryllium target which satisfy a $\pi3\overline{p2}$ tag to the corresponding untagged cross-section as a function of $\pi^0 p_T$. The tagged data are uncorrected for particle contaminations. Data are from the HIGH Čerenkov pressure sample only.	188
7.5	Ratio of the inclusive π^0 production cross-section for +530 GeV/c beam particles incident on the beryllium target which satisfy a $K4\overline{\pi2p2}$ tag to the corresponding untagged cross-section as a function of $\pi^0 p_T$. The tagged data are uncorrected for particle contaminations. Data are from the HIGH Čerenkov pressure sample only.	189
7.6	Ratio of the inclusive π^0 production cross-section measured at Čerenkov operating pressures of 6.31 psia and 6.24 psia for incident p as a function of $\pi^0 p_T$. The p tag employed in this measurement is $p2\overline{K3\pi2}$ while the $\pi3\overline{p2}$ and $K4\overline{\pi2p2}$ tagged cross-sections were also used in the contamination corrections.	191

7.7	Ratio of the inclusive π^0 production cross-section measured at Čerenkov operating pressures of 6.31 psia and 6.24 psia for incident π^+ as a function of $\pi^0 p_T$. The π^+ tag employed in this measurement is $\pi^+ 3\overline{p^2}$ while the $p^+ 2\overline{K^3\pi^2}$ and $K^+ 4\overline{\pi^2 p^2}$ tagged cross-sections were also used in the contamination corrections.	192
7.8	Inclusive π^0 cross-section per nucleon for 530 GeV/c p incident on beryllium as a function of $\pi^0 p_T$	193
7.9	Inclusive π^0 cross-section per nucleon for 516 GeV/c π^+ incident on beryllium as a function of $\pi^0 p_T$	194
7.10	Inclusive π^0 cross-section per nucleon for 0.5 TeV/c K^+ incident on beryllium as a function of $\pi^0 p_T$	195
7.11	Ratio of the inclusive π^0 cross-section for 516 GeV/c π^+ incident on beryllium to the cross-section for incident 515 GeV/c π^- as a function of $\pi^0 p_T$	197
7.12	Ratio of the inclusive π^0 cross-section for 516 GeV/c π^+ incident on beryllium to the cross-section for incident 530 GeV/c p as a function of $\pi^0 p_T$	198
7.13	Ratio of the π^0 cross-section for incident 516 GeV/c π^+ to that generated by incident 530 GeV/c p as a function of π^0 rapidity for $4.0 \text{ GeV}/c < p_T < 4.5 \text{ GeV}/c$. The distribution generated by the incident π^+ is characteristically shifted towards more forward rapidities than the p distribution. Data are selected from the LOW Čerenkov pressure sample only.	199
7.14	Inclusive π^0 cross-section per nucleon for 530 GeV/c p incident on beryllium as a function of $\pi^0 p_T$. The data are compared to the NLL QCD predictions for two choices of scale $Q = p_T$ and $Q = p_T/2$.	200

7.15	Inclusive π^0 cross-section per nucleon for 530 GeV/c p incident on beryllium as a function of $\pi^0 p_T$. Data are compared to NLL QCD predictions with k_T smearing included. The scale $Q = p_T/2$ has been employed.	201
7.16	Inclusive π^0 cross-section per nucleon for 516 GeV/c π^+ incident on beryllium as a function of $\pi^0 p_T$. The data are compared to the NLL QCD predictions for the two choices of scale $Q = p_T$ and $Q = p_T/2$	202
7.17	Inclusive π^0 cross-section per nucleon for 516 GeV/c π^+ incident on beryllium as a function of $\pi^0 p_T$. Data are compared to NLL QCD predictions with k_T smearing effects included. The scale $Q = p_T/2$ has been employed.	203

Chapter 1

Introduction

FERMILAB
LIBRARY

1.1 The Standard Model

During the last few centuries there has been remarkable progress in the understanding of the nature of matter and the forces responsible for physical phenomena. There are four known fundamental forces: the gravitational force between particles due to their mass, the electromagnetic force between charged particles, the weak force which is responsible for nuclear decays, and the strong force which binds protons and neutrons in nuclei. High energy physics involves the investigation of the constituents of matter and the interactions between those constituents. High energy collisions between particles (such as protons) are the most significant tool employed to investigate the fundamental constituents of matter and their interactions. When the colliding particles have substantial energy, the collisions probe distances much smaller than the proton radius and reveal the substructure of such particles. This short distance probing corresponds to very large momentum transfers (Q) between the interacting particles. At currently achievable energies, the effects of gravity may be neglected compared to the other forces when probing constituent interactions.

All matter is believed to be composed of combinations of three types of fundamental constituents classified as *quarks*, *leptons* and *gauge bosons*. A list of these

particles together with their mass and electric charge is shown in Table 1.1. [1] The quarks and leptons (which are both spin $1/2$ fermions) interact via the exchange of spin 0 gauge bosons. There is also a corresponding anti-particle for each particle type listed in Table 1.1. Anti-particles have the same mass but opposite charge relative to corresponding particle. At present, the most comprehensive model for describing these particles and their interactions is the *Standard Model* [2]–[5].

Leptons are fermions which interact via the electromagnetic and weak forces. There are a total of six leptons paired into three *generations* each consisting of a “massless” neutrino with zero electric charge and a massive charged partner. The leptons include the electron along with the corresponding electron neutrino (ν_e).

Quarks are the fermionic constituents of matter which interact via the strong, electromagnetic and weak forces. Six types or *flavors* of quarks have been identified: the up (u), down (d), strange (s), charm (c), bottom (b) and top (t). Each quark possesses either $-1/3$ or $2/3$ of the electron’s electric charge.

The gauge bosons include the photon (γ), the W^\pm and the Z^0 bosons all of which mediate electro-weak interactions involving both quarks and leptons. The *gluon* is the mediator of the strong force between quarks.

Quarks and gluons exhibit a conserved quantum number referred to as *color charge*, analogous to electric charge. However, unlike the photon, since the gluon has color charge, it may self couple resulting in additional Feynman diagrams which do not contribute to electromagnetic interactions. Quarks and gluons are referred to collectively as *partons*.

The directly observed strongly interacting particles, known as *hadrons*, are composed of quarks and gluons. The proton and the neutron are examples of hadrons. Only two classes of hadrons have been experimentally verified to exist – *baryons* and *mesons*. Baryons are composed of three valence quarks (qqq) while mesons are composed of a valence quark (q) and a valence anti-quark (\bar{q}). The

Particle	Symbol	Mass (MeV/c ²)	Electric Charge
QUARKS			
Up	u	2—8	+2/3
Down	d	5—15	-1/3
Strange	s	100—300	-1/3
Charm	c	1000—1600	+2/3
Bottom	b	4100—4500	-1/3
Top	t	180000 ± 12000	+2/3
LEPTONS			
Electron	e	0.51	-1
Electron Neutrino	ν_e	≈ 0	0
Muon	μ	105.66	-1
Muon Neutrino	ν_μ	< 0.17	0
Tau	τ	1777.00 ^{+0.30} _{-0.27}	-1
Tau Neutrino	τ_μ	< 24	0
GAUGE BOSONS			
Photon	γ	0	0
Gluon	g	0	0
W-Boson	W	80330 ± 150	+1
Z-Boson	Z	91187 ± 7	0

Table 1.1: The fundamental particles along with their corresponding quantum numbers.

Particle	Mass (MeV/c ²)	Quark Composition
p	938.27231 ± 0.00028	$ p\rangle = uud\rangle$
n	939.56563 ± 0.00028	$ n\rangle = udd\rangle$
π^+	139.56995 ± 0.00035	$ \pi^+\rangle = u\bar{d}\rangle$
π^-	139.56995 ± 0.00035	$ \pi^-\rangle = \bar{u}d\rangle$
K^+	493.677 ± 0.016	$ K^+\rangle = u\bar{s}\rangle$
K^-	493.677 ± 0.016	$ K^-\rangle = \bar{u}s\rangle$
π^0	134.9764 ± 0.0006	$ \pi^0\rangle = \frac{1}{\sqrt{2}} u\bar{u} + d\bar{d}\rangle$

Table 1.2: Valence quark compositions and masses of several hadrons. The proton and neutron are examples of baryons while the other particles listed are mesons.

quarks in hadrons radiate gluons which, in turn, convert into $q\bar{q}$ pairs. This process produces a quark/anti-quark *sea* within the hadrons in addition to the valence quarks and gluons. Gluons account for about 50% of the momentum in hadrons. The valence quark compositions of the particles relevant to this study are listed in Table 1.2. [1] The color charge of quarks and gluons corresponds, by analogy with traditional color theory of light, to the primary colors. All observable hadrons are colorless. In baryons, each valence quark possesses a different primary color thus yielding a colorless combination. In mesons, the anti-quark possesses the anti-color (i.e. complementary color) of the valence quark so that the resulting hadron is colorless.

The strong force is responsible for the permanent confinement of colored partons within hadrons. No single quark has yet been isolated. While quarks are tightly bound within hadrons for low energy interactions, as the momentum transfer, Q^2 , between interacting partons increases they behave increasingly as independent scatterers. In the limit that $Q^2 \rightarrow \infty$ the partons may be treated as totally independent scatterers. This phenomenon is known as *asymptotic freedom*. [6]-[9] However, the force between the quarks increases with increasing separation so that an isolated quark may not be extracted from the hadron. In sufficiently large Q^2 interactions, quarks will produce gluons as a result of the bremsstrahlung process. The gluons subsequently convert into $q\bar{q}$ pairs. The pairs themselves produce bremsstrahlung radiation and the process repeats, thus creating a cascade of partons. This process is known as *fragmentation*. The partons rapidly recombine to produce detectable, collimated showers (i.e. *jets*) of colorless hadrons many of which may possess large transverse momenta (p_T). [10]-[16] The π^0 meson occurs frequently in such high transverse momentum jets.

The theory describing the strong interactions between partons is known as *Quantum Chromodynamics* [2]-[5] (**QCD**). The rates of large Q^2 interactions between partons can be calculated by applying perturbation techniques to QCD theory. The parton-level cross-section calculations are expanded in terms of the *running coupling constant* [17], α_s , where

$$\alpha_s(Q^2) = \frac{4\pi}{\beta_0 \ln(Q^2/\Lambda^2)} \left[1 - \frac{\beta_1 \ln \{ \ln(Q^2/\Lambda^2) \}}{\beta_0^2 \ln(Q^2/\Lambda^2)} \right] \quad (1.1)$$

represents the expansion to *Next-to-Leading-Log* (**NLL**) order. Here

$$\beta_0 = 11 - (2n_f)/3 \quad (1.2)$$

and

$$\beta_1 = 102 - (38n_f/3) \quad (1.3)$$

where n_f is the number of quark flavors¹ available at that value of Q^2 and Λ is a parameter which must be determined empirically. For low Q^2 interactions, $\alpha_s > 1$ and perturbative calculations become inappropriate. However, as the Q^2 of the interaction increases, α_s becomes smaller so that perturbative calculations may be performed for sufficiently large values of Q^2 . In this domain, perturbative QCD has been demonstrated as a powerful tool in making predictions about parton interactions. Perturbation calculations have been performed at the Next-to-Leading-Logarithm (NLL) level [16], [18]-[20] for several processes. As NLL calculations become available, they provide a means of further testing the validity of QCD and investigating the parton structure of hadrons. Calculations of cross-sections for large Q^2 interactions involving hadrons using perturbative QCD requires a knowledge of three main quantities: (1) the Parton Distribution Functions [21]-[32] (PDF) of the interacting hadrons which specify the probability that a parton carries momentum fraction x of the parent hadron's momentum, (2) the differential cross-sections for parton-parton scattering and (3) the Fragmentation Functions (FF) which are the probability densities for obtaining a given hadron from the fragmentation of a specific parton emerging from the constituent interaction. The PDFs and FFs necessarily involve low Q^2 processes and, as such, are not suited to evaluation by current perturbative methods. The PDFs and FFs used in the cross-section calculations are determined from fits to empirical measurements.

In the parton model, the invariant differential inclusive cross-section for the production of high p_T hadrons is given by

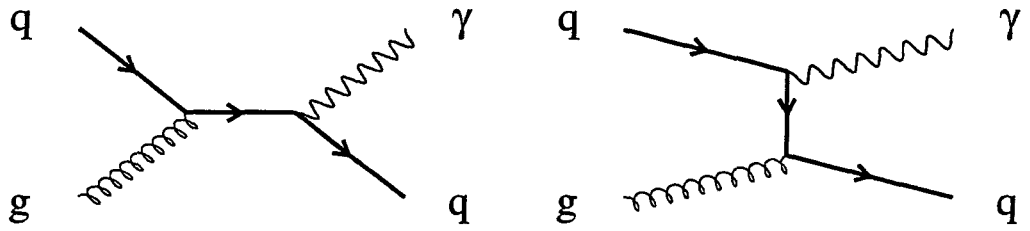
$$E \frac{d^3\sigma}{dp^3}(AB \rightarrow CX) = \sum_{abcd} \int dx_a dx_b dz_c G_{a/A}(x_a, Q^2) G_{b/B}(x_b, Q^2) D_{C/c}(z_c, Q^2) \frac{\hat{s}}{z_c^2 \pi} \frac{d\sigma}{d\hat{t}}(ab \rightarrow cd) \delta(\hat{s} + \hat{t} + \hat{u}). \quad (1.4)$$

¹The number of quark flavors depends on the available energy. Quarks of larger mass have higher production thresholds.

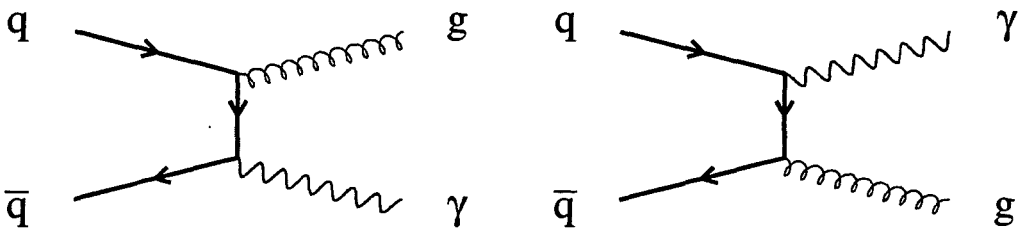
Here $\hat{s} = (\mathbf{p}_a + \mathbf{p}_b)^2$, $\hat{t} = (\mathbf{p}_a - \mathbf{p}_c)^2$ and $\hat{u} = (\mathbf{p}_a - \mathbf{p}_d)^2$ are the Mandelstam parameters where \mathbf{p}_i is the four-momentum of parton i . $G_{i/I}$ is the PDF, which depends upon Q^2 and represents the probability that parton i carries fraction x_i of the parent hadron I 's momentum. The FF, $D_{J/j}$, which is also a function of Q^2 , is the probability that hadron J is produced with a momentum fraction between z and $z + dz$ by the fragmentation of parton j . The parton-level differential cross-section is given by $\frac{d\sigma}{d\hat{t}}$.

The experimental investigation of the production of high transverse momentum particles in strong interactions provides an opportunity to test the validity of these perturbative QCD calculations.

A particularly interesting signal to investigate is the production of single photons directly as a result of the hard scattering of constituents. This process of direct-photon production [16] is appealing because the photon coupling is well known. Furthermore, since the photon is already colorless, it emerges directly from the hard scatter and the kinematics of the parton are readily measured. In addition, there are only two leading order processes which contribute to direct-photon production. Those processes are illustrated in Figure 1.1. The ‘‘Compton’’ diagram represents the strong-force analog to the electromagnetic Compton scattering process. This process involves the scattering of an incident quark and an incident gluon resulting in the absorption of the gluon and emission of a direct-photon. The annihilation process involves the annihilation of a quark anti-quark pair and production of a direct-photon and gluon. In either process, in addition to the direct-photon, a parton emerges which fragments to produce a jet of hadrons. The measurement of the direct photon cross-sections provides a means of probing the gluon distributions of hadrons because the ‘‘Compton’’ process is directly sensitive to the gluon content of the interacting hadrons. The production of the direct photon is coincident with a quark or gluon which fragments to produce a high p_T



Compton Diagrams



Annihilation Diagrams

Figure 1.1: Feynman diagrams showing the “Compton” and annihilation processes which contribute to first-order direct photon production.

jet. As the direct photon is produced electromagnetically, the cross-section is suppressed relative to gluon radiation by a factor of order α_{em}/α_s , where α_{em} is the coupling constant for electromagnetic interactions (fine structure constant) and α_s is the *running coupling constant* for strong interactions. Once these background issues are addressed for low Q^2 (≈ 2 (GeV/c)²), this results in a suppression of direct-photon production relative to hadron production of order $\approx 10^{-3}$. Thus measurements of direct photon cross-sections will be dominated by hadron background at low p_T . At sufficiently high Q^2 , however, α_s decreases substantially and a direct photon signal may be extracted. It is essential, however, to measure the backgrounds contributed by hadrons. The dominate source of hadron background in the direct photon measurement is due to the electromagnetic decays of π^0 mesons in high transverse momentum jets.

1.2 Motivation

Fermilab fixed target experiment E706 was designed with the primary goal of investigating direct photon production in hadron interactions to elicit information about the gluon PDF of hadrons. The dominant source of background to the direct photon measurement is due to the electromagnetic decays of high p_T π^0 . These π^0 mesons are produced during the fragmentation of partons emerging from hard scatters between the partons in the incident beam and the partons in the target. These π^0 mesons frequently decay in $\gamma\gamma$ pairs, thus generating the background to the direct photon signal. E706 is well suited to the measurement of production cross-sections for large p_T π^0 mesons. As the beam incident on E706 is composed of π^\pm , K^\pm and p , the production cross-sections may be measured for these different incident particle types. A careful measurement of the high p_T π^0 production is essential to the extraction of the direct photon cross-sections.

The measurement of π^0 production cross-sections for incident protons and pions also contributes to our understanding of the fragmentation process. These data on production of high transverse momentum π^0 mesons provides further tests of the validity of QCD calculations at the current next-to-leading-logarithm order.

Chapter 2

The Meson West Spectrometer

The Meson West spectrometer consisted of a large array of detectors dedicated to the measurement of direct photon cross-sections. The major systems included a modified differential Čerenkov detector used to identify charged beam particles incident on a variety of targets, a tracking system surrounding the target region, an electromagnetic calorimeter, an hadronic calorimeter and a forward calorimeter. Numerous auxiliary devices assisted in defining beam incident on the targets, particles produced in target interactions and various experimental triggers. In addition, four walls of veto scintillator provided identification of muons traveling near the beam.

2.1 The Meson West Beamline

Protons accelerated to 800 GeV/c momenta by the Fermilab accelerator, called the Tevatron, were extracted and split between three primary beamlines: PROTON, NEUTRINO and MESON. Each beamline was subdivided into a number of secondary lines which delivered beam to the fixed target experiments. The Meson West Čerenkov counter and spectrometer were located in the MESON WEST (MW) beamline. The MW secondary beamline was further sectioned into a number of enclosures. These enclosures were numbered sequentially in the direction of

beam propagation as MW x where x is the enclosure number. All beamline elements most directly relevant to this study were located in the MW6, MW7 and MW8 enclosures as well as MW9 (which is the actual MW experiment hall). The beam transport elements are shown schematically in Figure 2.1. The 800 GeV/c primary proton beam interacted with the MW production target in the MW6 enclosure, producing secondary protons, pions and kaons. Some of the charged secondaries were then transported to the MW experimental hall where a small fraction interacted in the experimental targets. The only major detector located in the MW8 enclosure was the Čerenkov detector. All other E706 detectors were located in the MW9 experiment hall.¹

The secondary charged beam particles were transported from the primary target area to the E706 targets by an array of beamline elements. Included were dipole magnets to bend the paths of charged particles and provide momentum selection, quadrupole magnets for focusing of particle trajectories, spoiler magnets² and collimators. In addition, numerous scintillation counters and segmented wire ion chambers (SWICs) were used to monitor the beam flux and spatial distributions of charged beam particles at strategic points in the beamline. The theory of beam transport and the roles of the various elements are discussed below and in Chapter 5.

2.1.1 Beam Structure and Spill Cycle

Charged particles were confined to 1 ns time intervals, known as *buckets*. The time between buckets was 19 ns as shown in Figure 2.2. The accelerator operated on a 57 s cycle. For the first 34 s of each cycle, most conventional beamline magnets were

¹The experiment hall also housed the detectors for the E672 high mass dimuon experiment which acquired data concurrently with E706.

²Unwanted charged particles, such as muons, may propagate in a halo parallel to the beam. Spoiler magnets swept such particles away from the beamline.

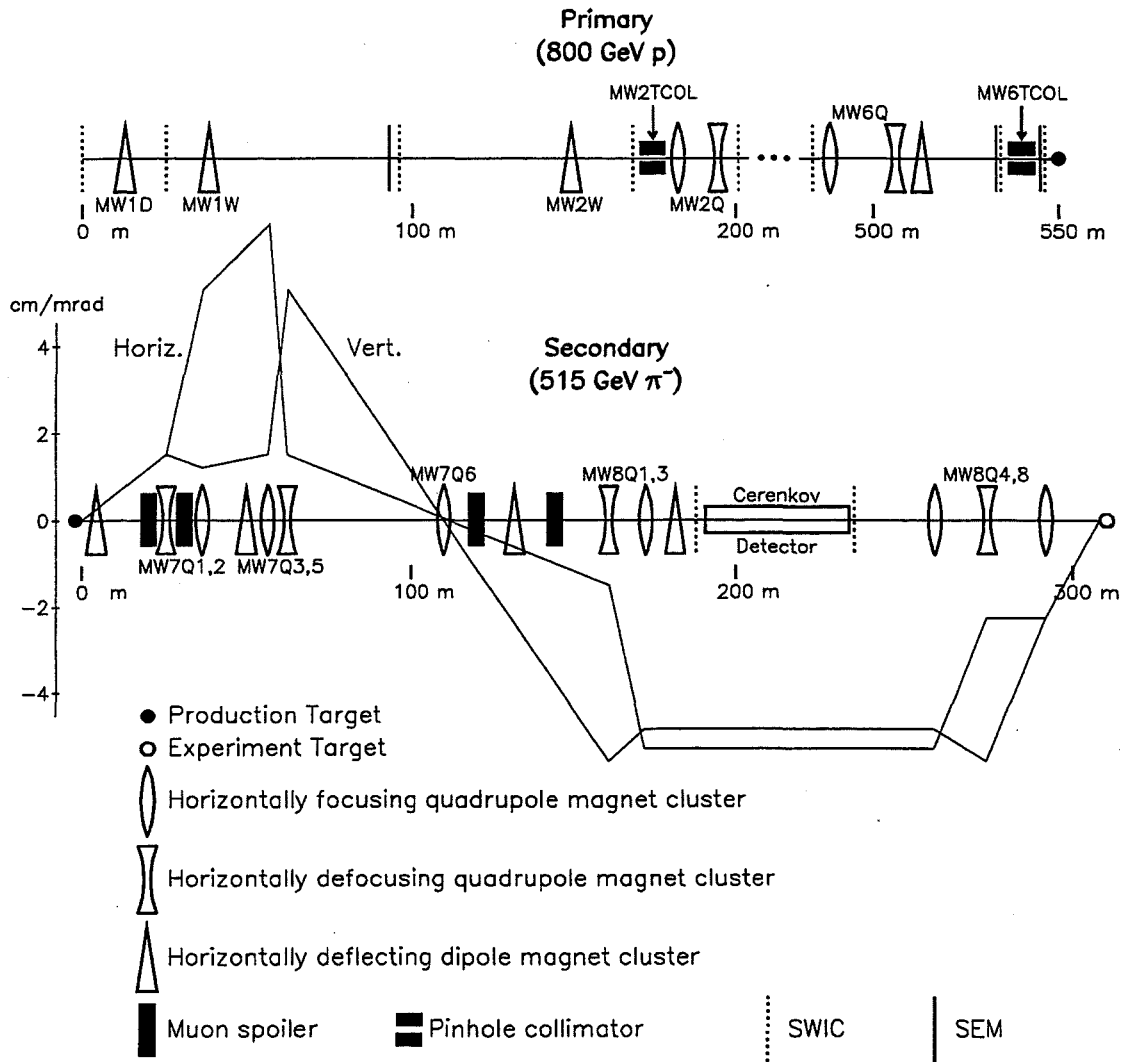


Figure 2.1: Meson West beam transport elements. The lines marked "Horiz." and "Vert." represent the relative angular skewing of the beam with respect to the beam direction in the $x-z$ and $y-z$ planes respectively. Note that the trajectories are parallel throughout the Čerenkov detector.

Spill Structure

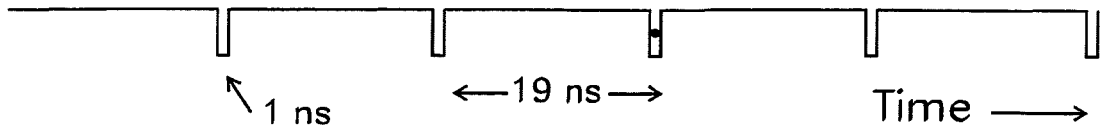


Figure 2.2: Schematic diagram of the beam spill structure. The small dark circle represents a beam particle confined to a time period of about 1 ns.

ramped to their operating currents to reduce power requirements and minimize the risk of overheating. For the remaining 23 s of each cycle, known as a *spill*, beam was transported to the fixed target areas.

2.1.2 Production of Secondary Beam Particles

The MW beamline was divided into two sections, the primary and secondary beamlines. The MW beam operated in three modes during the 1991 data acquisition period (referred to as the 1991 *run*). In two of the modes 800 GeV/c protons interacted with the MW primary target to produce secondary protons, pions and kaons with mean momenta of ≈ 500 GeV/c. Here the *mean* beam momentum³ corresponds to the mean of the momentum distribution of the incident beam particle type. For +530 GeV/c incident beam, the proton, referred to as the *majority* particle, was accompanied by a small admixture of π^+ and K^+ known as *minority* particles. The magnet polarities could be reversed in the secondary beamline thus allowing either negative or positive secondaries to be transported. For negative polarities, the π^- was the majority particle, accompanied by minority K^- and \bar{p} .

³In contrast, the *reference* beam momentum corresponds to the momentum possessed by a hypothetical beam particle which moves along the beamline axis (i.e. through the center of every magnet aperture).

Majority Incident Particle	Mean Beam Momentum (GeV/c)	Reference Beam Momentum (GeV/c)	Flux (Particles per spill)
p	+800	+800	2×10^{11}
p	+530	+538	2×10^{12}
π^-	-516	-538	5×10^{12}

Table 2.1: Majority beam particle yields at the primary production target required to generate $\approx 2 \times 10^8$ particles on the experiment target. Data given for each mode of operation.

Measured nominal mean beam momenta and corresponding beam fluxes are given in Table 2.1 [33] for the majority particle for each mode of operation. The mean momenta for the minority particles varied slightly from the mean momentum of the majority particle. In these secondary beam modes, the primary target consisted of 3/4 interaction lengths of beryllium [34].

In the third mode, 800 GeV/c primary protons were transported directly to the experiment hall from the Tevatron. The corresponding mean beam momentum and flux transported down the primary beamline is given in Table 2.1.

In the secondary beam modes, many of the incident 800 GeV/c primary protons did not interact in the production target and were transported beyond the target. In the -516 GeV/c mode of operation, there was no risk of transporting non-interacting primary protons down the secondary beamline. To avoid the risk of transporting non-interacting primary protons down the secondary beamline in the +530 GeV/c mode the 800 GeV/c primary protons were made to intercept the primary target at a *production angle* of 1.4 mrad relative to the acceptance of the

secondary beamline. Thus, the non-interacting protons were directed safely into the beam dump while allowing positive secondaries to be transported safely into the secondary beamline [34].

2.1.3 Beam Transport

Charged beam particles were transported from the Tevatron to the MW Čerenkov detector and the E706 targets by a series of elements including magnets for steering and focusing of the beam as well as auxiliary devices for collimation and monitoring of the beam distributions at various points in the beamline. Control and monitoring of the beamline elements was accomplished using EPICURE [35] (ExPerImental areas beamline Control system User Resource Enhancement). The status of the beamline elements (e.g. magnet currents) was recorded every few spills during the data acquisition period by EPIDAQ, the EPICURE data acquisition software.

Dipole Magnets

Charged particle trajectories are bent by magnet fields. The fundamental equation governing the motion of charged particles in a magnetic field is the Lorentz force equation

$$\frac{d\mathbf{p}}{dt} = q(\mathbf{v} \times \mathbf{B}), \quad (2.1)$$

where \mathbf{p} and q are the particle's momentum and electrical charge respectively, \mathbf{v} is the particle's velocity and \mathbf{B} is the applied magnetic field. A *dipole* magnet provides a nearly uniform magnetic field resulting in radial bending of charged particle trajectories in a plane perpendicular to the applied field. Several dipole magnets were included in the MWEST beamline. In addition to beam steering, the mean beam momentum was selected by varying dipole magnet currents and, hence, the applied magnetic field.

Three types of dipole magnets were employed in the MW beamline. The primary target was immediately followed by three dipole magnets used to select the mean momentum of transported particles from the broad spectrum of produced secondaries.

Two additional types of dipoles were used to steer the MW beam [36]. The 4-2-240⁴ *bending dipole magnet* is a powerful bend magnet used to steer the beam. The 4-4-30 *Vernier dipole magnet*, of much weaker field strength, was used to make small corrections to the beam direction.

Beam steering was accomplished by varying the dipole magnet currents and, hence, the field strengths of each magnet. For each type of magnet, a calibration curve was acquired [36] for B versus I where I is the applied current in amps and B the resulting magnetic field in kilogauss. The B versus I calibration curve for the 4-2-240 dipole is shown in Figure 2.3. The response of the magnets is linear with $B(I) = 3.86 \times 10^{-3}I$ below saturation. Some typical operating currents and corresponding magnetic field strengths are shown in Table 2.2 for transport of the +530 GeV/c secondary beam.

Quadrupole Magnets

The quadrupole magnets used to focus the MW beam were of the 3Q120⁵ type [36]. These quadrupoles were used to produce a focused beam spot on the experiment target and to make the particle trajectories as parallel as possible throughout the region of the Čerenkov detector. The effects of dispersion were also minimized at the E706 target by using quadrupole magnets to recombine rays of different

⁴The standard nomenclature for dipole magnets is as follow: The first two number represent the horizontal and vertical aperture dimensions in inches, respectively. The last number represents the length of the magnet in inches.

⁵For quadrupole magnets, the standard nomenclature is as follows: The first number represents the aperture dimension in inches. The 'Q' represents the fact that the magnet is a quadrupole, the last number represents the length of the magnet in inches.

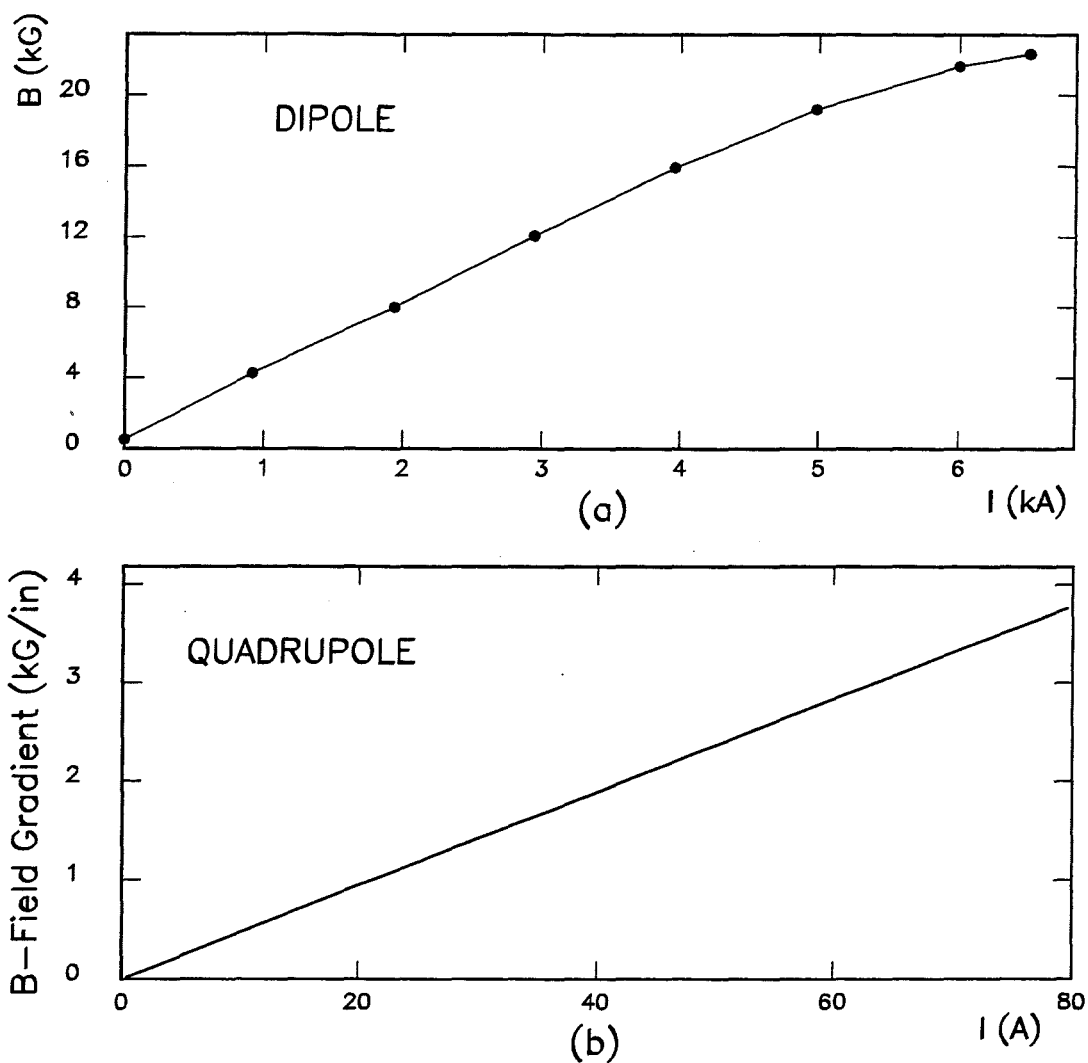


Figure 2.3: Calibration curves for (a) 4-2-240 dipole magnet (points represent actual data while the solid curve represents a fit to the data) and (b) 3Q120 quadrupole magnet (only linear fit shown).

Dipole Magnets	Current (A)	Field Strength (kG)
MW7W1	2106	8.13
MW7W2	1760	6.80
Quadrupole Magnets	Current (A)	Field Gradient (kG/in)
MW7Q1	79	3.726
MW7Q2	79	3.726
MW7Q3	79	3.726
MW7Q4	73	3.443
MW7Q5	73	3.443
MW7Q6	63	2.974
MW8Q1	52	2.453
MW8Q2	62	2.925
MW8Q3	62	2.925

Table 2.2: Meson West magnet currents for the transport of secondary beam with a nominal momentum of $+530$ GeV/c. The magnet polarities are reversed for the transport of -516 GeV/c beam, but the field magnitudes vary by not more than a few percent relative to the $+530$ GeV/c values.

momenta. Each quadrupole magnet characteristically produced a magnetic field gradient which focused the beam in a plane containing the beamline axis while simultaneously defocusing in the perpendicular plane also containing the beamline axis [37]. To provide focusing or parallelism throughout an extended region, it was necessary to employ quadrupole doublets or triplets in close proximity which were approximately matched in field strength.

As with the dipole magnets, calibration curves were available for the 3Q120 quadrupole magnet [36] (Figure 2.3). The resulting current versus field-gradient relation is given by $G(I) = 0.019I$ where G is the field gradient in kG/in. Considerable shaping of the beam distribution was accomplished using numerous quadrupole magnets in the MW beamline. Typical currents and field gradients are listed in Table 2.2.

Segmented Wire Ion Chambers

Segmented Wire Ion Chambers (SWICs) were used to monitor the spatial distributions of charged secondary beam particles at various locations in the MW beamline. SWICs consist of AuW plated Ni wire anodes enclosed between two windows of Ti [38] with wire spacings of either 1 or 2 mm. The wires are typically oriented either horizontally or vertically, transverse to the beam direction. The space between the windows was filled with a mixture of Ar and CO₂ gases. Passing charged beam particles ionize the gas resulting in a drift of electrons to the anode wire. The resulting signals were used to monitor the transverse distributions of beam particles during data acquisition. This information was used to steer the beam and control the beam optics to meet experimental requirements. SWIC profiles were also used to assist in modeling the beam distributions in the off-line data analysis (Chapter 5).

2.2 The Meson West Beamline Čerenkov Detector

The production of Čerenkov radiation provides a non-destructive means of identifying the mass (i.e. *tagging*) of the charged constituents of high energy particle beams. The MW Čerenkov detector [39] was a modified differential [40] counter with three concentric rings of photomultiplier tubes (hereafter referred to as *phototubes*) for simultaneous identification of the three dominant types of charged particles in the MW beam.⁶ The MW Čerenkov detector used gaseous helium as the radiating medium.

As a thorough understanding of the theory of Čerenkov radiation was essential for the detector design and operation and for the subsequent data analysis, a brief review of the theory is provided here followed by a detailed description of the hardware, optics, data acquisition software, electronics and the gas pressure/temperature control system of the Čerenkov detector. Additional details may be found elsewhere [41]. A complete description of the analysis of data acquired with the Čerenkov detector is provided in Chapter 5.

2.2.1 The Theory of Čerenkov Radiation

Semi-Classical Theory

It is well known [42] that charged particles propagating faster than the speed of light in the surrounding medium will emit light, known as *Čerenkov radiation*, in the visible and ultraviolet regions of the spectrum. The light is emitted in a forward cone relative to the particle's direction of propagation. The cone angle,

⁶The mass of the muon is too close to that of the pion to be resolved with the Čerenkov detector. A measure of the muon content of the beam was provided by the forward calorimeter as discussed below and in Chapter 5.

known as the Čerenkov angle, is given by

$$\cos \theta_0 = \frac{1}{n\beta} \quad (2.2)$$

where θ_0 is the Čerenkov angle, $\beta=v/c$ is the speed of the charged particle and n is the refractive index of the medium. Because the radiation cone opens outward, away from the particle's direction of propagation, each photon can be detected without intercepting the trajectory of the particle.

The Čerenkov angle clearly depends on the mass of the incident particle via the equation

$$\beta = \frac{p}{\sqrt{p^2 + m^2}}. \quad (2.3)$$

where p and m are the particle's momentum and mass, respectively. The dependence of the Čerenkov angle on mass provides a non-invasive means of uniquely identifying charged particles of known momentum.

The refractive index for gaseous helium as a function of wavelength at STP is given by [43]

$$n_0^2 = 1 + 6.927 \times 10^{-5} \left(1 + \frac{2.24 \times 10^5 \text{Å}}{\lambda^2} + \frac{5.94 \times 10^{10} \text{Å}}{\lambda^4} + \frac{1.72 \times 10^{16} \text{Å}}{\lambda^6} + \dots \right) \quad (2.4)$$

where λ is given in Ångstroms. Including temperature and pressure dependence yields [44]

$$n - 1 = \frac{PT_0 Z_0 (n_0 - 1)}{TZ_i \left[1 + \frac{1}{6} (n_0 - 1) \left(1 - \frac{PT_0}{T} \right) \right]} \quad (2.5)$$

where P is the operating pressure of the medium normalized to standard pressure, $T_0 = 273$ K, T is the operating temperature of the medium, $Z_0 = 1.00053886$ is the (unitless) compressibility of helium at STP and

$$Z_i = 1 + \left(7.4082 \times 10^{-9} T^2 - 6.179 \times 10^{-6} T + 1.67442 \times 10^{-3} \right) P \quad (2.6)$$

is the (unitless) compressibility at the operating temperature and pressure.

For incident +530 GeV/c protons, $1 - \beta = 1.60 \times 10^{-6}$. With $\lambda = 200$ nm,⁷ $T = 293$ K and $P = 6.24$ psia (a standard operating pressure) we find that $n - 1 \approx 1.5 \times 10^{-5}$ so that $\theta_0 \approx 5$ mrad.

Classically, the energy radiated per unit path length by a unit charge is of the form

$$\frac{dE}{dx} = \frac{e^2}{c} \int \left(1 - \frac{1}{n^2\beta^2}\right) \omega d\omega. \quad (2.7)$$

It can be shown [45] from a semi-classical treatment of this equation that the wavelength distribution of emitted Čerenkov photons is given by

$$\frac{dN}{d\lambda} = \frac{2\pi\alpha_{em}L \sin^2 \theta_0}{\lambda^2}. \quad (2.8)$$

Here α_{em} is the fine structure constant, dN is the number of photons emitted with wavelength between λ and $\lambda + d\lambda$ and L is the length of radiating medium to which the particle is exposed. Integrating over all relevant wavelengths yields the mean number of photons emitted by a single passing charged particle of mass m and momentum p .

Quantum Mechanical Corrections

It can be shown that quantum mechanical corrections to the above formulae result in a negligible perturbation to the Čerenkov angle (Equation 2.2) and the mean number of emitted photons (Equation 2.8). Jelley et al. [45] have shown that the second order quantum mechanical correction to Equation 2.2 is

$$\cos \theta = \frac{1}{n\beta} + \frac{\Lambda(n^2 - 1)}{2\lambda n^2} \equiv \cos \theta_0 + \Delta \quad (2.9)$$

where

$$\Lambda = \frac{\sqrt{1 - \beta^2}\lambda_0}{\beta} = \lambda_0 \frac{m}{E}. \quad (2.10)$$

⁷This is the peak wavelength of the Čerenkov wavelength distribution taking the optical cut-offs of the Čerenkov counter into account.

Here $\lambda_0 = h/mc = 2.4$ pm is the Compton wavelength of the electron and E is the energy of the particle. For incident +530 GeV/c protons we find that $\Delta \approx 10^{-13}$. This correction is clearly negligible for our purposes.

The quantum mechanical corrections for the radiated energy require additional terms [45]:

$$\frac{dE}{dx} = \left(\frac{e}{c}\right)^2 \int \left(1 - \frac{1}{n^2\beta^2} \left\{1 + n^2 \left(\frac{\hbar\omega}{mc^2}\right) + \frac{n^4}{4} \left(\frac{\hbar\omega}{mc^2}\right)^2\right\}\right) \omega d\omega. \quad (2.11)$$

For +530 GeV/c protons, the quantum mechanical correction terms are found to be on the order of 10^{-9} and 10^{-18} , respectively, relative to the leading classical term of unity. The quantum mechanical corrections to the energy loss per unit path length and, hence, the variation in the number of emitted photons is also entirely negligible.

Diffraction Effects

A more complete treatment of the semi-classical theory of Čerenkov radiation [46] requires a modification of Equation 2.8 to include angular smearing due to diffraction effects:

$$\frac{dN}{d\lambda d \cos \theta} = \frac{2\pi\alpha L \sin^2 \theta_0}{\lambda^2} \left(\frac{L}{\lambda}\right) \left\{\frac{\sin \phi}{\phi}\right\} \quad (2.12)$$

where

$$\phi(\theta) = \pi \frac{L}{\lambda} \left[\frac{1}{n\beta} - \cos \theta \right]. \quad (2.13)$$

When the quantum mechanical formula for the Čerenkov angle is included to second order (Equation 2.9) it can be shown that angular smearing of the photon distributions will occur. This results in a smearing of the resulting *pressure curves* (discussed in Chapter 5) given by

$$\Delta P(\text{psia}) = \frac{\theta \Delta \theta}{g}, \quad (2.14)$$

where $g = 2.2 \times 10^{-6} \text{ psia}^{-1}$ is a characteristic of helium gas⁸ at room temperature and

$$\Delta\theta = \frac{\lambda}{L \sin \theta}. \quad (2.15)$$

For a peak wavelength of 200 nm, a counter length of about 43 m and a characteristic Čerenkov angle of $\approx 5 \text{ mr}$ we find that $\Delta\theta \approx 10^{-6}$ so that $\Delta P \approx 0.002 \text{ psia}$. This value is comparable with the pressure stability of the Čerenkov detector (see below) and is well below the level of precision required to reliably establish particle identities ($\approx 0.01 \text{ psia}$) and, so, diffraction effects are neglected in this analysis.

2.2.2 Čerenkov Hardware

Pressure Vessel

The Čerenkov detector consisted of a 43.40 m long, cylindrical, stainless steel pressure vessel (Figure 2.4). Gaseous helium served as the radiating medium for passing charged particles. The counter was operated at gas pressures between about 4 and 8 psia. The vessel was divided into two major parts. The *main vessel* was 33.05 m long with an inner diameter (i.d.) of 52 cm. To provide additional radiating material and, hence, more generated photons, a 10.35 m long cylindrical *extension vessel* was connected directly to the main vessel forming a single pressurized chamber. The extension was divided into three sections. The most upstream section (relative to the direction of beam propagation) was 9.14 m long with an i.d. of 11 cm. The next section was 0.61 m long with a T-section of i.d. 21.6 cm for connection to a vacuum pump (described below) and a bellows which was removed when opening the detector for service. The last section was 0.60 m long with an i.d. of 11 cm and was an integral part of the flange which sealed the upstream end of the main vessel (henceforth known as the *upstream*

⁸The factor g includes information about the compressibility of helium and, so, actually depends on temperature.

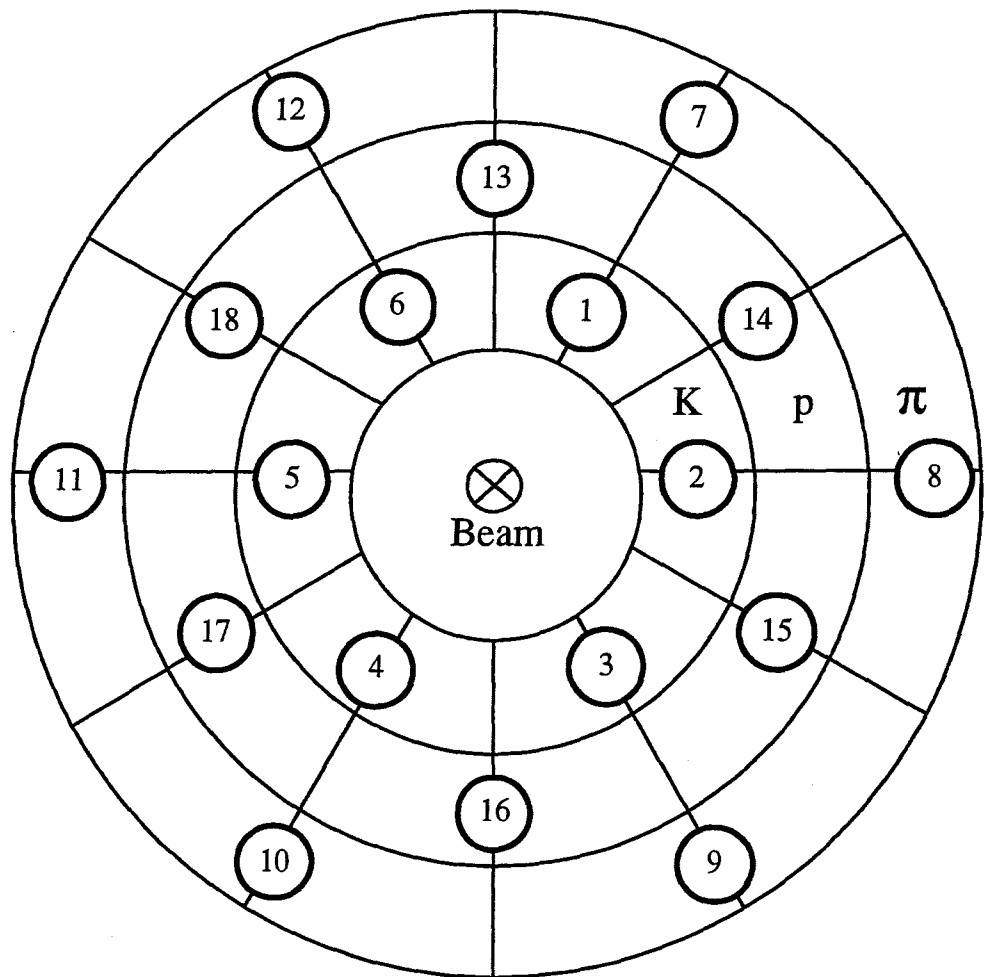
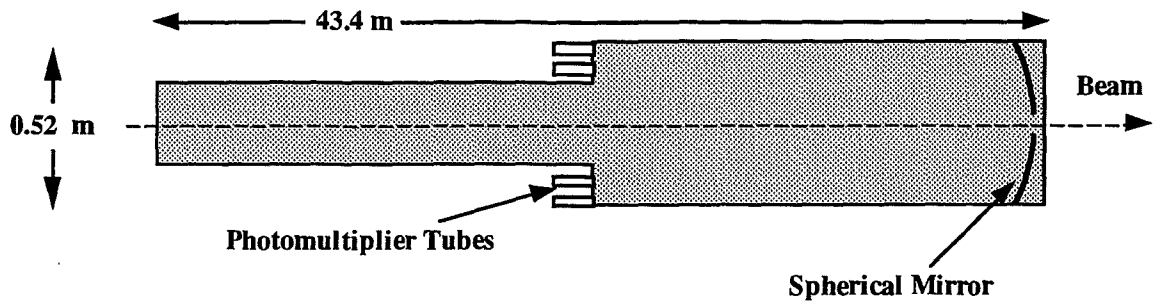


Figure 2.4: Longitudinal and transverse profiles of the Meson West Čerenkov detector. Only two rings of phototubes are shown in the longitudinal profile. Phototube mounting arrangement is shown in the transverse profile. Each ring of phototubes is labeled according to the particle which it was designed to tag.

flange).

2.2.3 Čerenkov Optics

Spherical Mirror

Čerenkov photons propagating through the counter in the direction of the incident beam (i.e. *downstream*) were reflected by a 47 cm diameter spherical mirror mounted at the downstream end of the detector. The photons then traveled back upstream parallel to the counter axis (Figure 2.5) for detection by the array of phototubes. The mirror had a radius of curvature of 64.80 m and a half-wavelength

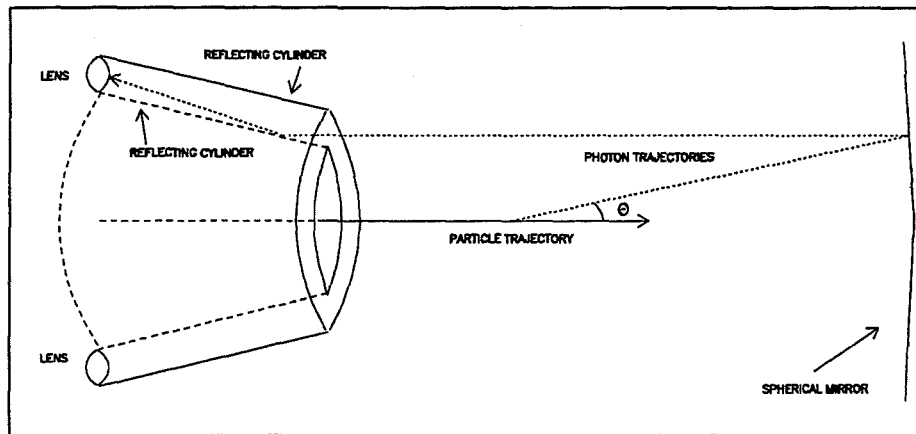


Figure 2.5: Transverse profile of raytrace of Čerenkov photon from point of emission to interception by lenses.

coating of MgF_2 to reduce unwanted multiple reflections.

Remotely driven stepper motors allowed the mirror to be rotated about vertical and horizontal axes oriented transverse to the counter axis. The mirror was aligned for data acquisition by first steering the incident 800 GeV/c beam to make the beam as parallel to the counter axis as possible while still maintaining the quality of the focus at the experimental targets. The mirror was then moved in order to center the Čerenkov light on the phototube rings.

Photomultiplier Tube Mounting

Light reflected by the spherical mirror was filtered by a system of mirrors and lenses (described below) and focused onto the faces of eighteen fast, high gain phototubes mounted external to the upstream end of the main vessel. The phototubes were mounted parallel to the counter axis in three concentric rings (Figure 2.4) with six phototubes per ring. Each ring of phototubes was named for the particle which it was designed to detect.⁹ Hence we have the proton (p), kaon (K) and pion (π) phototube rings. The phototubes in each ring were spaced azimuthally by 60° . Note that the p ring phototubes were staggered azimuthally by 30° relative to the other tubes. Each phototube was separated from the pressure vessel by a fused silica window (see below).

The internal optical system, described below, resulted in a radial shift for light arriving at the K phototubes relative to the counter axis. This required that the K phototubes be mounted closer to the counter axis than the p phototubes which were designed to identify the highest mass particle in the beam. As a result of this shift, the longitudinal focal position of light arriving at the K phototubes was shifted relative to the focal positions for the other phototubes. To compensate, the K phototubes were further offset longitudinally from the upstream flange by spacers of 16 cm length. The radial positions of the phototube axes relative to the counter axis were 16.58, 10.38 and 19.59 cm for the p , K and π phototube rings.

Counter Windows

Eighteen circular apertures of 4.9 cm i.d. were machined directly into the upstream flange to allow for passage of light from the pressure vessel to the phototubes.

⁹Note that increasing the pressure in the detector results in an increase in the Čerenkov angle for any particle at a fixed incident particle momentum. Hence, light from any particle could be made to fall within any ring of phototubes. The labels of the phototube rings merely correspond to the particle type which they were meant to tag at the design operating pressure.

The apertures were covered by fused silica windows 1.3 cm thick and 7.62 cm in diameter. The windows were mounted to the flange apertures by annular aluminum mount brackets which bolted directly onto the flange. Each mount bracket was set into a 0.64 cm deep annular depression machined directly into the flange around each aperture. A circular channel was machined into this annulus in order to accommodate a vacuum O-ring. The O-ring and the window were then held in place by the aluminum mount bracket. The window transmittances were measured at 95 to 96% throughout the relevant wavelength range.

Nitrogen Purge

As any accidental helium leakage from the counter into the phototubes would result in lowered phototube efficiency, all phototubes were offset longitudinally from the counter windows by 1.85 cm and a purge of dry N₂ was passed continuously through this gap. The windows prevented leakage of N₂ into the main vessel.

Photomultiplier Tubes and Bases

Three types of phototubes were used to detect Čerenkov photons. The phototubes on the π and p rings were all Hamamatsu R1332Q except for phototubes $p3$, $p4$ and $\pi3$ which were RCA C31000M phototubes. The K phototubes were all Philips XP2020Q phototubes. All phototubes had quartz windows with a useful diameter of 4.4 cm for light transmission in the near ultraviolet spectral region.

All phototubes were plateaued using both a ⁶⁰Co source as well as 800 GeV/c primary protons to determine the optimal operating voltages. The p phototubes operated at a bias voltage of 1650 V while the π and K phototubes operated at voltages of 1750–1800 V. Voltage was applied to each phototube through a fast base.¹⁰ Voltage was supplied by a LeCroy 1440 Programmable Multichannel High

¹⁰Designed by the Fermilab Physics Department, Electrical Engineering Division.

Voltage Supply [47] maintained in the MW experimental hall. The voltage could be controlled remotely from the MW counting house¹¹.

The Philips phototubes had characteristic gains of about 5×10^5 while the other phototubes had gains around 2.5×10^5 . Actual gains varied slightly from one phototube to another.

Lenses

Light reflected by the spherical mirror was subsequently focused onto the phototubes by one of four concentric rings of 1000-grade fused silica lenses (Figure 2.5). Each ring consisted of six plano-convex lenses. The innermost ring, radially, was the proton (p) ring, designed exclusively to focus light from protons onto the p ring of phototubes. The next ring of lenses, the kaon (K) ring, was designed to focus light from kaons to the K ring of phototubes. The third ring of lenses, known as the pion-kaon (πK) ring focused overlapping light from both pions and kaons onto special optics (described below) which separated and directed the light into the appropriate ring of phototubes. The outermost ring of lenses, the pion (π) ring, focused light from pions onto the π ring of phototubes.

The lenses were cut from plano-convex master thin lenses¹² [48] (Figures 2.6–2.9 [49]). Master lenses of two thicknesses were used. For the p and K lens rings, lenses were cut from master lenses of 2.54 cm thickness and 24.4 cm diameter. For the πK and π rings, master lenses of 3.81 cm thickness and 29.5 cm diameter were used. All lenses were cut in sections which focused light to the same focal point as that of the corresponding master lens and coincident with the design center of the corresponding mounted phototube.

¹¹The counting house was a building external to the experiment hall where remote monitoring and control of data acquisition was performed at run time.

¹²The master lenses were produced by Dynasil. The Čerenkov lenses were cut at Los Alamos National Laboratory.

Transverse to the optical axis, each lens was shaped as a section of arc. The lenses were originally cut so that the centers of the arcs would coincide with the counter axis. Later design modifications introduced small radial shifts in the mounted lens positions to improve the separation of overlapping light from pions and kaons. All lenses were cut to an azimuthal acceptance of 58° , leaving 2° for mounting purposes.

The inner (i.d.) and outer (o.d.) arc diameters were 19.050 cm and 32.588 cm respectively for the p lenses. The corresponding i.d and o.d for the K lens arcs were 32.614 cm and 33.828 cm. For the πK lens, the measurements were 33.884 cm and 35.560 cm. The π lenses had specifications of 40.818 cm and 46.025 cm. The arc centers were measured from a point which was shifted from the center of the master lens by 16.589 cm, 18.336 cm, 19.606 cm and 20.876 cm for the p , K , πK and π lenses in that order.

All lenses had a focal length of 63.0 cm at a wavelength of 300 nm. The lenses had transmittances of $\approx 80\%$ at 185 nm with a cut-off at 160 nm. The transmittance curve for the lenses is shown in Figure 2.10.¹³

Lens Mount Plate

The lenses were mounted with the optical axis parallel to the counter axis. The lenses were fixed to the upstream side of an aluminum plate machined with eighteen apertures of the same shape as the corresponding lens (Figure 2.11 [49]). The lenses were mounted with the planar side in contact with the mount plate. Each p and π lens utilized a single aperture known as the p and π lens mount apertures respectively. Each K and πK lens was very thin in the radial dimension. These lenses shared single apertures, known as the πK lens mount apertures, in pairs.

¹³The curve was digitized from data provided in the Dynasil manual as implemented in the Čerenkov Monte Carlo simulation.

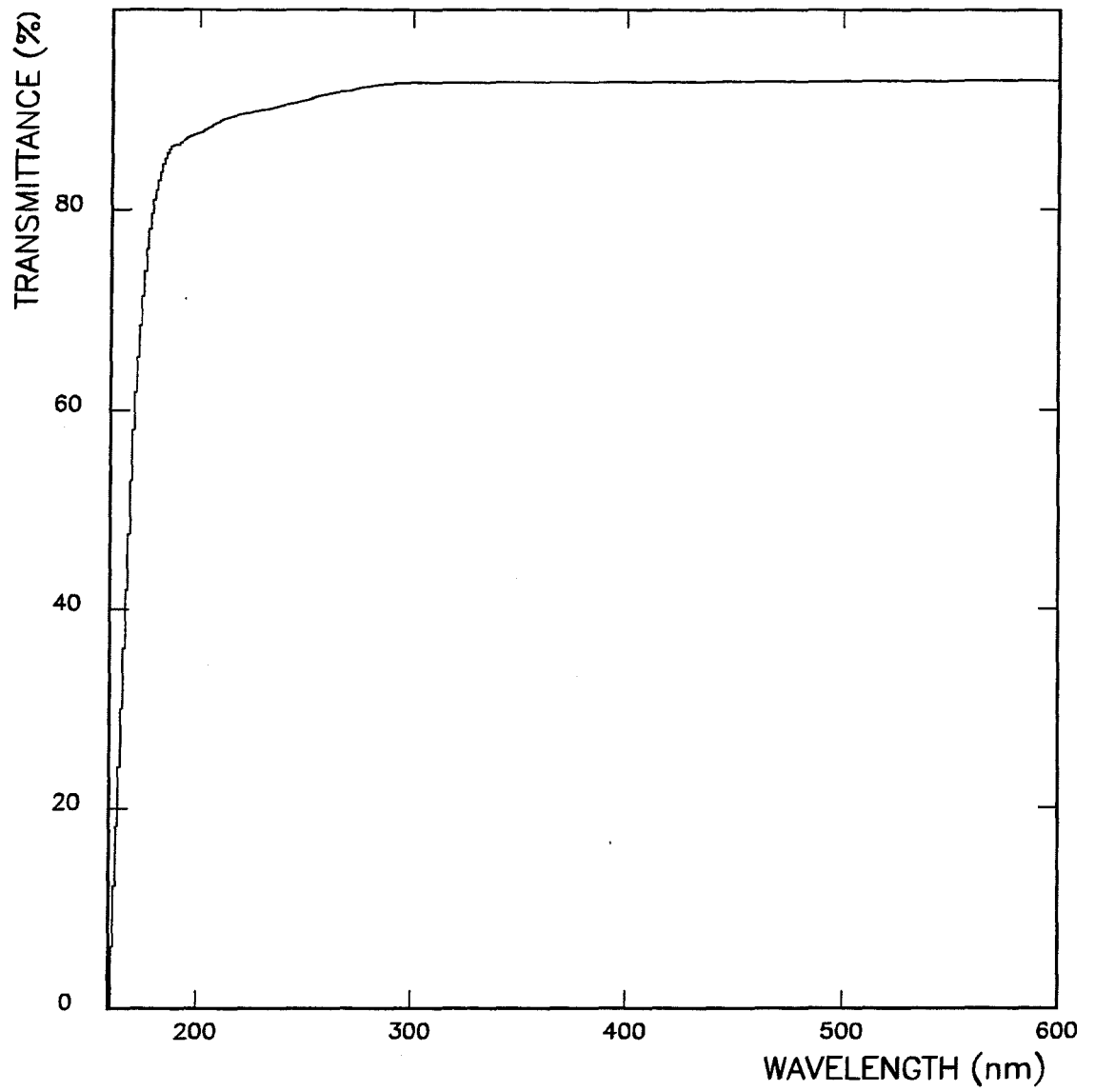


Figure 2.10: Transmittance curve for the Čerenkov lenses.

The apertures were machined to azimuthal acceptances of 57° . The inner (i.d.) and outer (o.d.) aperture diameters from innermost to outermost (radially) are 19.812 cm and 32.222 cm for the p apertures, 32.990 cm and 33.822 cm for the πK ring and 41.418 cm and 45.416 cm for the π apertures. A central circular aperture of 15.24 cm diameter allowed for the passage of beam particles.

Reflecting Cylinders

Mounted to the downstream end of the lens mount plate were three concentric, aluminum, cylindrical reflecting shells with axes parallel to the counter axis¹⁴ (Figures 2.12–2.14 [49]). The cylinders were reflective on both the inner and outer surfaces¹⁵ and were designed to help direct light from the spherical mirror onto the lenses (Figure 2.5). The cylinders were numbered 1–4 from inner to outermost radially. Cylinder 1 was in the shape of a right circular cylinder 15.4 cm long with 17.78 cm i.d. and 19.05 cm o.d. The outer two cylinders were each 15.24 cm long. Cylinder 3 had a cone angle of 1.375° on the inner surface and 13.895° on the outer surface. The i.d. and o.d. of cylinder 3 at the upstream end were 34.554 cm and 41.415 cm respectively, tapering to 33.823 cm and 33.873 cm at the downstream end. The inner and outer surfaces of Cylinder 4 had cone angles of 13.9° and 0° respectively. The i.d. and o.d. were 45.415 cm and 47.308 cm upstream, and 37.874 cm and 47.308 cm respectively at the downstream end. The region inside cylinder 1 was solely for passage of the beam. The region between cylinders 1 and 3 accepted all light incident on the three innermost lens rings. The region between cylinders 3 and 4 channeled light only onto the π lenses. Monte Carlo studies (Chapter 5) indicate that photon reflections were actually rare except in

¹⁴Another cylinder, labeled cylinder #2 was used during the 1990 data acquisition period. This cylinder was removed for the 1991 run and, so, is not discussed here, but is included in the numbering of the cylinders discussed below.

¹⁵Cylinders were 6061T6 aluminum, polished by the Howard Clausing Co.

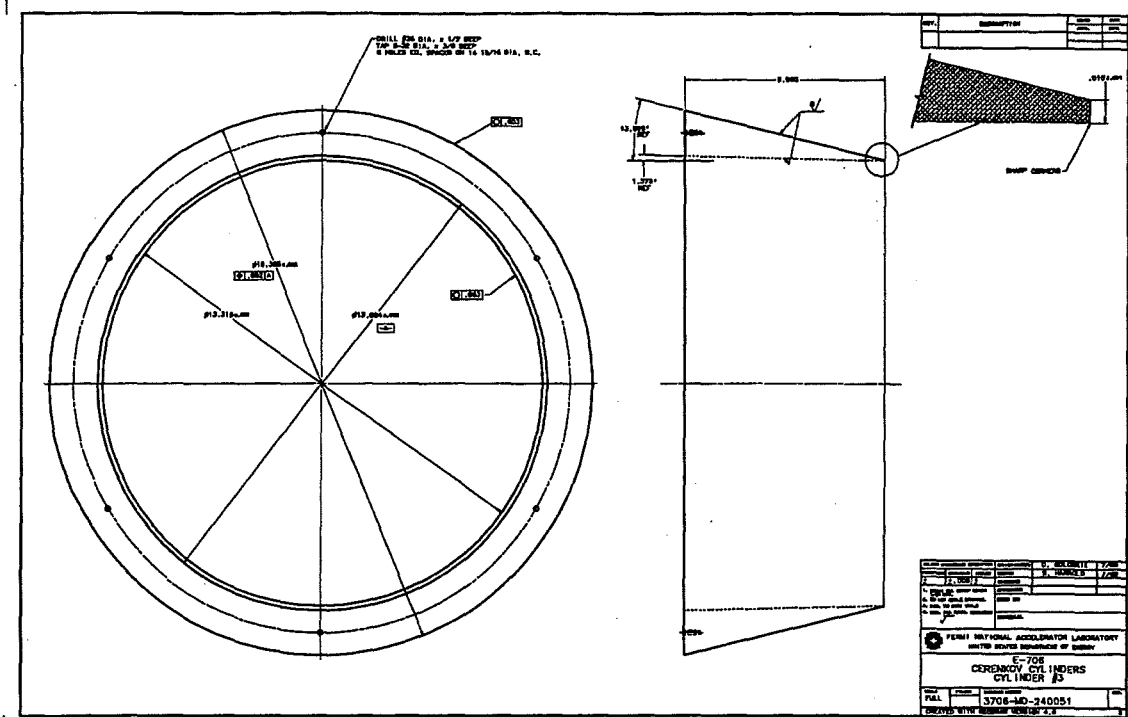


Figure 2.13: Design specifications for the middle cylinder (#3).

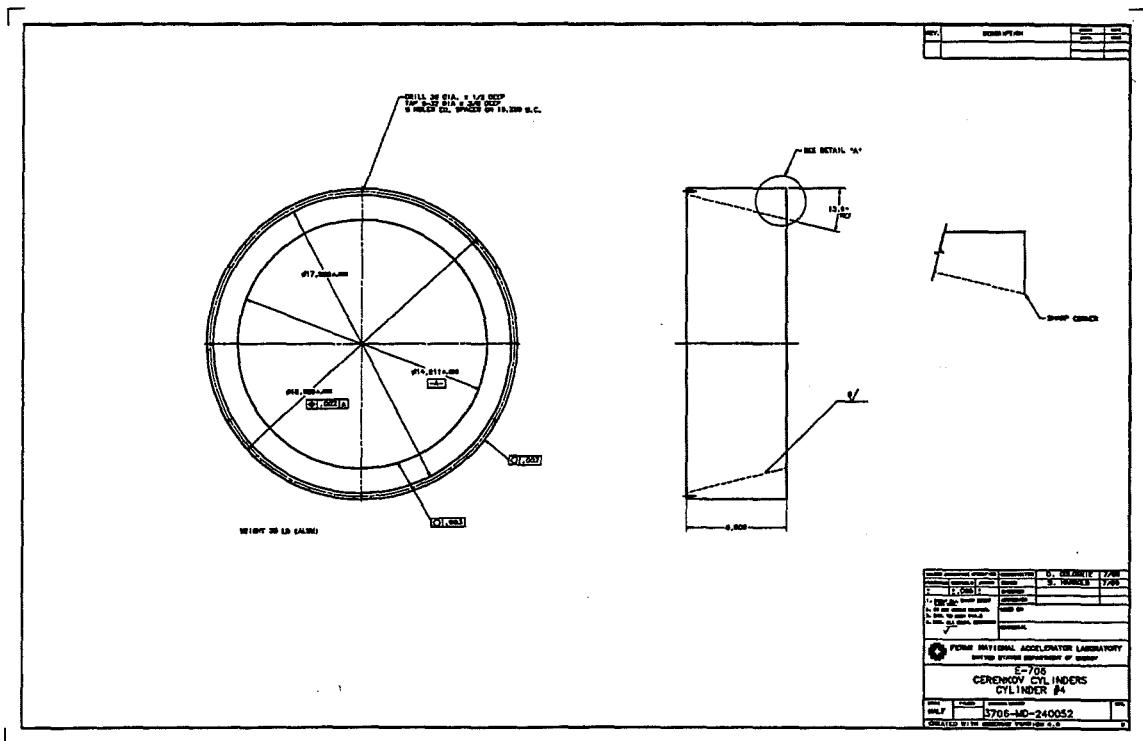


Figure 2.14: Design specifications for the outermost cylinder (#4).

the outermost channel.

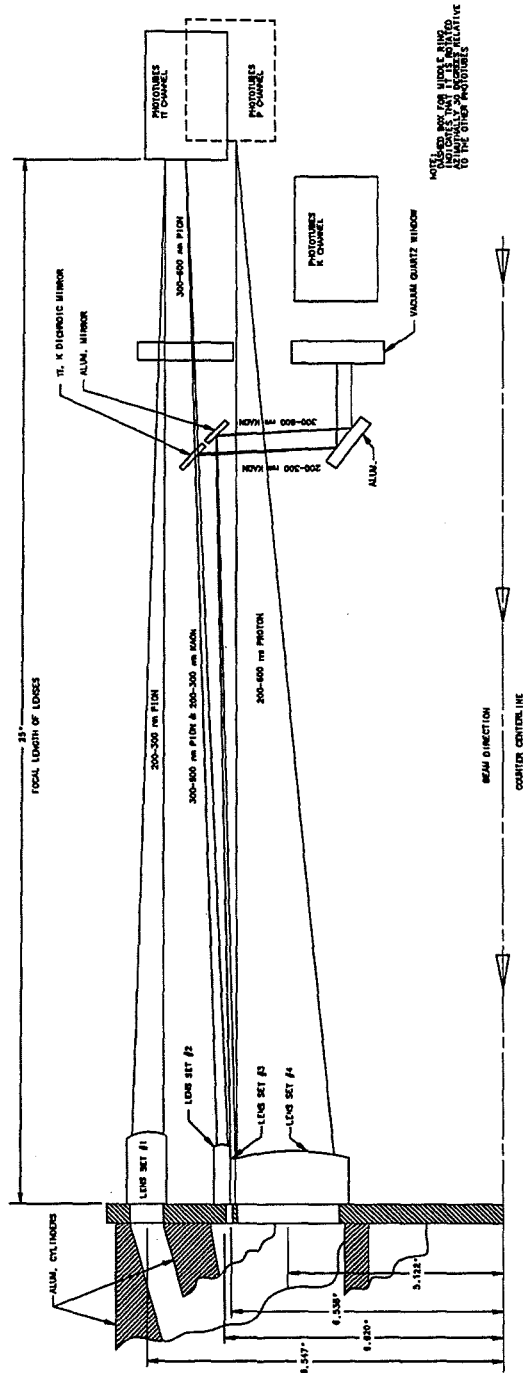
Laser Mirrors

Light from kaons in the 200–300 nm wavelength range overlapped with 300–600 nm light from pions. As this could result in mis-identification of pions or kaons, flat dichroic laser mirrors were used to separate the spatially overlapping light based on the different wavelength characteristics. The light transmitted by each πK lens was subsequently intercepted by a laser mirror¹⁶ which transmitted at wavelengths above 300 nm but reflected strongly below this wavelength. Figure 2.15 illustrates the effect of the laser mirrors in separating the overlapping light. A parameterization of the reflectance and transmittance curves is shown in Figure 2.16.¹⁷ There were six mirrors in one-to-one correspondence with the lenses. The mirrors were secured to the inside of the upstream flange by aluminum channel mounts¹⁸ (a.k.a. *laser mirror mounts*) each consisting of a rectangular backplate (for mounting to the flange) and rectangular sides perpendicular to the backplate for mirror mounting (Figure 2.17 [49]). The mirrors were mounted in two channels, each machined at 45° to the backplate. The upper channel was thinner near the backplate to accommodate a thin, flat aluminum mirror dedicated to reflecting light from the K lens into the innermost ring of phototubes. The laser mirror was held in a wider portion of the same channel just above the aluminum mirror. The two mirrors made contact to prevent loss of light. The lower channel held a thin, flat aluminum mirror used to reflect light from the upper mirrors into the K ring of phototubes. The mirrors were positioned so that the laser mirrors would intercept the overlapping light from kaons and pions while the upper aluminum mirror

¹⁶Acton Research Corporation (ARC).

¹⁷These are the curves as implemented in the Monte Carlo program (Chapter 5) and were digitized from curves provided in the ARC catalog.

¹⁸Produced by the Fermilab Physics Department, Mechanical Engineering Division.



INVEST CERENKOV COUNTER OPTICS

Figure 2.15: Schematic diagram of raytrace of Čerenkov radiation from the lenses to the phototubes. The effect of the laser mirrors in separating the overlapping light from incident kaons and pions is illustrated.

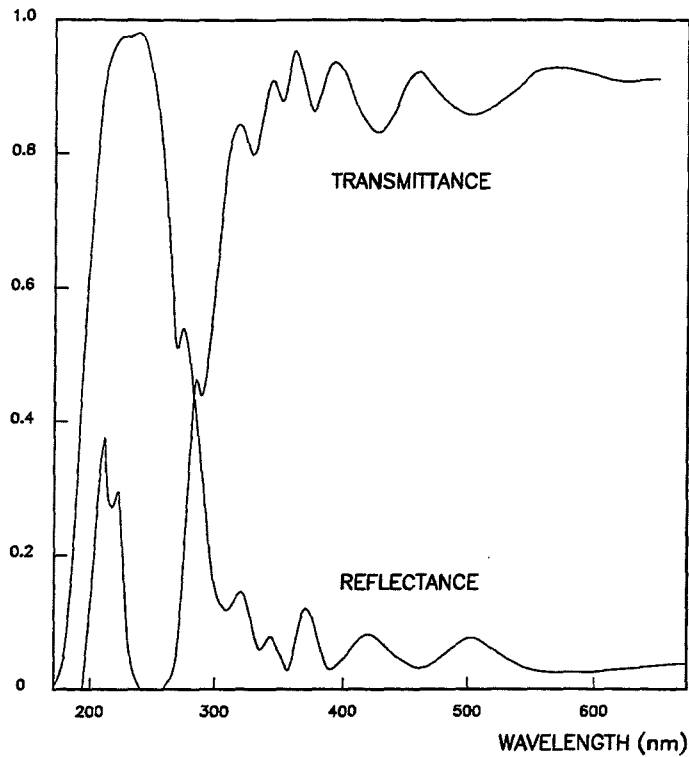


Figure 2.16: Transmittance and reflectance curves for the dichroic laser mirrors.

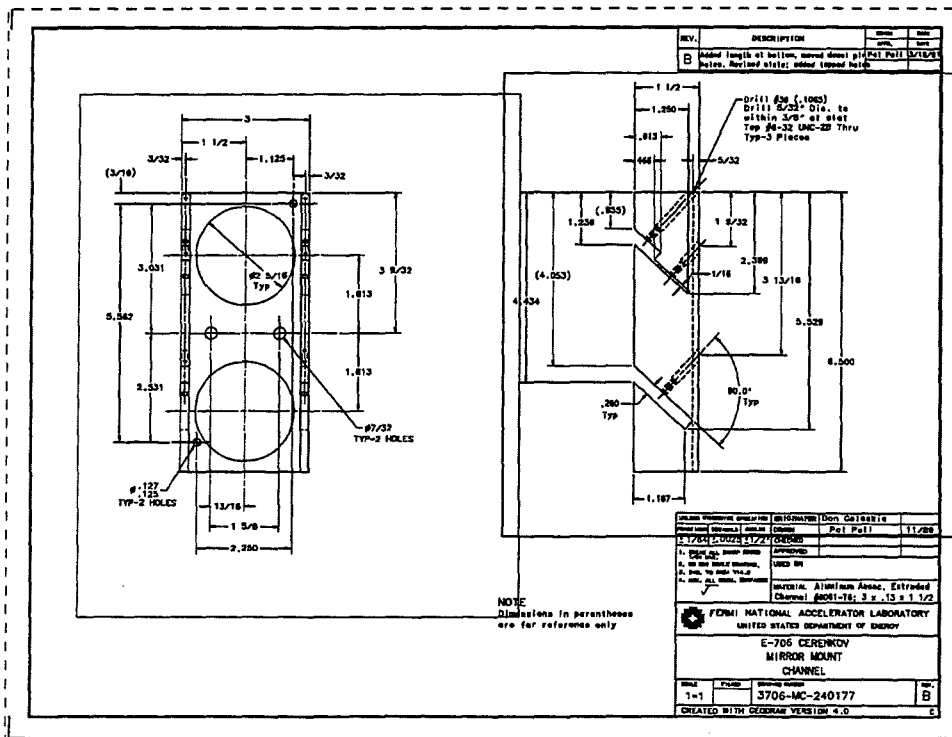


Figure 2.17: Design specifications for laser mirror mount.

intercepted light from the K lenses only.

All mirrors were 6.67 cm wide in the transverse dimension with an effective aperture of 6.13 cm when mounted. The laser mirror was 0.67 cm thick and 1.27 cm high (along the laser mirror mount channel). The upper and lower aluminum mirrors were 2.91 cm and 7.61 cm high respectively.

Two circular apertures were machined into the backplate of the laser mirror mount to allow for passage of photons to the desired phototube. Both apertures were 5.92 cm in diameter and were positioned to coincide with the radial positions of the K and π phototubes.

2.2.4 Gas System

The detector was filled with helium of 99.995% purity supplied by pressurized cylinders located in the MW9 experiment hall. Up to four cylinders could be connected simultaneously to a high pressure manifold via CGA580 connectors [50]. All cylinders shared a single regulator.¹⁹ Following the regulator was a trap²⁰ to remove moisture from the helium. The gas was then transferred ≈ 95 m to the Čerenkov detector. At the detector, the helium passed through two additional filters. The first consisted of copper (Figure 2.18). wire pads cleaned with freon. This filter removed oxygen and other impurities from the gas line. The second filter was another Scott Specialty gas moisture trap to further purify the helium. This final trap was followed by a second regulator. Pressure gauges before and after the filters were used to monitor for pressure drops.

The Čerenkov detector could be filled and evacuated both locally (in the beam-line) and remotely (from the MW counting house). These operations were usually performed remotely. Evacuation was accomplished using an Edwards E2M40 vac-

¹⁹Matheson Gas Regulator #8-250-580 rated for operation at 20-250 P.S.I.

²⁰Scott Specialty Gas Moisture Trap #53-44R

ČERENKOV GAS SYSTEM

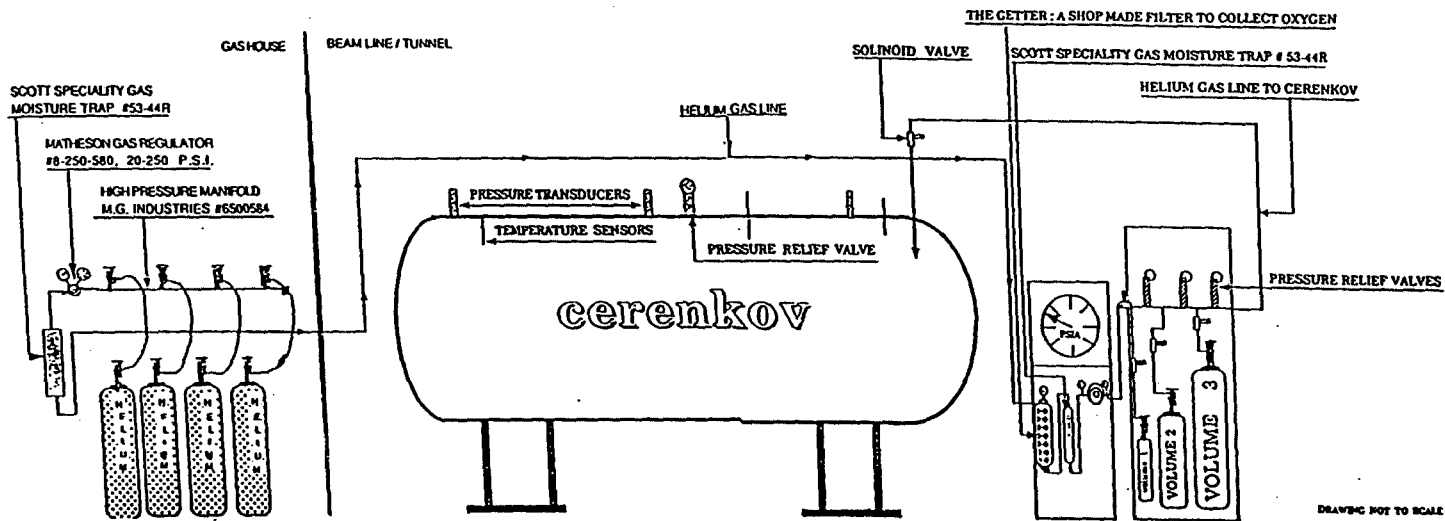


Figure 2.18: Schematic diagram of the Čerenkov gas system.

uum pump with an EH500A mechanical booster. The pump speed was rated at 190 ℓ/s . The evacuation system was separated into three sections by two electronic timers.²¹ One timer opened a solenoid valve to allow the pressures in the detector and the pump to equalize. This prevented large pressure gradients from damaging the internal optics. The second timer controlled a gate valve.²² The pump and blower started after a 2 s delay. To prevent overpressuring, the Čerenkov detector was also outfitted with relief valves.²³

The gas system was equipped with a number of solenoid valves²⁴ to control the fill rate. Following the second regulator, two solenoid valves in series allowed the detector to be filled at a uniform rate. Between these two solenoid valves were three small gas cylinders. Opening the first valve while the second (Figure 2.18). remained closed allowed the three volumes to be filled independently without filling the detector's main vessel. This valve could then be closed and the second opened to allow any one of the fixed volumes to be dumped into the main vessel. These volumes were thus used to increase the pressure in the main vessel by fixed increments. The volumes corresponded to measured pressure increments of 0.02, 0.05 and 0.12 psia. Solenoid valves connected to each of the fixed volumes allowed for independent filling and dumping of each volume. Combinations of two or more volumes could also be dumped into the counter simultaneously. The solenoid valves were leak tested prior to data acquisition.

The solenoid valves were controlled electronically and could be operated locally (beamline) or remotely (MW counting house). Switching could be (Figure 2.18). accomplished either manually or by computer control. Six basic switches were available - FILL, REFILL, VOLUME1, VOLUME2, VOLUME3 and EVACUATE.

²¹Guardian "PET 1418-PROGRAMMABLE".

²²VAT VACUUM VALVE, series 10, model 1040-ue 44, VAT INC., Woburn, MA.

²³ASME M5159 Safety Relief Valves.

²⁴ASCO 2-Way Internal Pilot Operated Solenoid Valves, (Normally Closed).

The VOLUME switches were in one-to-one correspondence with the three small fill cylinders. To dump a fixed volume of helium into the detector, any one or more of the VOLUME valves could be opened. After closing the VOLUME valves, the cylinders could be refilled by opening the REFILL switch. Opening the FILL and REFILL valves simultaneously allowed direct filling of the detector from the helium source. With the FILL valve closed, the EVACUATE switch was used to start the vacuum pump operating sequence.

The pressure was found to be stable to within < 0.005 psia during the course of any beam spill.

2.3 The Meson West Spectrometer

The MW experiment hall (Figure 2.19), located at the end of the MW beamline, housed all of the E706 detectors except the Čerenkov counter. The spectrometer included several targets (Figure 2.20) surrounded by a tracking system, electromagnetic and hadronic calorimeters downstream of the target/tracking region and a forward calorimeter. Beam definition was provided by various scintillation counters. As the π^0 candidates were reconstructed from data acquired with the electromagnetic calorimeter, emphasis will be given to this detector.

2.3.1 Hadron Shield

The hadron shield was located at the far upstream end of the experiment hall. The hadron shield consisted of a stack of steel plates 4.7 m long, 4.3 m wide and 3.7 m high used to strip off unwanted hadrons and low energy muons traveling parallel to the beam which might otherwise mimic events of interest in the calorimeters. The shield had a 10 cm wide central vertical slot. Steel slabs which normally filled this aperture could be removed to allow for calibration of the electromagnetic calorimeter by steering the beam vertically across the face of the liquid argon

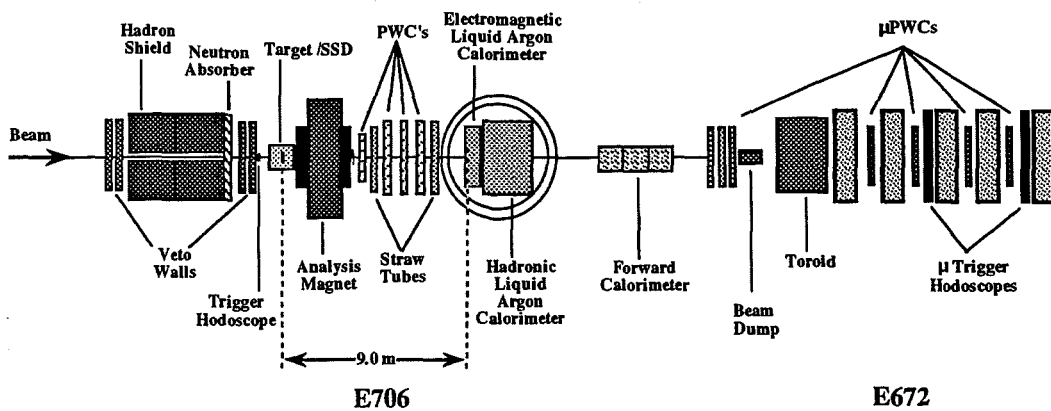


Figure 2.19: Schematic layout of the detectors in the Meson West spectrometer.

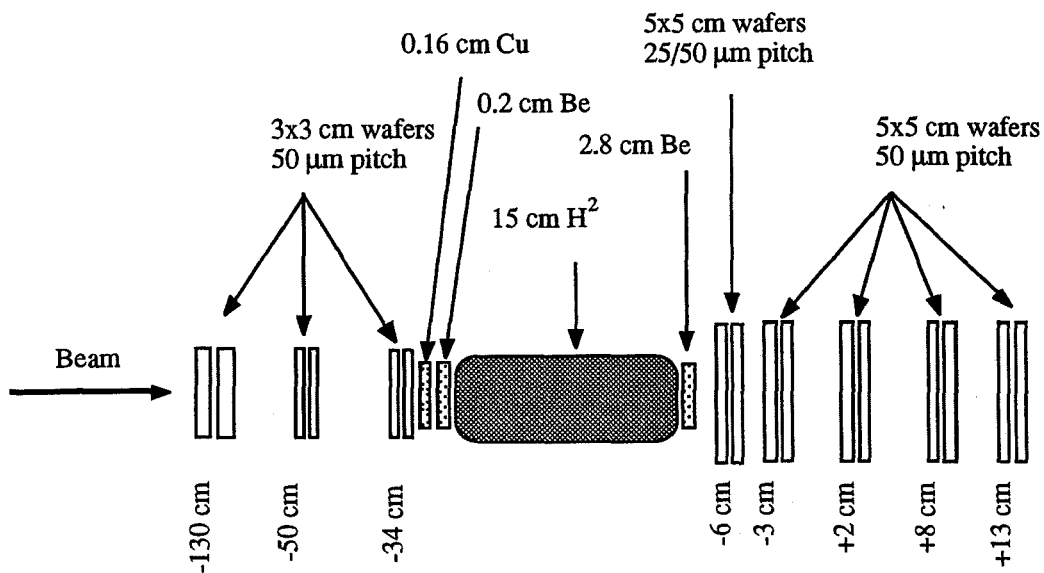


Figure 2.20: Schematic layout of the E706 targets and Silicon Strip Detectors (SSDs).

calorimeter (below). An evacuated beam pipe penetrated the center of the vertical slab to allow for unimpeded passage of the incident beam particles.

2.3.2 Veto Walls

Four planes of scintillator, known as *Veto Walls* [51] were used to identify muons in the beam halo. Low energy muons traveling at large radii with respect to the beamline were capable of mimicking high transverse momentum events in the electromagnetic calorimeter (described below). Two veto walls each were located just upstream and just downstream of the hadron shield. The information from these veto walls was used to reject events both during data acquisition (online) and during the data analysis (offline).

2.3.3 Beam Hodoscope and Hole Counters

The incident beam particles in the experimental hall were identified by the *beam hodoscope*. The hodoscope consisted of three planes each with twelve scintillator strips transverse to the incident beam. Each strip was 3.5 cm long. The strip widths varied as shown in (Figure 2.21). The three hodoscope planes were labeled the X, Y and U views in order looking downstream. Strips were oriented vertically in the X view, horizontally in the Y view and rotated at a 45° angle with respect to the vertical in the U view. The *hole counter* consisted of four rectangular scintillator paddles each with a quarter of a circular disk removed from one corner. The paddles were placed in a 2 cm × 2 cm array in such a way that the modified corners combined to form a circular hole of 0.95 cm diameter in the center of the array. The hole was centered on the beam hodoscope. Ideally, the incident beam was centered on the hole. The hole counter was then used to define the useful beam particles by vetoing events generated by particles which were far from the nominal beam centerline.

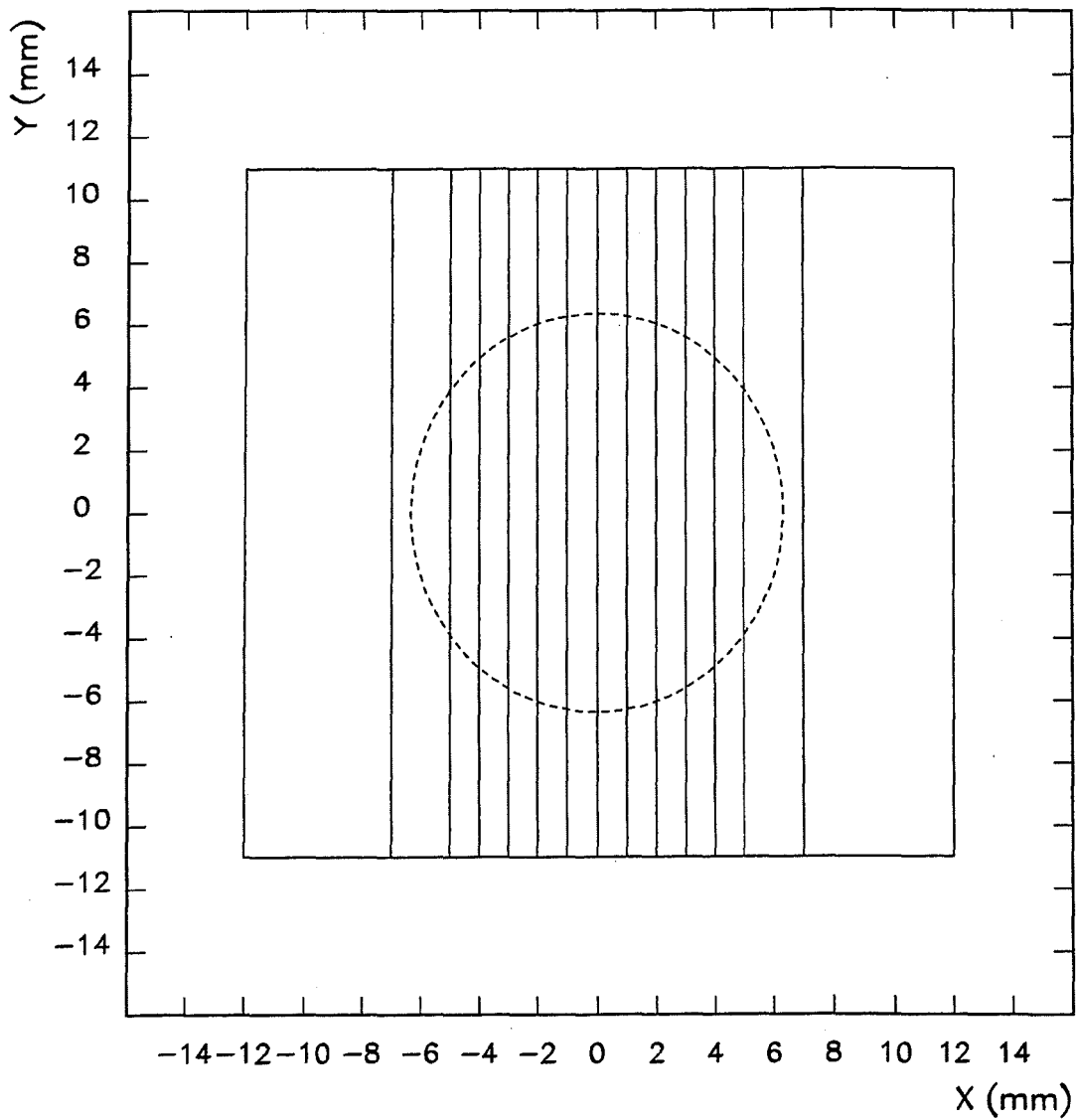


Figure 2.21: Schematic diagram of the Meson West hodoscope showing the X-view scintillator strips only. The dashed circle represents the nominal edge of the hole counter.

Target	Thickness (cm)
Upstream Be Window	0.249 ± 0.003
Downstream Be Window	0.282 ± 0.003
Be Target	$2.540 \pm$
Cu Targets	0.156 ± 0.001
LH ₂ Target	$15.340 \pm$
Si Wafers	$0.030 \pm$

Table 2.3: Lengths of the E706 targets.

2.3.4 Interaction Counters

The interaction counters were used to identify interactions of incident beam in the target region. Two rectangular scintillator paddles each were mounted to the upstream and downstream faces of the analysis magnet, shadowing the active region of the calorimeters. A hole was cut into each scintillator pair to avoid detection of non-interacting beam particles.

2.3.5 Targets

The targets used during the 1991 run included beryllium, copper, and liquid hydrogen (Figure 2.20). In addition, the silicon strip detectors (see below) provided enough silicon to serve as a fourth target material. The various targets and their lengths are listed in Table 2.3. The various target materials were employed by E706 for nuclear dependence studies. Only interactions occurring in the beryllium target are considered in this analysis.

2.3.6 Charged Particle Tracking

A high resolution tracking system [52] provided measurements of the momenta, and sign of the charges for particles produced in the targets. This information was also used to reconstruct the locations of the interactions in the targets. The tracking system included several components. The Silicon Strip Detectors (SSDs),

Proportional Wire Chambers (PWCs) and Straw Tube Chambers provided track measurements both upstream and downstream of the targets. An analysis magnet provided a transverse impulse to charged particles in order to analyze the momentum and charge of the tracks. The track positions were correlated with the positions of showers detected in the electromagnetic calorimeter.

Silicon Strip Detectors

A total of eight Silicon Strip Detector [53] (SSD) modules (Figure 2.20) measured charged particle tracks both upstream and downstream of the targets. Three modules upstream of the targets were used to measure tracks generated by the charged beam particles incident on the targets, while the five modules downstream of the targets identified the tracks of charged particles from both non-interacting beam particles as well as those produced by interactions in the targets.

Each module, except for the first downstream module,²⁵ consisted of two square planes of $300\mu\text{m}$ thick silicon wafers etched with strips of $50\mu\text{m}$ pitch. The upstream SSDs planes each measured 3 cm on a side while the downstream SSDs were 5 cm square. For each module, the strips in the first plane (looking downstream) were oriented vertically while strips in the second plane were horizontal. The SSDs had an angular resolution of 0.1 mrad and interaction vertex position resolutions of $350\mu\text{m}$ longitudinally and $10\mu\text{m}$ in the transverse dimensions.

Charge deposited by passing charged particles was collected and processed through 16-channel pre-amplifiers. The resulting signals were subsequently discriminated and latched for readout.

²⁵The first downstream SSD module was etched with strips of $25\mu\text{m}$ pitch.

Analysis Magnet

A 400 ton steel dipole analysis magnet located 2 m downstream of the targets provided a 444 MeV/c vertical impulse to charged particles produced in the targets. The magnet aperture increased from 36.5 cm by 25.4 cm at the entrance to 137.2 cm by 124.5 cm at the downstream end.

Mirror plates were mounted at both the upstream and downstream ends of the magnet to reduce field fringe effects.

Proportional Wire Chambers

Four Proportional Wire Chamber [54] (PWC) modules located just downstream of the analysis magnet were used to reconstruct the trajectories of charged particles produced in target interactions. A PWC module is shown schematically in Figure 2.22. Each PWC module consisted of four proportional wire *view* planes. The first plane had wires oriented vertically (X-view) and the second plane had wires oriented horizontally (Y-view). To correlate measurements made in the X- and Y-views, an additional pair of planes, the U-view and the V-view were included. Wires in the U- and V-views were rotated with respect to the X- and Y-views by 37° . This provided two distinct orthogonal pairs of planes resulting in unambiguous *space track* identification.

Each view plane consists of between 480 and 1120 gold plated tungsten anode wires of 20 μm diameter strung between two 25 μm thick graphite coated mylar cathode planes each roughly 2 m square. The wire spacing was 0.25 cm yielding an angular resolution of 0.3 mrad. The cathodes were maintained at a voltage of ≈ -3 kV. The region between the cathode planes was filled with a mixture of 79.7% argon, 18% isobutane, 1.1% isopropyl alcohol and 0.1% freon. Incident charged particles ionized the argon resulting in a drift of electrons to the anode

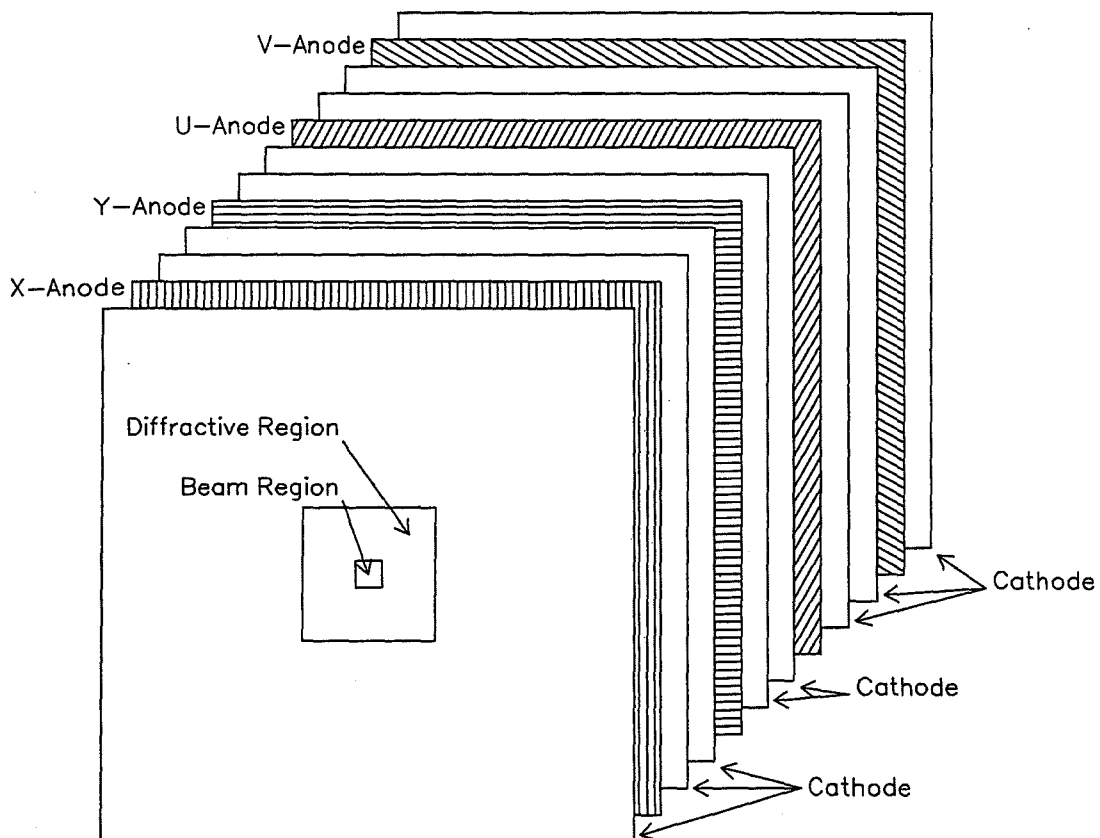


Figure 2.22: Schematic layout of the proportional wire chambers (PWCs).

wires. The resulting electronic signals induced in the wires were then amplified, discriminated and latched by the data acquisition system for readout.

Straw Tube Chambers

The Straw Tube Chambers [55], [56] were used to improve the precision of the measurement of track parameters and to assist in linking the tracks detected upstream and downstream of the magnet by the other tracking detectors. There were two straw tube chambers each consisting of two modules. Each module had four planes of straw tubes. Each plane consisted of long²⁶ mylar tubes with a total of between 128 and 166 tubes per plane. The tubes in the first module (looking downstream) were aligned vertically (X-view) and the tubes in the last module were horizontal (Y-view). Each tube had a diameter of 1.0 cm for the upstream chamber and 1.6 cm for the downstream chamber. Alternating planes of tubes in each module were offset by one-half of a tube diameter (shown in cross-section in Figure 2.23) in order to optimize the resolution of the chambers. The inside surface of each tube was coated with 8 μm of aluminum which served as the cathode. A gold plated tungsten wire of 20 μm diameter positioned in the center of each tube served as the anode. The Straw Tube Chambers had an angular resolution of 0.06 mrad. Each tube was filled with a mixture of 50% argon and 50% ethane and a voltage of 1700 to 1800 V was applied to each anode wire. Passing charged particles ionized the gas resulting in a drift of electrons to the anode wire. The data acquisition system for the Straw Tube Chambers was similar to that for the PWCs except that the signals were processed by time-to-digital converters (TDCs) prior to latching. This provided a measurement of the time for electrons to drift to the anode. Calibration studies of the electron *drift time* in the Straw Tube chambers provided measured time-to-distance relations from which the distance of

²⁶The tubes ranged in length from 167 to 280 cm depending on the module.

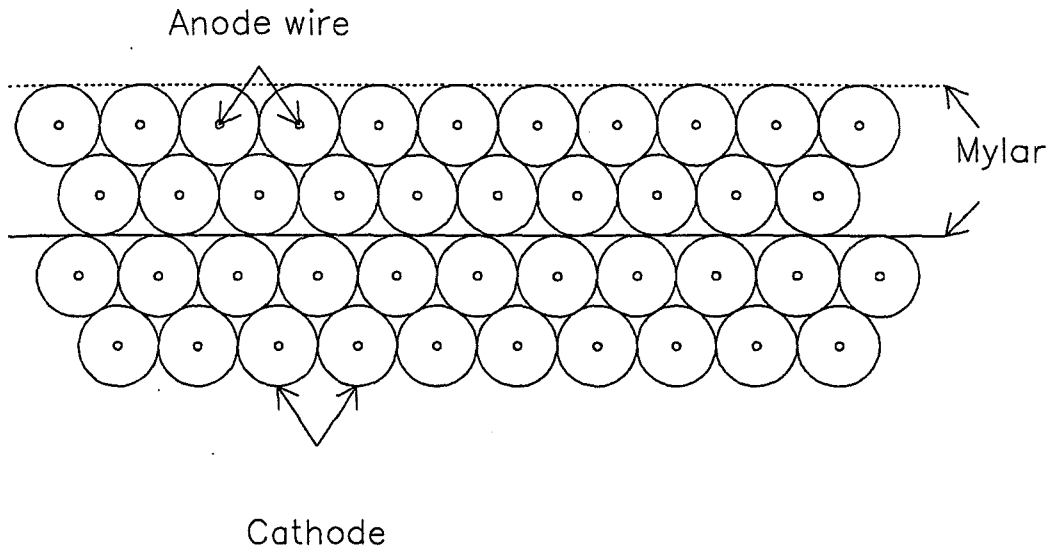


Figure 2.23: Schematic diagram of a straw tube bundle.

the charged particle path from the anode wire could be determined. This was used in the off-line analysis for improved resolution on the measurement of tracks.

2.3.7 Liquid Argon Calorimeter

The E706 liquid argon calorimeter [57], [58] (LAC) was used to identify both the electromagnetic and hadronic products of target interactions. Photons produced directly in target interactions as well as photons resulting from meson decays were identified by the electromagnetic calorimeter (EMLAC) while hadrons were identified by the hadron calorimeter (HALAC). Emphasis will be given here to the EMLAC as data from this detector were analyzed to provide a measure of the inclusive cross-sections for the π^0 mesons.

The LAC (Figure 2.24) was suspended in a cylindrical, stainless steel cryostat 5.2 m in diameter and 6.4 m deep. The cryostat was capped with a cylinder of mild steel 1.8 m high and of the same diameter as the cryostat. The cryostat and

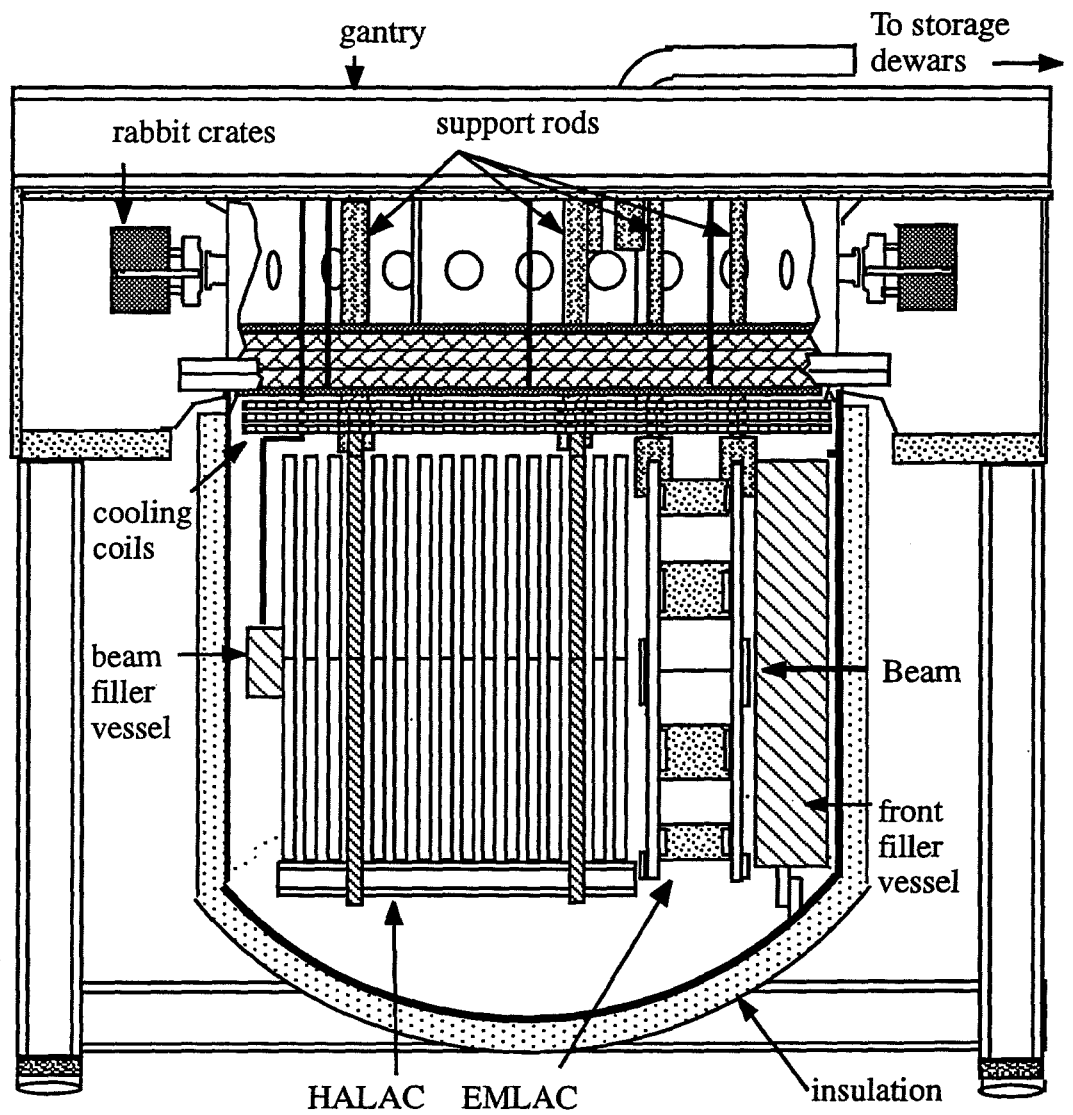


Figure 2.24: Schematic diagram of the liquid argon calorimeter (LAC).

cap were supported from a gantry constructed of steel I-beams. The gantry was mounted on Hillman rollers allowing the cryostat to be moved transverse to the incident beam for calibration studies.

The readout electronics were maintained in a Faraday room surrounding the cap of the cryostat in order to shield the electronic signals from external noise. Numerous feedthroughs in the cryostat cap allowed for readout and calibration of all instrumented channels as well as access for thermocouples, strain gauge monitors and heaters. Signals were transmitted to/from the Faraday room using optical couplers and transformers which isolated the Faraday room electronics from external noise.

The cryostat was filled with liquid argon (LAr) which served as the ionizing sampling medium for incident particles. Several layers of insulation surrounded the cryostat to maintain thermal isolation.

Along the beam axis of the calorimeters was a 40 cm diameter longitudinal region which allowed for passage of the beam which did not interact in the target. The cylinder axis was aligned with the beam axis. This central region was filled with a stainless steel *filler vessel* containing gaseous helium in order to minimize interactions of these beam particles in the calorimeter. To minimize interactions in the uninstrumented region of the cryostat upstream of the LAC, an additional filler vessel containing low density foam²⁷ was bolted to the inside of the cryostat in the region between the upstream face of the cryostat and the EMLAC.

Electromagnetic Calorimeter

The electromagnetic calorimeter (EMLAC) detected photons and electrons which were produced directly in target interactions or resulted from particle decays. The upstream face of the EMLAC was ≈ 9 m downstream of the targets and the axis

²⁷Rohacell foam.

of the EMLAC was aligned with the beam axis.

The EMLAC contained 66 cells (Figure 2.25), each with a diameter of 3 m. A cell was divided into four mechanically independent quadrants each of which consisted, sequentially, of a 0.2 cm thick lead absorber layer, a 0.25 cm gap filled with LAr, a 0.159 cm thick copper clad G-10 anode board and another 0.25 cm gap filled with LAr. Each quadrant was further divided in half to form octants for purposes of instrumentation.

The copper on the anode board was cut into strips either radially (ϕ -strips) or azimuthally (r -strips). The anode boards alternated between r -boards and ϕ -boards with the most upstream plane having r -strips.

The lead absorber converted incident photons into e^+e^- pairs. The pairs would subsequently bremsstrahlung and the process repeated resulting in showers of e^+e^- pairs in the lead. The cascade of e^+e^- pairs ionized the LAr and the resulting charge produced detectable currents in the anode board strips which were subsequently read out by the EMLAC electronics. This provided a direct measure of the energy of incident showers. Various calibrations, discussed in later chapters, were performed in order to establish the relationship between the charge and the detected energy of the incident particle.

The ϕ -strips allowed for measurement of the azimuthal positions of showers. The energy resolution at large radii and correlations between energy detected on r - and ϕ -strips were both enhanced by dividing each ϕ quadrant into inner and outer regions with a boundary at 40.2 cm. There were 96 inner ϕ -channels and 192 outer ϕ -channels in each quadrant.

As showers opened outward from a common vertex in the target, the centroid of a single shower in the EMLAC will shift towards larger radius as the shower passes through the EMLAC. To facilitate shower reconstruction, the corresponding r -strips in consecutive cells were radially offset and increased in width from the

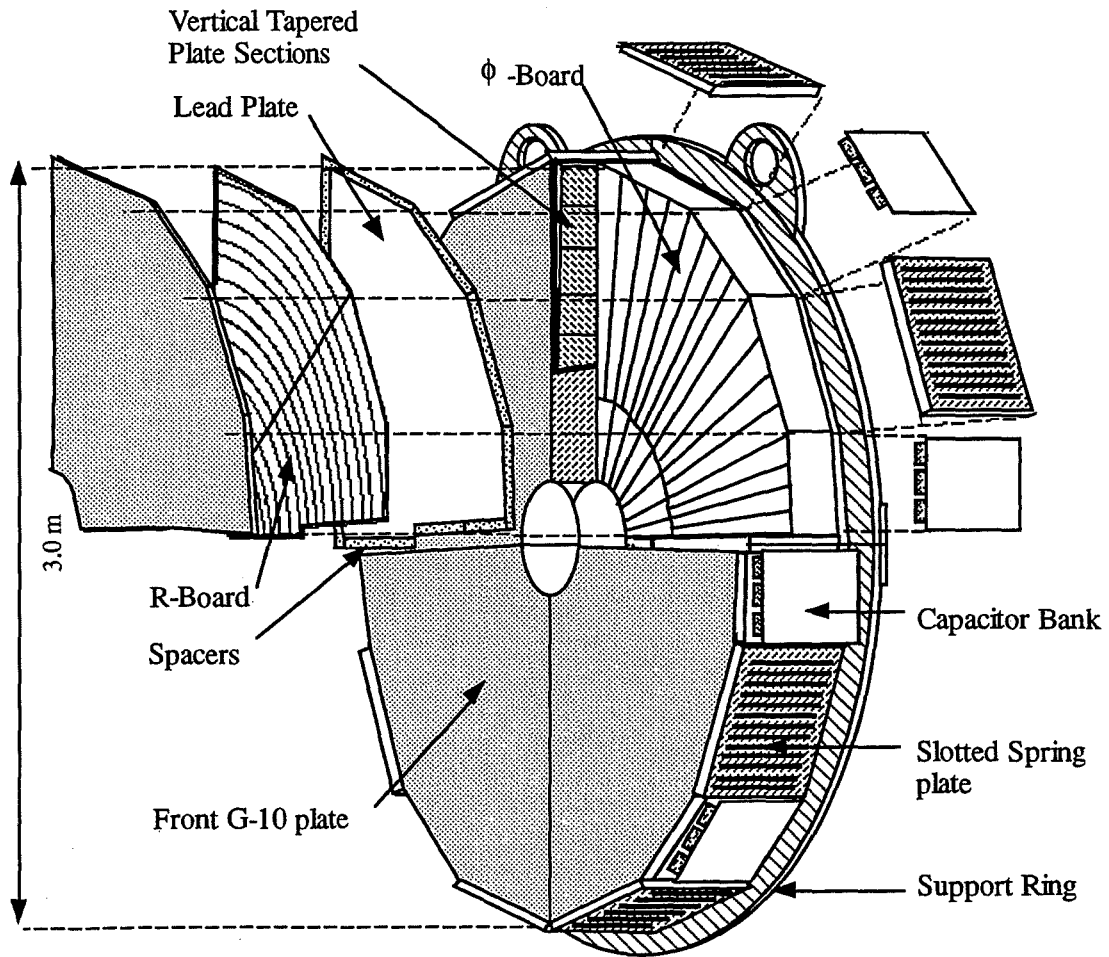


Figure 2.25: Schematic diagram of an electromagnetic calorimeter (EMLAC) cell.

front to the back of the detector. These strips were said to be *focused* on the target region. The focus point was located 900 cm upstream of the EMLAC. Focusing was used to reject showers for which the corresponding particle trajectories did not point back to the target region. The strip widths on the first r -board were 0.55 cm.

The resulting electronic signals were summed separately for the 11 most upstream r -boards and for the 22 downstream r -boards. These were referred to as the *front* and *back* sections of the EMLAC, respectively. The ϕ -plane readouts were summed in the same fashion. The front and back sections were read out independently with a total of 6272 readout channels.

Hadron Calorimeter

In addition to the EMLAC, the cryostat also housed a calorimeter designed to detect hadrons produced in target interactions [59]. The hadron calorimeter (HALAC) consisted of 53 cells divided into a *front* section of 14 cells and 39 in the *back* section. Each cell was 4 m in diameter and consisted of a 2.54 cm thick 410 stainless steel absorber followed by anode planes sandwiched between two double sided copper clad $G-10$ boards which served as cathodes. Between the anode and cathode planes there was a 3 mm gap filled with liquid argon. The anode plane consisted of two copper clad $G-10$ sheets placed back-to-back so that the copper faced outward. The copper was cut into equilateral triangular "pads" which, like the EMLAC, were focused at the target. (Figure 2.26). The large pad size was chosen because hadronic showers tended to be much broader than electromagnetic showers.

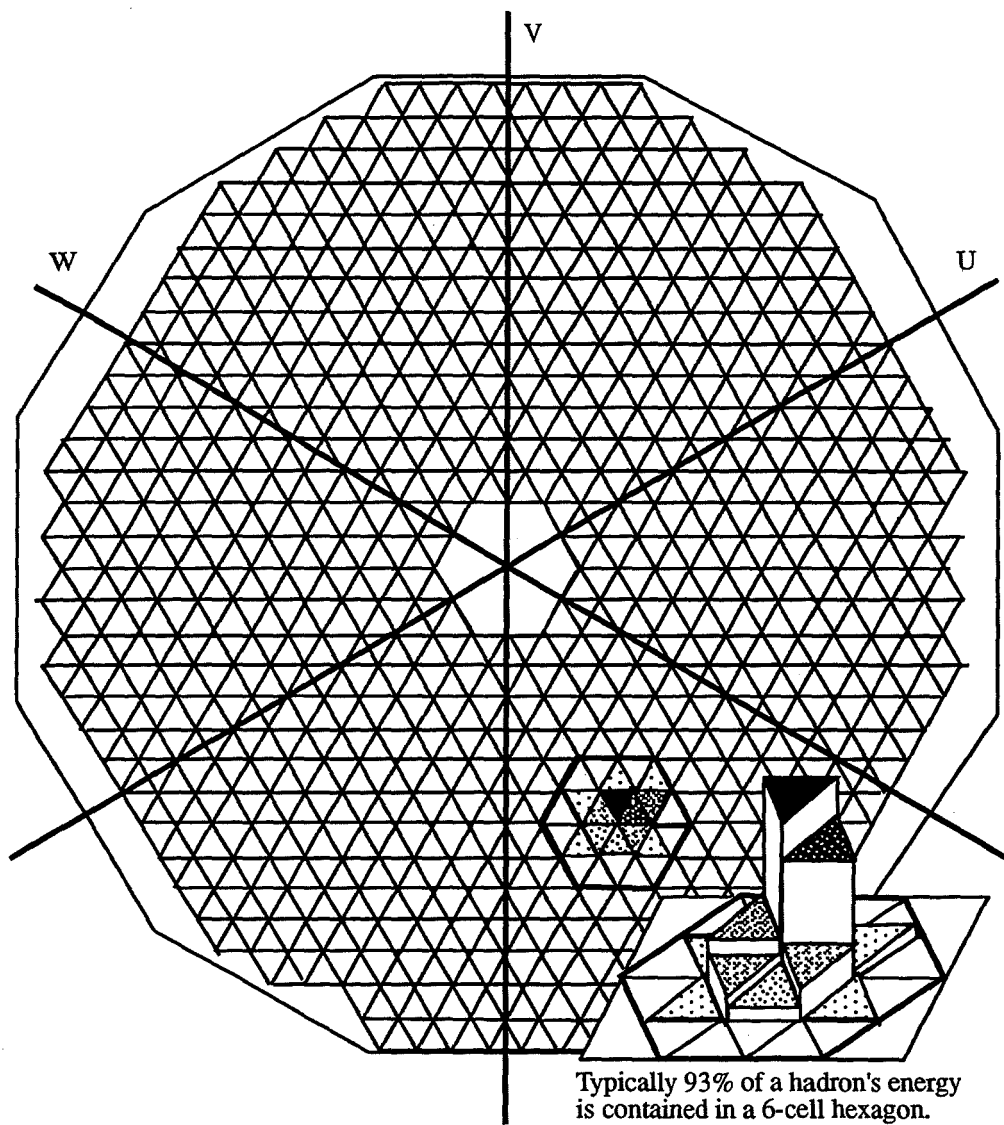


Figure 2.26: Schematic diagram of an hadron calorimeter cell showing the triangular readout pads.

2.3.8 Forward Calorimeter

The forward calorimeter (FCAL) [60] was designed to measure the energy carried by products of target interactions which passed completely through the central hole in the LAC. The FCAL consisted of three modules each 1.14 m in diameter (Figure 2.27). Each module contained 32 steel plates each 1.9 cm thick alternating

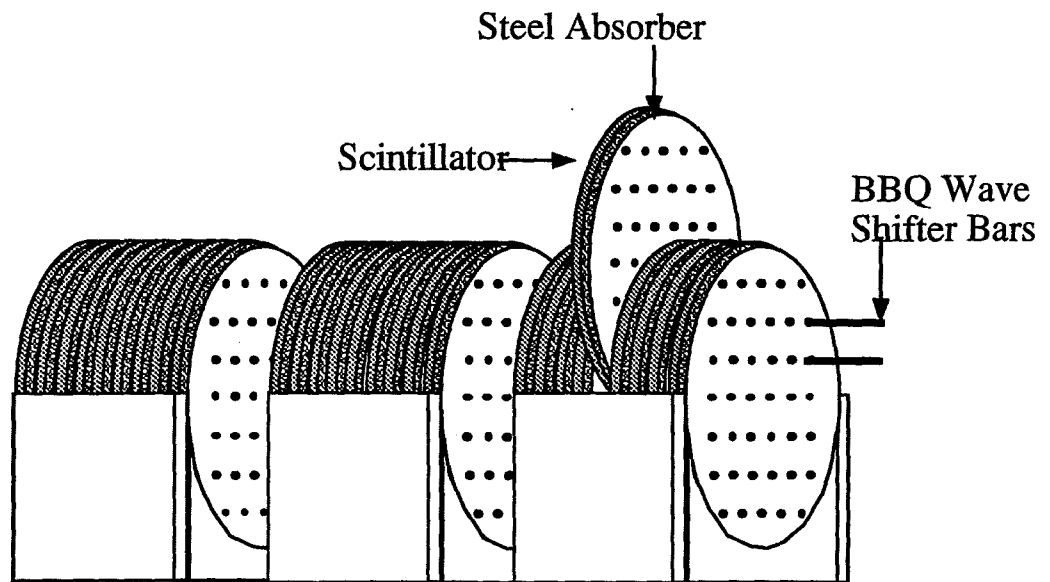


Figure 2.27: Schematic diagram of the forward calorimeter (FCAL).

with 0.48 cm thick scintillator sheets for a total of 10 interaction lengths of material. A rectangular array of 76 longitudinal holes in each module were filled with acrylic wave shifter rods. The rods shifted ultraviolet light from the scintillators into the visible region for detection by phototubes. Non-interacting beam particles passed

through a central aperture 3.2 cm in diameter.

The forward calorimeter was also used to measure the energy deposited by beam muons [61] thus providing a measure of the muon content of the MW beam. The impact of these measurements on the Čerenkov data analysis is discussed in Chapter 5.

Chapter 3

E706 Data Acquisition System and Triggers

The E706 general data acquisition (DA) system [62] (Figure 3.1) was controlled by a DEC μ VAX running the VAXONLINE data acquisition control program [63]. The VAXONLINE software was divided into four primary tasks. GLOBAL_MENU served as the user interface, RUN_CONTROL controlled the data acquisition, data readout by the various devices were concatenated by EVENT_BUILDER and OUTPUT wrote the resulting data onto 8mm cassette tapes for storage and off-line analysis.

During the 1991 data acquisition period, a total of about 4.1×10^7 events were written to ≈ 1000 tapes. Data were divided into sets known as *runs*. The total accumulated statistics for all data acquisition periods are summarized for each mode of operation in Table 3.1.

The data which the μ VAX concatenated were read from four devices: Three PDP-11 computers (referred to as ROCH, MU and NEU) and FASTBUS [64]. FASTBUS handled data from the LAC and straw tube chambers. The ROCH-PDP was responsible for the FCAL readout, MU-PDP read out data from the E672 di-muon system and NEU-PDP read out the trigger, Čerenkov, PWC, SSD and other discrete logic information. All PDP readouts were based on the CAMAC [65]

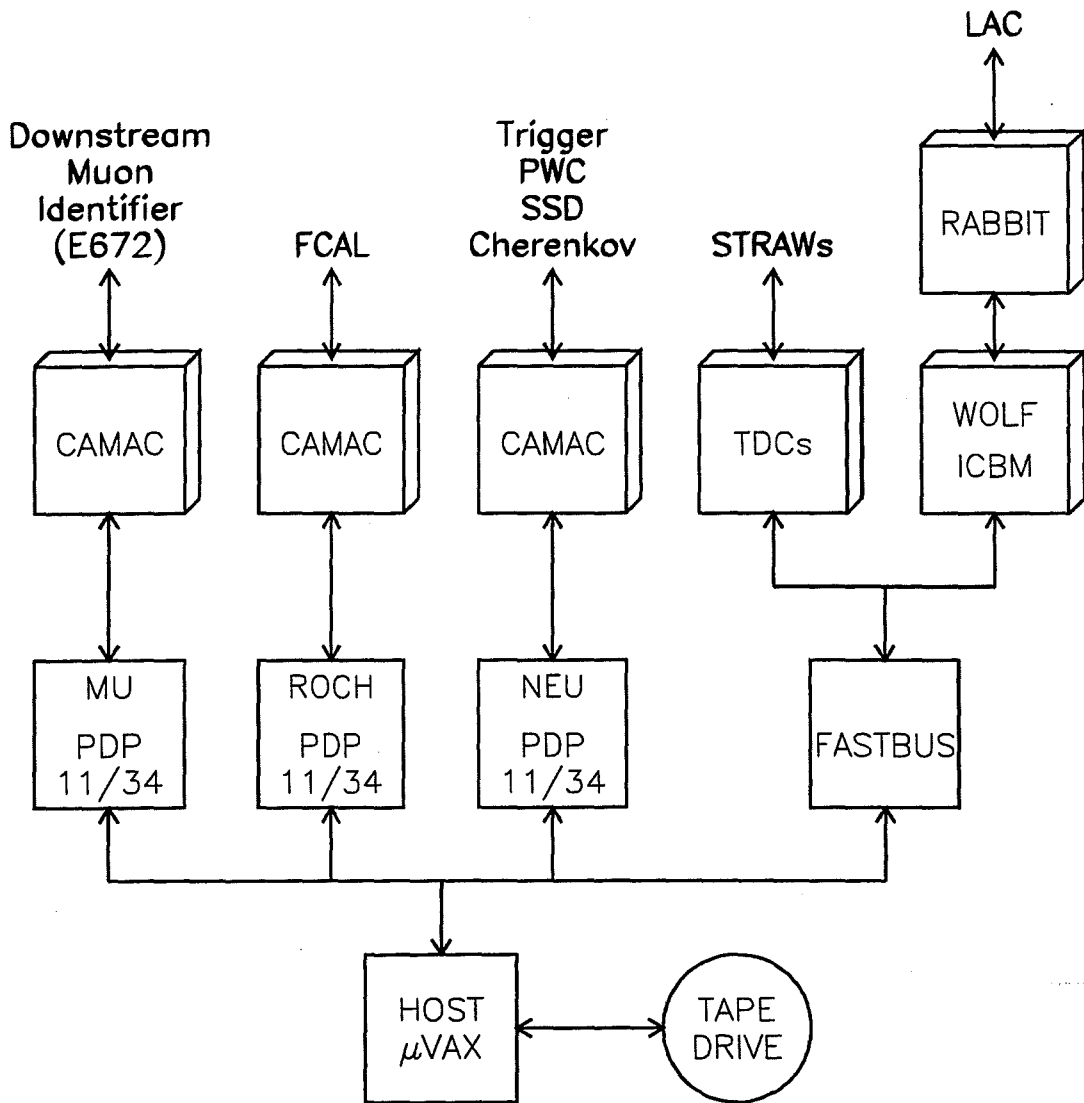


Figure 3.1: Schematic diagram of the data acquisition system.

Data Acquisition Period	Mode of Operation	Number of Recorded Events
1988	-500 GeV/c	2×10^6
	+500 GeV/c	3×10^6
1990	-515 GeV/c	30×10^6
1991	+800 GeV/c	23×10^6
	+530 GeV/c	14×10^6
	-516 GeV/c	4×10^6

Table 3.1: Summary of the total statistics accumulated by E706 for each mode of operation.

communications protocol.

A separate system was used to control and monitor the pressure and temperature of the Čerenkov detector. This system was also used to acquire data which were used exclusively in the Čerenkov analysis. Only the EMLAC and Čerenkov data acquisition systems are described in detail here.

3.1 Čerenkov Data Acquisition System

3.1.1 Čerenkov Pressure and Temperature Monitoring

Three pressure transducers monitored the gas pressure in the Čerenkov detector. One transducer was located at the upstream end of the detector¹, one at the center² of the detector and one at the downstream³ end. All transducers functioned in the pressure range of 0 to 25 psia with readout voltages of 0 to 5 V. The transducer signals were read out at the MW counting house using an IBM-PC clone⁴ (hereafter referred to simply as the PC). These data were stored on the PC and later transferred to a μ VAX for subsequent analysis.

¹Setra Systems Pressure Transducer #280E

²Omega Pressure Transducer #PX941-025GI

³Omega Pressure Transducer #PX941-025AI

⁴Zenith Data Systems Advanced Personal Computer, Model HF-241-80.

In addition, one temperature and one pressure transducer were simultaneously read out by EPIDAQ. These readout channels were calibrated independent of the OMEGA system. EPIDAQ was also used to read out the data from the SWICs. EPIDAQ read data from the beamline CAMAC system and subsequently stored the data on tape. The parallel pressure readout channels allowed for off-line correlation between the data acquired by the two systems (i.e. PC and NEU-PDP).

A systematic difference between calibrations of the OMEGA and the EPIDAQ readouts yielded the measured relationship:

$$P_{\Omega} = 1.023P_E + 0.499 \quad (3.1)$$

where P_{Ω} and P_E are the pressures in psia as read by the OMEGA and EPIDAQ systems respectively.

3.1.2 Čerenkov Phototube Signal Readout

The Čerenkov phototube signals were amplified at the detector prior to transmission to the experiment hall. At the experiment hall the signals were discriminated and fanned-out to two separate readout paths. One path latched the status of each phototube signal (above a preset threshold) (NEU-PDP), while the second path scaled logical combinations of the status of phototube signals for on-line monitoring of the counter (NEU-PDP and PC). Data from both readouts were used in the off-line analysis.

Amplification

Each phototube signal was twice amplified at the detector by voltage gain factors of 10 for a net gain of 100. Amplification was provided by LeCroy 612 and 612A 12-Channel Photomultiplier Amplifiers [47].

The signals were then transmitted ≈ 90 m to the experiment hall using air-core cable.⁵ The amplification and the air-core cable were both employed to compensate for signal attenuation between the phototube and the experiment hall.

Discrimination

Following transmission to the experiment hall, the signals were discriminated to reject background noise. LeCroy 4416 16-Channel Programmable Updating Discriminator⁶ units were used for this purpose. Discriminator thresholds were set to 30 mV for the p phototubes and 50 mV for the K and π phototubes.

Only phototube signals above the set threshold levels generated signals which were recorded. This discrimination reduced spurious background signals which might otherwise mimic signals produced by the incident beam particles. The discriminators were controlled remotely via the NEU-PDP.

Delays

After discrimination, each signal was delayed using LeCroy 4418 16-Channel Programmable Logic Delay/Fan-Out⁷ units in order to meet experimental timing requirements. The delays could be controlled remotely via the NEU-PDP. These units also fanned the signals out to the two parallel readout channels. One channel stored the logical status of each phototube signal above threshold using specially designed units known as Minnesota latches (described below). These units latched the status of the phototube signals whenever events satisfying experimental triggers were detected. The second channel scaled logical combinations of phototube signals (over threshold) for monitoring.

⁵CableWave Systems, SLA 38-50J, 50 Ω impedance.

⁶The LeCroy 4416 modules were rated to handle data acquisition rates up to 150 MHz

⁷Designed to handle data acquisition rates of > 100 MHz.

Minnesota Latches

The first parallel readout channel utilized specially designed latches known as Minnesota latches [66]. Each Minnesota latch channel stored the status of a phototube signal (above threshold) in a ring buffer for up to 255 time buckets. When a trigger was satisfied, the storage process was halted and the data in the buffer were read out for the triggered (*in-time*) bucket and seven buckets before and seven buckets after the in-time bucket. This yielded a time history of the phototube status for fifteen buckets surrounding the in-time bucket for each event. Due to a relative timing shift of 2 buckets between the Čerenkov detector and the beam hodoscope, only 13 buckets were available for the data analysis as illustrated in (Figure 3.2). The data were stored temporarily in the NEU-PDP buffer for subsequent concatenation with data from the other detectors. The data were finally transferred to tapes for storage and off-line analysis. Thus, for each triggered event a 15 bucket (285 ns) time history of the status of each phototube was stored on tape.

Scalers

The other parallel readout channel utilized LeCroy 4508 Dual 8-Input/8-Output Fully Programmable Logic Units⁸ to construct logical coincidences and *vetos* (i.e. anti-coincidences) of discriminated phototube signals. Such coincidences were used to monitor the status of the counter on-line and assist in steering the incident beam to optimize the beam distribution at the detector. The logical coincidences as a function of counter pressure (i.e. *pressure curves*) were also used extensively in the off-line analysis. The 4508 Logic Units could be programmed remotely by downloading instructions through the NEU-PDP computer.

The phototube signal coincidences were counted to provide on-line monitor-

⁸Designed to handle data acquisition rates of > 65 MHz.

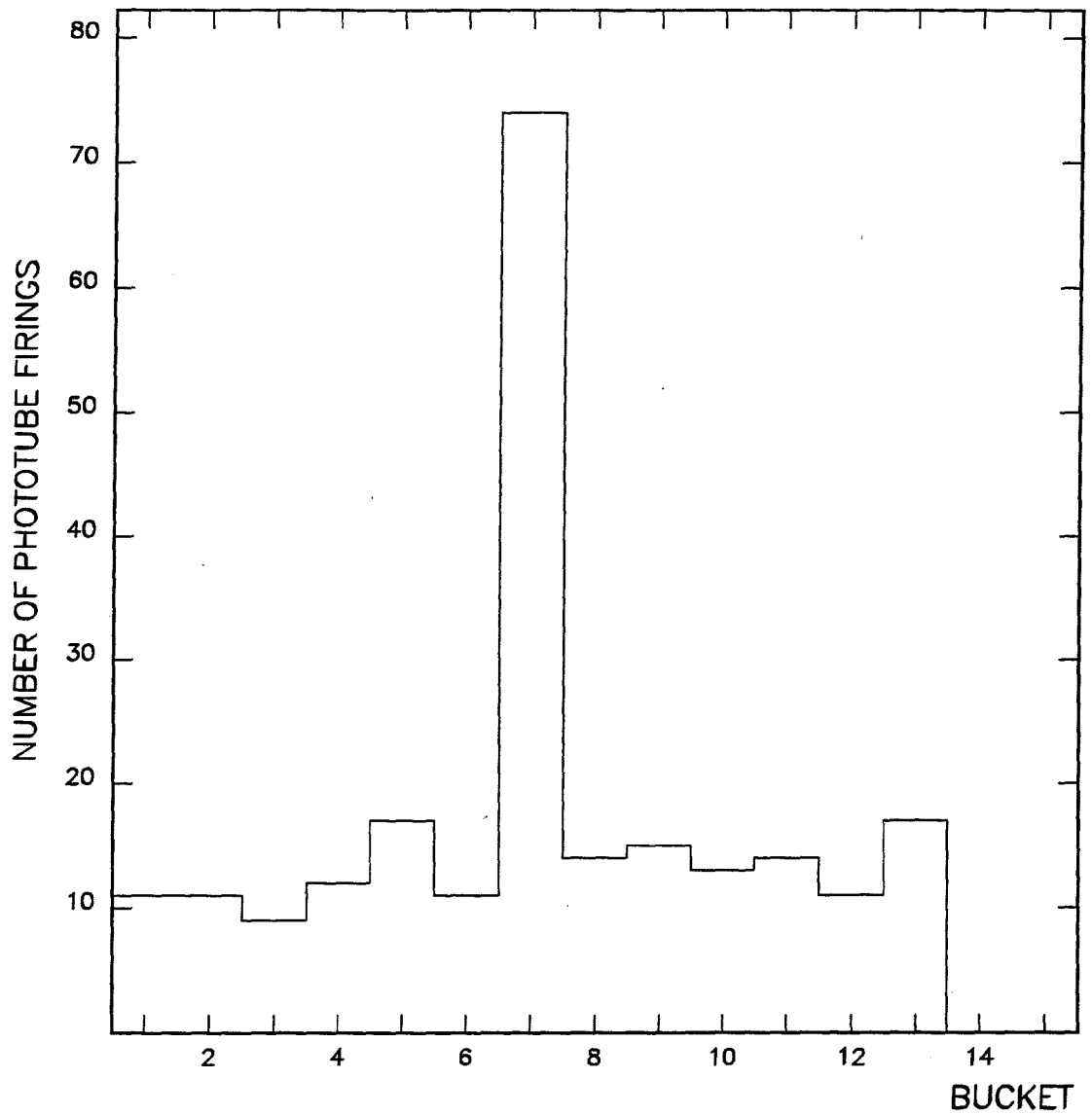


Figure 3.2: Time history of the status of phototube *K2* around the in-time bucket (bucket 7) for an individual run. The in-time bucket is enhanced due to the trigger requirement.

ing by either LeCroy 4434 32-Channel 24-Bit Latching Scalers⁹ or LeCroy 2551 12-Channel 100MHz Scalers. The data were stored on a spill-by-spill basis. Additionally, the data were transmitted to the PC via the NEU-PDP buffer, for select runs, thus allowing the scaled data to be used in the reconstruction of pressure curves for both on-line and off-line analysis. The data were later transferred to the VAX for long term storage¹⁰ and analysis.

3.2 EMLAC Data Acquisition

Signals from the EMLAC strips were amplified by specially designed [67] low impedance integrating amplifiers. The amplified signals were then fanned out to three separate channels. A fast readout channel allowed signals from the r -strips to be summed quickly in order to form early trigger decisions as to whether or not to activate the full readout process for an event of interest (see the trigger section below). Another channel provided a sample and hold circuit. For each channel, this circuit used a preset (programmable) delay to sample the channel's status before the arrival of the signal (BEFORE) and at the signal peak (AFTER). These values were digitized using ADC units. The difference between the AFTER and BEFORE signal measurements provided a measure of the total charge and, hence, total energy read from that channel. The third path fed time-to-voltage converters to provide a measurement of the arrival time for EMLAC showers.

Calibration tasks were performed periodically on the EMLAC to monitor the stability of the gains and pedestals¹¹ of the various channels and record this information for later use in the data analysis.

⁹Designed for data acquisition rates of > 30 MHz

¹⁰The data were also backed up on separate tapes.

¹¹A pedestal is the "background" read from a channel in the absence of signals in that channel.

3.3 The E706 Trigger

In order to investigate rare processes it was desirable to select for later analysis only events which satisfied restrictive criteria for physics of interest (e.g. events containing high transverse momentum showers.). This was done in an effort to minimize the dead time due to limitations of the data acquisition (and reconstruction) rate. The trigger [51],[68],[69] was implemented in three stages — the minimum bias **BEAM** and **INTERACTION** requirements, the **PRETRIGGER** requirements and the High p_T trigger requirements.

3.3.1 The Beam and Interaction Requirements

The **BEAM** requirement was satisfied when a signal above threshold was detected in at least one scintillator strip in each of at least two of the three beam hodoscope planes. **BEAM1** required that **BEAM** be satisfied in coincidence with the requirement that not more than one hodoscope plane had two or more clusters¹² of scintillators with signals above threshold. Thus **BEAM1** effectively rejected most events with more than one incident beam particle (known as *multiple occupancy*).

The signal **INT** was generated whenever there was a coincidence between **BEAM** and signals in at least two of the four interaction scintillators, thus indicating that an interaction took place in the target. The **CLEAN** requirement was that no **INT** signal was generated in the 3 buckets before or the 3 buckets after the in-time bucket¹³. The definition of a live interaction, **LIVE_INT1**, was then formed from the logical combination

$$\mathbf{LIVE_INT1} = \mathbf{BEAM1} * \overline{\mathbf{BH}} * \mathbf{CLEAN} * \mathbf{INT} * \mathbf{READY} \quad (3.2)$$

¹²A cluster was defined as a set of one or more adjacent scintillator strips with signals above threshold in a single hodoscope plane. Distinct clusters are required to be non-adjacent and non-overlapping.

¹³The after requirement was dropped during the latter part of the 1991 run.

where “*” represents the logical AND operator. Here $\overline{\text{BH}}$ represents the requirement that none of the scintillators in the beam hole counter produced signals above threshold. The signal **READY** indicates that the data acquisition system was ready to record data. The **LIVE_INT1** signal served as the strobe to query the higher level triggers.

3.3.2 p_T Measurement

As the E706 triggers were based on measurements of the p_T deposited in the EMLAC by incident showers, it was necessary to convert the energy deposited in the EMLAC strips into p_T measurements. The total p_T of a shower which deposited energy in N adjacent strips is given by

$$p_T = \sum_{i=1}^N E_i \sin \theta_i \quad (3.3)$$

where E_i is the energy deposited in the i th strip as provided by the fast readouts described above. θ_i is the angle which the i th strip subtends at the target as calculated from the radial position of the shower in the EMLAC and the distance from the target. The calculation of p_T was performed on-line by specially designed [51] hardware. This p_T measurement was used in making fast trigger decisions on-line.

3.3.3 The Pretrigger Requirements

The **PRETRIGGER** was used to quickly identify candidate events which deposited a sufficient amount of p_T in an octant of the EMLAC. The net p_T deposited in *either* the inner 128 r -strips of the octant *or* the outer r -strips was required to be at least 1.7 GeV/c to satisfy the 1/2 **GLOBAL** requirement. In order to reject events with apparent high p_T due to the accidental pile-up of signals from previous interactions in coincidence with signals from the current interaction, an **EARLY_PT** condition required that no p_T above 1.5 GeV/c be deposited in the

triggering octant over the previous 200 ns. To identify events due to beam halo muons which might otherwise mimic events of interest, a **VW** signal was generated from the signals from the four planes of veto scintillator which shadowed the quadrant satisfying the 1/2 **GLOBAL** requirement. This signal can be expressed as

$$\mathbf{VW} = (\mathbf{VW1}_i + \mathbf{VW2}_i) * (\mathbf{VW3}_i + \mathbf{VW4}_i) \quad (3.4)$$

where $\mathbf{VW}x_i$ represents the x th veto wall shadowing the i th quadrant of the **EMLAC**. The “+” represents the logical OR operator. Power supplies generated regular spikes which could potentially compromise the information of interest. These spikes were detected and such events were rejected with a **SCRKILL** requirement. **SCRKILL** rejected data in coincidence with voltage spikes from the power supplies. The full **PRETRIGGER**, defined by

$$\mathbf{PRETRIGGER} = \mathbf{LIVE_INT1} * \mathbf{1/2\ GLOBAL} * \overline{\mathbf{EARLY_PT}} * \mathbf{SCRKILL} * \overline{\mathbf{VW}}, \quad (3.5)$$

was implemented on an octant-by-octant basis. When the pretrigger was satisfied, the status of the spectrometer elements was latched while the event was further evaluated.

Once a **PRETRIGGER** was satisfied for a particular octant, the trigger logic determined whether this interaction had actually deposited sufficient energy in a local region of that octant of the **EMLAC** to warrant reading out the event.

3.3.4 The Local Triggers

Each 16 strip group overlapped adjacent groups by 8 strips in order to optimize the sensitivity of the trigger to energy deposition by individual photons. The overlapping groups protected against large apparent threshold variations for showers

falling near the edges of a particular group, since such showers were near the center of the overlapping group.

The Local signals were subjected to Low (≈ 3.0 GeV/c) and High (≈ 3.5 GeV/c) discriminator thresholds to generate Single Local Low (SLL) and Single Local High (SLH) triggers. To enhance the statistics of the high p_T data relative to the lower p_T data, the SLL trigger was prescaled by a factor of 200 (that is, only one of every 200 events satisfying the SLL trigger requirements was written to tape).

3.3.5 Lower Bias Triggers

To provide information on the performance of the high p_T triggers and to accumulate sufficient data to populate the lower p_T regions of the meson production spectra, several other prescaled triggers were installed. The prescaled beam trigger required

$$\text{BEAM * CLEAN * READY} \quad (3.6)$$

and was prescaled by a factor of 10×15^5 . The prescaled interaction trigger required

$$\text{BEAM * INT * CLEAN * READY}$$

and was prescaled by a factor of 2×15^5 . A fraction of the pretriggers were also written to tape. This helped to ensure that the trigger was really generated by a small number of particles depositing sufficient p_T in a relatively small region of the EMLAC.

Chapter 4

Event Reconstruction

The kinematics of the particles produced in the interactions selected by the high p_T triggers and recorded by the DA were reconstructed on an event-by-event basis by a software package developed explicitly for this purpose by the experimenters. That event reconstruction process is outlined below.

4.1 MAGIC

The data were analyzed offline using a program called **MAGIC** which utilized dynamic memory allocation. [70]. **MAGIC** controlled the sub-programs which reconstructed data from the various detectors. **MAGIC** and the reconstruction programs were written and maintained in FORTRAN-77 on VAX-VMS and UNIX operating systems. **MAGIC**'s versatility allowed it to read data in either raw, unpacked or reconstructed formats. Furthermore, **MAGIC** was capable of reading either real or Monte Carlo data. The reconstruction programs used most extensively for this work included **DLREC**, **EMREC** and **PLREC**. **DLREC** [69] was used to evaluate the discrete logic data including data from the Čerenkov detector, the beam hodoscope, interaction counters, veto walls and the trigger data. **EMREC** [71],[72] reconstructed showers detected by the EMLAC. **PLREC** [52] reconstructed the paths of charged particles through the spectrometer and evaluated

the charges and momenta of those particles produced by charged particles in target interactions. Additional reconstructors, described elsewhere, included **FCREC** for reconstruction of data from the FCAL and **HCREC** [56] used to reconstruct showers in the HALAC. The use of external *control cards* allowed **MAGIC** to select the desired reconstruction programs in order to process only data of immediate interest.

MAGIC was maintained using the **PATCHY** code-management software [73]. **PATCHY** allowed multiple users to simultaneously modify and compile their own versions of sections of the **MAGIC** code while maintaining a standard library version in a common area. This allowed for greater flexibility in performing independent studies while maintaining the requisite cohesiveness in the overall collaborative effort.

4.2 Discrete Logic Reconstructor

As the name implies, the Discrete Logic REConstructor (**DLREC**) was used to reconstruct information acquired by detectors which latched and stored data in a discrete (0/1) format including the Minnesota latches and LeCroy 4508 Programmable Logic Units. **DLREC** produced summary banks which stored the discrete data in the bits of ≈ 40 integer words. These data included the status of all Čerenkov detector phototubes, LAC triggers, hodoscope planes, interaction counters and veto wall counters. In addition, **DLREC** provided information used to identify and flag internal inconsistencies and failures in the various trigger logic and Minnesota latch readout channels.

4.3 Planes Reconstructor

The PLanes REConstruction Program (**PLREC**) was used to reconstruct the charges and momenta of charged particles detected by the tracking system. These tracks were used to identify the location of the interaction of the incident beam with the target material. The data reconstruction was divided into several stages. A more complete description of **PLREC** may be found elsewhere [52].

4.3.1 Beam Tracks

Tracks produced by beam particles incident on the target region were reconstructed from data acquired by the SSD modules upstream of the targets. Candidate *beam tracks* were required to have a minimum of at least two hits in each view of the SSDs. For each view, 3-hit tracks were reconstructed first. This entailed identifying all pairs of hits in the first and third planes in a given view in order to form 2-hit tracks candidates. A search was then performed on the hits in the middle plane to locate hits within $75\mu\text{m}$ of the 2-hit track candidate. The resulting χ^2 per degree of freedom was required to be less than 3.0 in order for the candidate to qualify as a 3-hit track. After identifying all 3-hit tracks, the program proceeded to reconstruct the remaining 2-hit track candidates using less stringent requirements.

4.3.2 PWC Tracks

As with the beam tracks, PWC tracks were first reconstructed separately in each view. Again, the code generated candidate view tracks using the first and last planes with hits (i.e. *end planes*) and then looked for nearby hits in the intervening planes. Such *view tracks* were required to have at least three hits. Pairs of the resulting X- and Y-view tracks were then matched to search for hits in the available U- and V-views in order to identify *space track* candidates. The U- and V-view

hits were required to be within 1.5 wire spacings of the location projected from X- and Y-view tracks pair. The resulting space tracks were required to have a total of at least 13 hits with 2 or more hits in each view and a χ^2 requirement similar to the beam track definition. This procedure was then repeated starting with the pairs of view tracks from the U- and V-views and matching to the X- and Y-hits to minimize inefficiency. Duplicate tracks were rejected.

From the unused hits, additional tracks were then reconstructed using the same procedure but with less stringent requirements. Also reconstructed were “partial” tracks which left the acceptance of the PWCs without passing through all modules.

4.3.3 Straw Tracks

Tracks in the straw tube chambers were identified by first requiring that the reconstructed PWC tracks, projected to the straw tube chambers, lay within 3.5 mm of straw tube hits. At least 4 matching hits in the straw tubes and a minimum of 2 hits in each view were required to define a *view track*.

An iterative global fitting of the straw tube and PWC hits was then performed. With each iteration, the required distance from the PWC track projections was reduced to improve the quality of the fit. Surviving tracks were referred to as *straw tracks*.

4.3.4 SSD Tracks

The same scheme employed for track reconstruction in the PWCs was used for the SSD track reconstruction. View tracks were produced by fitting straight lines to pairs of points in the SSD end planes. Hits in the intervening planes were then required to occur within fixed search windows. The five SSD modules downstream of the targets were used to improve the measurements of the PWC and Straw Tube detectors. These measurements were also used to improve the linking between the

PWC and Straw Tube tracks and the SSD tracks at the center of the analysis magnet.

Incident *beam tracks* were reconstructed from the three most upstream modules (*beam SSDs*). Here the first and third modules were used as end planes. The beam track was chosen as the space track with the smallest impact parameter.

4.3.5 Linking

Once all tracks were identified, the downstream tracks were all projected to the SSDs. Tracks whose projections fell within the acceptance of the SSDs were considered as candidates for linking. Such candidate tracks were then projected to the Z location of the center of the analysis magnet. The differences in position, ΔX and ΔY , between upstream and downstream tracks in the X- and Y-views respectively were required to fall within a momentum dependent linking window for the track segments to be considered linked. Furthermore, the slopes of the upstream and downstream tracks as measured in the X- and Y-views were required to match within a fixed window. A one-to-one correspondence was established between upstream and downstream tracks for tracks satisfying these criteria. The closest SSD track to a downstream track was said to be *best linked*.

4.3.6 Vertex Reconstruction

The SSD tracks were used to reconstruct the location of the interactions of the incident beam with the target. Vertices were reconstructed separately in the X- and Y-views. The transverse position of the vertex was determined by searching pairs of view tracks which minimized the impact parameters of the incident tracks¹ in both the X- and Y-views. The longitudinal position of a vertex was calculated as a weighted average location determined for the two views vertices.

¹Beam tracks which obviously passed through without interacting were not considered.

The full reconstruction algorithm was much more complicated, involving multiple iterations with less stringent requirements at each stage in order to analyze data which failed to provide reconstructed tracks and vertices in the first iteration. This discussion is only intended to provide a flavor for the structure of the analysis.

4.4 Tracking System Momentum Scale Calibration

The tracking system momentum scale calibration was established using reconstructed $K_S^0 \rightarrow \pi^+ \pi^-$ and $J/\psi \rightarrow \mu^+ \mu^-$ decays detected in the tracking data. The K_S^0 was reconstructed from secondary vertices which produced pairs of oppositely charged tracks. The J/ψ mesons were reconstructed using the E706 tracking system data selected via the E672 high mass dimuon triggers. The invariant mass distributions for the K_S^0 and J/ψ are shown in Figure 4.1. The calculated masses are consistent with the accepted values.

4.5 Electromagnetic Shower Reconstructor

Showers in the EMLAC were reconstructed by the ElectroMagnetic showers REConstructor (EMREC) in several stages. First, the ADC counts readout from the EMLAC strips were converted to energy units. EMREC then located groups of strips with candidate signals and performed a fit to the energy distributions from such groups to attempt reconstruction of shower peaks. Peaks from a single view (r - or ϕ -view) were referred to as GAMMAs and were considered as candidates for photons. The GAMMAs in the r - and ϕ -views were correlated to provide photon measurements. the photon arrival time was determined based upon the TVC data to allow rejection of out-of-time showers. Only a summary is presented here. A complete description of the shower reconstruction algorithm may be found

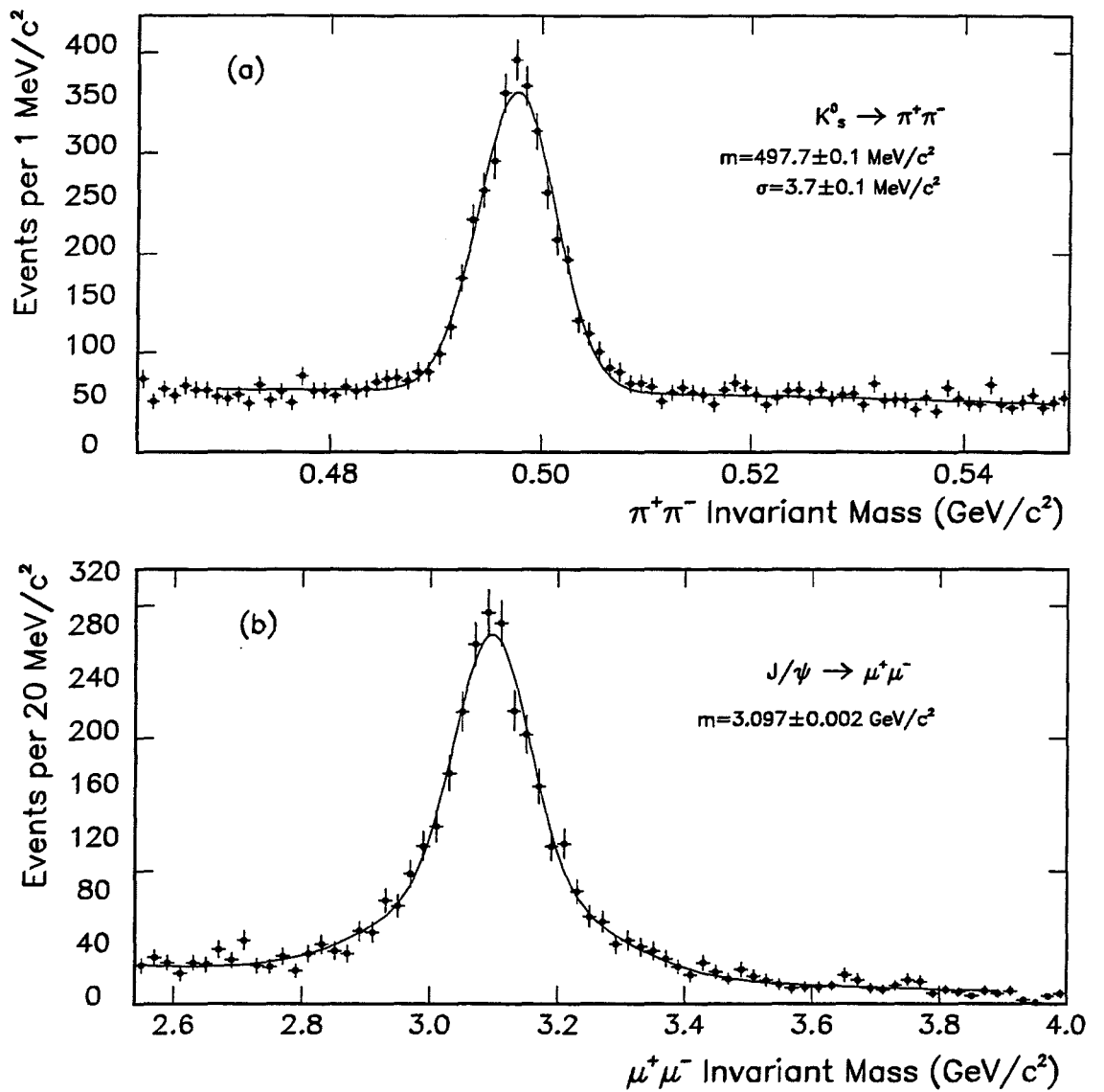


Figure 4.1: Mass distributions for (a) $K_s^0 \rightarrow \pi^+ \pi^-$ and (b) $J/\psi \rightarrow \mu^+ \mu^-$ as reconstructed from tracking data. Here m and σ represent the mean and width of a gaussian fit to the data with a linear background. The measured masses compare well with the accepted nominal values of $M_{J/\psi} = 3.097 \text{ GeV}/c^2$ and $M_{K_s^0} = 0.498 \text{ GeV}/c^2$.

elsewhere [72],[74].

4.5.1 Conversion of ADC Counts to Energy

The amplified ADC counts read from each channel of the EMLAC were converted to energy measurements using the equation

$$E_i = A \times G_i \times (N_i - N_{0_i}). \quad (4.1)$$

Here E_i is the energy of the i th strip, $A = A(t)$ is a time dependent scaling factor to account for the fact that the observed uncalibrated energy response of the EMLAC varied slowly with time² A includes the conversion factor from ADC counts to energy which was found to be time dependent, G_i is a correction for the gain of the amplifier channel,³ N_i is the ADC value from the i th channel and N_{0_i} is the pedestal offset for the i th channel. The gains and pedestals were periodically measured during the data acquisition period in order to account for any time variations which might occur.

4.5.2 Groups and Peaks

Groups were identified separately for the r and ϕ -views. A group was identified if (a) the total energy deposited within 16 adjacent strips was above 600 MeV, (b) at least 3 inner ϕ strips (2 outer ϕ -strips) had energies over 80 MeV (95 MeV) and (c) the highest strip energy was over 300 MeV (350 MeV).

Peak strips within a group were identified if the group possessed a single strip energy of at least 300 MeV (350 MeV for outer ϕ -strips). Furthermore, the derivative of the energy distribution was required to change sign. The peak was also required to be bounded on both sides by either energy minima or one of the group's end strips.

²The nature of the time dependence of the detector energy scale, $A(t)$ is illustrated below

³Gain corrections were normalized to the overall average gain for all EMLAC channels.

4.5.3 GAMMAs

Once all peaks were identified the shapes of the energy distributions were fit in order to estimate the energy associated with each peak in any multi-peak group. The shower shapes differed between the front and back sections due to spreading as the shower developed in the EMLAC. As a result, the shower shapes were parameterized separately for the front and back sections. The fits were based on an iterative minimization of χ^2 where

$$\chi^2 = \sum_i \frac{1}{\sigma_i} \quad (4.2)$$

Here E_i is the actual energy deposited in the i th strip, E_i^{fit} was the corresponding energy deposited in i th strip as calculated from the fit function and σ_i^2 is the uncertainty in the energy of the i th strip as calculated from the energy resolution of the EMLAC.⁴ The energy of the GAMMA was then obtained by integrating the resulting fit function in order to account for shower tails below threshold. The energy of the resulting photon was taken as the sum of the energies of the correlated GAMMAs.

GAMMAs in the r - and ϕ -views were correlated to obtain photon measurements. To be identified as a photon, GAMMAs must first be correlated based on their physical locations in the different views. Correlation was based in part on the fact that GAMMAs produced by a single photon shower tended to have approximately the same energy in the r - and ϕ -views.

4.6 Calibration of the EMLAC

Because the inclusive neutral meson and direct photon cross-sections fall rapidly with p_T , the calibration of the energy response [62],[?] of the EMLAC must be

⁴The energy resolution of the EMLAC was characterized as $\sigma^2(E) = (0.01)^2 E^2 + (0.16)^2 E + (0.22)^2$.

determined with care. Small uncertainties in the energy calibration result in large uncertainties in the final p_T spectrum as illustrated in Figure 4.2. This section discusses the corrections implemented to properly calibrate the EMLAC energy response and briefly illustrates some of the cross checks employed to evaluate the integrity of the calibration. The calibration was evaluated using the observed π^0 , η and ω mesons as well as the response of the calorimeter to incident electrons. The π^0 and η mesons were reconstructed from their two photon ($\gamma\gamma$) decay mode. The two photon mass is given by

$$M^2 = 2E_1E_2(1 - \cos \theta), \quad (4.3)$$

where E_1 and E_2 are the reconstructed photon energies and M is the two photon invariant mass. θ is the opening angle between the pair of photons in the frame in which the energies are evaluated.

4.6.1 Time Dependence Correction

The energy response of the calorimeter varied with time as illustrated in Figure 4.3 which shows the ratio of the uncalibrated reconstructed π^0 mass to the nominal value plotted as a function of *beam days* (i.e. days on which beam was delivered to the experiment). A correction⁵ was applied to the raw data prior to processing by EMREC to account for this effect.

4.6.2 Octant Corrections

Due to variations in voltage, lead thickness, electronics, etc. there were octant-to-octant variations in the reconstructed meson masses. Corrections were applied octant-by-octant for these variations.⁶ As the photons from the η decays had a

⁵The correction was based on a third order polynomial fit to the data shown in Figure 4.3.

⁶Such variations were typically on the order of 5%

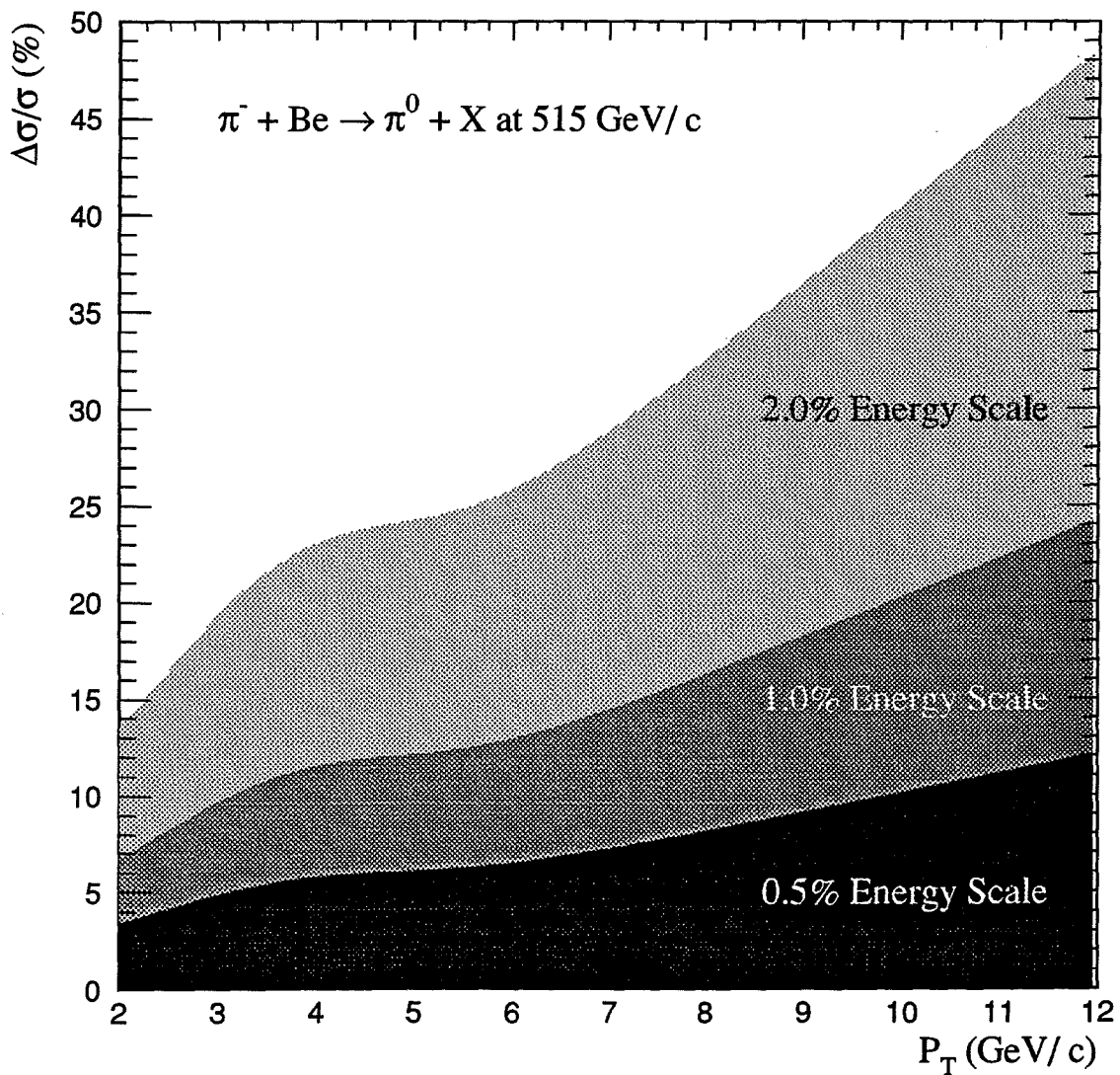


Figure 4.2: Sensitivity of the measured π^0 p_T spectrum to the uncertainty in the calibration of the EMLAC energy response for π^0 mesons produced in π^-N interactions at 515 GeV/c.

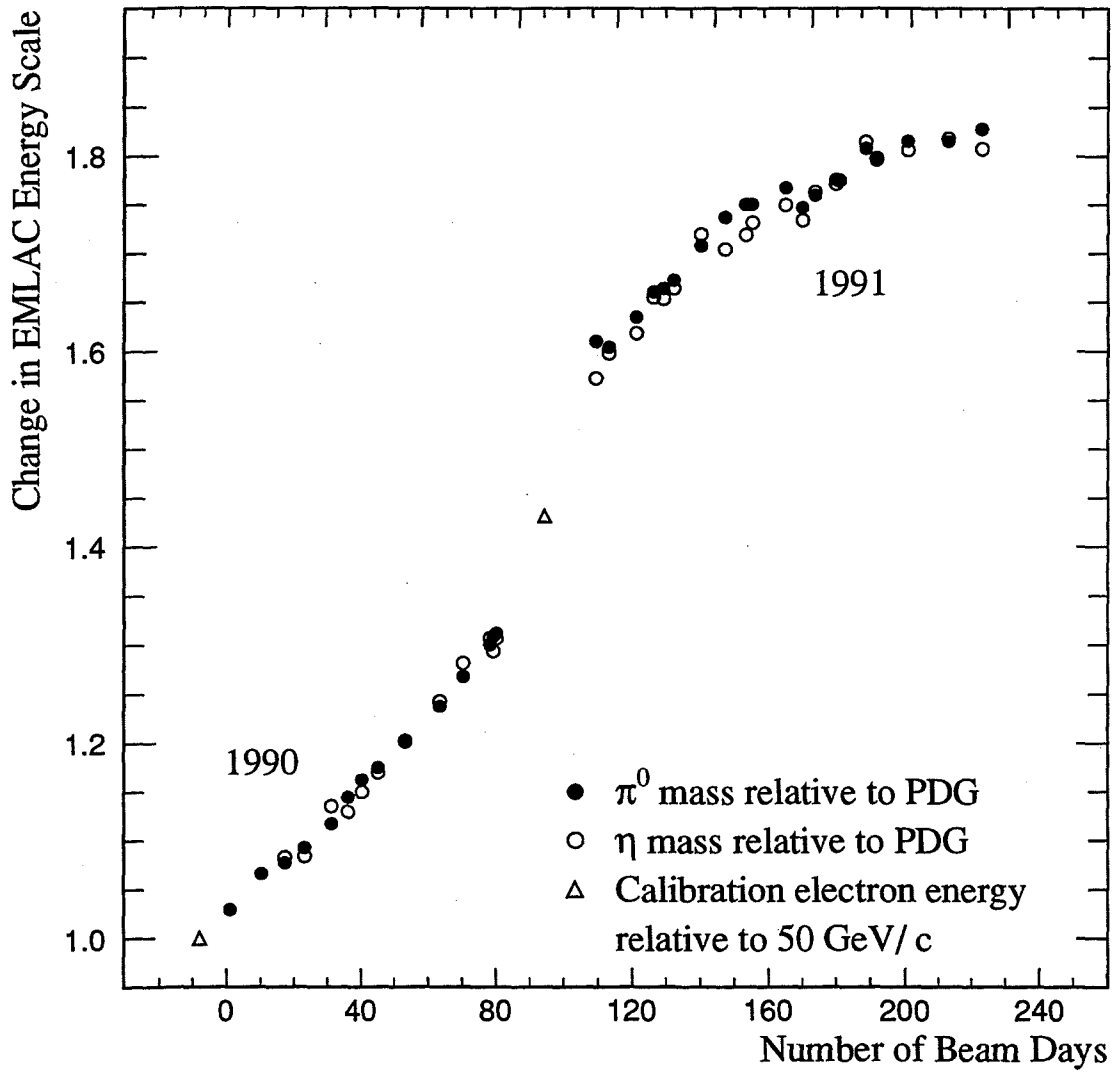


Figure 4.3: Time dependence of the energy response of the EMLAC plotted as a function of beam days. The vertical axis represents the ratio of the reconstructed meson masses to their accepted nominal values. The mass ratio for the reconstructed 50 GeV/c electron's used to calibrate the EMLAC is also shown.

much larger opening angle than photons from π^0 s, the final octant corrections were evaluated using scaling factors based on the reconstructed η mass.

4.6.3 Energy Loss Correction

A correction was applied for the energy deposited in the material preceding the active region of the EMLAC. On average, electrons showered sooner in the EMLAC than did photons. This is reflected in Figure 4.4 which shows the average energy loss for incident photons and electrons as a function of reconstructed energy.

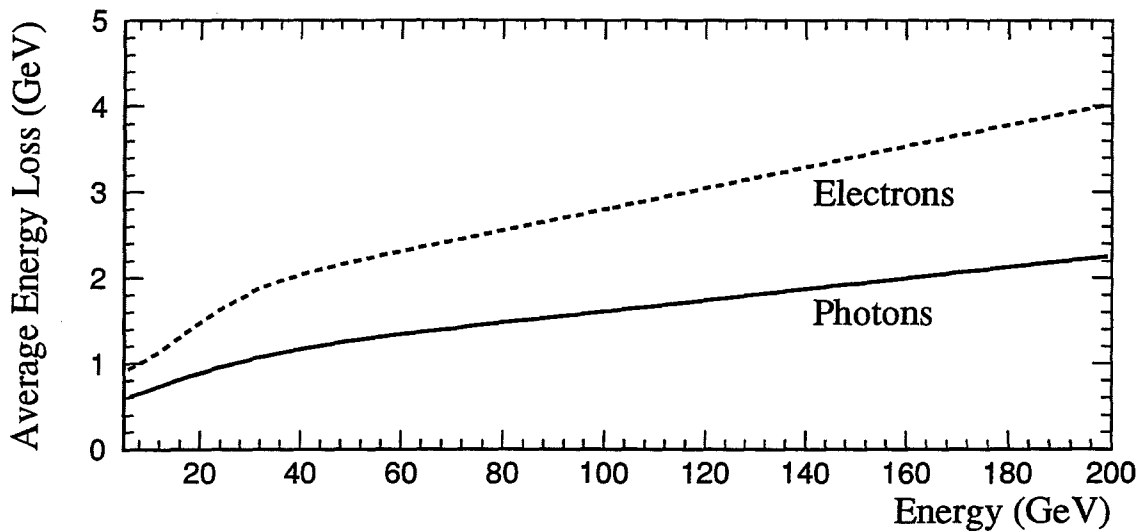


Figure 4.4: Distributions for energy lost by electrons (dashed) and photons (solid) in the material upstream of the EMLAC as a function of the reconstructed energy. Data were generated using the E706 Monte Carlo program.

These curves were calculated using the E706 Monte Carlo program described in Chapter 6. The energy loss was averaged over the entire front face of the EMLAC and the resulting correction was applied for each photon used in this analysis.

4.6.4 Boundary Corrections

In the region of the inner/outer ϕ boundary, the ϕ GAMMA energy was over-estimated. This was accounted for by using only the r -view GAMMA energy measurement in this region. Here the photon energies were calculated as twice the energies of the r -view GAMMAs rather than the sum of the energy of the GAMMAs in the two views.

4.6.5 Radial Position Corrections

The response of the calorimeter was found to depend on radial position of the shower in the EMLAC as illustrated in Figure 4.5 which shows the π^0 and η masses normalized to their nominal values prior to correcting for this effect. The ZMP sample is discussed in the next subsection. The data plotted represent the ratio of the EMLAC energy, E , to the momentum, P , as measured with the tracking system, plotted as a function of radius in the EMLAC. This radial dependence was essentially independent of particle type and shower energy. The correction was determined from an octant-by-octant fit to the reconstructed π^0 mass as a function of the radial position of the π^0 . The reconstructed η mass averaged over all octants was then used to “fine tune” the correction.

4.6.6 π^0 and η Mesons in the $\gamma\gamma$ Mode

Figure 4.6 shows the $\gamma\gamma$ invariant mass distributions after calibration of the EMLAC response. The figure shows signals from the two photon decay mode of the π^0 and η mesons. The resulting masses are consistent with the nominal values.

4.6.7 ω Mesons in the $\pi^0\gamma$ Mode

Figure 4.6 shows the $\pi^0\gamma$ invariant mass distribution in the region of the ω meson. The measured mass of the ω meson is consistent with nominal value. This

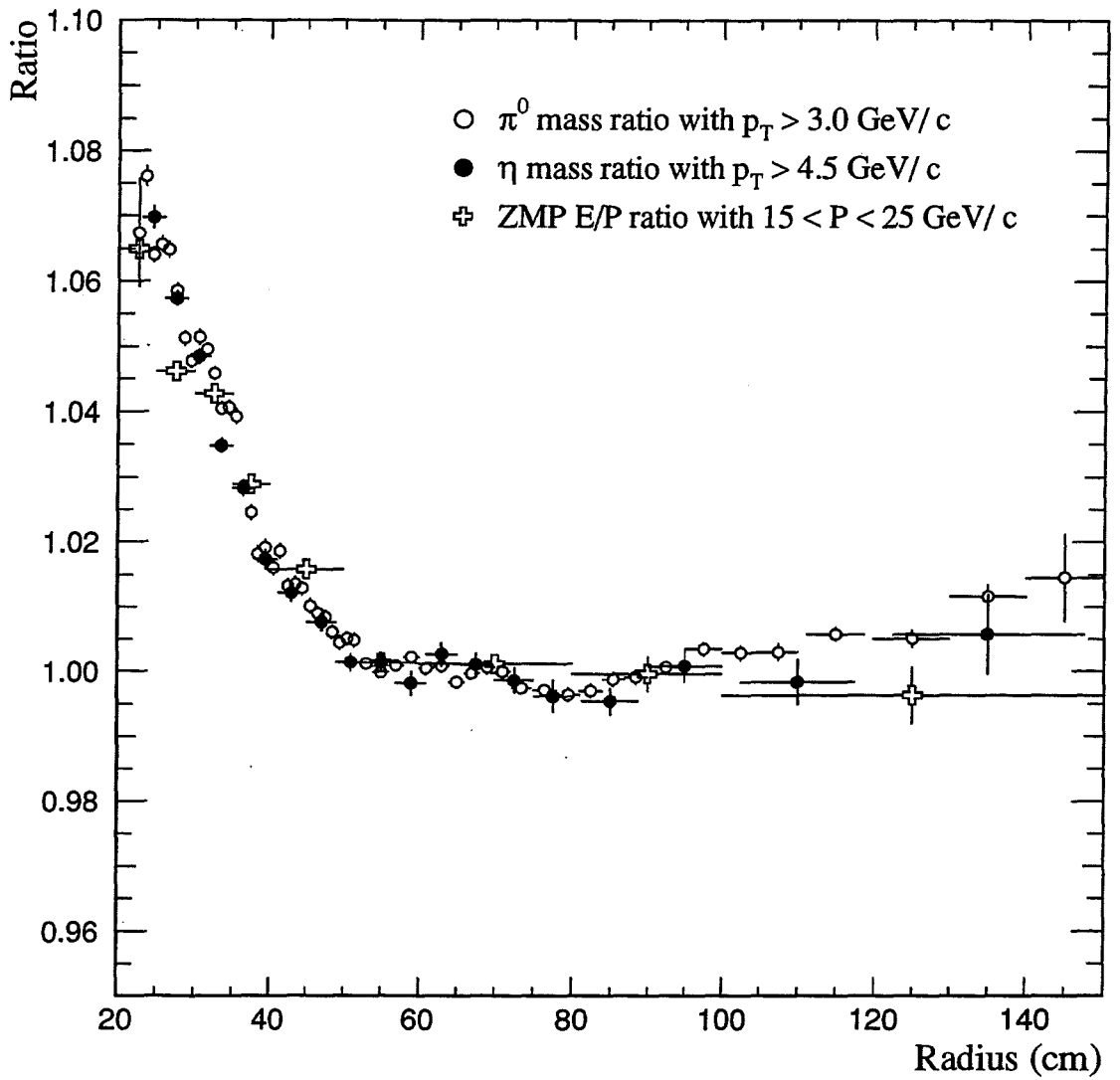


Figure 4.5: Radial dependence of the energy scale for π^0 and η mesons. Data are plotted as a ratio of the meson mass to the accepted nominal value. For the ZMP sample, data are plotted as the ratio of E/P. The time dependence correction has already been applied to the data in this plot. Results are from the 1991 data sample.

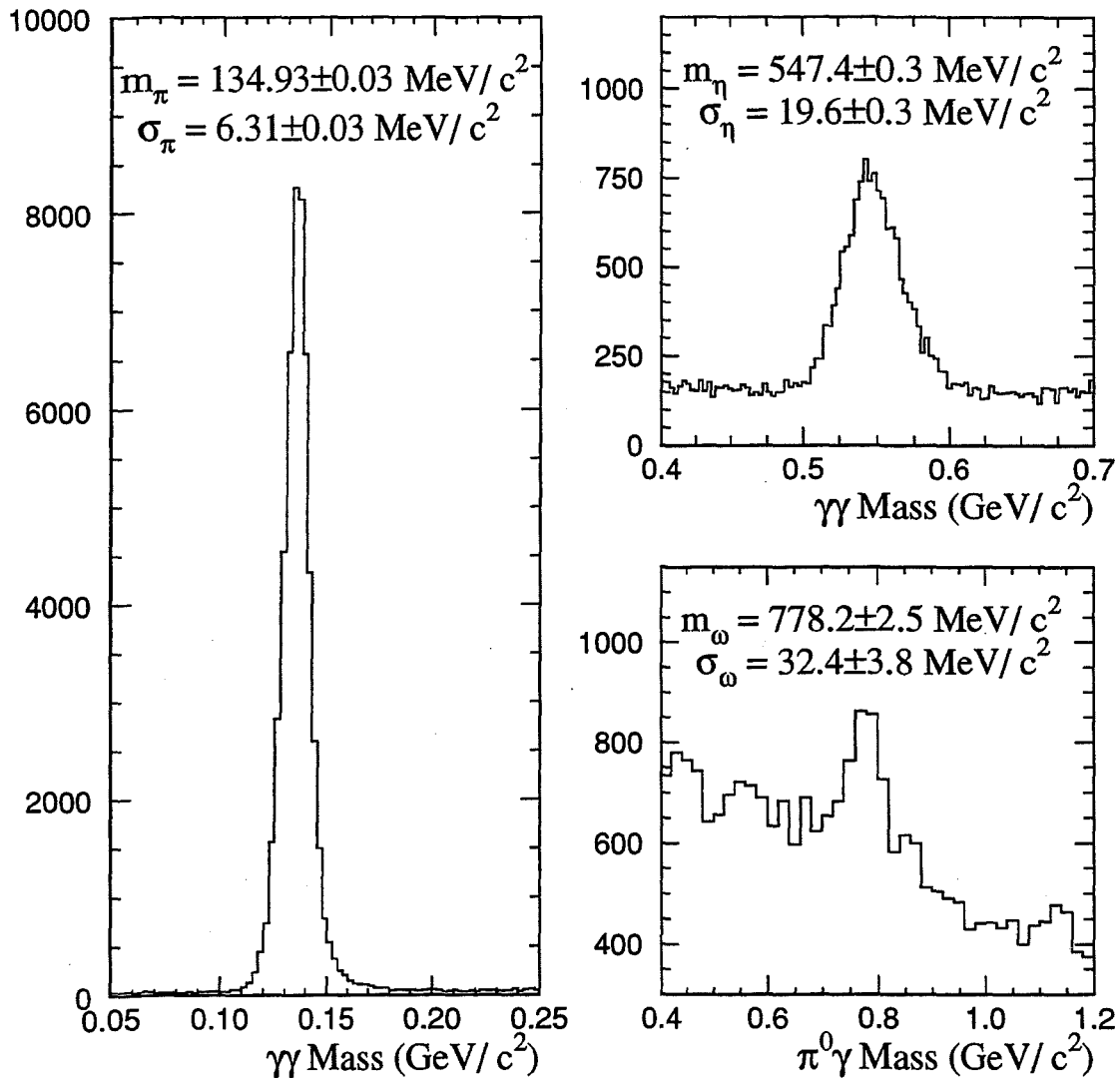


Figure 4.6: Invariant mass distributions showing the π^0 and η signals in the $\gamma\gamma$ mode. $\pi^0\gamma$ invariant mass distribution showing the ω signal. Here m and σ represent the mean and width of a gaussian fit to the data with a linear background. The values compare well with the accepted nominal values of $134.98 \text{ MeV}/c^2$, $547.5 \text{ MeV}/c^2$ and $781.9 \text{ MeV}/c^2$ in order. Results are from the 1991 data sample.

provides an independent verification that the energy response of the EMLAC was well calibrated.

4.6.8 Zero Mass Pairs

Some of the photons from the electromagnetic decay of particles produced in the target converted into e^+e^- pairs in the target material upstream of the analysis magnet. The invariant mass of the e^+e^- pair is $2m_e$ (essentially zero). Such e^+e^- pairs are henceforth referred to as zero mass pairs (ZMP).

The tracks of the e^+e^- pair were detected by the tracking system and the electrons also initiated showers in the EMLAC thus allowing for an independent measurement of the momentum and energy of the electrons. This provides a consistency check on the EMLAC energy scale calibration and a means of aligning the LAC with respect to the tracking system. The SSDs upstream of the analysis generally cannot resolve the tracks of ZMPs due to the small opening angle between the tracks. However, the magnet provided a sufficient impulse to separate the oppositely charged tracks in the X-Z view of the downstream tracking detectors allowing them to be detected as two independent tracks in the downstream tracking system. The ZMP sample was defined by the following requirements (a) the two reconstructed tracks have opposite charge, (b) the downstream tracks intersect near the magnet center in the X-Z view, (c) the downstream tracks have nearly the same slope in the Y-Z view and (d) the projection of the tracks to the front of the EMLAC are within 1.5 cm of showers having $E_{front}/E_{total} > 0.2$. Here E_{front}/E_{total} is the ratio of energy deposited in the front section of the EMLAC to the total deposited in both front and back sections. The E_{front}/E_{total} requirement is imposed to discriminate against hadrons which frequently deposit most of their energy in the back section of the EMLAC.

The invariant mass of photon and ZMP combinations is shown in Figure 4.7.

Both the π^0 and η signals are apparent.

Figure 4.8(a) shows the mean π^0 mass (compared to the nominal mass) for π^0 s detected via the $\gamma\gamma$ decay mode where one photon converted in the target region. Data are plotted as a function of the energy of the unconverted photon. The kinematics of the converted photon were determined entirely from the tracking system data. The uniformity of the measured π^0 mass versus photon energy illustrates the linearity of the calibrated EMLAC response. The masses of the reconstructed π^0 and η mesons are slightly lower than the nominal values. As indicated in Figure 4.8(b), this is attributed to the effect of bremsstrahlung as the leptons traverse the target.

Similarly, the $e^+e^-e^+e^-$ invariant mass distribution for pairs of converted photons is plotted in Figure 4.9. The data represent a sample for which both photons converted into e^+e^- pairs in the target region. The pair mass was reconstructed entirely from tracking data. The observed mass of the π^0 is also smaller than the nominal value and consistent with the above bremsstrahlung interpretation.

It should be noted that the bremsstrahlung interpretation does not influence the determination of the tracking system momentum scale as the π and μ decay products of the K_S^0 and J/ψ do not experience a significant amount of bremsstrahlung energy loss in the target and, so, it is expected that the masses of these particles should be consistent with the nominal values.

Based upon the reconstructed signals and the measured linearity of the calorimeter response, the uncertainty in the calibrated energy response is estimated to be $< 0.5\%$ resulting in an uncertainty on the π^0 cross-section of about 5% averaged over the relevant p_T range (see Figure 4.2).

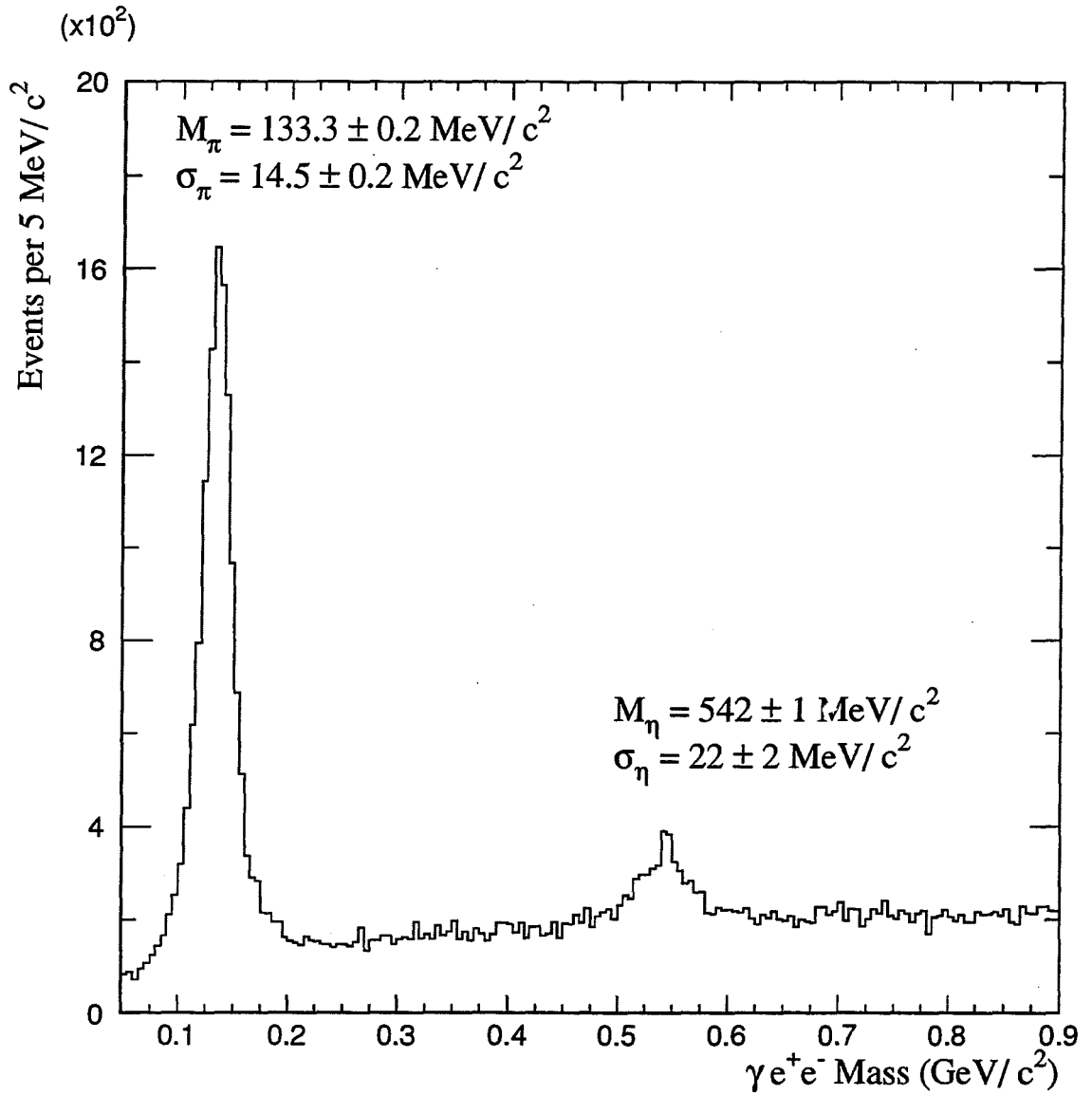


Figure 4.7: Two photon invariant mass where one photon converts into a ZMP in the target region for $p_T > 3.0 \text{ GeV}/c$.

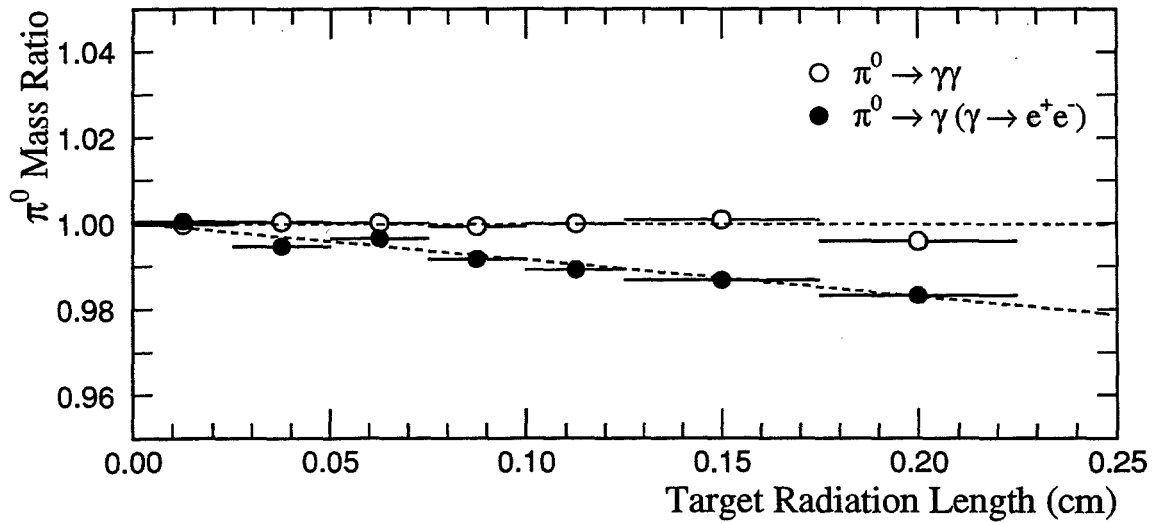
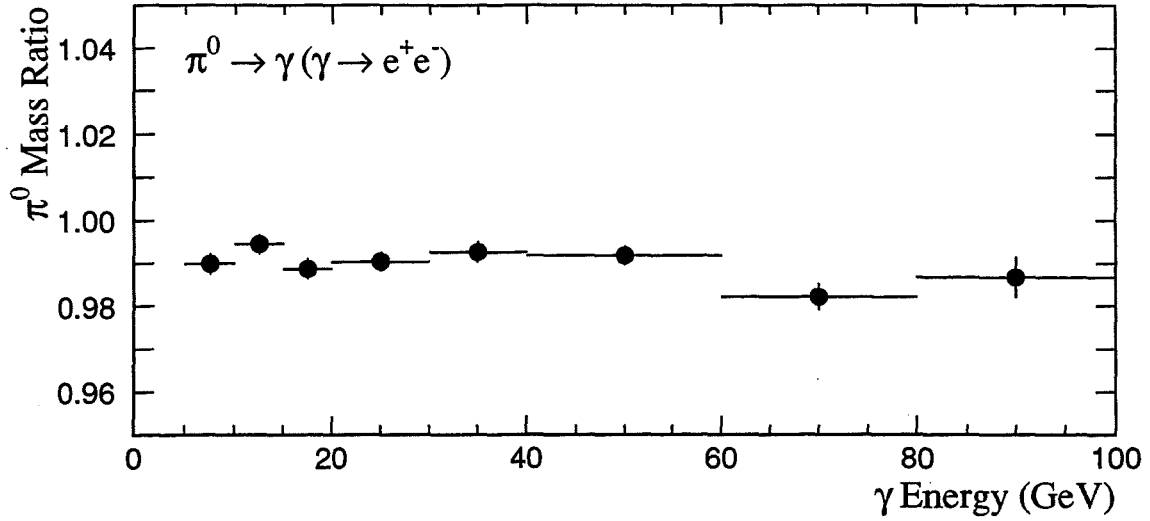


Figure 4.8: Ratio of the γe^+e^- mass to the accepted π^0 value as a function of reconstructed photon energy and as a function of target radiation length compared with the reconstructed π^0 mass when neither photon converts. The decrease in the γe^+e^- mass with target length is clearly consistent with the bremsstrahlung theory and satisfactorily explains the reduction in the reconstructed π^0 mass. • - $p_T > 0.8$ GeV/c. ○ - $p_T > 3.0$ GeV/c. Results are from the 1991 data sample.

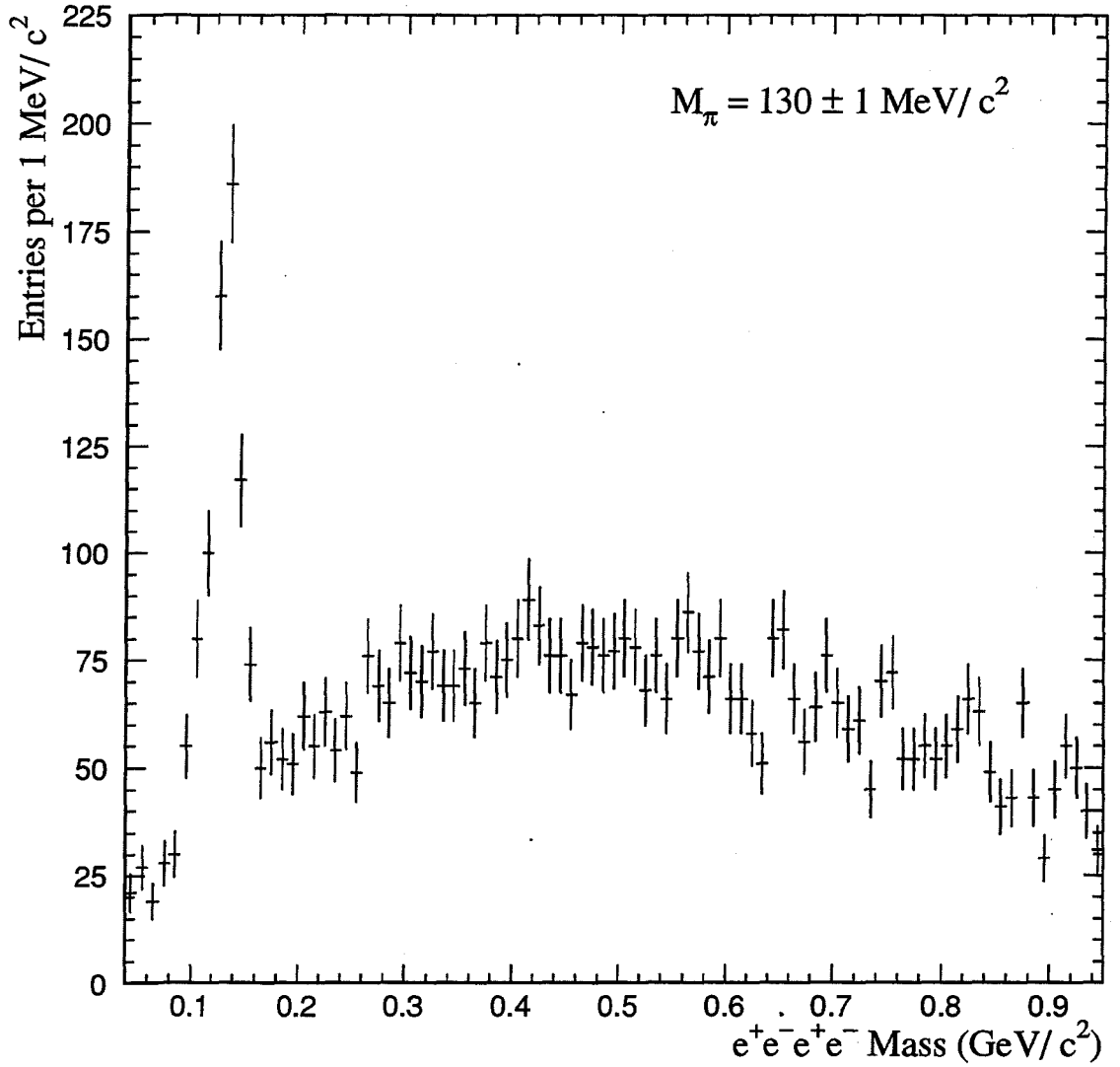


Figure 4.9: The $e^+e^-e^+e^-$ invariant mass distribution for electrons resulting from the conversion of $\gamma\gamma$ pairs in the material upstream of the EMLAC. Data are representative of the 1990 π^- sample with $p_T > 0.5 \text{ GeV}/c$. The π^0 signal is evident.

Chapter 5

Identification of Incident Beam Particles

The MW Čerenkov detector was used to identify the mass of the individual charged beam particles incident on the E706 target. The analysis of data from the Čerenkov detector is described in detail in this chapter.

5.1 Particle Tags

The Čerenkov detector was capable of identifying (i.e. *tagging*) incident charged beam particles based on differences in Čerenkov angle which, in turn, depend on the mass and momentum of the incident particle. To tag a specific particle type, a minimum number of phototubes were required to provide signals above threshold (i.e. *fire*) in the ring of phototubes designed to tag that type of particle. For example, an incident particle could be tagged as a pion if two or more phototubes fire in the π -ring of phototubes, represented symbolically by $\pi 2$. Note that any number of phototubes could be required to fire in coincidence. Increasing the required number of phototube signals in coincidence reduced the background rate from spurious noise or accidental misidentification (i.e. *contamination*) by non-tag particle types, but also resulted in lowered tagging efficiency. In addition, signals from the other phototube rings were often used as a veto to reduce the probability

of mis-tagging. The $\pi 2$ tag in the example above could be modified to include a veto of NOT two or more phototubes firing in the p -ring (i.e. one or less). The veto would then be written $\overline{p2}$ where the bar represents the logical NOT of a $p2$ coincidence. The full tag in this example is labeled $\pi 2 \overline{p2}$.

5.2 Čerenkov Pressure Curves

Various tag coincidence probabilities were measured as a function of the helium pressure in the Čerenkov detector. A sample pressure curve is shown, on a semi-logarithmic scale, in Figure 5.1 for a $K4\pi 2\overline{p2}$ coincidence.¹ Three peaks are visible in this curve. These peaks were produced, in order of increasing pressure, by pions, kaons and protons in the incident +530 GeV/c beam. The largest peak corresponds to the majority particle, the proton, while the smaller peaks correspond to the minority particles in the +530 GeV/c beam, i.e. the pions and kaons. The relative size of the peaks is closely correlated with the relative abundance of that particle type in the beam (known as the *particle fraction*). The curve was acquired by counting the number of occurrences for which the chosen tag logic was satisfied during each spill. The count was then normalized to the corresponding BEAM count for that spill (Chapter 3). The curve then represents the probability that *any* incident charged beam particle will satisfy the tag logic as a function of pressure.

Note that while the operating pressure *could* be chosen to direct light from any particle type into any ring of phototubes, the operating pressure in the Čerenkov counter was set to optimize the tagging of pions using the π -ring of phototubes. The Čerenkov detector was designed to *simultaneously* tag the three different particle types for a *single* operating pressure. This is illustrated by overlaying three

¹Note that this represents a kaon tag requiring four or more phototubes to fire in the K -ring while requiring less than two phototubes fire in the π -ring and less than two phototubes fire in the p -ring.

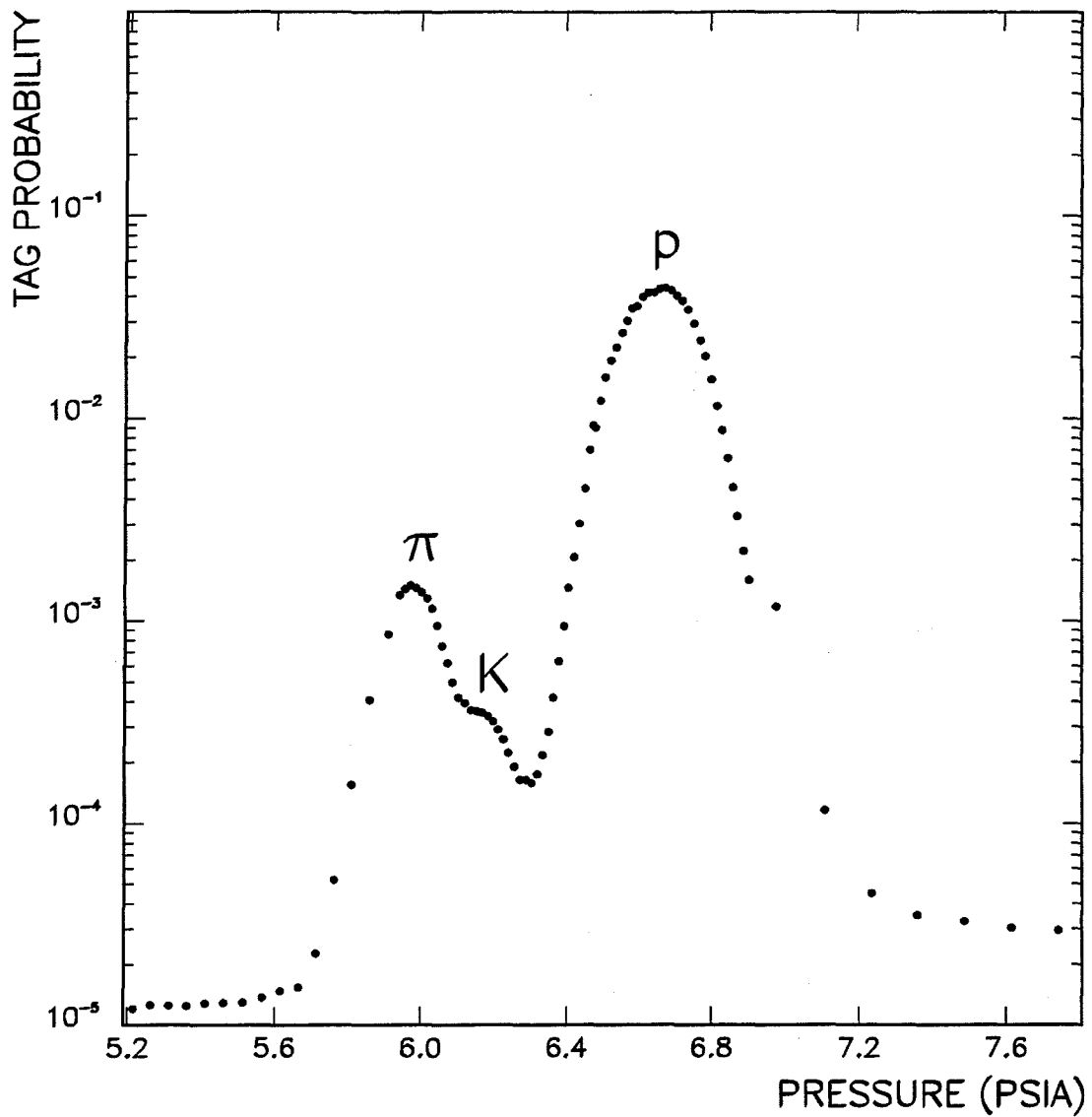


Figure 5.1: Pressure curve for the $K4\pi2p2$ tag logic (kaon tag) with incident +530 GeV/c beam. Peaks are labeled by particle type. Note that the plot is on a semi-logarithmic scale.

pressure curves — one for each of three characteristic particle tags (Figure 5.2). Each curve is labeled with the corresponding tag logic. For each curve, the particles responsible for producing each peak/plateau² are labeled. It can be seen that for an operating pressure of about 6.3 psia the counter can simultaneously tag protons, kaons and pions using the corresponding phototube rings.

A perfectly resolved peak (*single particle pressure curve*) would correspond to light emitted by a single particle type. Such a curve would provide the probability for tagging that particular particle type as a function of pressure. The contamination in the tag would then be due only to the accidental background associated with that tag logic. The overlap of two or more single particle pressure curves would correspond to light from two or more different incident particle types contributing to a single curve. The actual pressure curves clearly suggest that most tags will include contributions (*contamination*) from misidentified (i.e. non-tag) particles. For example, in the kaon tag, the peak produced by light from kaons overlaps the peak due to light from pions³ for this particular tag (Figure 5.3). This indicates that for operating pressures useful for tagging kaons, some pions will be misidentified as kaons by this particular tag. Similarly, the pion peak in the pion tag included contributions from both protons and kaons. To account for the impact of this particle misidentification on the cross-section measurements, it was necessary to assess the particle type composition of each tag.

²That a given particle type produces curve shapes which vary from one channel to another simply reflects differences in the geometrical acceptances and optics associated with each channel. For example, a given particle type will produce clear peaks in the *K*-ring of phototubes while producing broad plateaus in the *p*- and π -rings. This is due to the fact that the *p* and π channels possess very broad apertures while light reaches the *K*-phototubes only through very thin lenses.

³There was also a very small contribution from the proton peak.

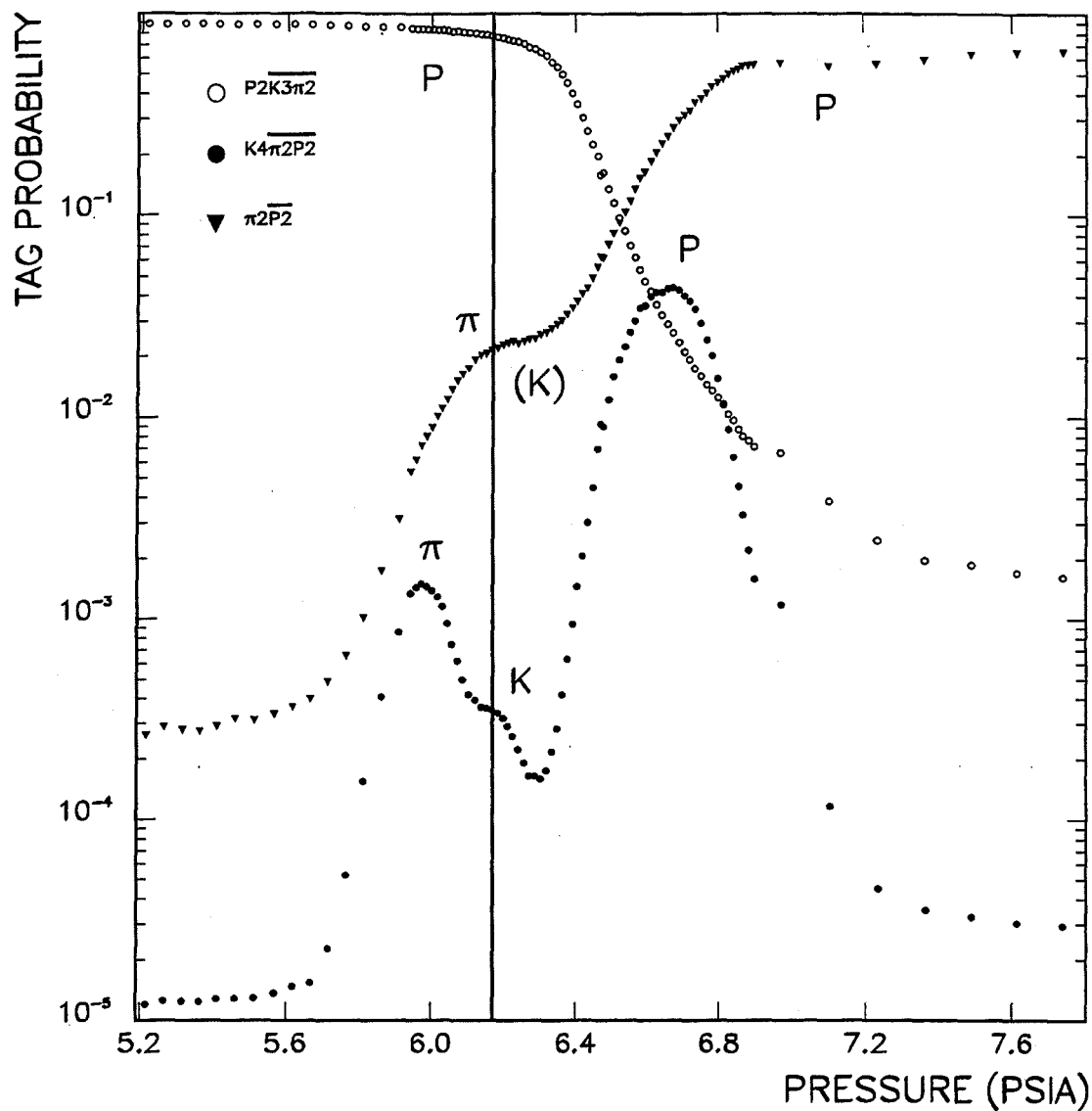


Figure 5.2: Pressure curves for pion, kaon and proton tags with incident +530 GeV/c beam. Each curve is labeled by tag logic. Peaks/plateaus are labeled by the associated particle type. Plot is on a semi-logarithmic scale. The solid vertical line represents a typical operating pressure. The line clearly passes through the desired peaks for tagging each particle type with the appropriate coincidence logic.

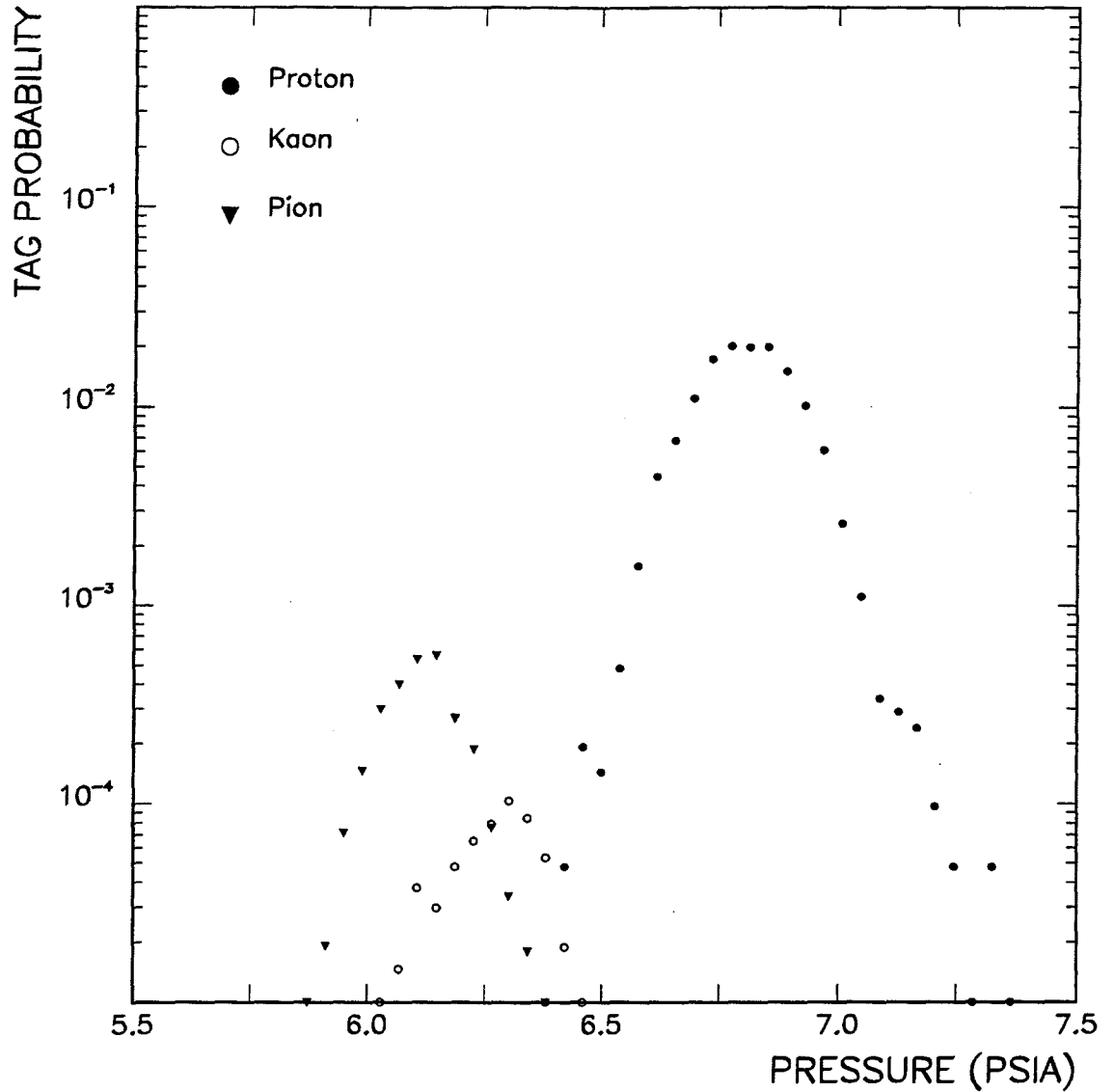


Figure 5.3: Overlapping single particle pressure curves contributing to the $K4\pi2p2$ coincidence with incident +530 GeV/c beam. The curves are labeled according to the type of particle producing the curve. The curves are taken from a Monte Carlo simulation. The actual pressure curve would correspond to a superposition of all contributing single particle pressure curves. Each generated single particle pressure curve was weighted to account for the relative particle fractions in the beam. Weights were taken from the following analysis. Data were acquired during runs 14896-14898.

5.3 Overview of Čerenkov Analysis Methods

In an effort to measure the desired tag efficiencies and contaminations, the performance of the Čerenkov counter was studied in detail.

A pressure curve acquired from a beam containing three charged particle types is equivalent to the superposition of three separate single particle pressure curves, each weighted in proportion to the appropriate particle fraction. To determine the probability of tagging a given particle, it was necessary to determine the intrinsic probability for the chosen tag logic to tag *any* particle and the particle type composition of each tag (used in weighting the single particle pressure curves) including assessing the probability that the tag was due to background noise.⁴

To determine the probability for particle misidentification a decision was made to model the shapes of the single particle pressure curves generated by each of the three particle types in the incident beam. In this way the contributions to the composite pressure curves from each particle type could be extracted. For each tag, the superposition of the three generated curves, each weighted according to the appropriate particle fraction, provided a complete fit to the full pressure curve. The particle type composition and the probability for particle misidentification could then be determined for each tag.

Several methods were considered for fitting the pressure curves. Studies of the pressure curve shapes revealed that the curves attributed to a single incident particle type were generally asymmetrical (Figure 5.4). Gaussian fits to such curves yielded unacceptable uncertainties on the measurements of the tag contaminations. Furthermore, the shapes of the single particle pressure curves were dependent on the type of incident beam particle as indicated by Monte Carlo studies in Figure 5.5.

⁴Background noise included phototube dark current effects, particles not associated with the beam which passed directly through the phototubes and stray light in the detector.

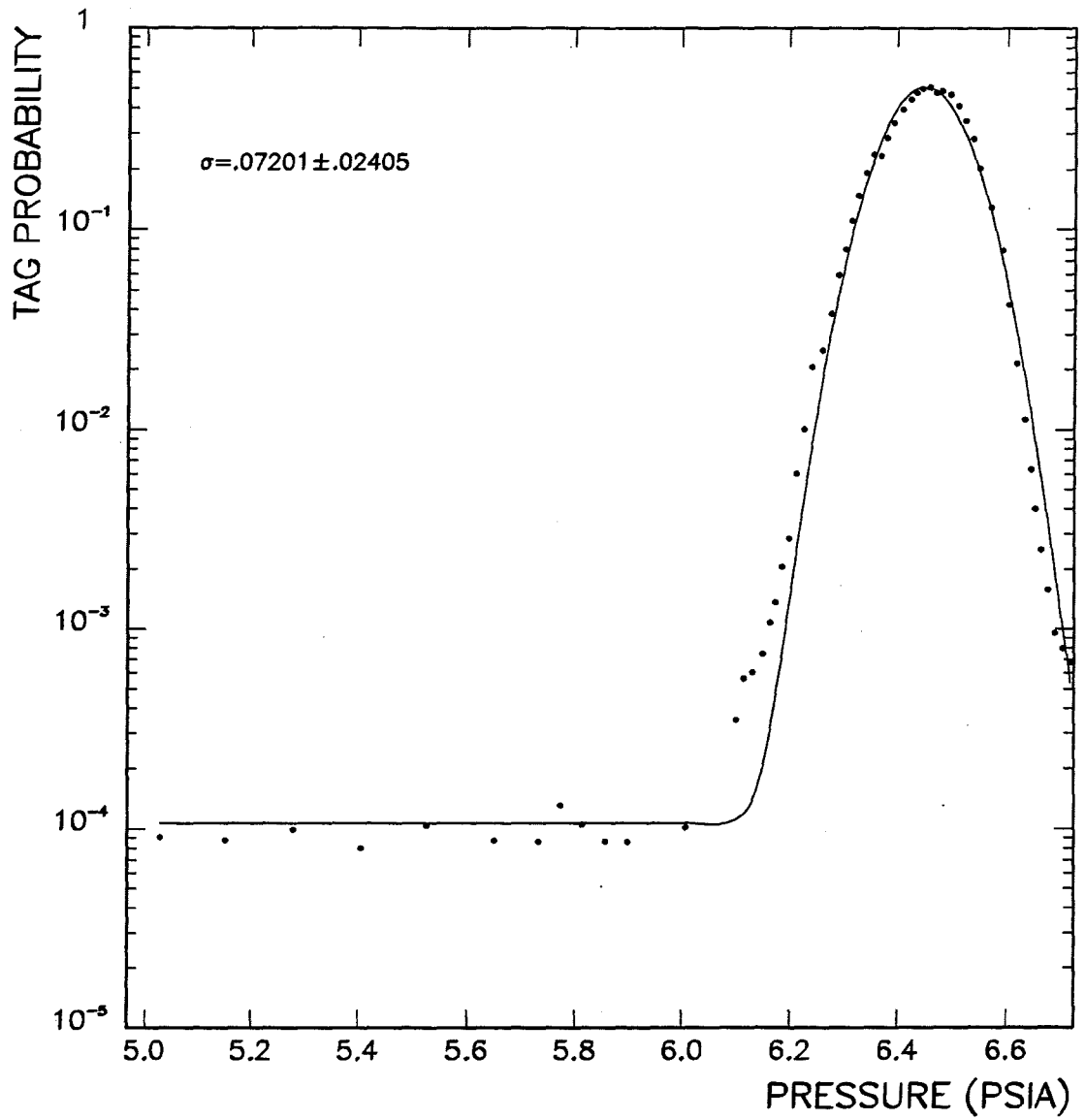


Figure 5.4: Pressure curve taken with 800 GeV/c incident protons illustrating asymmetry in the $K4\pi2p2$ coincidence. Data acquired online using scalers are represented by the solid points. The solid line represents a gaussian fit to the data.

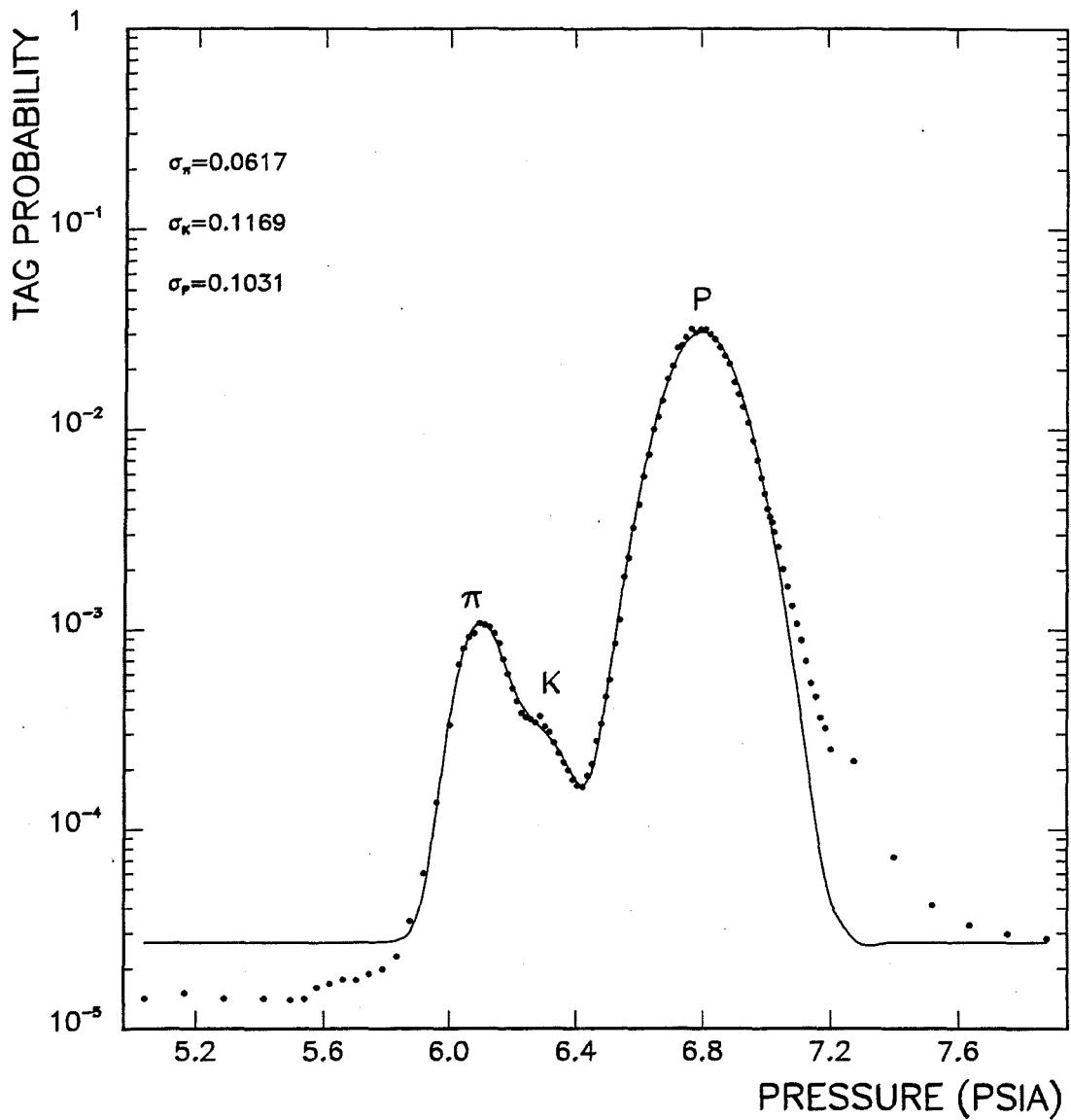


Figure 5.5: Pressure curve taken with incident +530 GeV/c beam illustrating the shape differences for peaks produced by different incident particle types. The solid points represent data acquired online using scalers. The solid line represents the fit of 3 gaussian curves plus a flat background to the data. The π curve is clearly narrower than the p and K curves.

These studies indicate that the curve shapes depend in a non-trivial way on the wavelength distribution of generated light, geometrical and optical constraints and on the phase space distributions of the incident beam particles. Though some simplification occurs when the beam distributions are symmetrical about the counter axis, this generally was not the case. A model of the beam distributions and a full Monte Carlo simulation of the detector were thus used to fit the pressure curves for each particle type. The Monte Carlo program simulated the performance of the Čerenkov detector in order to determine the efficiencies and particle type composition for each particle tag.

5.4 Monte Carlo Simulations

Pressure curves were simulated using a Monte Carlo program which models the propagation of particles and photons through the optics and geometrical apertures of the Čerenkov detector. The program provides a relatively complete description of the geometry and optics of the Čerenkov counter based on actual measurements when available and design specifications where measurements were not available. The 800 GeV/c beam spatial distributions were nearly gaussian at the Čerenkov detector and were entirely composed of protons since this was a primary beam. The optical and geometrical parameters of the simulation were established by fitting the 800 GeV/c pressure curve data using such approximations for the incident beam distributions. Many of the +530 GeV/c and -516 GeV/c beam distributions were asymmetrical and were modeled using an additional Monte Carlo simulation program. As an understanding of beam transport is essential for the simulation of the charged particle distributions incident on the detector, beam modeling will be discussed first.

5.4.1 TURTLE Simulation of the +530 GeV/c and -516 GeV/c Beams

Many of the +530 GeV/c and -516 GeV/c beam distributions were asymmetrical. These asymmetries influenced the firing probabilities of the individual phototubes. In order to account for such asymmetries in the Čerenkov Monte Carlo simulation, the phase space distributions for these beams momenta were modeled using the TURTLE⁵ [76] Monte Carlo simulation program [37]. TURTLE simulates charged particle production and subsequent transport through an array of beam-line elements.

Particle Production

TURTLE simulates the production of charged secondaries by 800 GeV/c protons incident on a beryllium target using a model [77] derived from fits to absorption cross-section measurements [78]. In this model the probability density for the production of particles in the momentum range from p to $p + \Delta p$ and solid angle between Ω and $\Omega + \Delta\Omega$ is given by the formula

$$\frac{d^2 N}{dp d\Omega} = BX \frac{(1 - X)^A (1 + 5e^{-DX})}{\left(1 + \frac{p_T^2}{M^2}\right)^4}. \quad (5.1)$$

Here $X = p/p_0$ where $p_0 = 800$ GeV/c is the momentum of the incident protons, p is the lab momentum of the produced secondary particle and p_T the corresponding transverse momentum of the secondary. The parameters A, B, D and M resulting from the absorption cross-section fits are given in Table 5.1. The predicted yields for the relevant secondary particles transported down the MW beamline are shown in Figure 5.6.

The production model is based on absorption data for a 50 cm thick beryllium target. For beryllium targets of different lengths, the production probability must

⁵Trace Unlimited Rays Through Lumped Elements

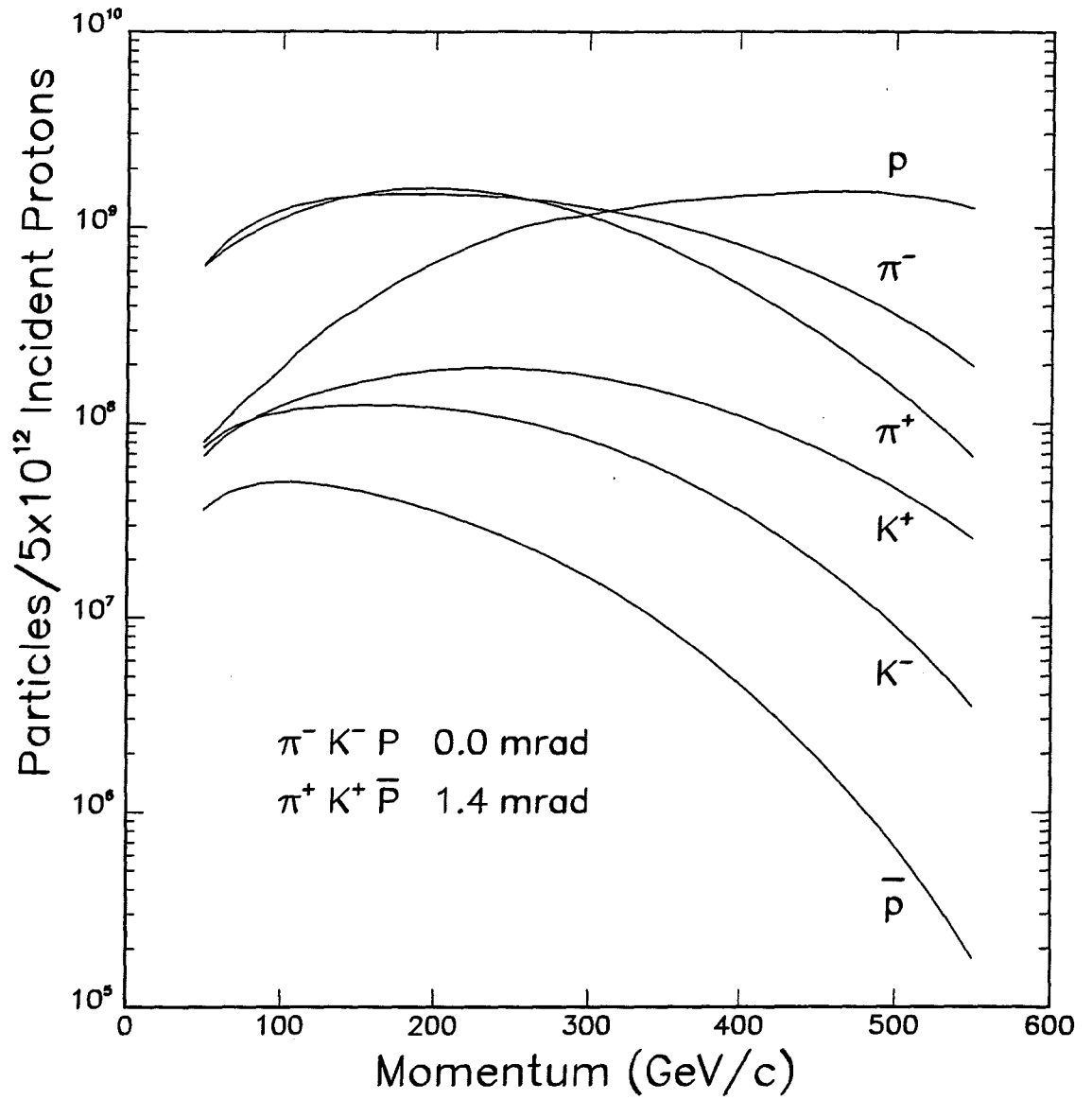


Figure 5.6: Secondary particle yields for 800 GeV/c protons incident on beryllium calculated from the production model. Yields are shown in particles per 5×10^{12} protons incident on the Meson West production target. The production angles for each polarity are listed.

Particle	A	B	D	M^2
p	1.708	3.510	-4.314	1.043
π^+	3.598	177.2	27.00	0.7077
K^+	2.924	14.15	19.89	1.164
π^-	4.122	70.60	11.29	0.8932
K^-	6.107	12.33	17.78	1.098

Table 5.1: Production model parameters from fits to the absorption cross-section measurements.

be weighted by the factor

$$g(L) = \frac{e^{-\frac{L}{\lambda(s)}} - e^{-\frac{L}{\lambda(p)}}}{1 - \frac{\lambda(p)}{\lambda(s)}}. \quad (5.2)$$

Here L is the thickness of the target, $\lambda(p)$ is the absorption length for incident protons and $\lambda(s)$ the absorption length for produced secondaries. For secondary protons, $\lambda(s) = \lambda(p)$, and this reduces to

$$g(L) = \frac{L}{\lambda(p)} e^{-\frac{L}{\lambda(p)}}. \quad (5.3)$$

The production model used by **TURTLE** was modified [79] to account for the 1.4 mrad production angle required in the production of the +530 GeV/c secondary particles.⁶

⁶The non-zero production angle was implemented as a safety precaution to prevent excessively high radiation levels which could otherwise have resulted from accidentally transporting high intensity primary protons down the secondary beamline.

Beamline Coordinates

The transport of charged beam particles may be analyzed by sequentially calculating the effect of each beamline element on the relevant phase space parameters describing each charged particle trajectory. The conventional phase space coordinates [37] used to model beam transport systems are illustrated in Figure 5.7. All particle trajectories are referenced to the trajectory of a hypothetical particle possessing the mean momentum of the beam. There are six phase space coordinates for each particle trajectory - x , y , x' , y' , Δp and ℓ . Here ℓ is the length of the projection of the particle's trajectory onto the reference trajectory. The positive ℓ direction corresponds to the direction of beam propagation (along the reference trajectory). The variables x and y represent the transverse distances of the particle's trajectory from the reference trajectory at longitudinal position ℓ as measured in the rest-frame Euclidean coordinate system of the reference beam particle. The y coordinate is always chosen to be upward with respect to absolute beamline coordinates (i.e. upward from the ground) and the x coordinate is chosen to be to the left (horizontally) when looking in the direction of beam propagation. x' and y' represent the angles which the particle trajectory makes with the tangent to the reference trajectory at longitudinal position ℓ in the $x - \ell$ and $y - \ell$ planes respectively. Note that these are, equivalently, a measure of the transverse components of momentum, p_x/p and p_y/p where p is the particle's momentum. Finally, Δp is the deviation of the particle's momentum from the momentum of the reference trajectory.

Raytrace of Particles Through Beamline Elements

The propagation of particle trajectories through the array of beamline elements was simulated using matrix methods analogous to those of light optics. The effect

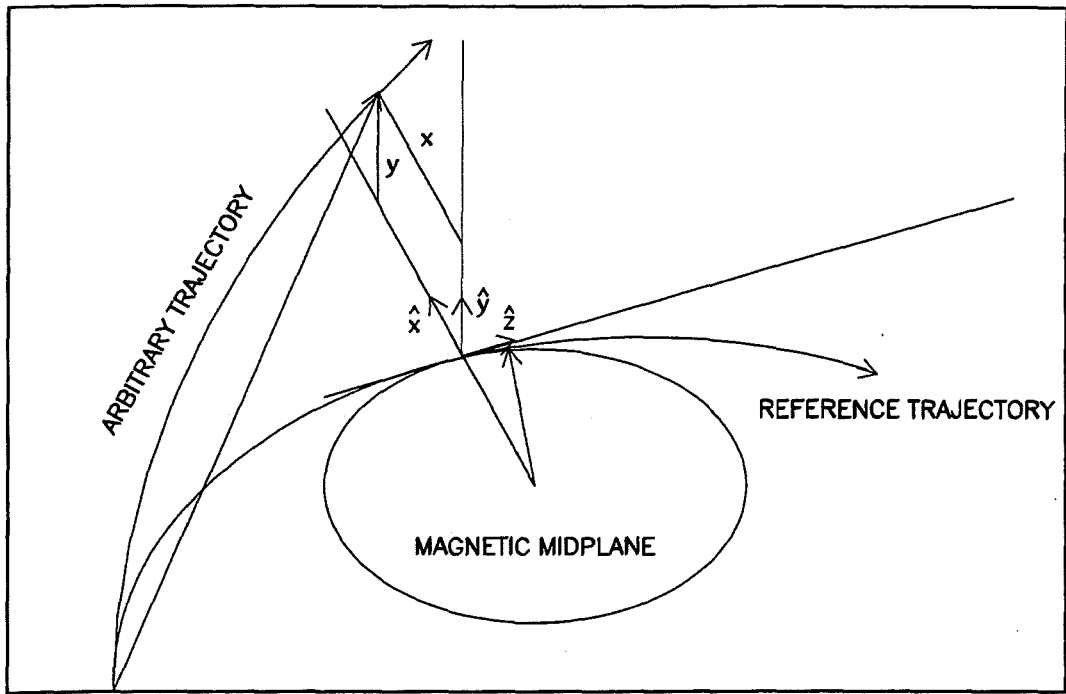


Figure 5.7: Conventional beamline coordinates showing the central trajectory and magnetic midplane.

of each beamline element⁷ (including empty *drift* spaces) is represented by the action of a matrix operating on the vector of phase space coordinates.

The magnetic field strengths employed in **TURTLE** were initially fixed according to the values of the actual currents applied to the magnets at run time. The currents were then varied within their systematic uncertainties to achieve acceptable fits to the available SWIC profiles. The longitudinal positions of the beamline elements were fixed in the **TURTLE** program according to the measurements provided by Fermilab alignment group personnel [34].

The **TURTLE** program was run on a VAX computer using the VMS operating system. A fixed number of beam particles were generated using the production model described above and subsequently traced through the array of beamline elements to the upstream entrance of the Čerenkov detector. For each particle reaching the Čerenkov detector, the phase space parameters describing that particle's trajectory were written to external data files. For each particle type, a separate file was created for the five relevant beam parameters⁸ and for each particle type. The files were subsequently transferred to a Silicon Graphics platform which uses the UNIX operating system. There the Čerenkov Monte Carlo simulation program utilized the **TURTLE** data to describe the trajectories of each beam particle incident on the Čerenkov detector.

A comparison of the resulting simulated spatial distributions with the corresponding SWIC profiles at the upstream entrance to the Čerenkov counter is shown in Figures 5.8 and 5.9 for the incident +530 GeV/c and -516 GeV/c beams. The **TURTLE** x , y , x' , y' and $\Delta P/P$ distributions are compared for the three particle types in Figures 5.10-5.14.

The sensitivity of the Čerenkov Monte Carlo simulation to the variations in

⁷The actions of the various elements were discussed in Chapter 2.

⁸The parameter ℓ was not used in the Čerenkov simulation.

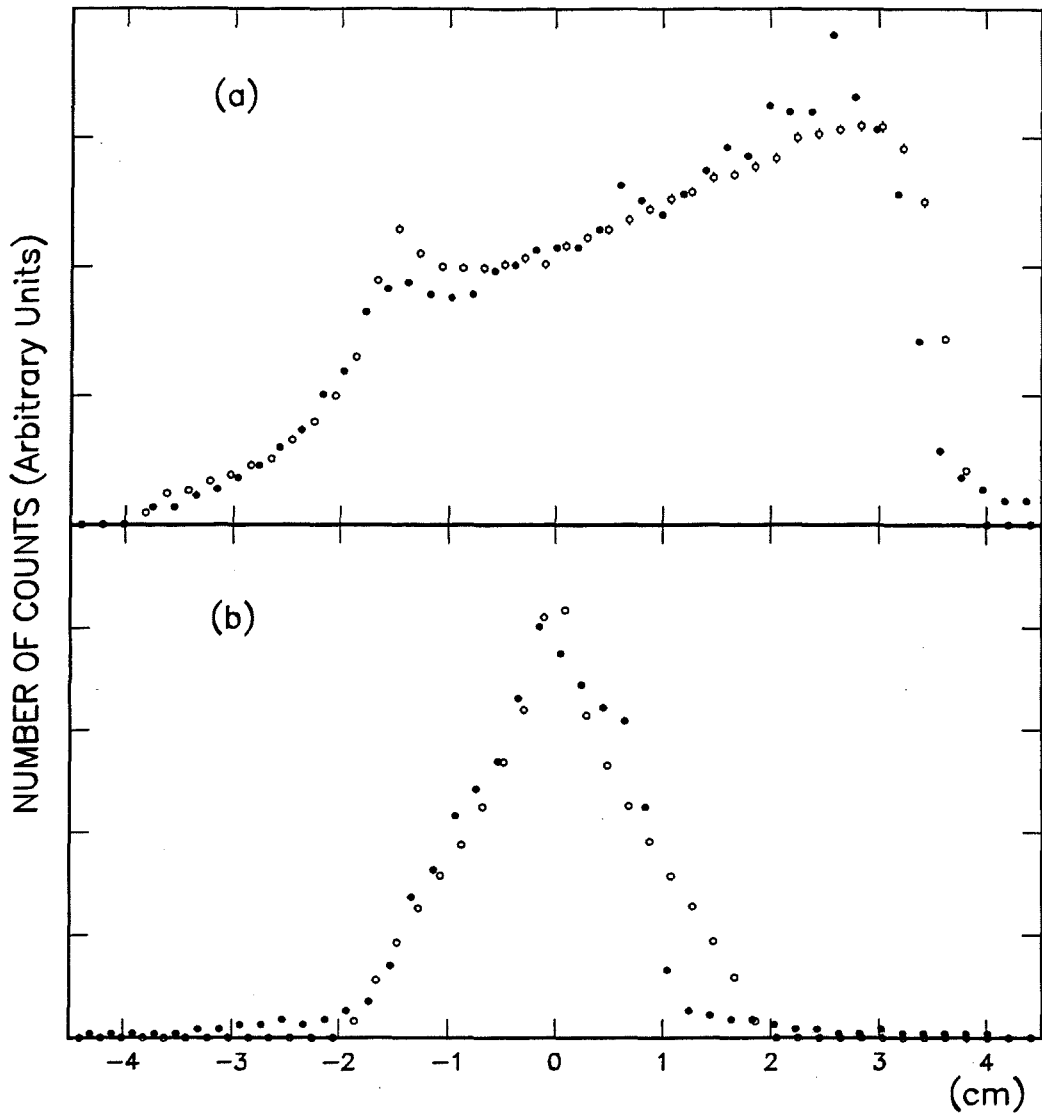


Figure 5.8: Comparisons of SWIC and **TURTLE** distributions for (a) the x -distribution of beam particles and (b) the y -distribution of beam particles at the entrance to the Čerenkov detector for incident $+530$ GeV/c beam. \bullet - **TURTLE** simulation for incident protons. \circ - SWIC data.

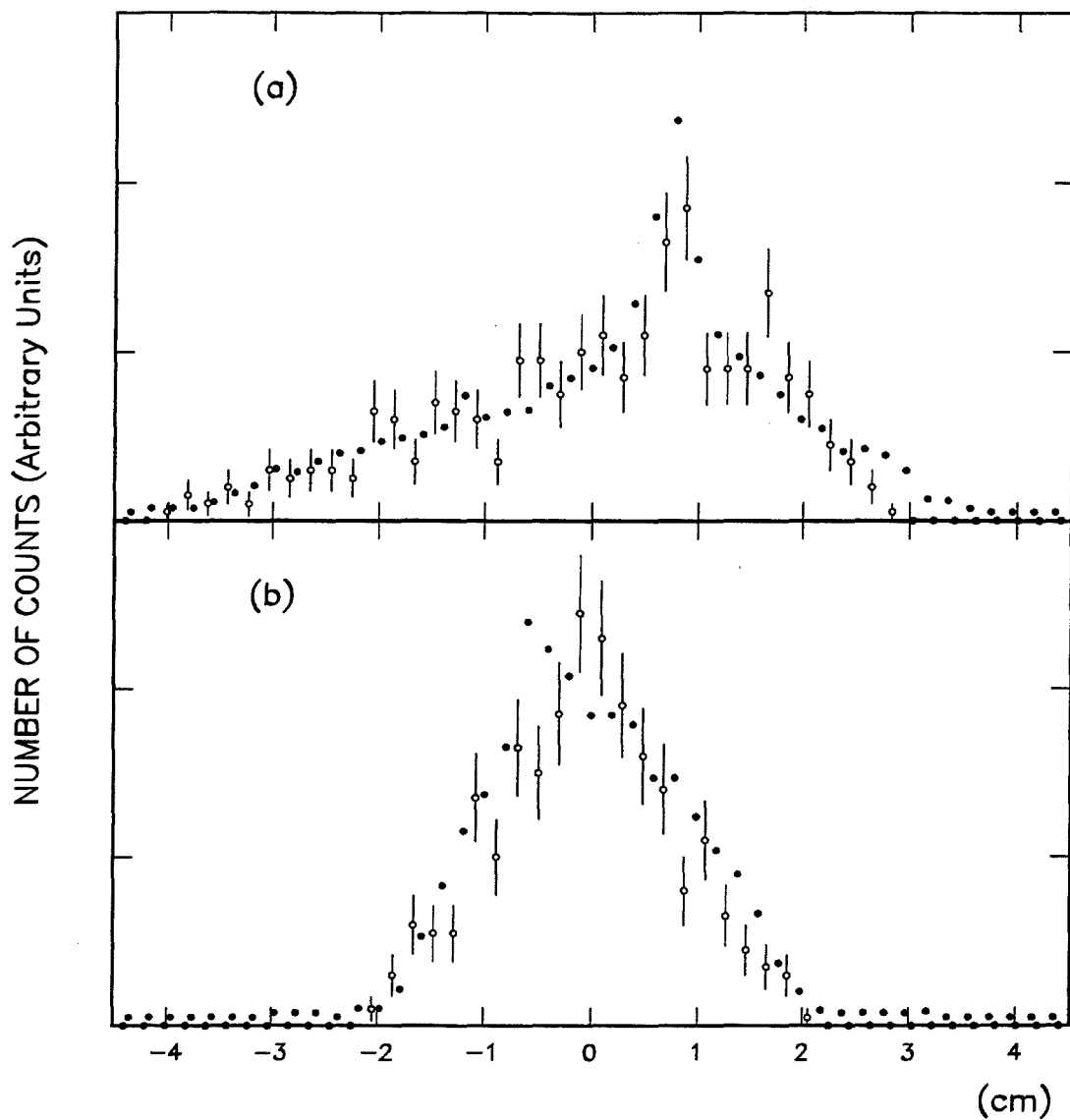


Figure 5.9: Comparisons of SWIC and TURTLE distributions for (a) the x -distribution of beam particles and (b) the y -distribution of beam particles at the entrance to the Čerenkov detector for incident -516 GeV/c beam. • - TURTLE simulation for incident protons. o - SWIC data.

beam distribution for the different incident particle types was tested by describing the incident particle as a proton in the simulation while reading beam parameters separately for incident protons, kaons and pions thus providing small systematic variations in the beam distribution of protons. The Čerenkov Monte Carlo simulation showed no observable sensitivity to this level of differences in the beam distribution for the various particle types. Furthermore, as such differences in beam distribution for the various particle types were comparable the discrepancy between the **TURTLE** simulation and the actual SWIC distributions these results provided confidence that the Čerenkov Monte Carlo simulation was not sensitive to the discrepancy between the **TURTLE** simulated beam distributions and the corresponding SWIC data distributions.

5.4.2 Čerenkov Monte Carlo Simulation

The coordinate convention used in the Čerenkov Monte Carlo simulation program was the same as in the **TURTLE** beam transport simulation program. The simulated counter pressure was incremented in uniform intervals over a pressure range characteristic of a real pressure curve.⁹ For each pressure increment, a fixed number of incident beam particles was generated. For each generated particle, the phase space parameters were read from the output files created by **TURTLE**. Each generated particle was then traced from the upstream counter entrance to the downstream end using vector raytrace methods [80],[81] taking into account losses due to geometrical aperture limits.

For each generated beam particle the mean number of Čerenkov photons emitted was determined by integrating the wavelength distribution (Equation 2.8) for the emission of photons provided by the semi-classical Čerenkov theory.¹⁰ The

⁹Typically, the simulation was performed over the pressure range of 5.5-7.5 psia.

¹⁰A ten-point Simpson's integration was used.

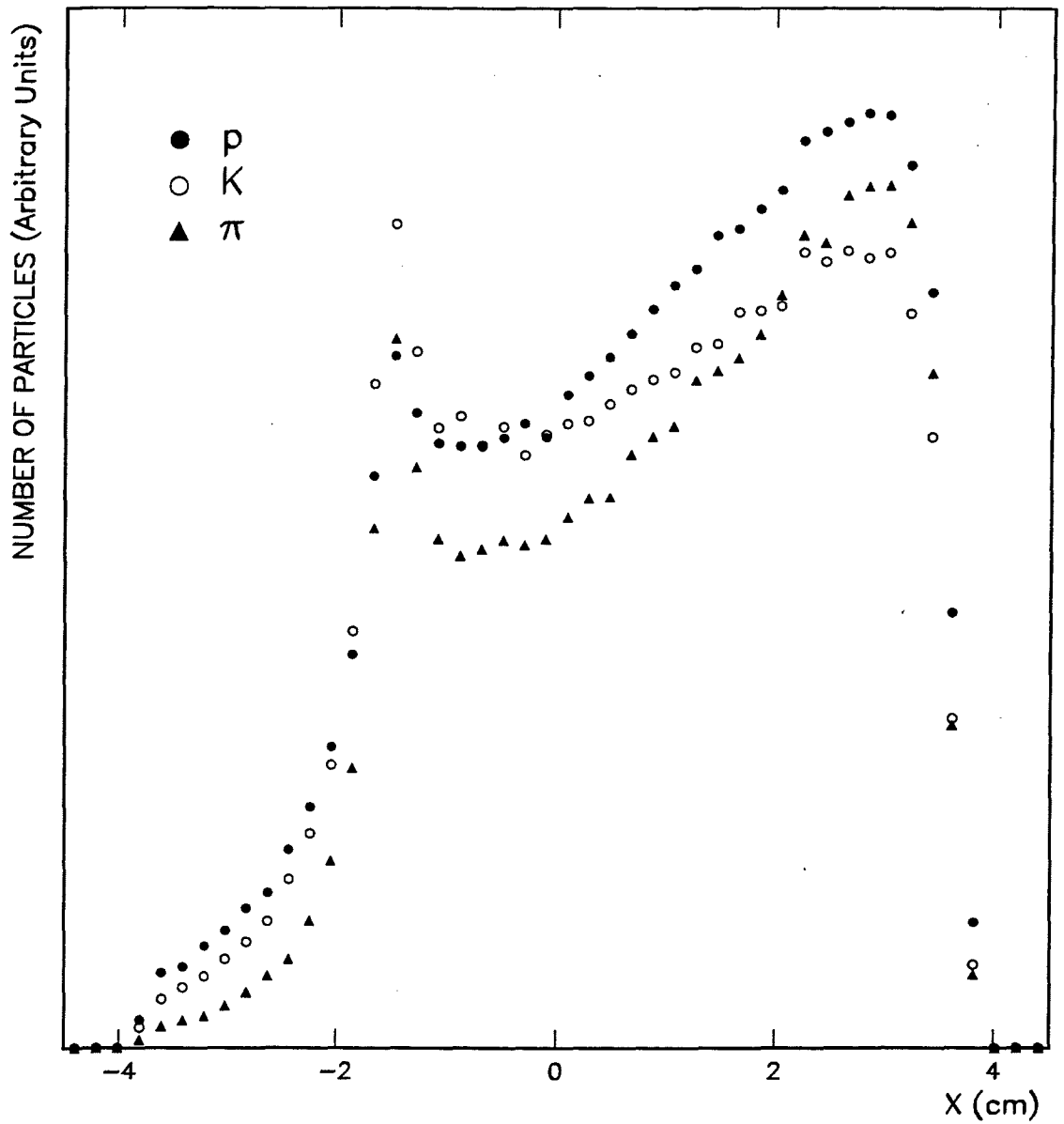


Figure 5.10: Comparison of the x distributions for each type of +530 GeV/c beam particle at the entrance to the Čerenkov counter as produced by the **TURTLE** simulation. The plots are normalized to the same number of generated particles for 100% population of each particle type in the beam.

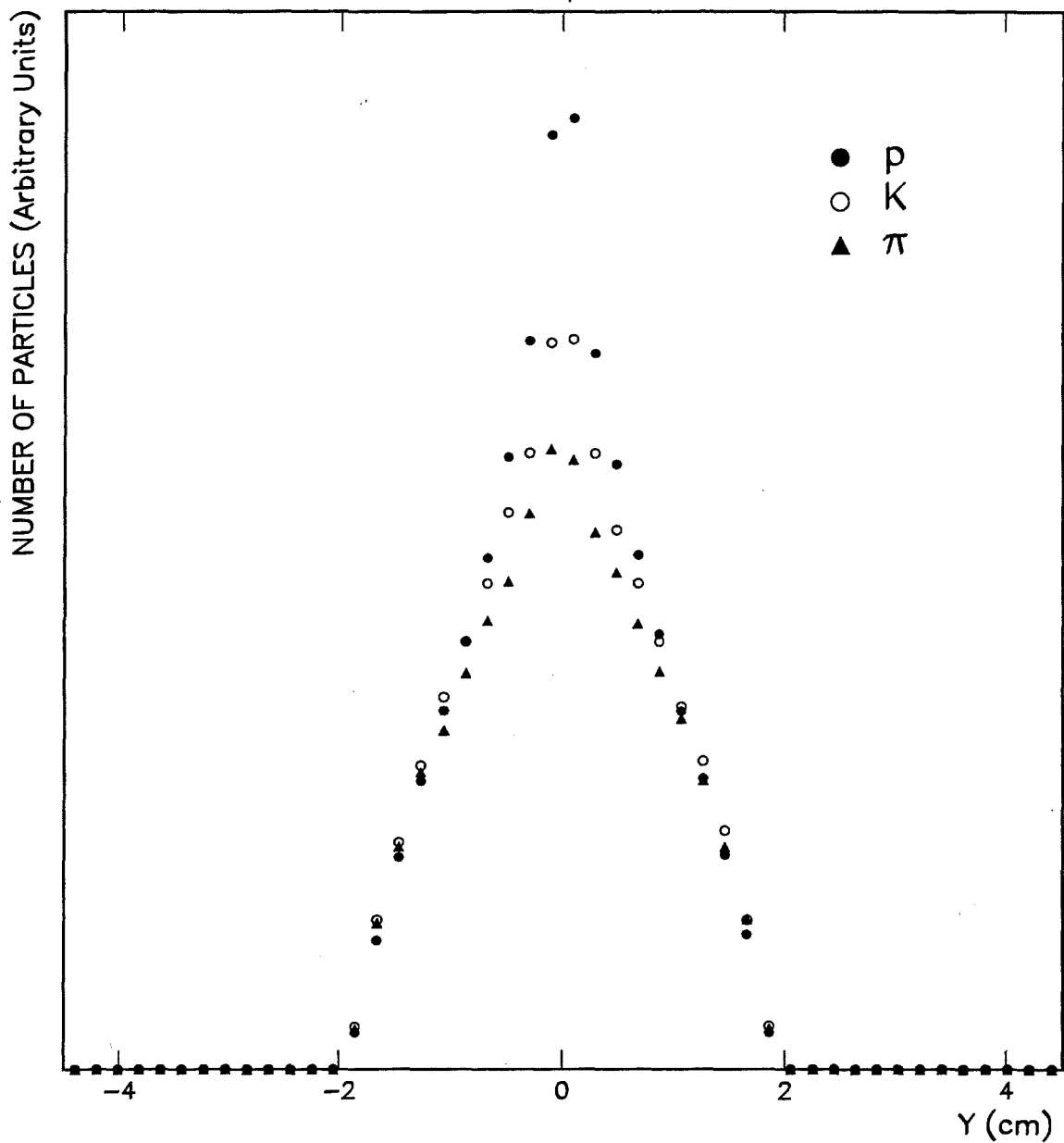


Figure 5.11: Comparison of the y distributions for each type of +530 GeV/c beam particle at the entrance to the Čerenkov counter as produced by the **TURTLE** simulation. The plots are normalized to the same number of generated particles for 100% population of each particle type in the beam.

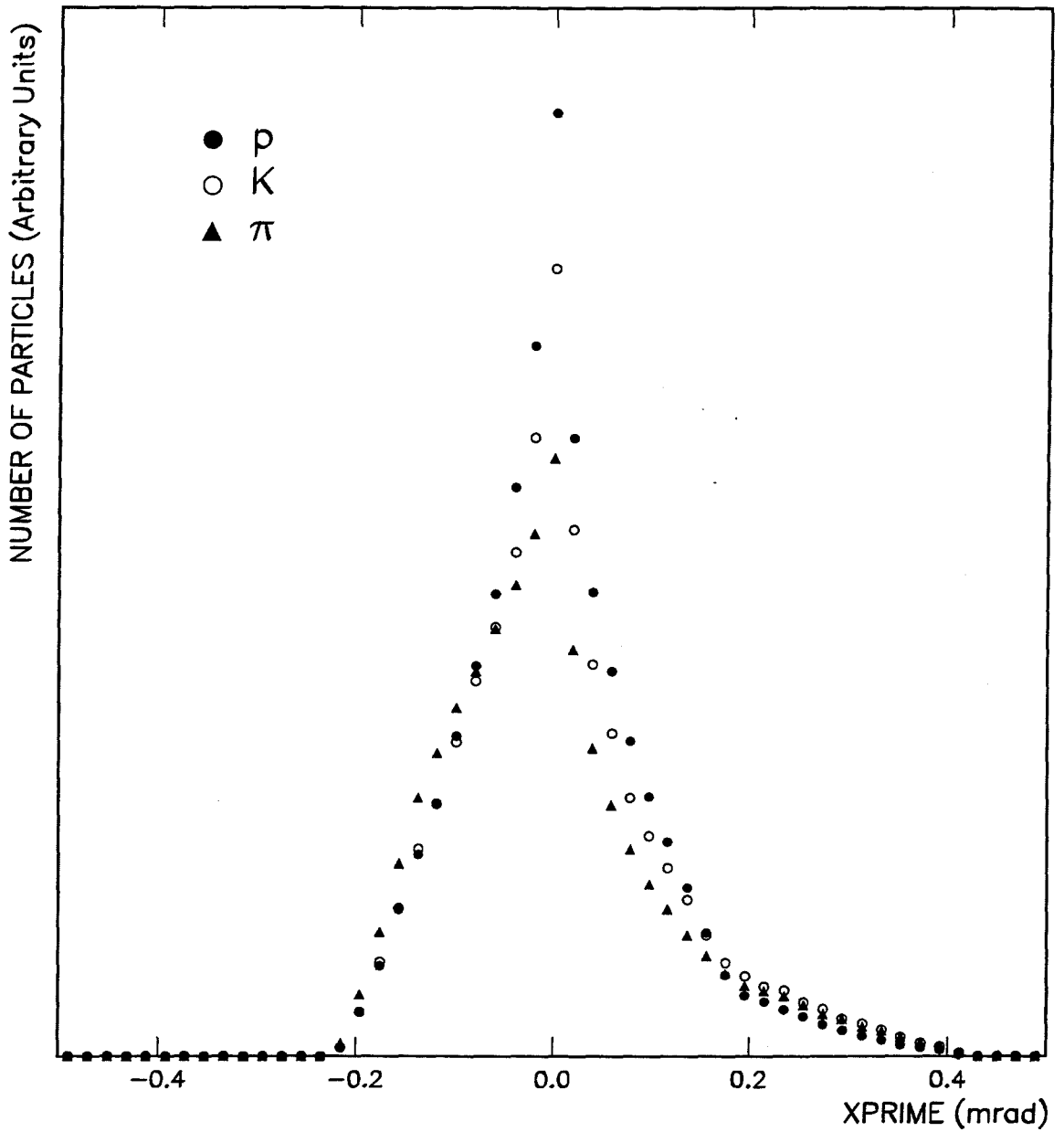


Figure 5.12: Comparison of the x' distributions for each type of +530 GeV/c beam particle at the entrance to the Čerenkov counter as produced by the **TURTLE** simulation. The plots are normalized to the same number of generated particles for 100% population of each particle type in the beam.

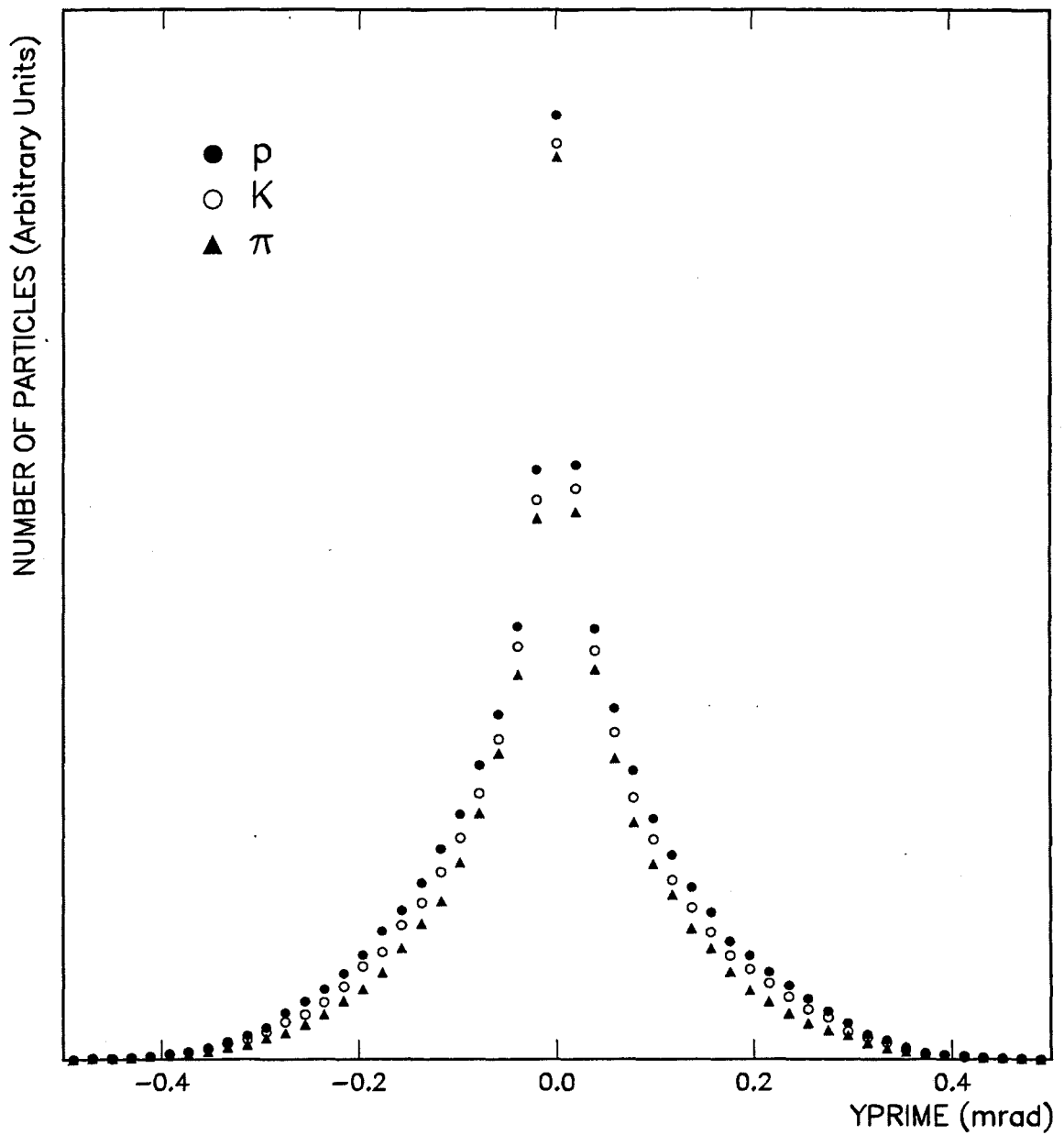


Figure 5.13: Comparison of the y' distributions for each type of +530 GeV/c beam particle at the entrance to the Čerenkov counter as produced by the **TURTLE** simulation. The plots are normalized to the same number of generated particles for 100% population of each particle type in the beam.

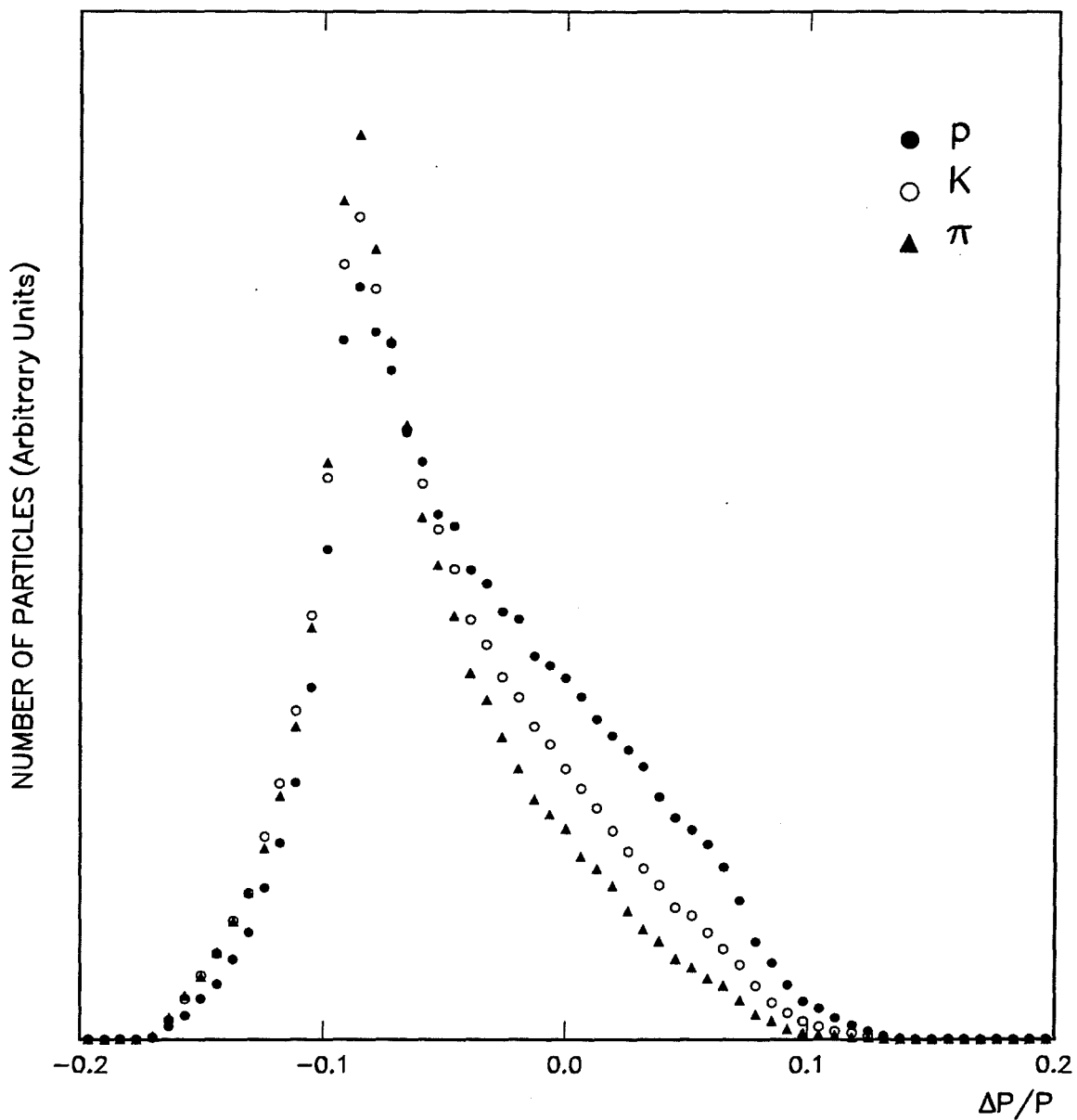


Figure 5.14: Comparison of the $\Delta p/p$ distributions for each type of +530 GeV/c beam particle at the entrance to the Čerenkov counter as produced by the **TUR-TLE** simulation. The plots are normalized to the same number of generated particles for 100% population of each particle type in the beam.

actual number of emitted photons was then selected from a Poisson distribution whose mean was given by the above integration. The emission of photons by beam particles was simulated by selecting the wavelength from the wavelength distribution using a weighted von Neumann hit-and-miss Monte Carlo by the method of deviates[82],[83]. The wavelength was then selected from the resulting weight function

$$\lambda = \frac{\lambda_1}{(1 - x(1 - \frac{\lambda_1}{\lambda_2}))}, \quad (5.4)$$

where λ_1 and λ_2 are the effective low and high limits of the Čerenkov wavelength distribution and x is a uniformly distributed random variable. The wavelength distribution as reproduced by the Monte Carlo program is shown in Figure 5.15.¹¹

The generated photons were emitted uniformly in both the longitudinal and azimuthal coordinates with respect to the direction of particle propagation (Figure 5.16). The polar (Čerenkov) angle was derived from Equations 2.2 through 2.6 taking into account the dependence of the refractive index on temperature, pressure and wavelength. Incident particles will generally trace a skewed path through the counter. To account for this, each photon trajectory was rotated from the incident particle's frame to the absolute frame of the Čerenkov counter using the appropriate Euler angles.

Each photon was individually traced, using vector raytrace methods to the appropriate phototube, taking into account the effects and losses due to all intervening optics and geometrical apertures (Figures 2.5 and 2.15). For convenience, the counter was divided into sextants to match the arrangement of phototubes. The impact of the optics and geometrical apertures on the raytrace were azimuthally symmetric from the emission of the photons to the lens mount plate. To simplify

¹¹The path length of the incident particle was properly taken into account in this weighting.

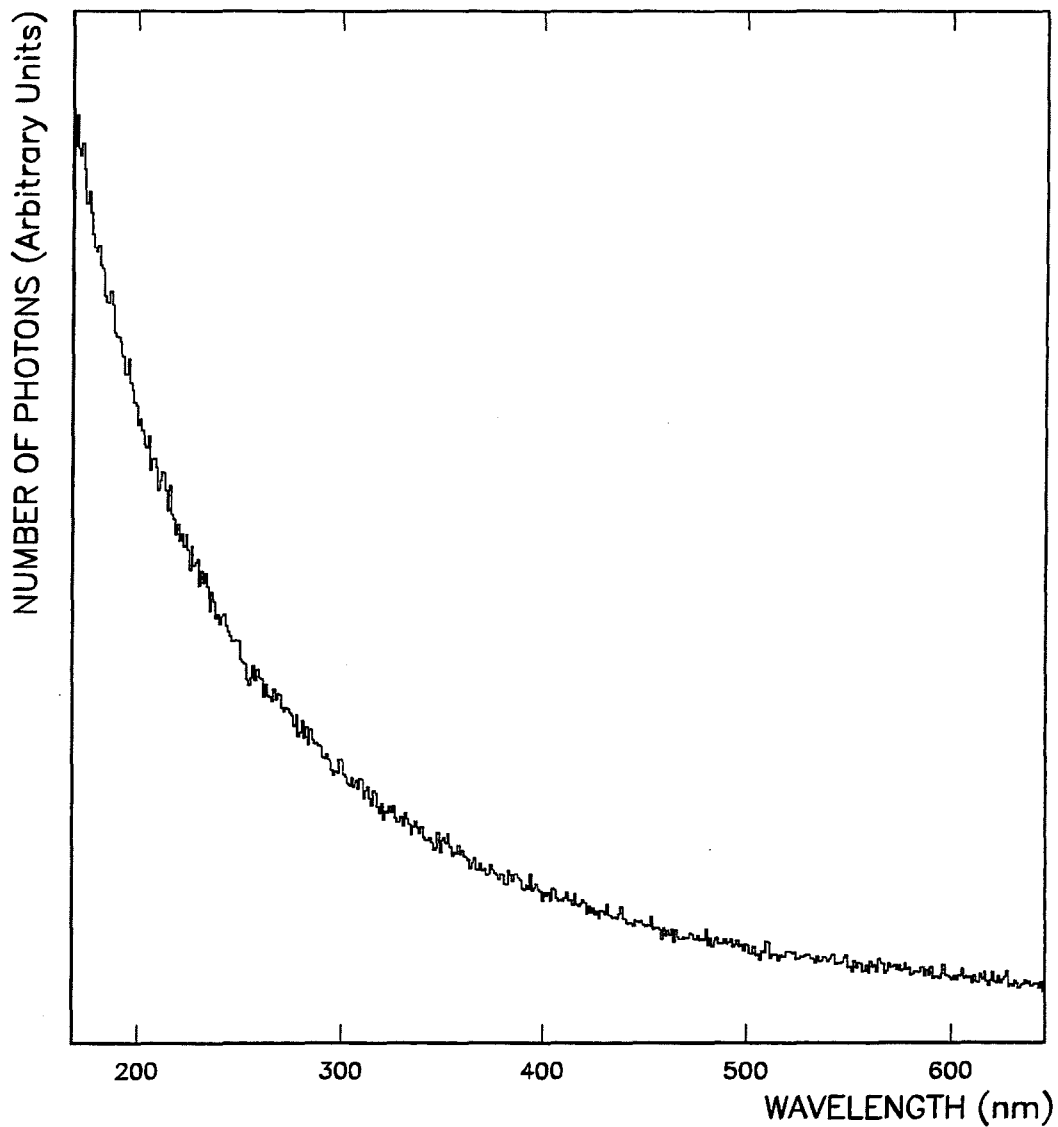


Figure 5.15: Čerenkov Monte Carlo results showing the wavelength distribution for emitted photons integrated over all relevant pressures for incident 800 GeV/c protons.

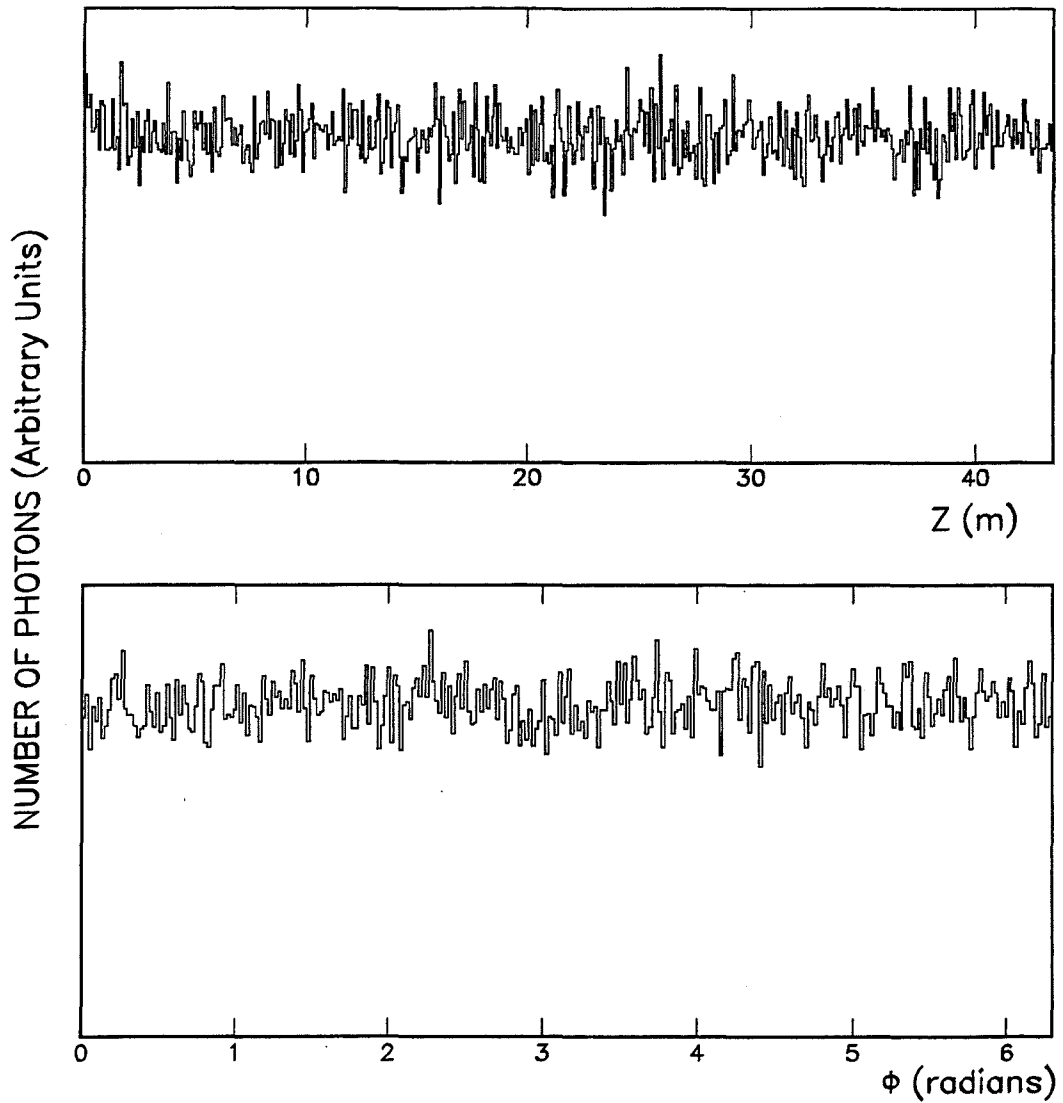


Figure 5.16: Čerenkov Monte Carlo results showing uniform distributions for (a) longitudinal position of the incident beam particle at the point of photon emission (relative to the upstream end of the Čerenkov counter) and (b) azimuthal angle of Čerenkov photon emissions with respect to the direction of particle propagation.

the raytrace, the photon was traced to the lens mount plate in the correct sextant. At this point a rotation was performed on all relevant vectors to place the raytrace in the "first" sextant¹² while maintaining a record of the original sextant for that photon. This simplified subsequent calculations involving the rectangular mirrors. Sample plots of the photon distributions at various key points in the raytrace are shown in Figure 5.17.

Photons which survive the raytrace and reach a phototube are subjected to additional losses due to the quantum efficiency of the phototube. The quantum efficiency is treated as a probability for the emission of a photoelectron. Photoelectrons produced by incident photons will cascade to produce detectable electronic signals. For all phototubes, the quantum efficiencies in the Monte Carlo were interpolated from digitizations of curves provided by the manufacturers. A sample quantum efficiency curve from the Monte Carlo implementation is shown in Figure 5.18.

Electric Polarization of Čerenkov Radiation

In addition to raytracing the photon trajectories, the Monte Carlo program was capable of tracing the electric field vectors of the photons. This allowed the characteristics of various optical elements to be evaluated as a function of the polarization state. Čerenkov radiation is highly polarized upon emission and remains very highly polarized upon incidence at the spherical mirror, reflecting cylinders and lenses thus making the analysis relatively simple. However, the geometry and orientation of the laser mirrors destroys this symmetry resulting in a mixed polarization state.

Light in the K and π channels is either reflected by the laser mirror assembly into the K -ring of phototubes, transmitted through the laser mirror to the π -ring

¹²I.e. the sextant which was symmetric about 0°

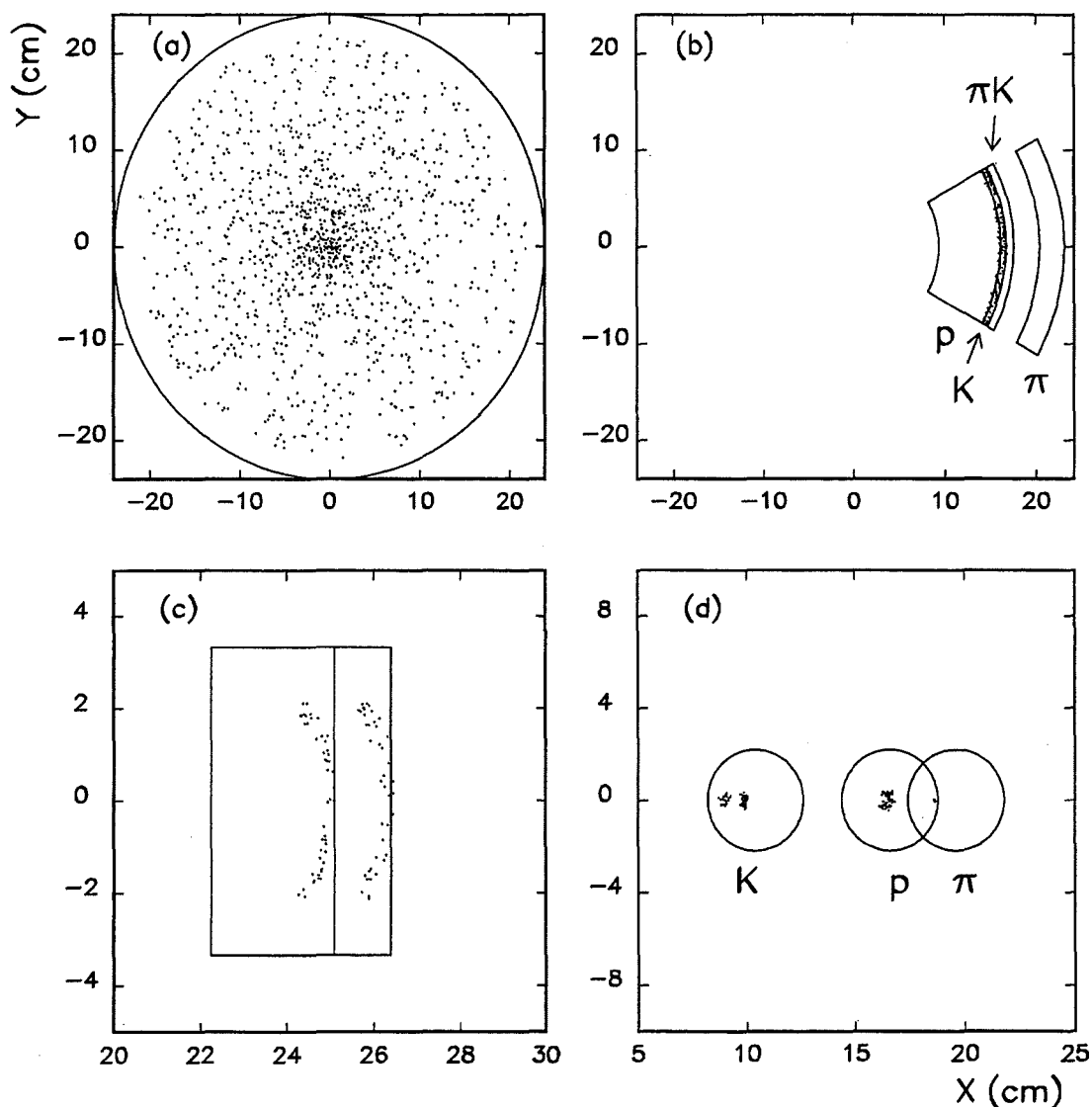


Figure 5.17: Monte carlo simulation of the two dimensional photon position distributions transverse to the Čerenkov counter axis at various points in the counter for incident +800 GeV/c protons and an operating pressure of 6.21 psia. The distributions are summed over all relevant wavelengths. Locations are at the (a) Spherical mirror. The circle represents the edge of the mirror. (b) Lenses. Only first sextant lenses are shown. The arcs represent lens edges. Photons are incident on the thin πK lens. (c) Laser mirror assembly. The smaller box represents the laser mirror. The larger box represents the flat aluminum mirror. (d) Phototubes. Photons are incident on both the K and p phototubes. The p (middle) phototube has been artificially rotated to place it along the same radius with the other phototubes resulting in the overlapping circles.

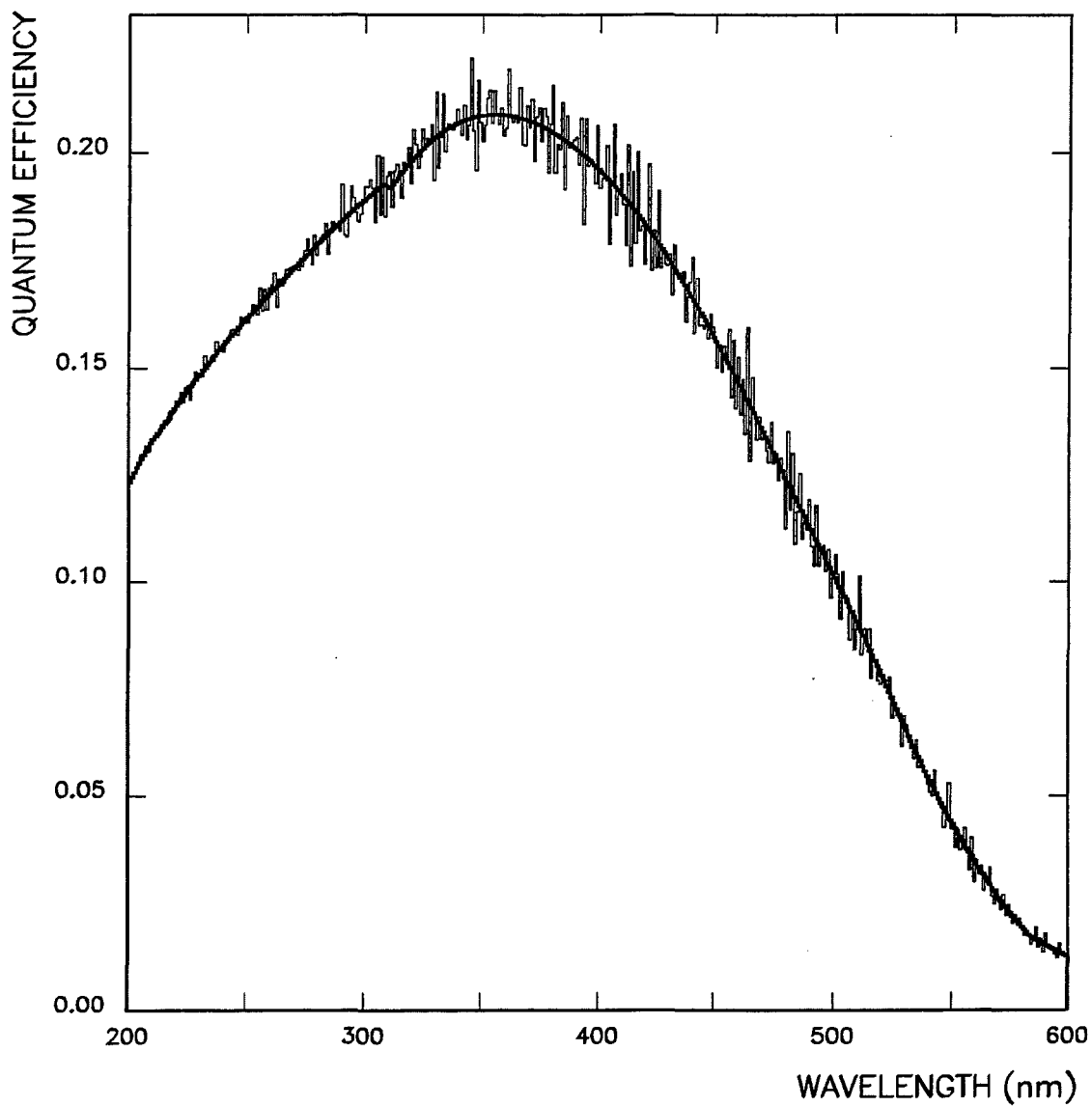


Figure 5.18: Quantum efficiency for the Philips XP2020Q phototubes. The solid curve is a digitization taken from the Philips manual. The histogram represents the curve generated by the Čerenkov Monte Carlo simulation.

of phototubes or absorbed by the mirrors. The reflection and transmission probabilities were taken from a digitization of available curves for unpolarized light at a 45° angle of incidence (Figure 2.16).¹³ The laser mirrors were designed to have a peak reflectance at 248 nm. In order to study the effects of polarization at the laser mirror, the complex refractive indices of the substrate and coating materials for the laser mirror as a function of wavelength were obtained from the manufacturer. However, the optical properties of the laser mirror were not available for the perpendicular and parallel polarization (*s*- and *p*-polarization, respectively) states separately. Furthermore, the manufacturer was unwilling to provide information on the coating thicknesses so that a full, detailed modeling of the actual coatings was not possible. Based on the knowledge that there were 24 alternating thin layers of two known materials deposited on the substrate and the assumption that the design was a modification of alternating quarter-wavelength layers (a standard design) a model employing transfer matrix methods was implemented in order to approximate the reflectance and transmittance. While the model proved incapable of determining the actual layer thicknesses and reflection/transmission curves for the independent polarization states, many of the essential features of the available curves for unpolarized radiation were reproduced (Figure 5.19). The reflectance peak is clearly evident at $\lambda_0 = 248$ nm as are the interference fringes at longer wavelengths. However, the long-wavelength "background" reflectance of this model mirror is clearly higher than that reported for the available unpolarized reflectance (Figure 2.16). The thicknesses of the layers were calculated to be $0.25\lambda_0$ and $0.31\lambda_0$. The reflectance and transmittance curves resulting from the transfer matrix model were useful in assessing the impact of the mixed polarization states on the reflection and transmission of incident Čerenkov radiation at the laser mirrors. The theoretical curves were used to set an upper limit on the

¹³Acton Research Corporation *High Power Excimer and UV Laser Optics* catalog.

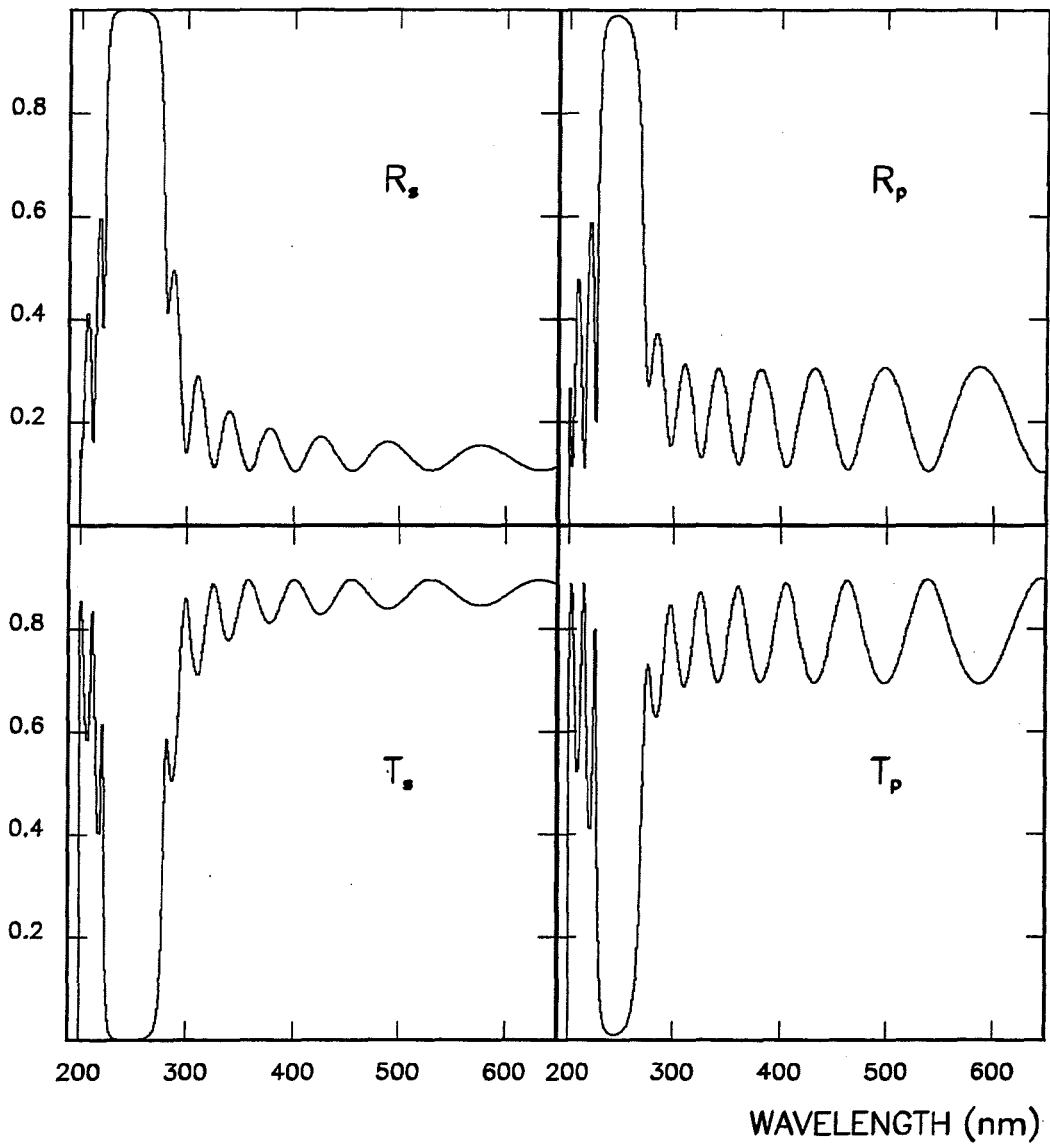


Figure 5.19: Laser mirror reflectance and transmittance curves for the *s*- and *p*-polarization states as reproduced by the transfer matrix model.

difference between the reflectances for the two polarization states (similarly for transmittance). This difference was used to express the p -polarization properties in terms of the s -polarization properties as a piecewise function of wavelength. Let

$$\frac{R_p}{R_s} = \epsilon, \quad (5.5)$$

where R_p and R_s represent the reflectance for s - and p -polarized radiation respectively. The reflectance, R , for unpolarized radiation may then be parameterized in terms of the independent polarization state by the expression

$$R = \frac{1}{2}(R_s + R_p) = \frac{1}{2}(1 + \epsilon)R_s \quad (5.6)$$

so that

$$R_s = \frac{2R}{1 + \epsilon} \quad (5.7)$$

and

$$R_p = 2R - R_s. \quad (5.8)$$

For the s - and p -polarization states of the transmittance, the treatment is the same. Thus a crude model for the reflectance for both the s - and p -polarization components could be determined as an expression of an upper bound on the difference between these states. By allowing the Monte Carlo program to trace the photon's electric field vector to the laser mirror the relative fraction of s - and p -polarization could be calculated for each photon. The resulting composite reflectance/transmittance curves could then be calculated from

$$R = aR_p + bR_s, \quad (5.9)$$

where a is the relative fraction of p -polarization and b the relative fraction of s -polarization (constrained by $a + b = 1$). The Monte Carlo program was then run first treating the incident light as unpolarized and employing the available curves for unpolarized light. The resulting values for a and b were recorded and the

program was then run again using the polarization curves from the transfer matrix model weighted by these a and b values. The results of the two runs are compared in Figures 5.20 and 5.21 for the single phototube pressure curves in the K and π channels. The results are seen to agree very well. As the Čerenkov Monte Carlo data did not exhibit any significant dependence on the polarization state of the incident radiation, the available curves for the reflectance and transmittance for unpolarized radiation were employed in the simulation. All subsequent calculations were performed by treating the radiation as unpolarized.

The availability of the refractive indices for the laser mirror substrate also provided a means of modeling the refraction of photon trajectories by the laser mirror so that each transmitted photon could be traced entirely through the mirror taking into account any aperture limits.

Phototube Efficiencies and Backgrounds

The individual phototube efficiencies and background firing probabilities were determined by fitting the Čerenkov Monte Carlo simulation to available *single phototube pressure curves* reconstructed from the Minnesota latch data. The in-time status of each phototube and BEAM were averaged spill-by-spill for all recorded events in each spill. The pressure values recorded at run time were correlated with the data on the phototube status on a spill-by-spill basis. The pressure values and latch data were then sorted "by hand" to eliminate spills for which the BEAM count was too low or too unstable to provide a reliable measurement. The latch data were summed over the spills for which the Čerenkov pressure was constant (within systematic uncertainties). The data were finally normalized spill-by-spill to the corresponding BEAM count. This yielded a measure of the individual phototube firing probabilities as a function of pressure.

Because photoelectrons were ejected in small, discrete integer numbers, the

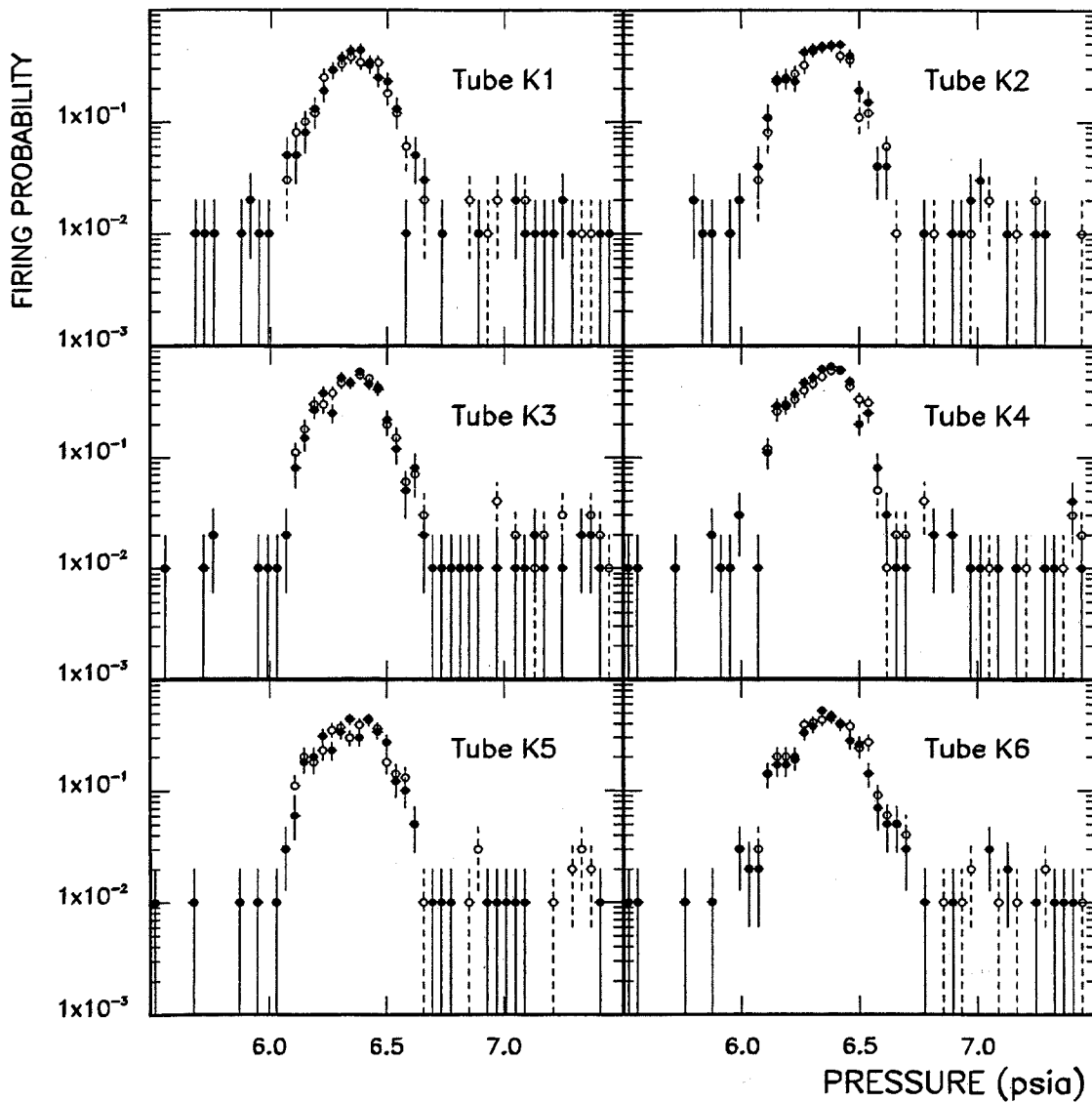


Figure 5.20: Comparison of single phototube pressure curves in the K channel for unpolarized (●) versus polarized (○). All results are from the Čerenkov Monte Carlo simulation.

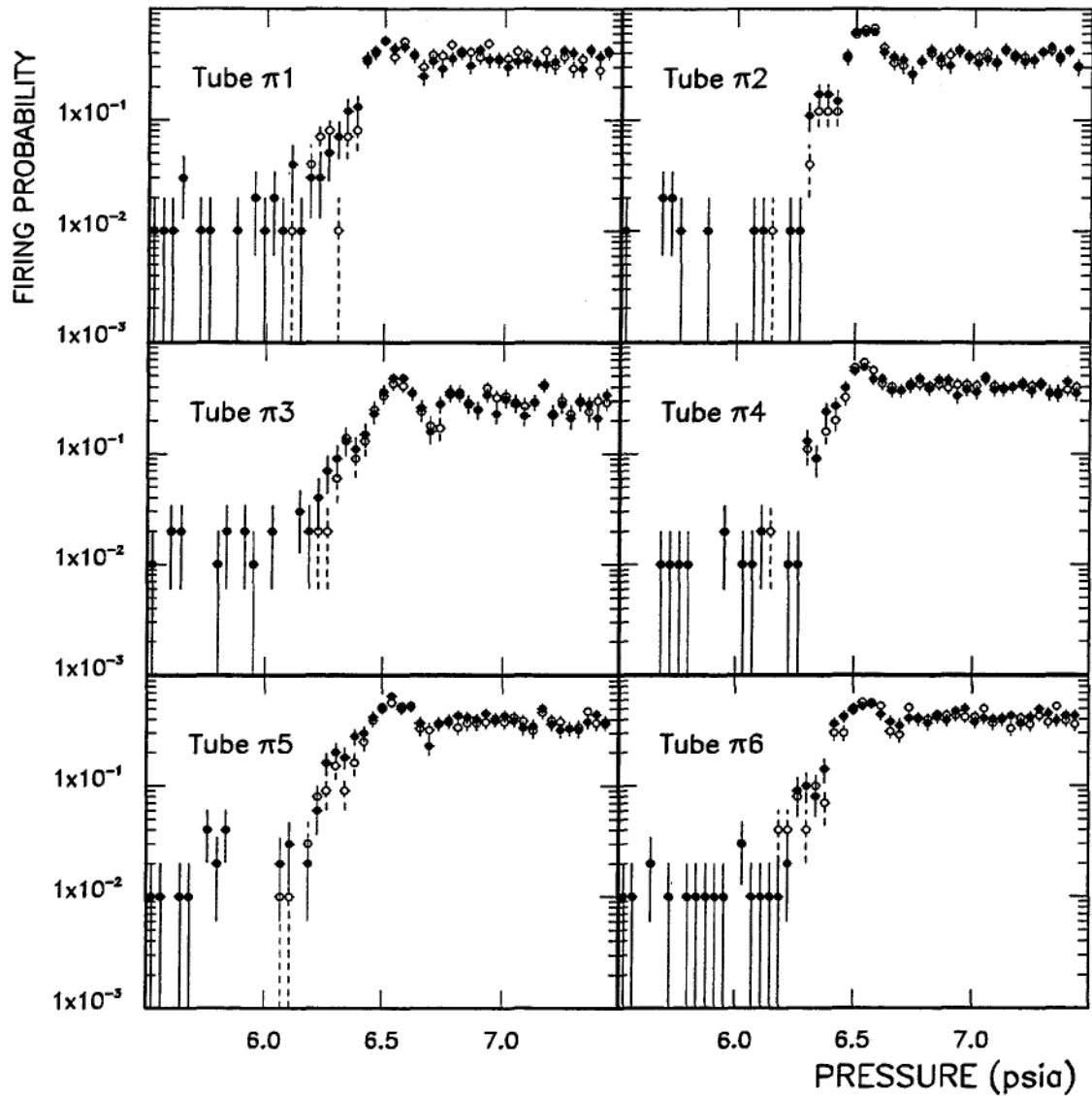


Figure 5.21: Comparison of single phototube pressure curves in the π channel for unpolarized (\bullet) versus polarized (\circ). All results are from the Čerenkov Monte Carlo simulation.

applied discriminator threshold for a given phototube tended to selectively accept an incoming signal if the number of generated photoelectrons was above some critical integer value. If the number of generated photoelectrons was below this value, the signal was rejected. As a result, the thresholds were parameterized in the Čerenkov Monte Carlo simulation in terms of the number of photoelectrons which generated signals above threshold. This value was evaluated independently for each phototube based upon the Monte Carlo fits to the single phototube pressure curves as reconstructed from the Minnesota Latch data.

For each pressure increment and incident particle, the total number of generated photoelectrons was accumulated for each phototube. This number was added to the total number of background photoelectrons resulting from the spurious firing of phototubes in the absence of a beam particle. The total number of photoelectrons generated by an incident particle was then compared to the number of photoelectrons required to produce a signal with a voltage above the corresponding discriminator's threshold.

The probability of satisfying Čerenkov tags for phototube coincidences including any vetos were similarly evaluated by the Čerenkov Monte Carlo simulation.

Simulation of the 800 GeV/c Pressure Curves

The 800 GeV/c beam consisted of protons¹⁴ transported directly from the Tevatron with very narrow spatial and momentum profiles. The beam trajectories were also very parallel throughout the Čerenkov detector so that any asymmetries associated with the beam were assumed to be negligible. Thus any asymmetries in the available pressure curves were assumed to arise from the geometrical, optical and electronic characteristics of the counter. The parameters representing these

¹⁴The population of minority particles in the 800 GeV/c beam was taken to be entirely negligible. This assumption was supported by the Čerenkov pressure curves which show that any additional particle types must occur with a relative fraction of $< 5 \times 10^{-7}$.

characteristics were established by fitting the 800 GeV/c pressure curves from data to those generated by Čerenkov Monte Carlo simulations.

For incident 800 GeV/c protons, the x and y distributions of incident beam particles just upstream and just downstream of the Čerenkov detector were fit to gaussian distributions (Figures 5.22 and 5.23). Approximate phase space parameters describing the incident 800 GeV/c beam were taken from the fits to the SWIC data. These parameters were then varied within systematic uncertainties to achieve a good fit to the 800 GeV/c pressure curves.

The geometrical and optical parameters describing the simulation were initialized to either measured or specification values as described above. To evaluate whether these values were appropriate, the Čerenkov Monte Carlo curves were fit to actual single phototube pressure curves acquired with incident 800 GeV/c proton beam. The geometrical and optical parameters were varied within systematic uncertainties to achieve a good fit to the actual pressure curves acquired from each of the three rings of phototubes. In addition, each curve was shifted by about +0.2 psia to account for a systematic pressure difference between the actual pressure readouts and the Čerenkov Monte Carlo simulation. Resulting fits for the single phototube pressure curves are shown in Figures 5.24 through 5.26. Fits to the coincidence curves are shown in Figure 5.27.

5.5 Composition of the Incident Beam and Tags

5.5.1 Muon Contamination

In addition to protons, pions and kaons, muons resulting from pion and kaon decays may also be transported by the MW beamline. The mass difference between the muon ($106 \text{ MeV}/c^2$) and the pion ($140 \text{ MeV}/c^2$) was too small to allow resolution by the MW Čerenkov detector. A comparison of the single phototube pressure

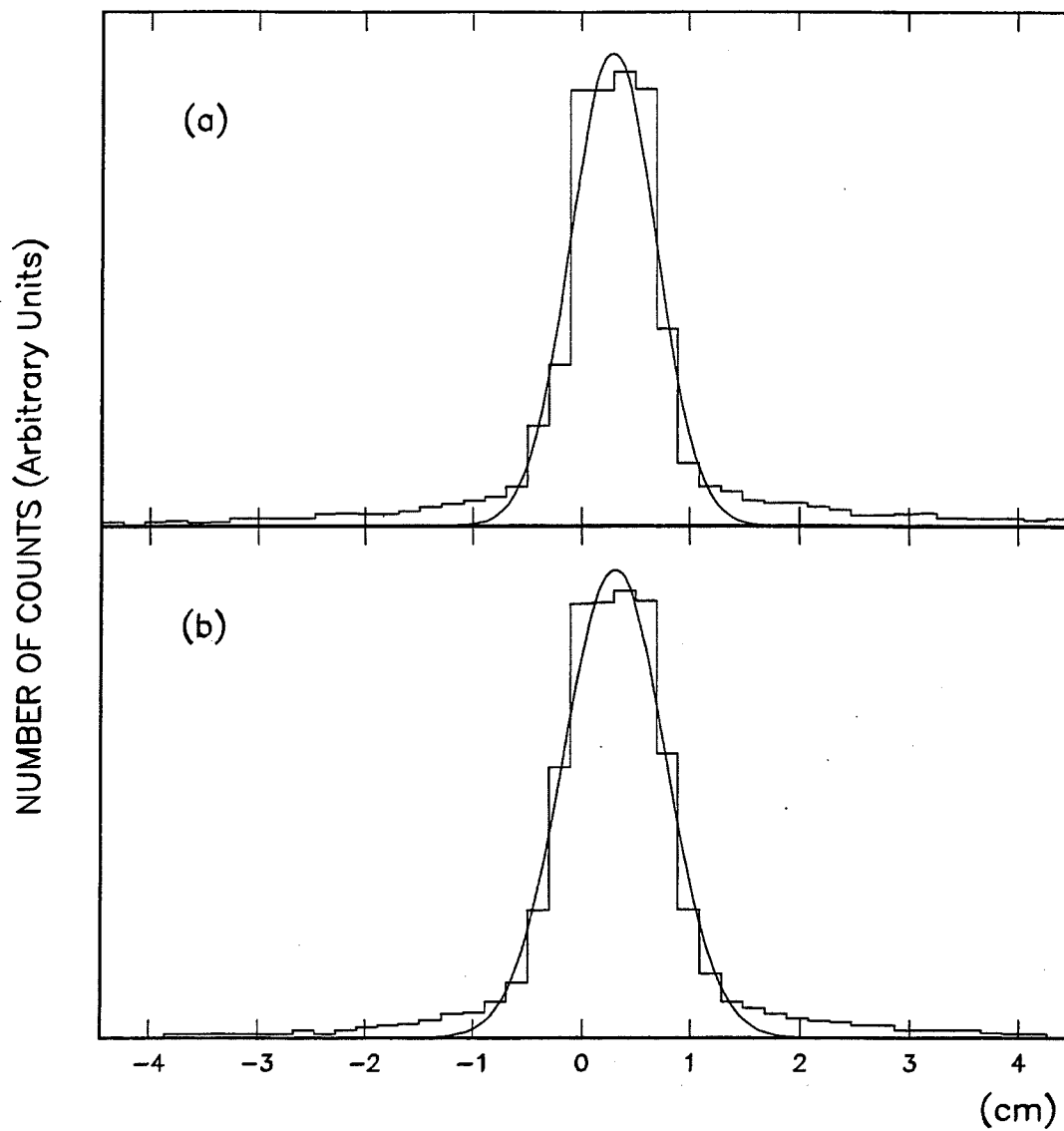


Figure 5.22: (a) SWIC x -distribution and (b) SWIC y -distribution for beam particles at the upstream entrance to the Čerenkov detector for incident 800 GeV/c beam. The histograms represent digitizations of actual SWIC profiles as read out by EPICURE for a single spill. The smooth curves are gaussian fits.

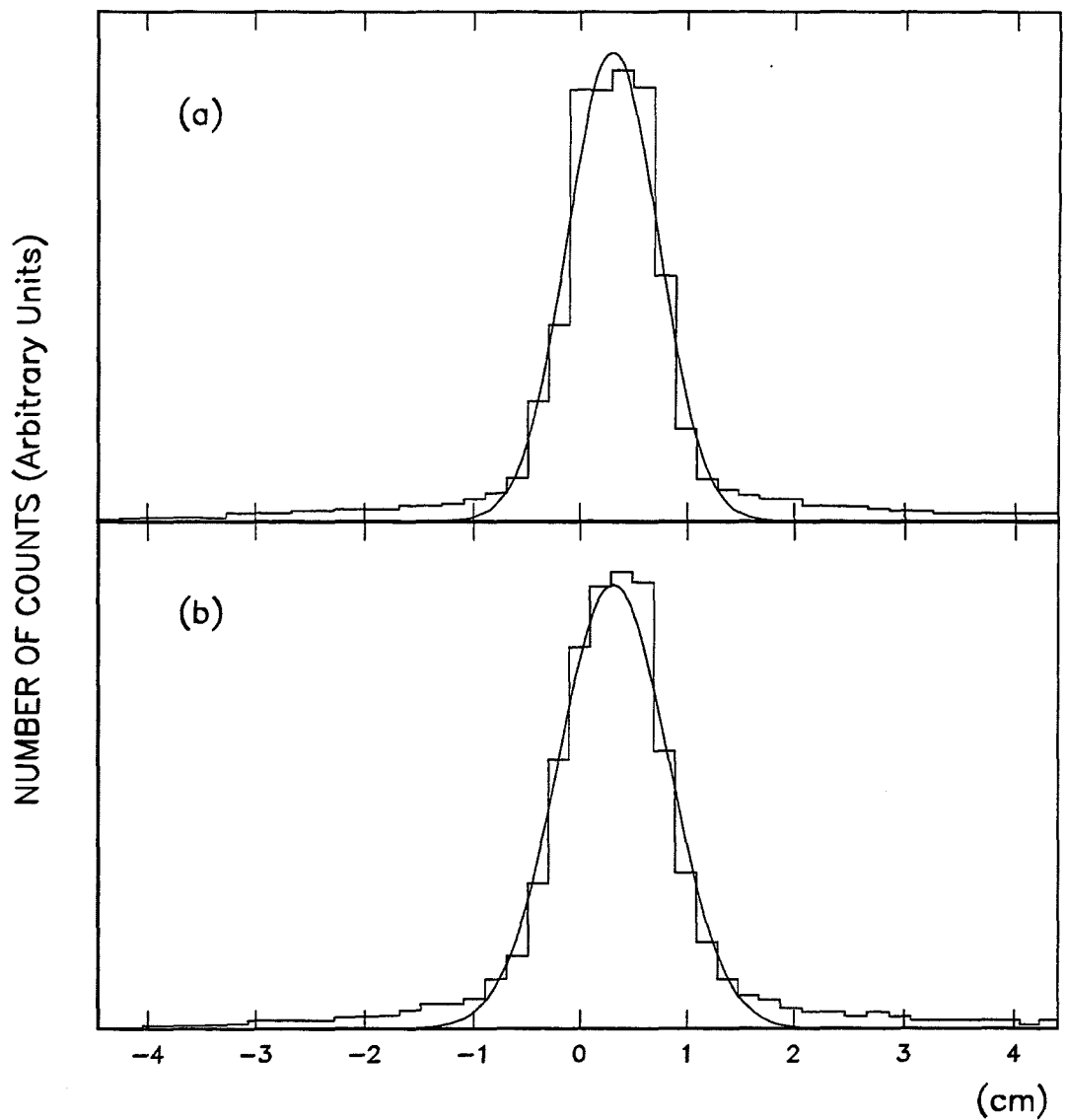


Figure 5.23: (a) SWIC x -distribution and (b) SWIC y -distribution of beam particles at the downstream entrance to the Čerenkov detector for incident 800 GeV/c beam. The histograms represent digitizations of actual SWIC profiles as read out by EPICURE for a single spill. The smooth curves are gaussian fits.

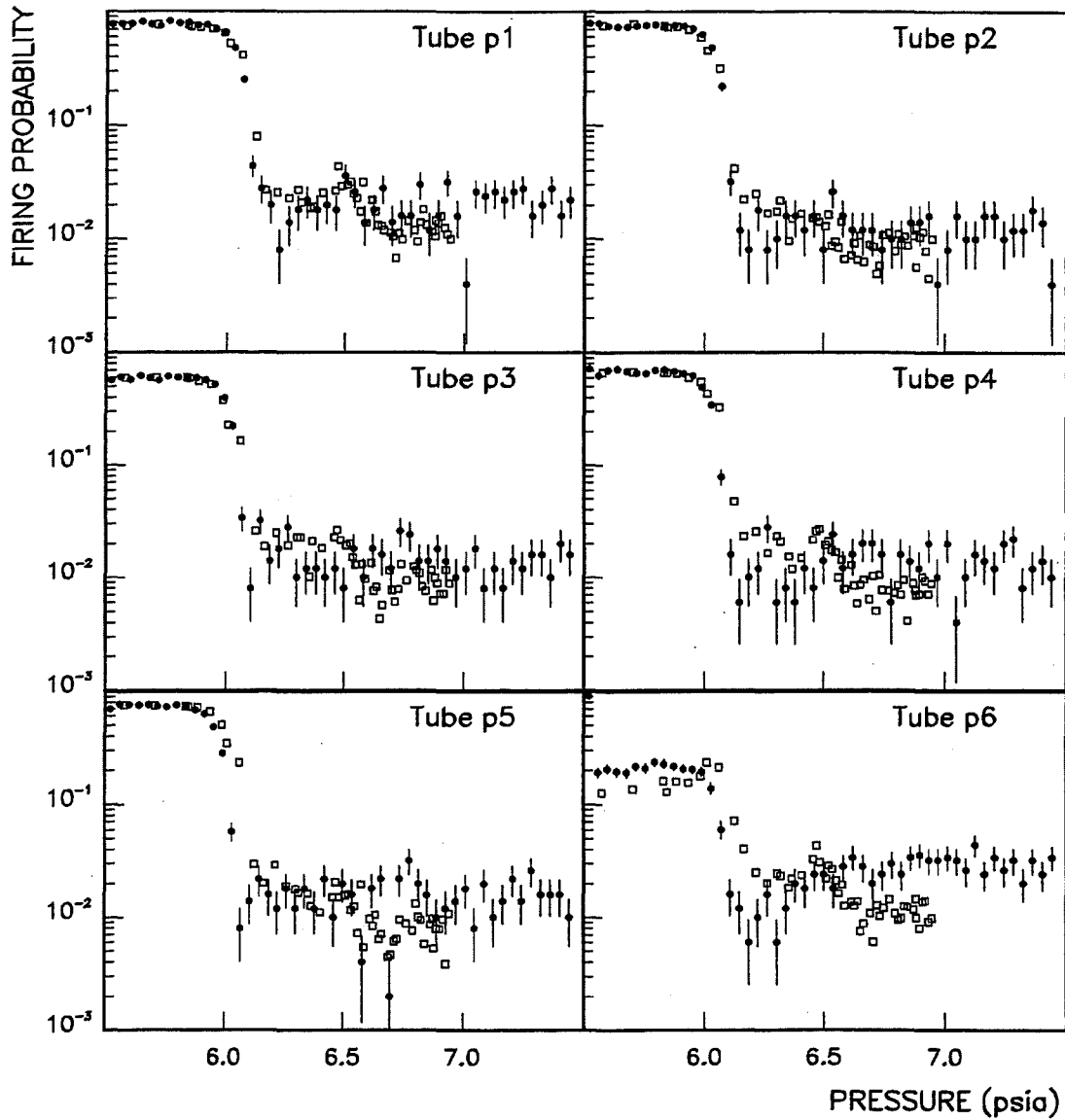


Figure 5.24: Single phototube pressure curves for the p phototubes with incident 800 GeV/c proton beam. \square – Minnesota latch data. \bullet – Čerenkov Monte Carlo simulation. Error bars are statistical only.

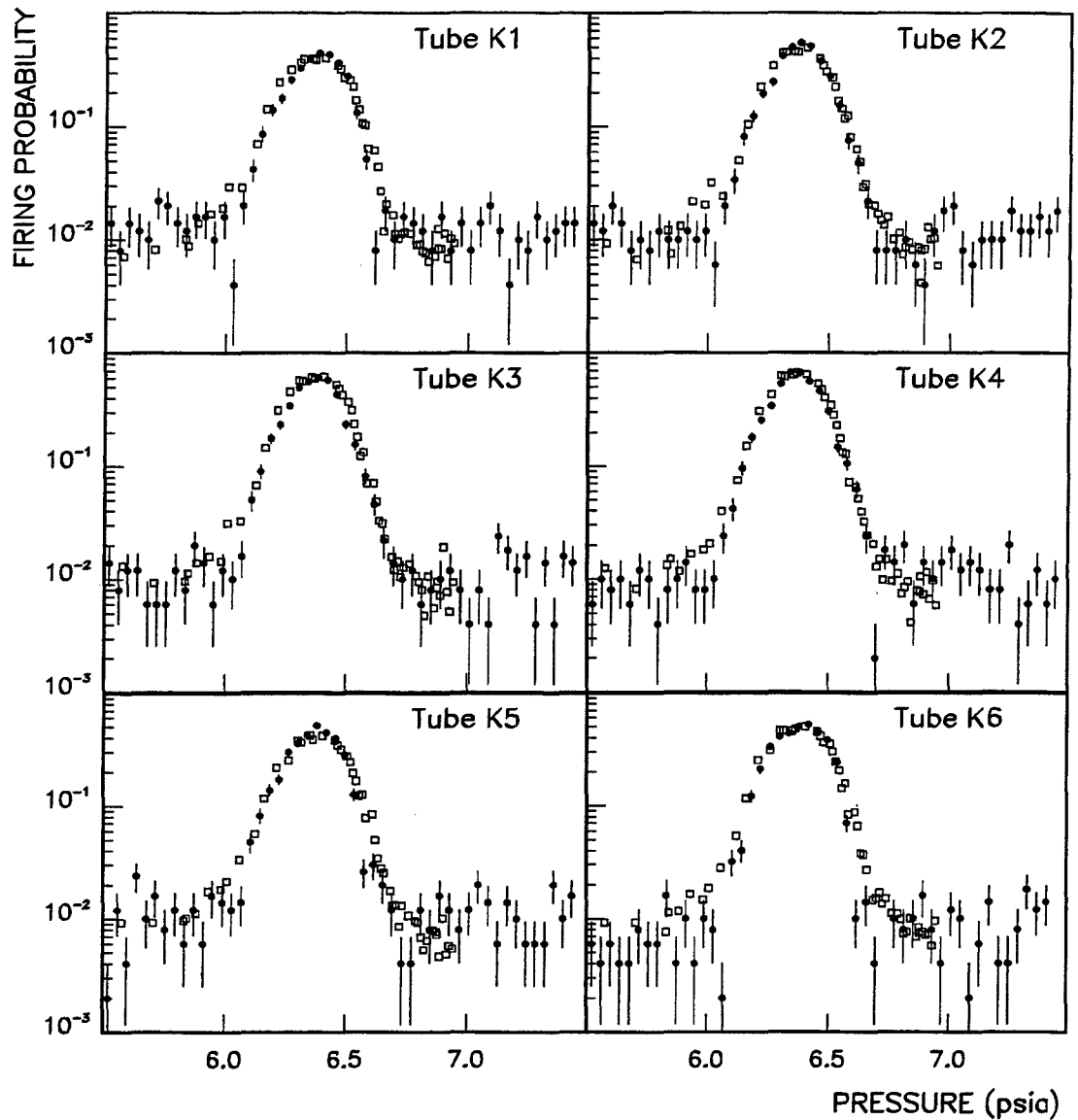


Figure 5.25: Single phototube pressure curves for the K phototubes with incident 800 GeV/c proton beam. \square - Minnesota latch data. \bullet - Čerenkov Monte Carlo simulation. Error bars are statistical only.

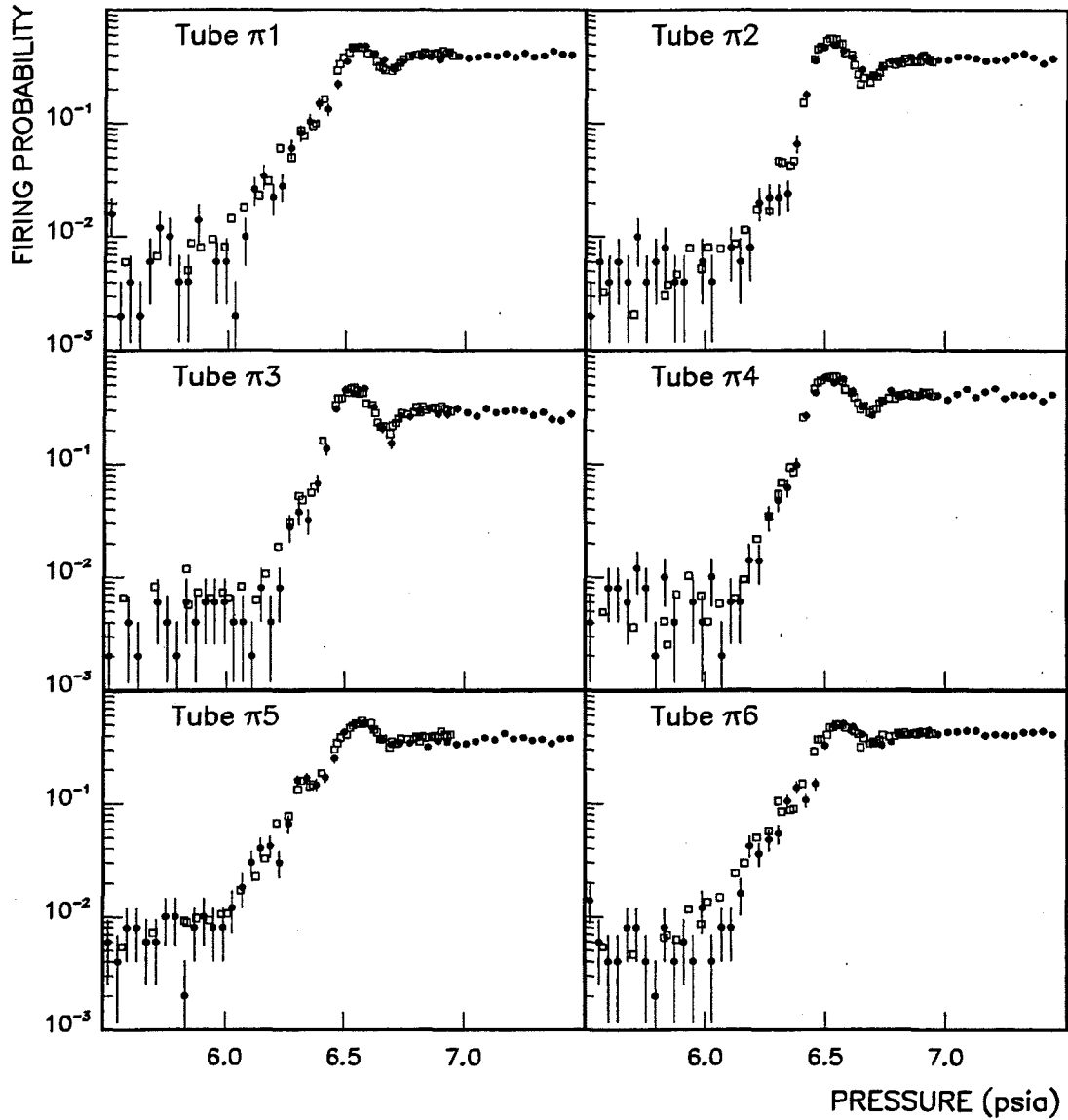


Figure 5.26: Single phototube pressure curves for the π phototubes with incident 800 GeV/c proton beam. \square - Minnesota latch data. \bullet - Čerenkov Monte Carlo simulation. Error bars are statistical only.

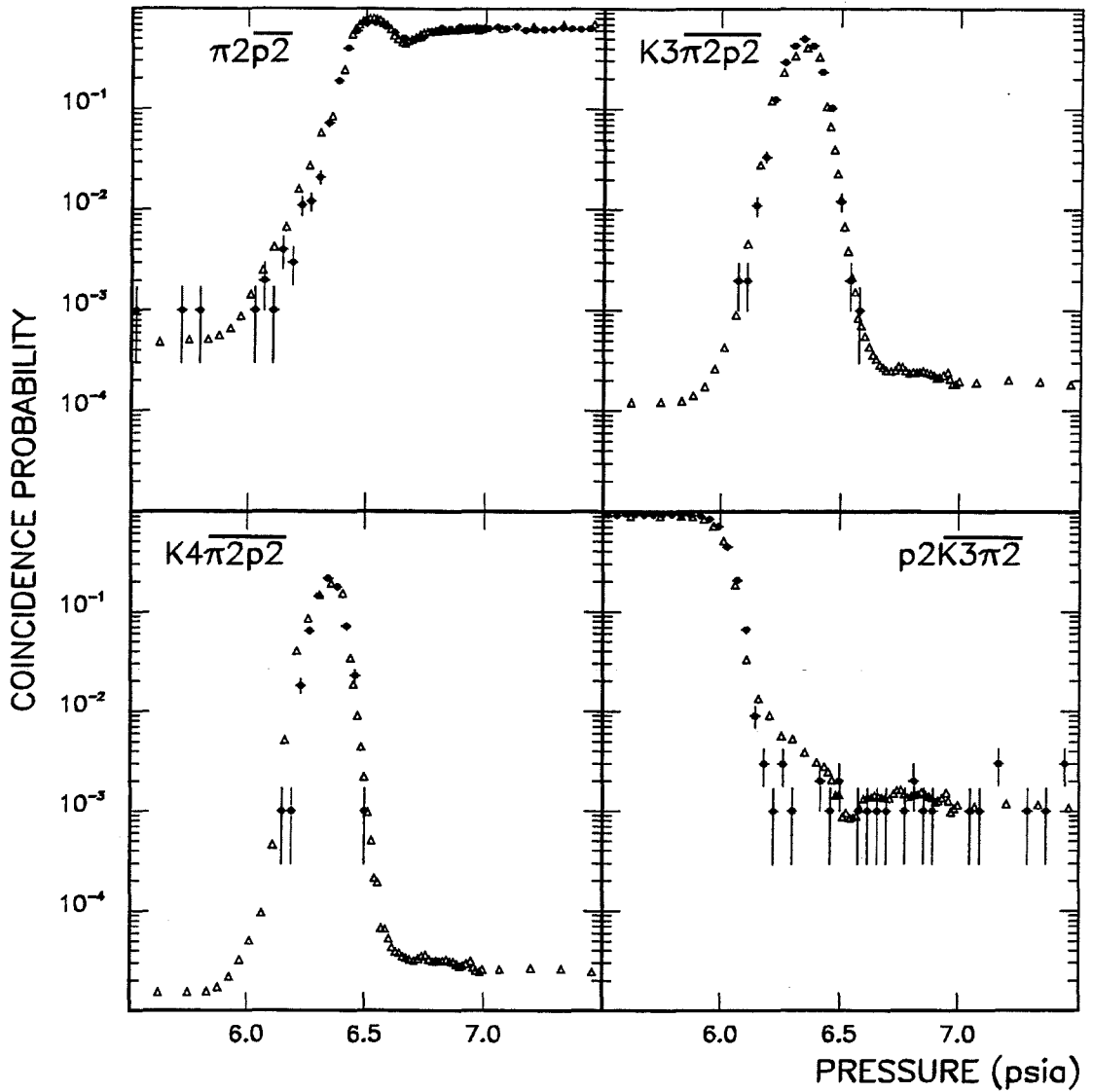


Figure 5.27: Monte Carlo fits to 800 GeV/c coincidence pressure curves for several tag requirements. Δ - pressure curves from actual scaler data. \bullet - Čerenkov Monte Carlo simulation. Errors are statistical only. Note that the plots are semi-logarithmic.

Beam Momentum (GeV/c)	Muon Fraction
+530 GeV/c	$0.00232 \pm 0.00071 \pm 0.00162$
-516 GeV/c	$0.00421 \pm 0.00064 \pm 0.00162$

Table 5.2: Muon population fractions in the Meson West beamline as measured using the FCAL.

curves generated by the Čerenkov Monte Carlo program for pions and muons is shown in (Figure 5.28). However, an upper limit was placed on the muon content of the MW beam for modes of operation using measurements from the FCAL [61]. These limits for the muon beam fractions are given in Table 5.2. Since these limits indicate that the muon content of the beam is small relative to the pion content, this source of potential contamination in the tagged pion data sample was neglected.

5.5.2 +530 GeV/c Pressure Curves and Beam Composition

The composition of the incident +530 GeV/c beam (as well as the various Čerenkov tags) was determined by fitting the Čerenkov pressure curves to weighted combinations of the pressure curves determined by the beam and Čerenkov Monte Carlo simulations previously described for incident protons, pions and kaons. Final pressure curve fits for the incident +530 GeV/c beam were obtained by running the Čerenkov Monte Carlo simulation independently for each type of incident charged beam particle, assuming 100% population for each type, in order to produce *single*

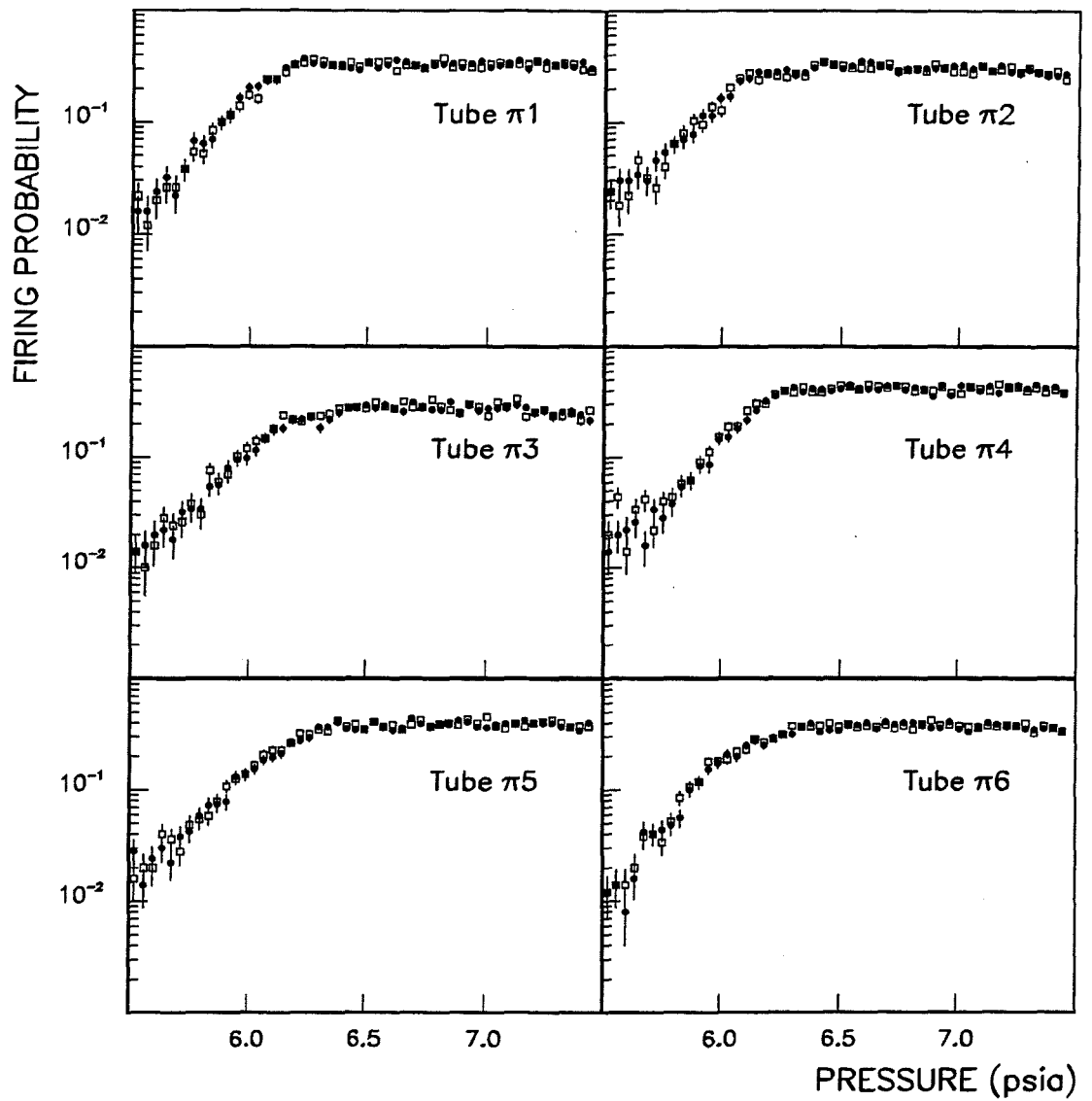


Figure 5.28: Comparison of single phototube pressure curves in the π -ring of phototubes for incident pions (●) and incident muons (□).

*particle pressure curves*¹⁵ (Figure 5.3). Each curve was shifted by about +0.2 psia to account for a systematic pressure difference between the actual pressure readouts and the results of the Monte Carlo simulation.

The Čerenkov Monte Carlo simulation was modified to account for multiple occupancy of the beam buckets. Evidence indicates that the beam buckets were not always occupied by a single particle. Measurements made using the low scalers demonstrated that the **BEAM1** requirement was not satisfied about 16.7% of the time that **BEAM** was satisfied. As **BEAM1** was implemented in order to reject firings of distinct multiple clusters of scintillator in the hodoscope, this was taken as a measure of the rate at which the beam buckets were occupied by multiple beam particles. As a first order approximation, it was assumed that this probability was dominated by dual occupancy of beam buckets with higher order occupancy levels being neglected. Furthermore, as preliminary measurements clearly indicated that the beam consisted of over 95% protons, the second beam particle was assumed to be a proton. The Čerenkov Monte Carlo simulation was modified to account for multiply occupied buckets by generating protons in coincidence with the primary particle using a uniform multiple occupancy probability of 16.7% for all pressures.

For a given tag logic, each constituent single particle pressure curve was weighted by a factor w_i to accommodate the relative population of that particle type in the beam and to account for the intrinsic efficiency of the given coincidence logic to tag any incident beam particle. Here $i = p, K$ or π . Each tag required a unique set of three weights. After weighting, the three curves were combined to yield a final fit to the actual pressure curve. The resulting fits for the single phototube pressure curves are shown in Figures 5.29 through 5.31.

Comparisons between the pressure curves acquired during the 1991 data ac-

¹⁵Not to be confused with single phototube pressure curves. Single particle curves may be logical coincidences of any number of phototube signals, but represent Čerenkov light emitted by only a single particle type.

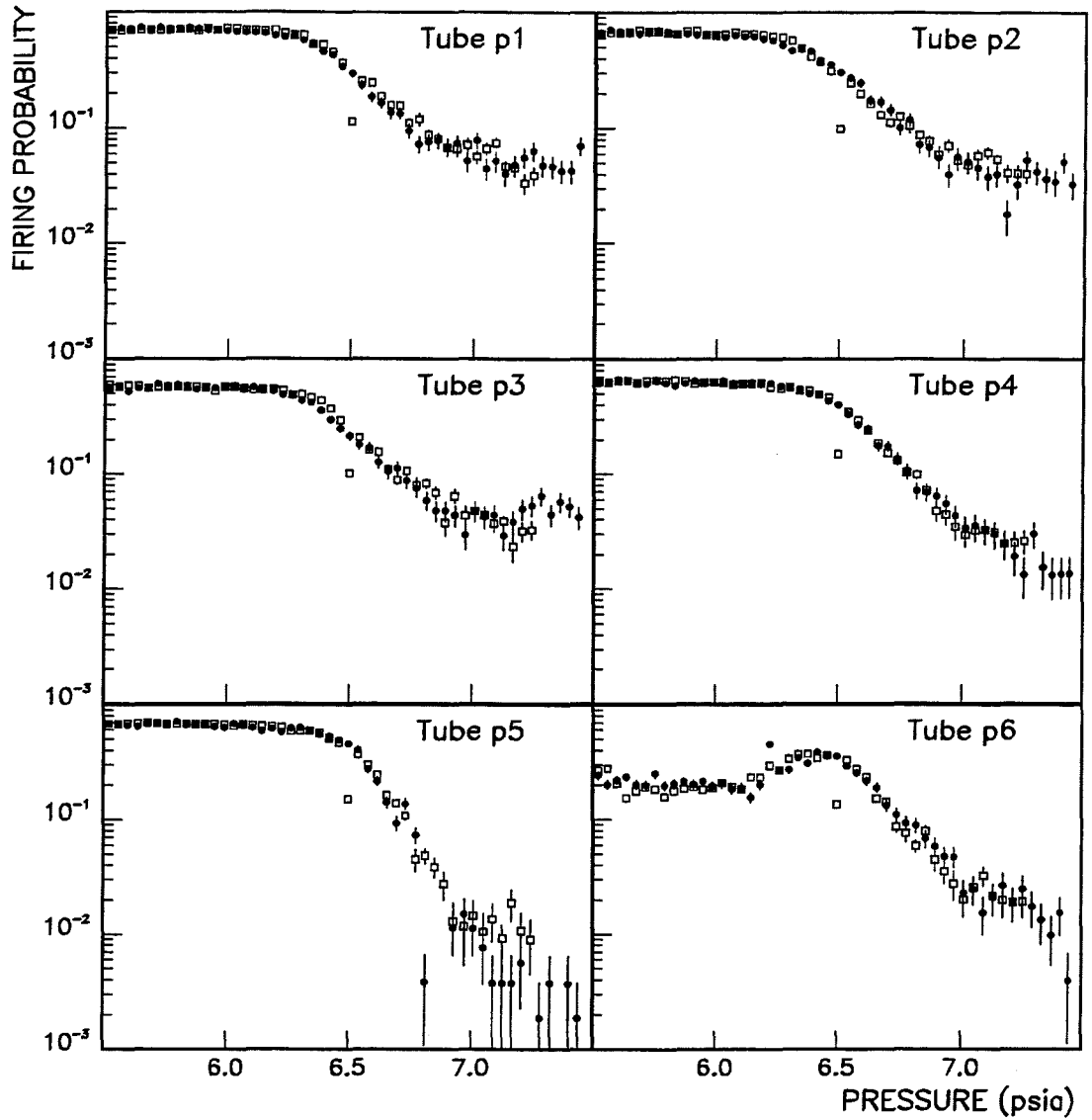


Figure 5.29: Single phototube pressure curves for the p phototubes with incident $+530$ GeV/c beam. \square - Minnesota latch data. \bullet - Čerenkov Monte Carlo simulation. Error bars are statistical only.

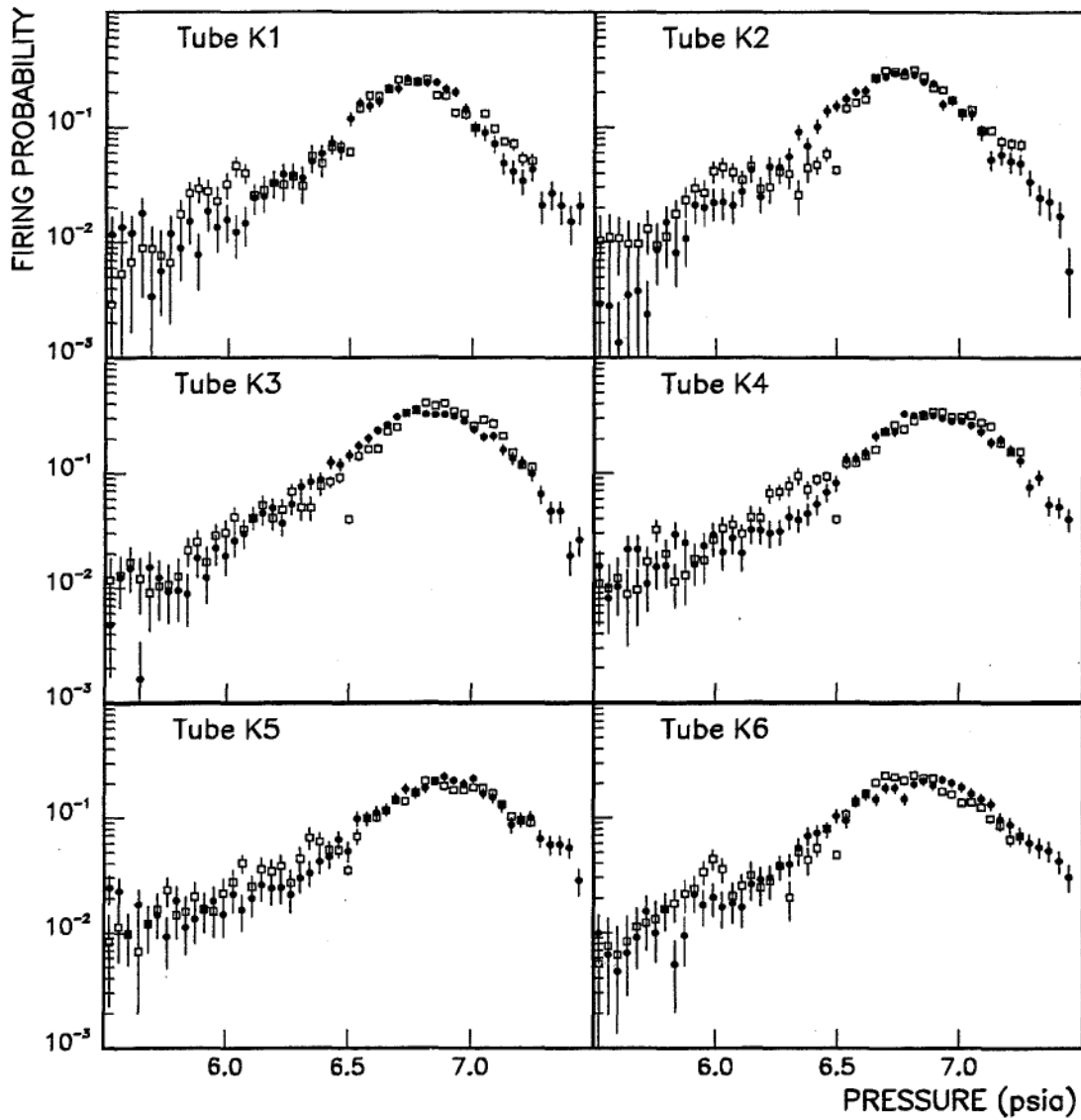


Figure 5.30: Single phototube pressure curves for the K phototubes with incident $+530$ GeV/c beam. \square - Minnesota latch data. \bullet - Čerenkov Monte Carlo simulation. Error bars are statistical only.

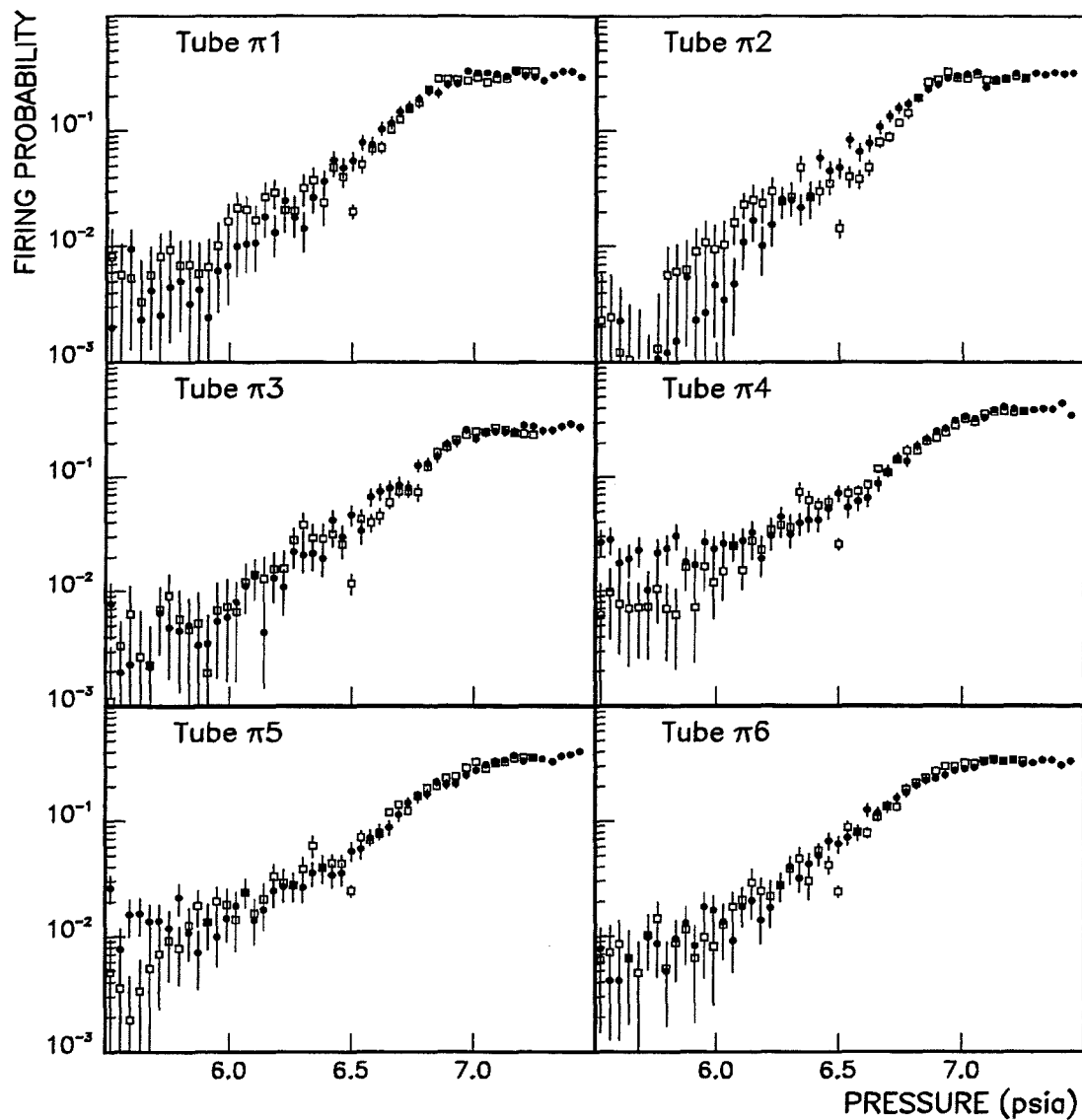


Figure 5.31: Single phototube pressure curves for the π phototubes with incident +530 GeV/c beam. \square - Minnesota latch data. \bullet - Čerenkov Monte Carlo simulation. Error bars are statistical only.

quisition period and the resulting Monte Carlo fits are shown for several logical coincidences in Figures 5.32 through 5.36.

The particle fractions in the beam were determined first by normalizing the weight factor, w_i for each constituent simulated single particle pressure curve to the peak value of the proton curve. This was done to account for intrinsic variations in the response of the detector to particles of differing mass. The composition of the +530 GeV/c beam was then calculated from the normalized weights, W_i , by the equation

$$x_i = \frac{W_i}{W_p + W_K + W_\pi} \quad (5.10)$$

This was done for several tags. Fits to the $K4\pi2p2$ and $K3\pi2p2$ pressure curves were most sensitive to the particle composition of the beam. The pion tags were much less sensitive. Thus, the beam composition was calculated from fits to the $K3\pi2p2$ and $K4\pi2p2$ pressure curves. The resulting values were then fed back into the fits to the $\pi3p2$ and $\pi2p2$ pressure curves to check for consistency. The resulting measured composition of the incident beam is given in Table 5.3.

5.5.3 +530 GeV/c Pressure Curves and Tag Compositions

For a chosen tag logic and operating pressure, the contamination (i.e. the fraction of tagged particles which are not of the desired particle type) in tagging a given particle type was determined from the Monte Carlo pressure curves by measuring the relative contributions from each of the single particle curves to the total fit pressure curve at that pressure. The resulting probabilities for each particle type to satisfy each tag are shown in Tables 5.4 and 5.5 (i.e. *Particle Type Composition of Tag*). These compositions are used in calculating the corrected cross-sections (Chapter 7).

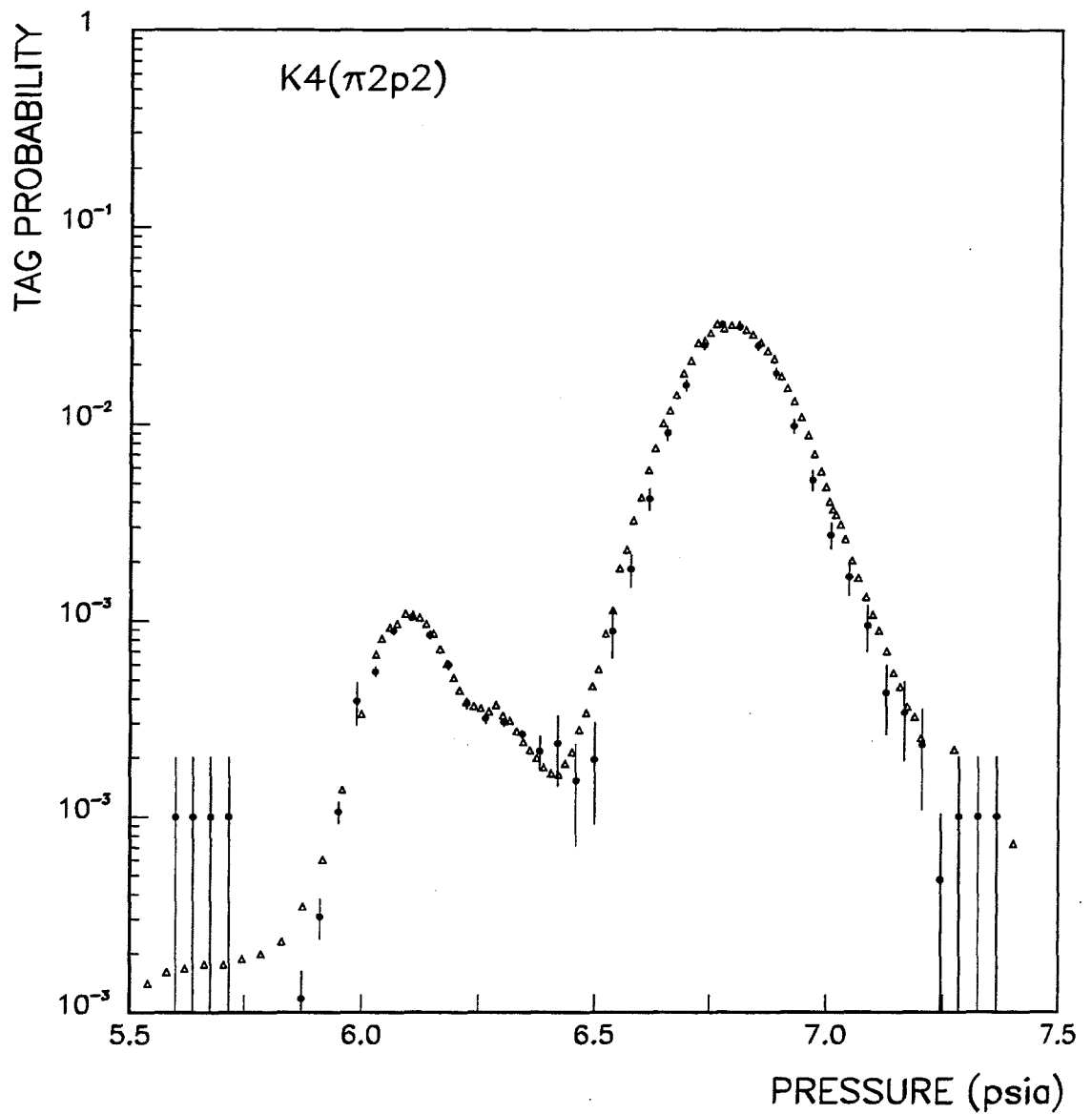


Figure 5.32: Monte Carlo simulation of the $+530 \text{ GeV}/c \text{ } K4\overline{\pi 2p 2}$ coincidence pressure curve. Open triangles represent actual pressure curves. Dark circles with error bars represent the results of the Monte Carlo simulation with statistical errors only. Actual pressure curves are from data acquired during runs 14211-14212. Note that the plots are semi-logarithmic.

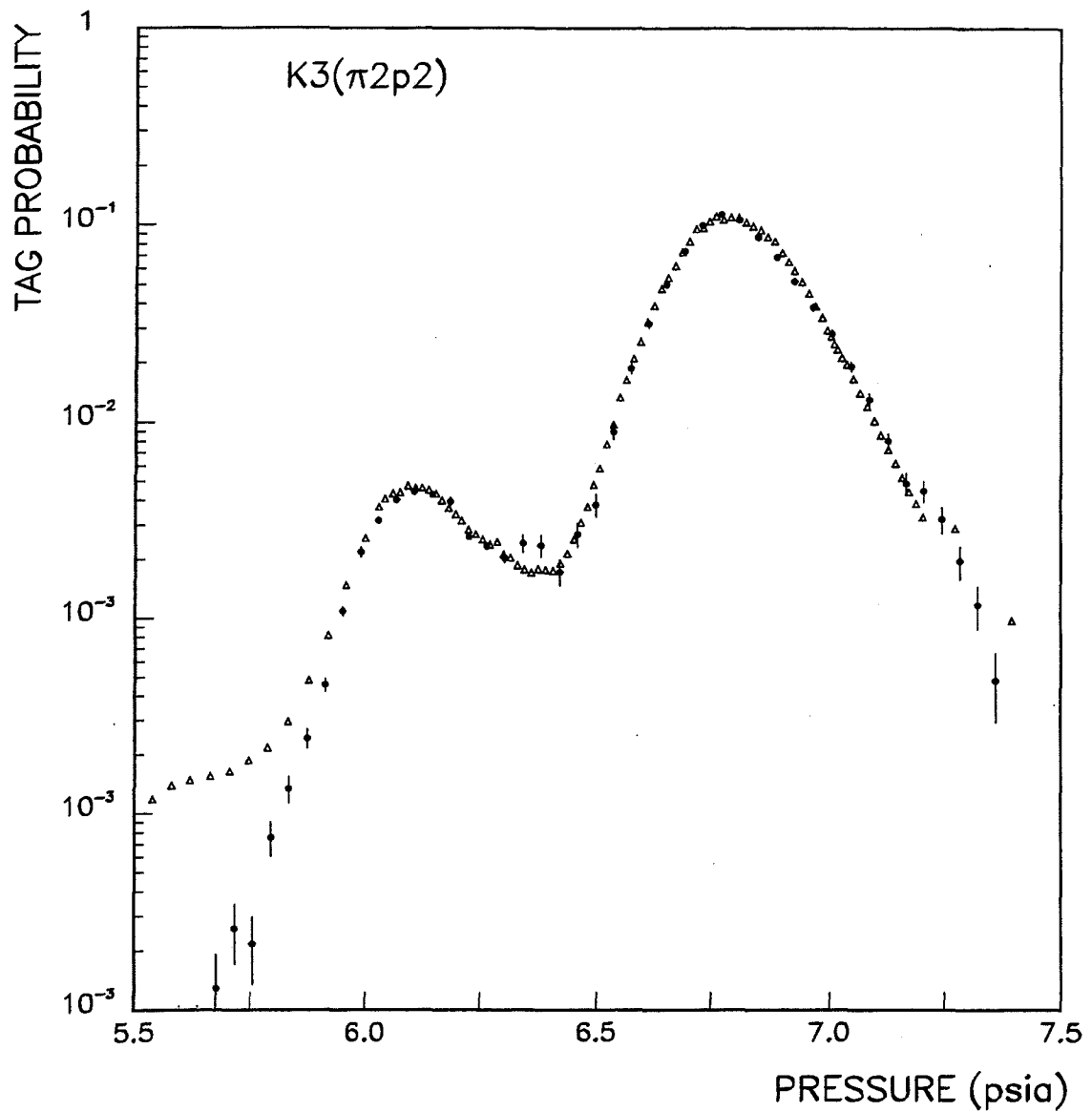


Figure 5.33: Monte Carlo simulation of the +530 GeV/c $K3\overline{\pi}2p2$ coincidence pressure curve. Open triangles represent actual pressure curves. Dark circles with error bars represent the results of the Monte Carlo simulation with statistical errors only. Actual pressure curves are from data acquired during runs 14211-14212. Note that the plots are semi-logarithmic.

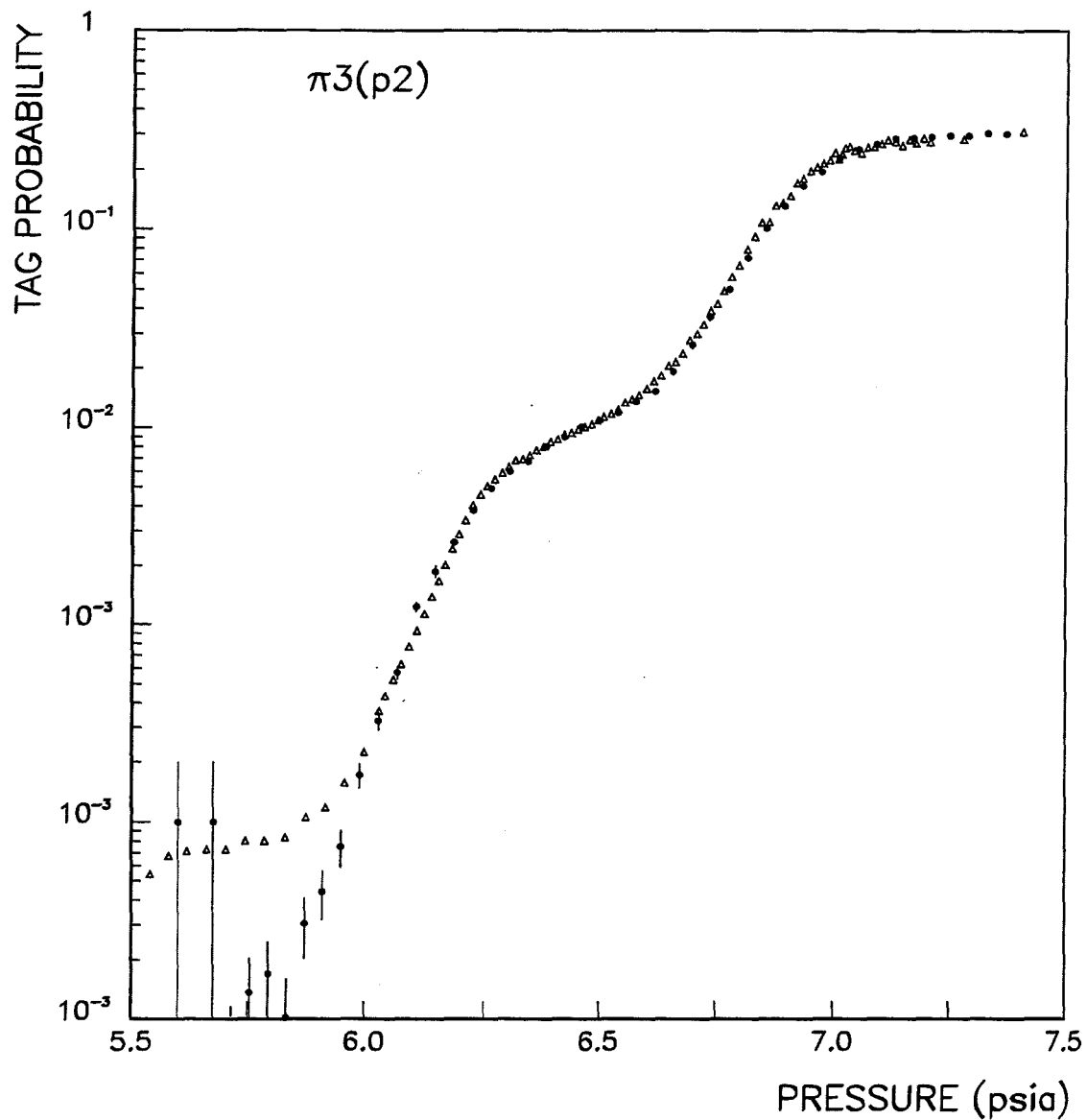


Figure 5.34: Monte Carlo simulation of the +530 GeV/c $\pi 3\bar{p} 2$ coincidence pressure curve. Open triangles represent actual pressure curves. Dark circles with error bars represent the results of the Monte Carlo simulation with statistical errors only. Actual pressure curves are from data acquired during runs 14211-14212. Note that the plots are semi-logarithmic.

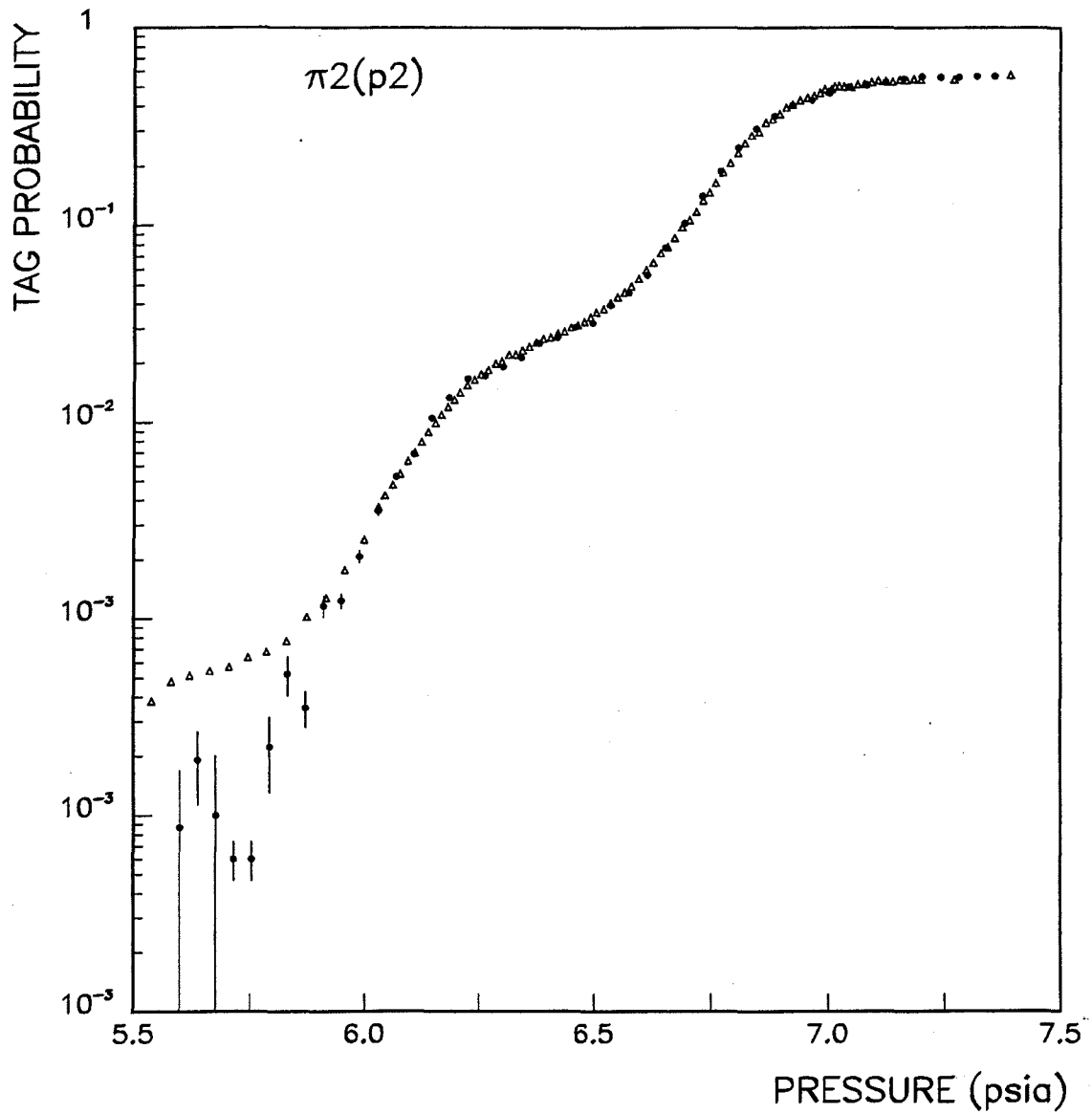


Figure 5.35: Monte Carlo simulation of the +530 GeV/c $\pi 2\overline{p 2}$ coincidence pressure curve. Open triangles represent actual pressure curves. Dark circles with error bars represent the results of the Monte Carlo simulation with statistical errors only. Actual pressure curves are from data acquired during runs 14211-14212. Note that the plots are semi-logarithmic.

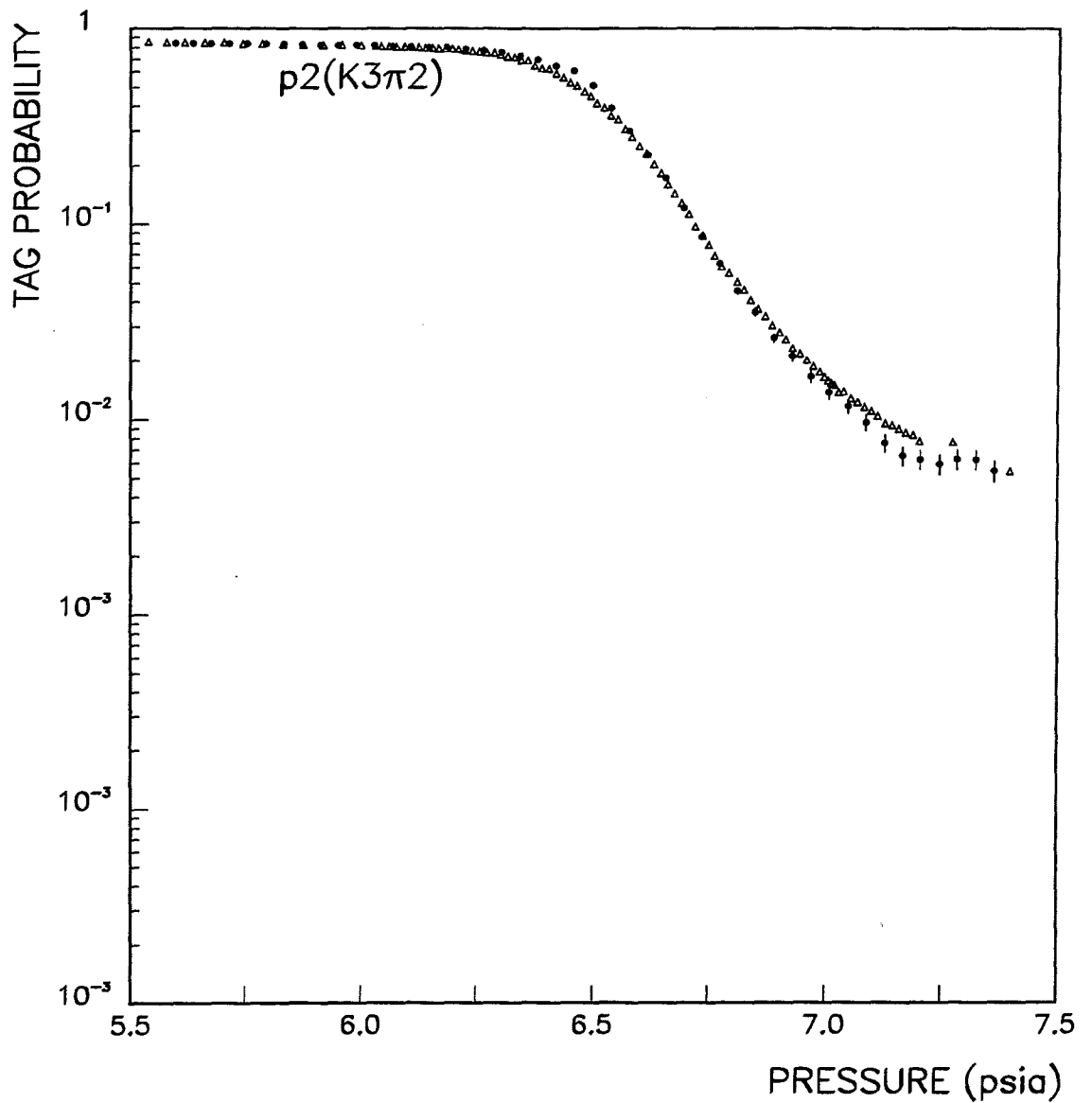


Figure 5.36: Monte Carlo simulation of the +530 GeV/c $p2\overline{K}3\pi2$ coincidence pressure curve. Open triangles represent actual pressure curves. Dark circles with error bars represent the results of the Monte Carlo simulation with statistical errors only. Actual pressure curves are from data acquired during runs 14211-14212. Note that the plots are semi-logarithmic.

Pressure Curve Fit	Incident Particle Type		
	p	π^+	K^+
$K4\overline{2p2}$	0.968	0.0259	0.0058
$K3\overline{2p2}$	0.966	0.0291	0.0049
Average	0.967	0.0275	0.0054

Table 5.3: Fractional particle type composition of the +530 GeV/c beam incident on the MWEST Čerenkov detector as determined from an analysis of the $K4\overline{2p2}$ and $K3\overline{2p2}$ pressure curves.

5.5.4 Fraction of Incident Beam Tagged

The fraction of all incident beam particles satisfying each tag type was measured using low bias data. There are two substantial sources of low bias data in the recorded E706 data sample, the prescaled beam triggers and the Minnesota Latch data for out of time ticks outside the region of the clean interaction filter. The fraction of incident beam satisfying each tag type was determined by the ratio of the number of such low bias buckets satisfying $\text{BEAM1} * \overline{\text{BH}}$ in coincidence with the desired tag to the number of the buckets satisfying $\text{BEAM1} * \overline{\text{BH}}$ averaged over the data sample contributing to the cross-section measurements.

The cross-section data sample is divided into two subsamples because the Čerenkov operating pressure was 6.31 psia during the first two-thirds of the +530 GeV/c data acquisition period and the pressure was about 6.24 psia during the remaining third of that data acquisition period. The sample accumulated at the 6.31 psia operating pressure is hereafter referred to as the HIGH pressure sample,

while the other sample is labeled the LOW pressure sample. The fractions of the beam tagged are of course different for these two samples, and they were measured independently. The results are shown in Tables 5.4 and 5.5 for assorted choices of Čerenkov tags in the column labeled “Fraction of Beam Tagged”.

5.6 Ratio of the π^+ and p Absorption Cross-Sections

A preliminary ratio of absorption cross-sections for incident tagged π^+ and tagged p was measured in order to illustrate that the Čerenkov tags were effective in separating the data samples based on incident particle type. This measurement was performed using the prescaled **BEAM** triggers. As an approximate measure of the absorption cross-section, the total number of tagged incident **BEAM1 * $\overline{\text{BH}}$** events generating reconstructed vertices within the beryllium target fiducial region were normalized to the total number of events satisfying **BEAM1 * $\overline{\text{BH}}$** from the Prescaled **BEAM** triggered sample. The fiducial region was defined by the circle $1.0 = (X + 0.2)^2 + (Y + 0.04)^2$ in the transverse plane and by the longitudinal limits $-10.08 \text{ cm} > Z > -7.84 \text{ cm}$ where X , Y and Z are the coordinates of the incident particles (see Figure 6.1). All distances are in cm. A sample transverse spatial distribution of all incident beam particles in the beryllium target fiducial volume is shown for the $p\overline{2\pi 2K2}$ tag in Figure 5.37. The target fiducial region is represented by the circle. The uncorrected absorption cross-section was then calculated for each applied tag using the formula

$$\sigma = \frac{1}{\rho \ell N_a} \frac{N_{fid}}{N_{inc}}, \quad (5.11)$$

where $\rho \approx 1.84 \text{ g/cm}^3$ is the density of beryllium, ℓ is the target length, N_a is Avogadro’s number, N_{inc} is the number of beam particles incident on the target and N_{fid} the number of particles which produce vertices within the fiducial region.

Tag	Fraction of Beam Tagged	Particle	Particle Type Composition of Tag
$p\overline{2K}3\pi\overline{2}$	$0.81424 \pm 6.8 \times 10^{-4}$	p	$0.996 \pm 1.28 \times 10^{-5}$
		K	$1.04 \times 10^{-3} \pm 3.18 \times 10^{-6}$
		π	$2.83 \times 10^{-3} \pm 1.24 \times 10^{-5}$
$K3\pi\overline{2p}2$	$2.51 \times 10^{-3} \pm 8.7 \times 10^{-5}$	p	$9.09 \times 10^{-2} \pm 1.29 \times 10^{-2}$
		K	$0.420 \pm 6.22 \times 10^{-3}$
		π	$0.489 \pm 7.24 \times 10^{-3}$
$K4\pi\overline{2p}2$	$5.97 \times 10^{-4} \pm 4.2 \times 10^{-5}$	p	$4.76 \times 10^{-2} \pm 2.27 \times 10^{-2}$
		K	$0.762 \pm 1.85 \times 10^{-2}$
		π	$0.190 \pm 6.07 \times 10^{-3}$
$\pi\overline{2p}2$	$2.580 \times 10^{-2} \pm 2.8 \times 10^{-4}$	p	$3.44 \times 10^{-2} \pm 2.84 \times 10^{-3}$
		K	$0.178 \pm 7.16 \times 10^{-4}$
		π	$0.787 \pm 2.37 \times 10^{-3}$
$\pi\overline{3p}2$	$9.92 \times 10^{-3} \pm 1.7 \times 10^{-4}$	p	$5.36 \times 10^{-3} \pm 2.18 \times 10^{-3}$
		K	$9.17 \times 10^{-2} \pm 6.94 \times 10^{-4}$
		π	$0.903 \pm 2.09 \times 10^{-3}$

Table 5.4: Fraction of all +530 GeV/c incident particles satisfying the **BEAM1 * BH** requirement which were tagged by the specified tag logic. Particle type composition of each particle type for each tag logic requirement. Boxed values represent the particle type which the tag logic was used to identify. All data acquired at an operating pressure of 6.24 psia. Errors are statistical only.

Tag	Fraction of Beam Tagged	Particle Type	Particle Type Composition of Tag
$p\overline{2K3\pi2}$	$0.70969 \pm 5.7 \times 10^{-4}$	p	$0.996 \pm 1.23 \times 10^{-5}$
		K	$7.73 \times 10^{-4} \pm 3.25 \times 10^{-6}$
		π	$2.38 \times 10^{-3} \pm 1.18 \times 10^{-5}$
$K3\overline{\pi2p2}$	$1.919 \times 10^{-3} \pm 5.5 \times 10^{-5}$	p	$0.412 \pm 1.18 \times 10^{-2}$
		K	$0.309 \pm 6.31 \times 10^{-3}$
		π	$0.279 \pm 5.98 \times 10^{-3}$
$K4\overline{\pi2p2}$	$2.73 \times 10^{-4} \pm 2.1 \times 10^{-5}$	p	$0.140 \pm 2.85 \times 10^{-2}$
		K	$0.766 \pm 2.56 \times 10^{-2}$
		π	$9.37 \times 10^{-2} \pm 5.07 \times 10^{-3}$
$\pi2\overline{p2}$	$2.873 \times 10^{-2} \pm 2.1 \times 10^{-4}$	p	$7.95 \times 10^{-2} \pm 2.31 \times 10^{-3}$
		K	$0.223 \pm 7.36 \times 10^{-4}$
		π	$0.698 \pm 1.82 \times 10^{-3}$
$\pi3\overline{p2}$	$1.016 \times 10^{-2} \pm 1.3 \times 10^{-4}$	p	$1.62 \times 10^{-2} \pm 2.06 \times 10^{-3}$
		K	$0.163 \pm 8.74 \times 10^{-4}$
		π	$0.820 \pm 1.90 \times 10^{-3}$

Table 5.5: Fraction of all +530 GeV/c incident particles satisfying the **BEAM1 * BH** requirement which were tagged by the specified tag logic requirement. Particle type composition of each particle type for each tag logic requirement. Boxed values represent the particle type which the tag logic was used to identify. All data acquired at an operating pressure of 6.31 psia. Errors are statistical only.

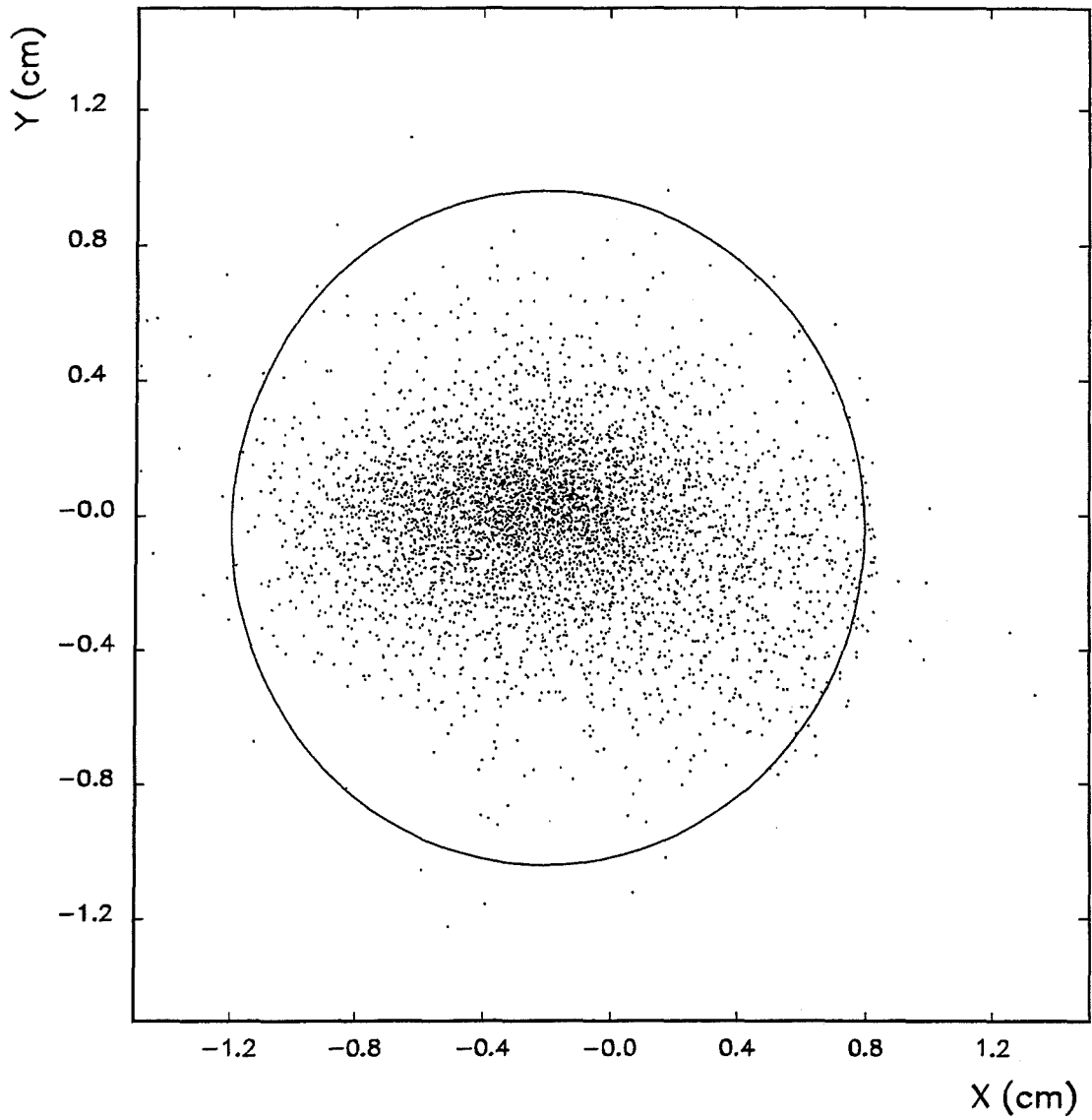


Figure 5.37: Distribution in the transverse plane of all beam particles incident on the beryllium target for a $p\overline{2\pi}2K\overline{2}$ tag. The circle represents the target fiducial region.

Tag	Uncorrected Cross-Section (mb)	Previous Results (mb)	60 GeV σ (mb)	200 GeV σ (mb)	280 GeV σ (mb)
$p2\overline{K}3\pi2$	190 ± 3	p	185	187	187
$\pi2\overline{p}2$	133 ± 14	π^+	138	139	140

Table 5.6: Uncorrected absorption cross-section compared to interpolated lower energy results based on measurement by Carroll et al.

The resulting uncorrected absorption cross-sections are compared in Table 5.6 with the previous measurements of Carroll [84]. This yields a ratio of $\sigma_\pi/\sigma_p = 0.703 \pm 0.081$. This ratio is clearly significantly different from unity which shows that the Čerenkov tag is effectively separating the incident beam into different particle types. These results are uncorrected for incident particle tag contamination, vertex reconstruction efficiency, material absorption, multiple interactions and multiple occupancy in the beam buckets. The corresponding ratio extracted from Carroll's data is $\sigma_\pi/\sigma_p \approx 0.75$, consistent with our measurement. The consistency between the uncorrected result and the measurements of Carroll et al. is encouraging.

Absorption cross-section ratios $\sigma(\pi x p 2 \overline{K} 2)/\sigma(p x \pi 2 \overline{K} 2)$ were measured for coincidence levels $x = 1, 2, 3$ and 4. The results are plotted in Figures 5.38 and 5.39 for operating pressures of 6.31 and 6.24 psia respectively.

The resulting values are clearly consistent within statistical uncertainties for the various coincidence levels and operating pressures. This further confirms the ability of the Čerenkov detector to separate the data based on incident particle type.

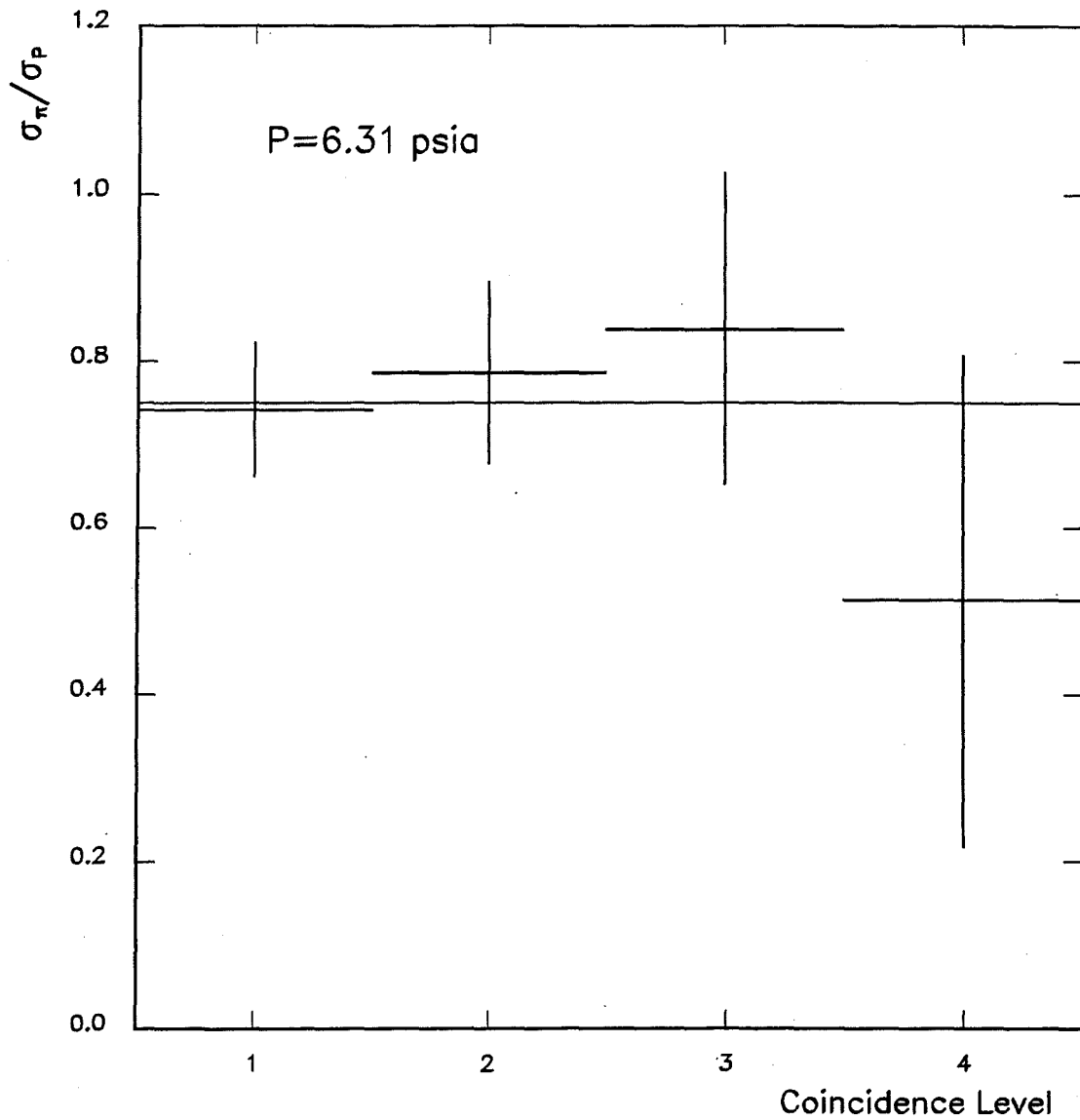


Figure 5.38: Absorption cross-section ratio, σ_{π}/σ_p , as a function of coincidence level for an operating pressure of 6.31 psia. Errors are statistical only. The mean value obtained by Carroll is represented by the horizontal line.

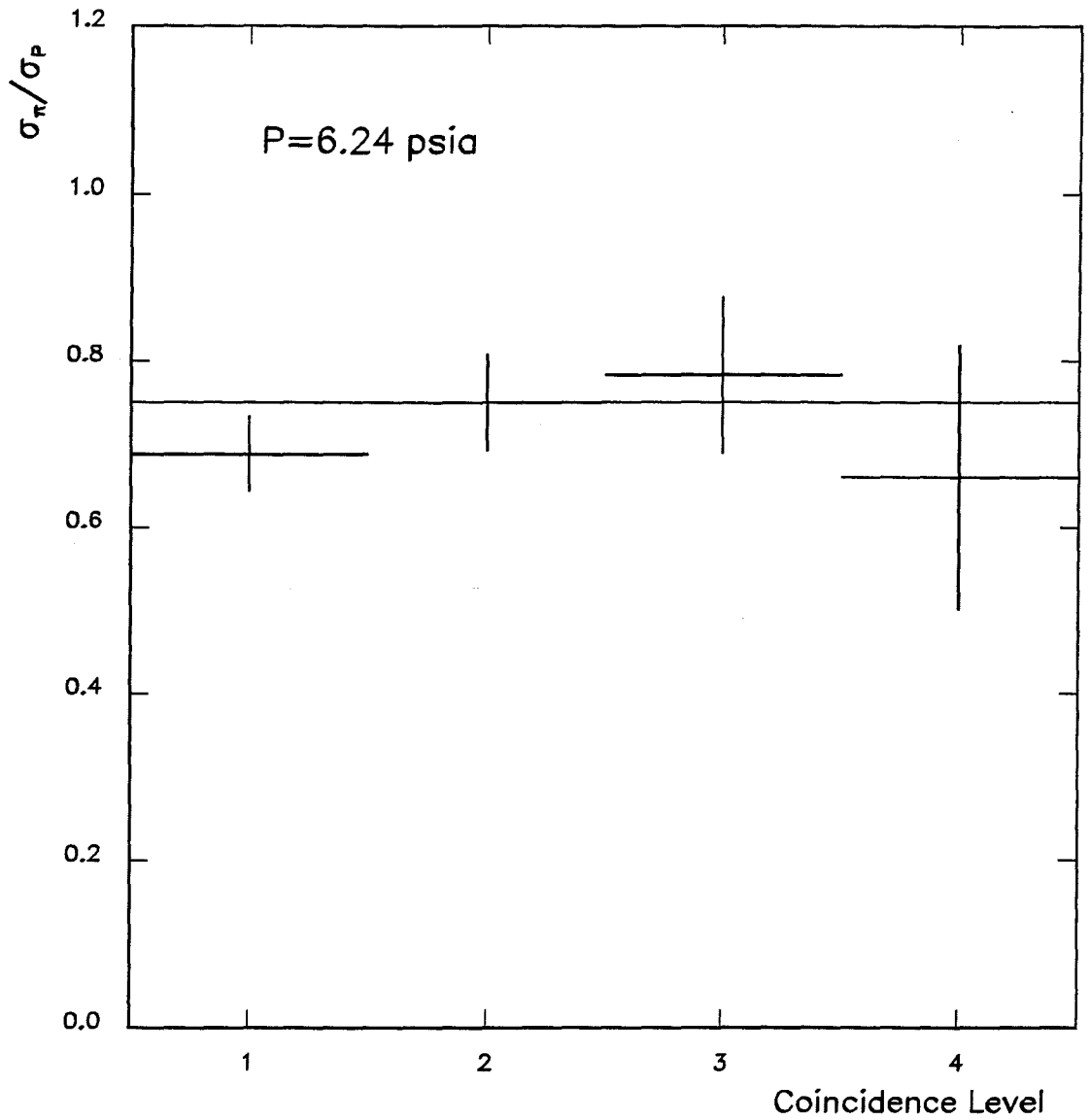


Figure 5.39: Absorption cross-section ratio, σ_{π}/σ_p , as a function of coincidence level for an operating pressure of 6.24 psia. Errors are statistical only. The mean value obtained by Carroll is represented by the horizontal line.

5.7 Čerenkov Data Selection

At this stage, the data samples were separated based on Čerenkov tags. The firing status of the individual Čerenkov phototubes were stored with the output data set from the cross-section code. This allowed tags to be formed and applied as selections to the data sample, yielding tags for each identifiable particle type. However, these tagged cross-sections were still subject to incident beam particle contaminations with corresponding uncertainties in the resulting corrected cross-sections. Furthermore, it was necessary to select only runs for which the operating conditions of the Čerenkov detector were stable enough to allow for a reliable measurement of the tag efficiencies and contaminations. Runs were excluded from contributing to the cross-section measurement based in part on the stability of various beamline and detector features.

As described in the section on the fraction of the incident beam tagged, the +530 GeV/c data set was split into two major subsets corresponding to the two operating pressures. These subsets were labeled HIGH and LOW in reference to the average Čerenkov operating pressure in each run range.

5.7.1 Collimation Effects

Figure 5.40 shows the average collimator settings as a function of run number for the two collimators relevant to this study. While the collimator positions are seen to change midway through the data taking period, the collimators are still wide enough to accept nearly 100% of the +530 GeV/c incident beam (see Figure 5.8) and, so, the effects of collimation were neglected.

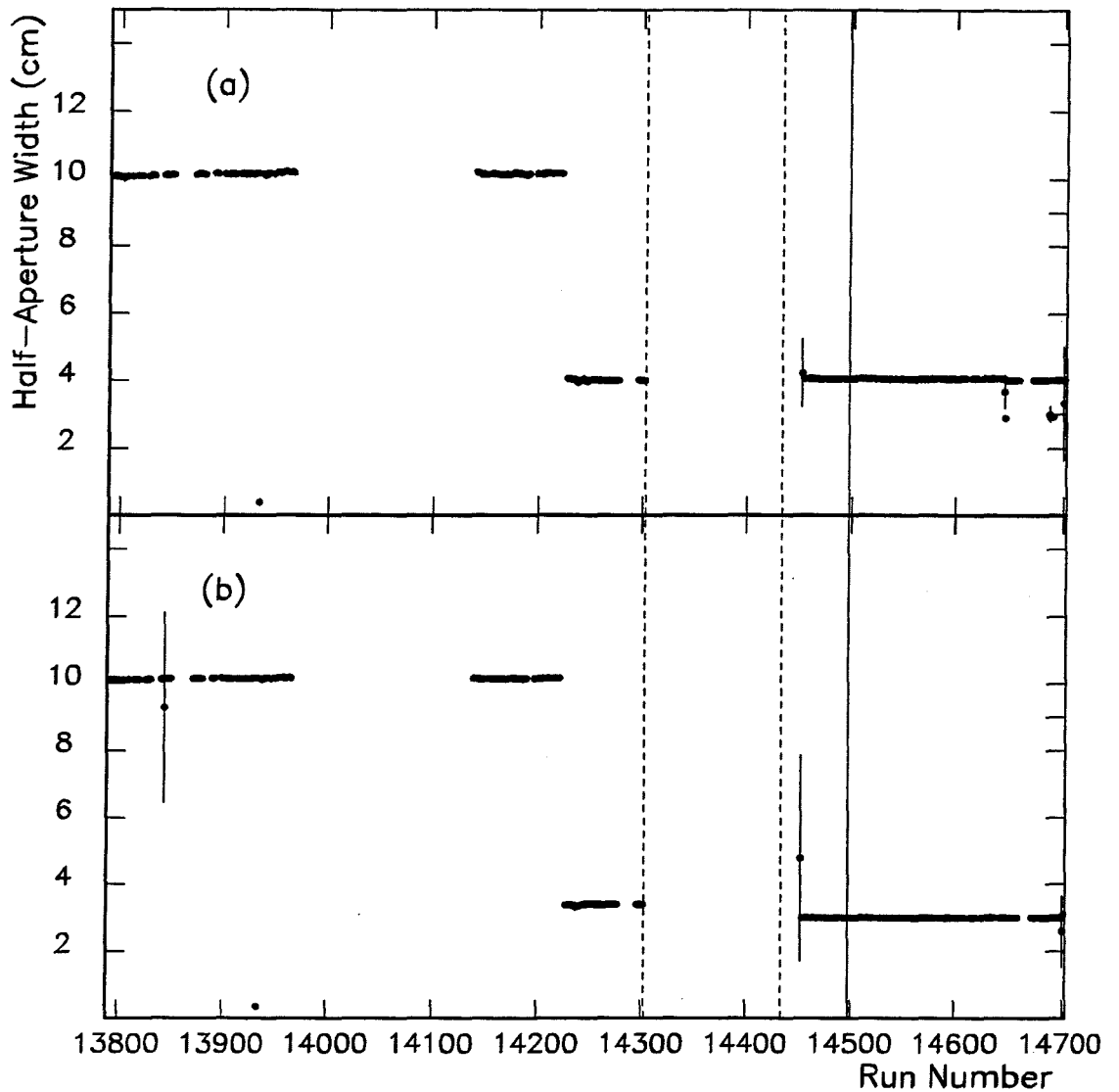


Figure 5.40: Collimator half-aperture size as a function of run number for incident +530 GeV/c beam for (a) horizontal and (b) vertical collimators. The solid vertical line represents the division between the HIGH and LOW pressure Čerenkov data samples. The dashed vertical lines bound the range of runs for the -516 GeV/c data acquisition period. Each error bar represents the RMS deviation taken over all spills in the run.

5.7.2 Stability of Magnet Currents

The average dipole magnet currents were found to be relatively stable as a function of run number as shown in Figure 5.41. The variations are on the order $\pm 2\%$. **TURTLE** studies indicate that the Čerenkov response is insensitive to this level of variation in the beam distributions. No selections were applied based on variations in magnet currents.

5.7.3 Pressure Stability

Perhaps the most sensitive issue in run selection is the operating pressure stability of the detector. Figure 5.42 is a plot of the average pressure as a function of run number for the +530 GeV/c data acquisition period. The two horizontal lines represent the two standard operating pressures – 6.24 and 6.31 psia.¹⁶ It should be recalled that pressure curve acquisition required that the pressure be varied over a wide range and, so, those runs will necessarily have a large spread in the measured pressure and may show average values far from the standard operating pressures. Such runs are excluded from the tagged cross-section measurements.

During periods of relative pressure stability the detector pressure was seen to rise very gradually with time. This is believed to indicate a very slow gas leak.¹⁷

Additional anomalies arise due to a variety of problems which included the accidental operation of the detector at the wrong pressure for short periods, beam steering, large beam intensity fluctuations, drifting of the direct current offsets on the Čerenkov amplifiers (rare) and work on Minnesota latches. The remainder of the runs have pressures relatively close to one of the two nominal operating pressures.

¹⁶The pressure was changed from 6.31 to 6.24 psia midway through the run to reduce the contamination in the pion tag.

¹⁷While efforts were made to prevent helium leakage, valve manufacturers indicated that no valves are produced which are guaranteed to be fully leak-proof against helium.

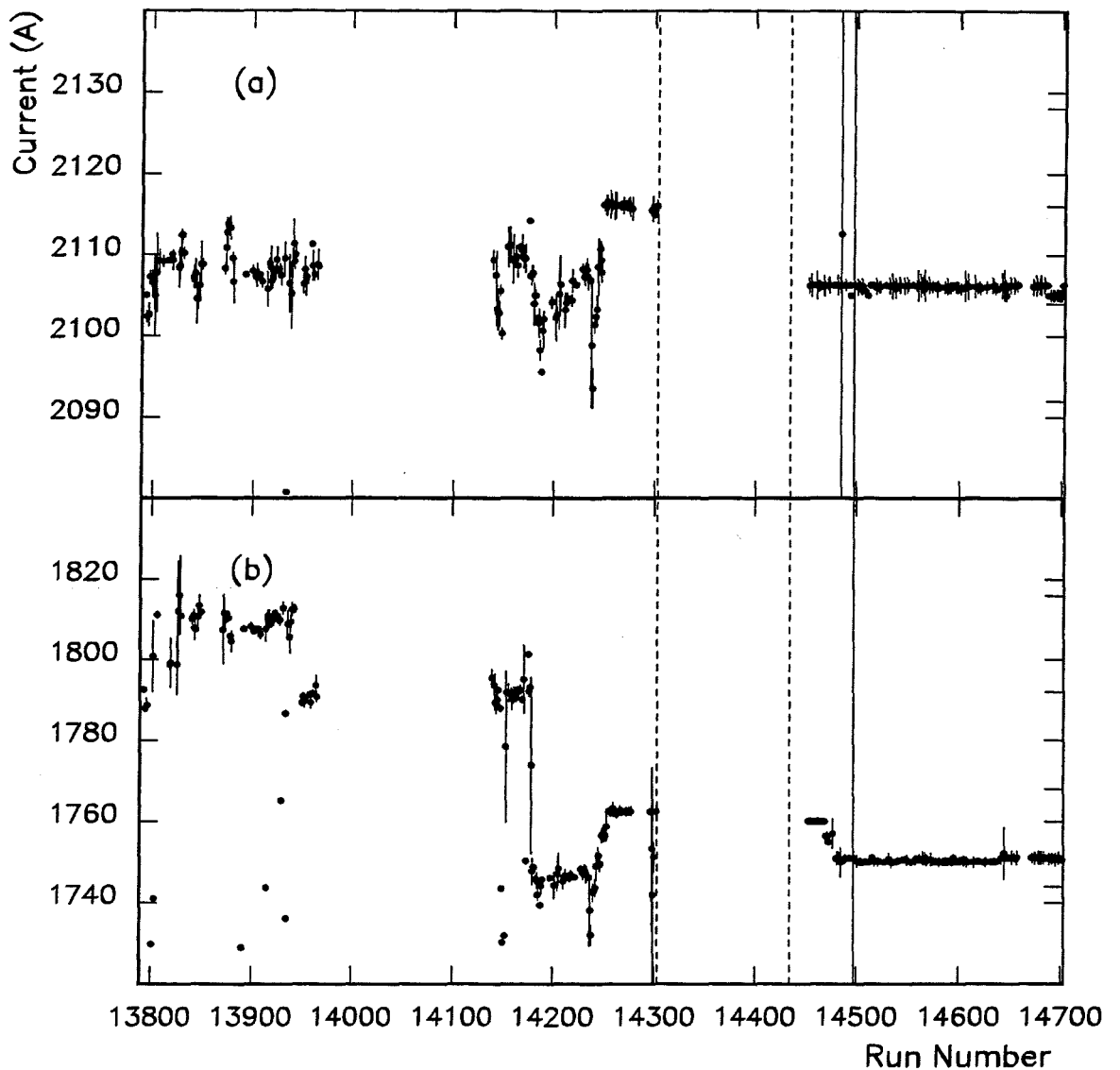


Figure 5.41: Dipole magnet currents as a function of run number for incident +530 GeV/c beam for (a) MW7W1 and (b) MW7W2. The solid vertical line represents the division between the HIGH and LOW pressure Čerenkov data samples. The dashed vertical lines bound the range of runs for the -516 GeV/c data acquisition period. Each error bar represents the RMS deviation taken over all spills in the run.

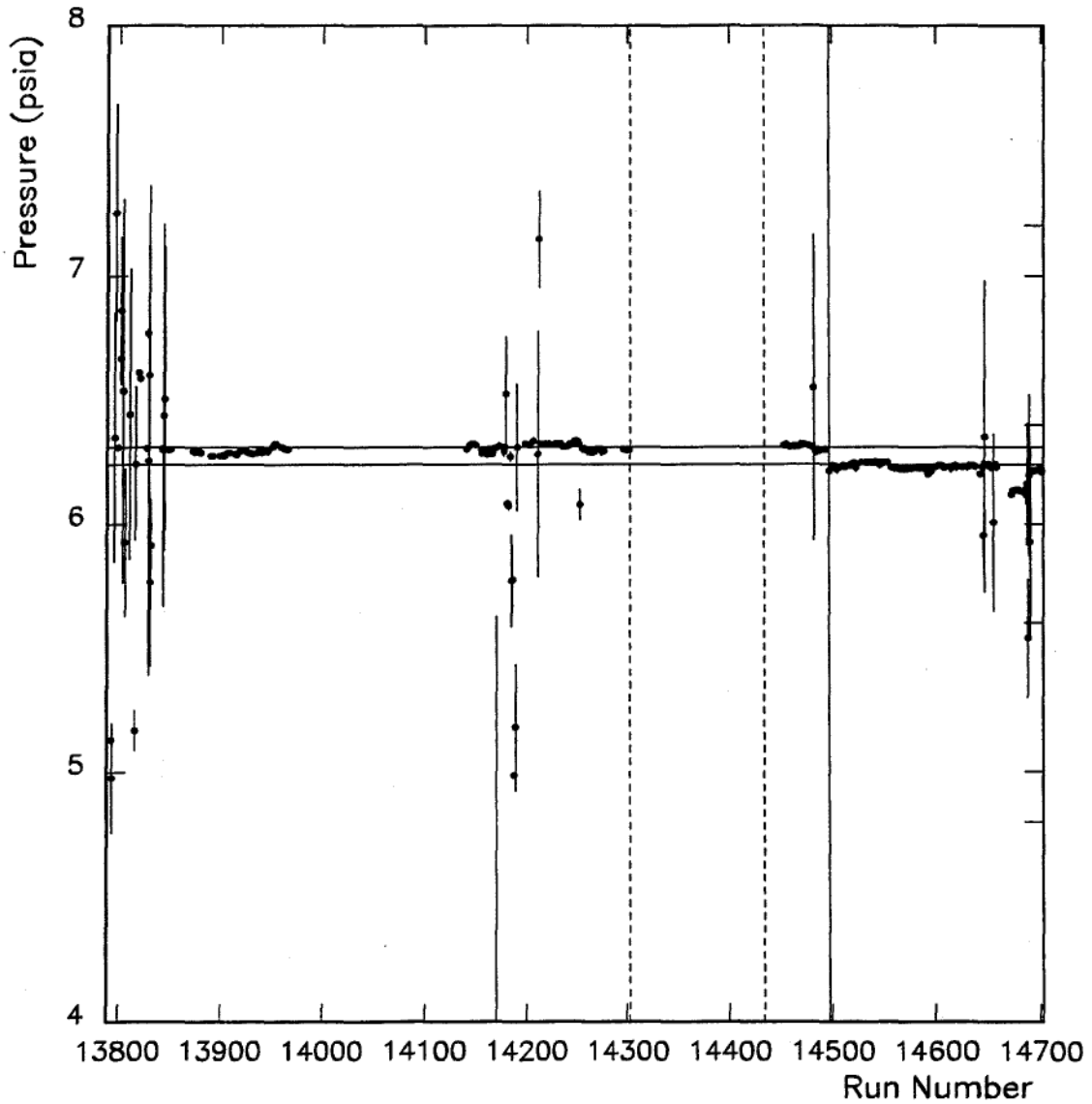


Figure 5.42: Operating pressure as a function of run number. The solid vertical line represents the division between the HIGH and LOW pressure Čerenkov data samples. The horizontal lines represent the two fiducial operating pressures at 6.24 and 6.31 psia. The dashed vertical lines bound the range of runs for the -516 GeV/c data acquisition period. Each error bar represents the RMS deviation taken over all spills in the run.

Chapter 6

Cross-Section Analysis

The cross-sections were calculated using a multi-authored program [72],[85] to select events, photons and photon pairs which satisfied the various criteria for acceptance as π^0 candidates. The selection process resulted in a need for various correction factors to compensate for the excluded data. As some of the correction factors were determined with the aid of the E706 Monte Carlo program, this will be discussed in the next section. The various data selection requirements and the associated corrections which were applied to the data in order to extract measurements of the π^0 cross-sections will be discussed in the remainder of the chapter.

6.1 E706 Monte Carlo

The performance of the EMLAC was simulated by the E706 Monte Carlo program. The E706 Monte Carlo program used HERWIG [86] to generate events of interest in the spectrometer. The particles generated by HERWIG were selected and allowed to propagate through the detector as simulated by GEANT [87]. GEANT allowed the user to describe various materials and geometries and propagate particles through the simulated detectors taking into account the physical processes which occur within the modeled materials. The E706 Monte Carlo used GEANT to simulate the construction of the spectrometer (including the calorimeters). The

materials, geometry and electronics of the EMLAC were described as completely as possible using GEANT. The generated particles were allowed to shower in the simulated EMLAC until they reached a minimum energy threshold. To minimize the simulation time below this threshold a separate program was used to parameterize the remaining energy loss. The Monte Carlo simulation was used to measure the energy loss of photons which showered prematurely in material upstream of the instrumented regions of the EMLAC. In addition, the efficiency for reconstructing the mesons from EMLAC showers was measured using the E706 Monte Carlo simulation. A few comparisons of Monte Carlo simulation results with real data will be presented below in the appropriate sections.

6.2 Data Selection and Corrections

Requirements were invoked in order to separate the data sample by incident particle type and target material. Additional requirements are introduced in order to reduce backgrounds. These selection criteria and the associated corrections are discussed below.

6.2.1 Tag Selection

Data were selected based on the Čerenkov tags which provided the highest level of statistics without compromising the quality of the data sample through contamination. The incident beam tags chosen for the final analysis of the +530 GeV/c data were $p2\overline{K}3\overline{\pi}2$, $\pi3\overline{p}2$ and $K4\overline{\pi}2\overline{p}2$ for incident protons, pions and kaons respectively.

6.2.2 Vertex Selection

The events of interest resulted from primary interactions in the beryllium target. The longitudinal distribution of reconstructed vertex locations is shown in Figure 6.1. Only events with reconstructed vertices in the range $-28.362 \text{ cm} < V_z <$

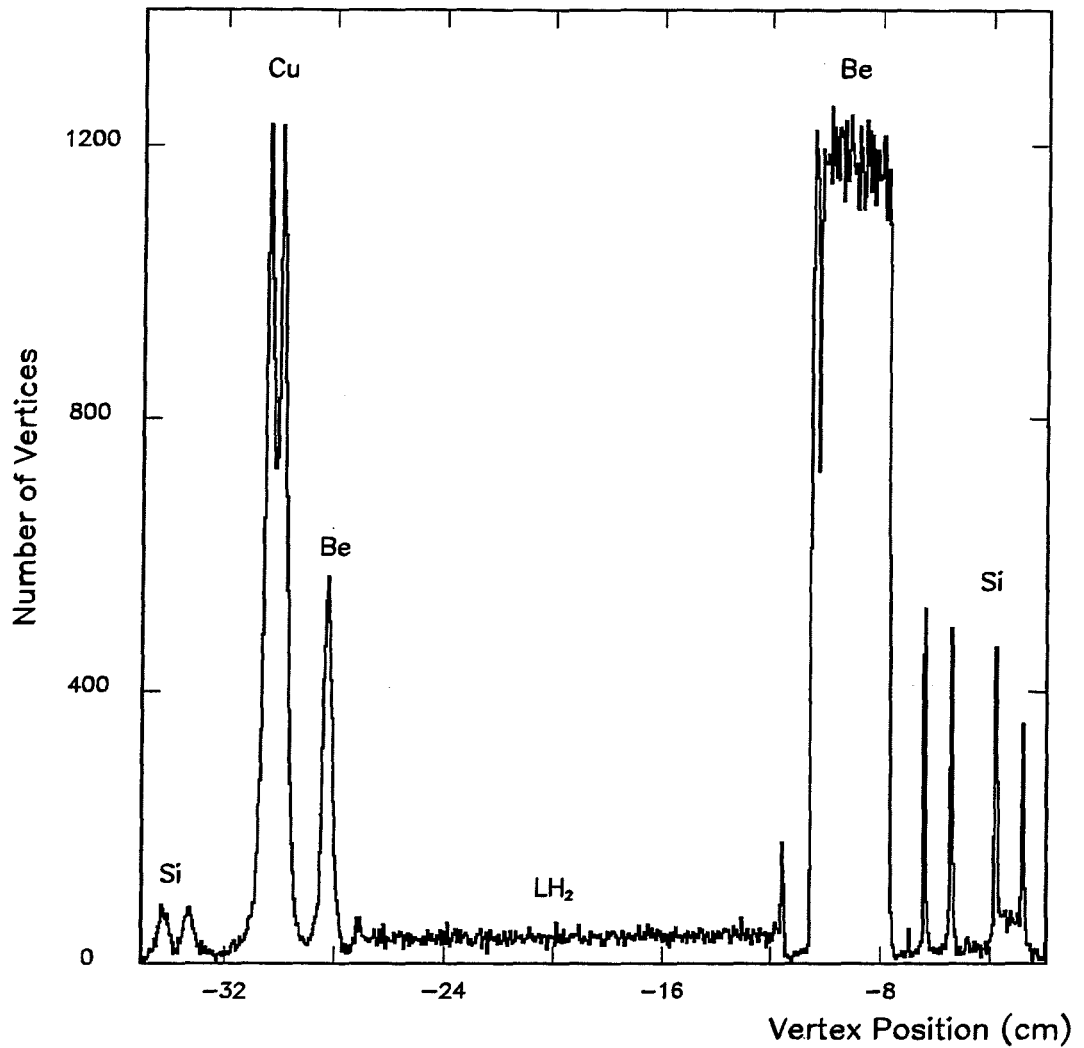


Figure 6.1: Distribution of vertices reconstructed from the E706 tracking data in the target region for π^0 candidates. The targets are labeled by material type. Data are corrected for beam absorption and photon conversions in the target materials. Data are taken from the LOW Čerenkov pressure sample only. No Čerenkov tag selections have been applied at this stage.

-28.113 cm and -10.524 cm $< V_z < -7.703$ cm were selected for this analysis where V_z is the longitudinal coordinate of the vertex.

The vertex reconstruction efficiency for the tracking system was estimated to be $\approx 99.6\%$ independent of longitudinal position. This estimate is based upon an analysis of simulated events from the E706 Monte Carlo event sample.

6.2.3 Photon Conversion Correction

As discussed in the section on the energy scale calibration, photons may convert into e^+e^- in material upstream of the EMLAC. Such losses were accounted for by calculating the probability that the detected photon might have converted before exiting the magnet aperture (based on a detailed knowledge of the material in the spectrometer). This probability was evaluated for each pair of photons and applied as a correction.

6.2.4 Fiducial Requirement

The photons which contributed to the $\gamma\gamma$ mass spectra were required to be away from the boundaries of the EMLAC acceptance to minimize sensitivity to reconstruction losses. Only reconstructed showers which were within the range of 22.7 cm $< R < 149.5$ cm in radius and which were at least two ϕ -strips away from the octant and quadrant boundaries contribute. Corrections for these acceptance losses were calculated using a simple geometrical Monte Carlo program.

6.2.5 Energy Asymmetry Requirement

As spin 0 mesons are expected to decay isotropically in the parent particle's rest frame, the cosine of the decay angle, $\cos \theta^*$, of either photon with respect to the parent particle's direction of propagation in the lab frame should be uniformly distributed as illustrated in Figure 6.2. The energy asymmetry, A , of the two

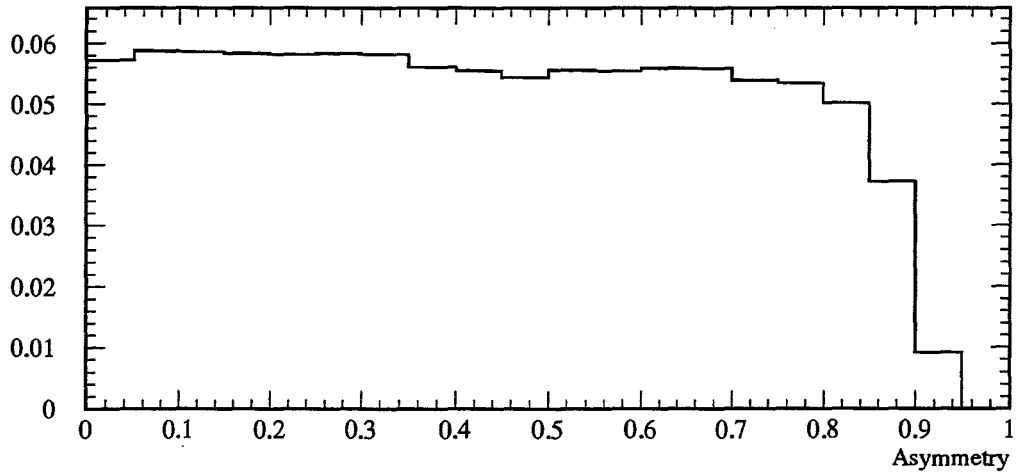
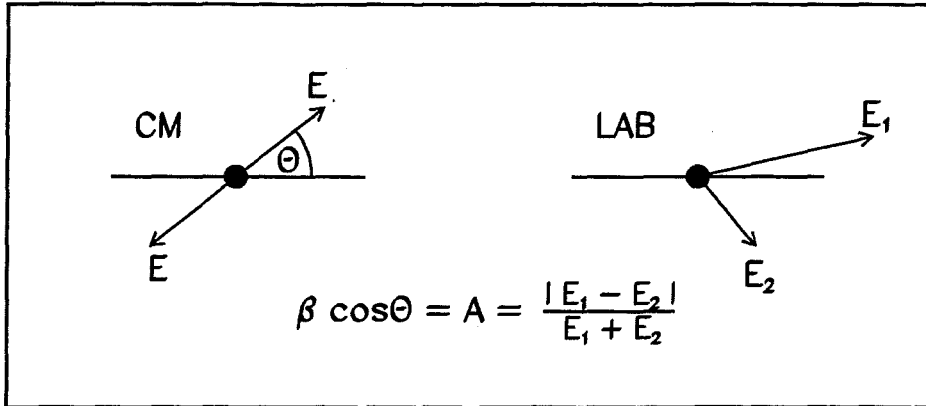


Figure 6.2: Top: Schematic diagram of the definition of energy asymmetry. Bottom: Energy Asymmetry distribution for photons from π^0 decays.

photons is related to θ^* by

$$A = \frac{|E_1 - E_2|}{E_1 + E_2} = \beta \cos \theta^* \quad (6.1)$$

where β is the speed (v/c) of the particle and E_1 and E_2 are the energies of the two photons.

The energy asymmetry distribution for the π^0 s candidates is compared in Figure 6.3 with the corresponding distribution generated from the E706 Monte Carlo simulation. This provides additional support for the E706 Monte Carlo model of the EMLAC. The measured distribution begins to decrease rapidly for $A > \approx 0.85$ due to reconstruction inefficiencies (discussed below). Two photon combinations with energy asymmetries above $A \approx 0.75$ were excluded and, since $\beta \approx 1$ for all detected particles, a correction of 4/3 was applied to account for this asymmetry cut.

6.2.6 Hadron Rejection

Hadrons were capable of producing showers which contributed to the backgrounds of the π^0 sample. Fortunately, hadrons frequently deposited most of their energy in the back section of the calorimeter. Thus, the ratio of the energy deposited in the front of the calorimeter to the total deposited energy, E_{front}/E_{total} , was generally small for hadronic showers. In fact, E_{front}/E_{total} was found to peak at about 0.7 for electromagnetic showers, but nearly zero for hadrons. The E_{front}/E_{total} distributions of particles showering in the EMLAC are shown in Figure 6.4.

The E_{front}/E_{total} distributions are compared with the corresponding E706 Monte Carlo generated distributions in Figure 6.5. The quality of the fit lends confidence that the E706 Monte Carlo simulation is useful in describing the performance of the EMLAC. Showers with $E_{front}/E_{total} < 0.2$ were excluded from the cross-section measurement. The correction for this requirement is included in the reconstruction

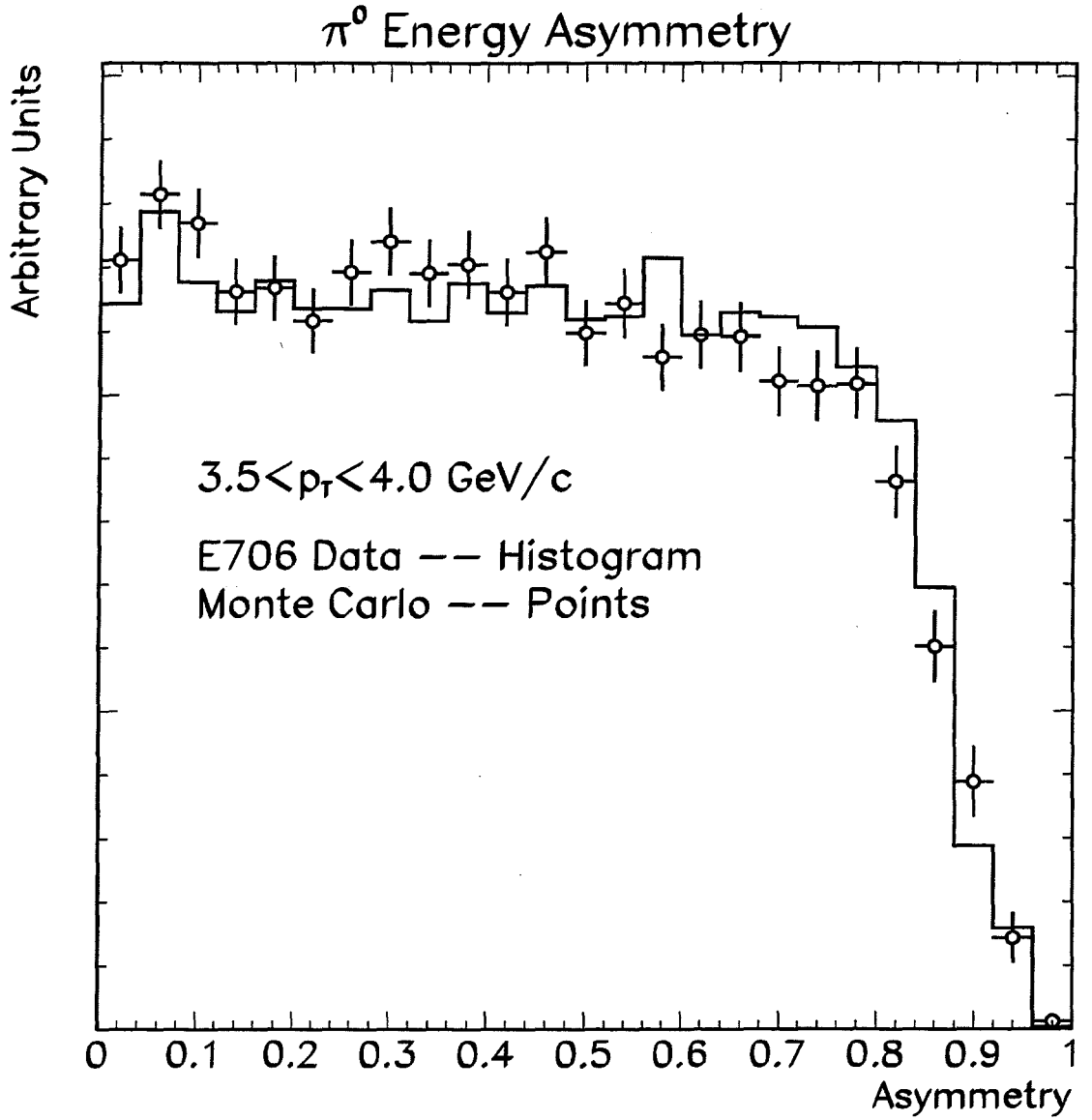


Figure 6.3: Comparison of E706 Monte Carlo generated asymmetry distribution with reconstructed data.

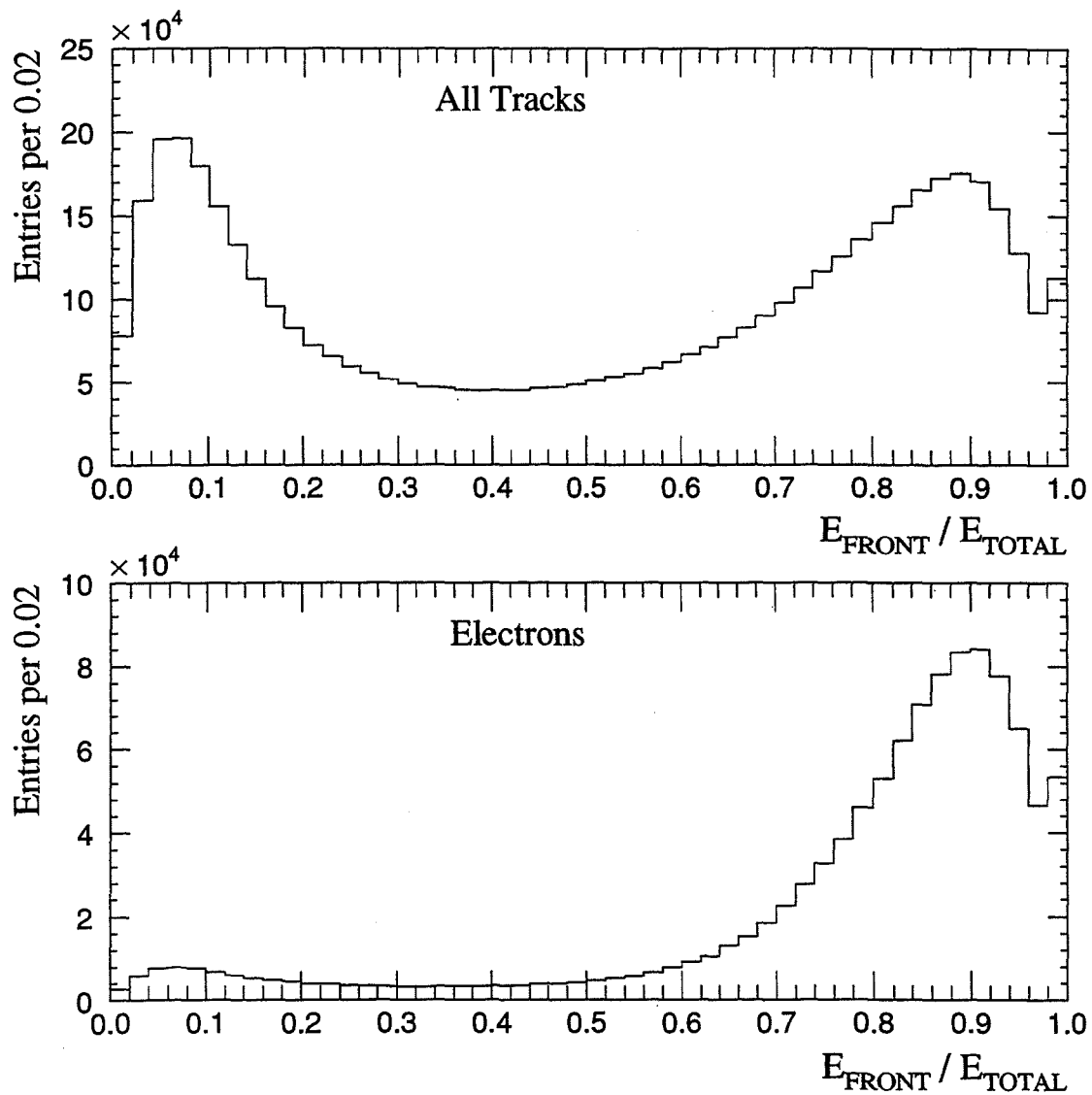


Figure 6.4: $E_{\text{front}}/E_{\text{total}}$ distributions for all particles showering in the EMLAC and for only electrons showering in the EMLAC. Hadrons deposit most their energy in the back section of the EMLAC.

$\gamma E_{front}/E_{total}$ Distributions

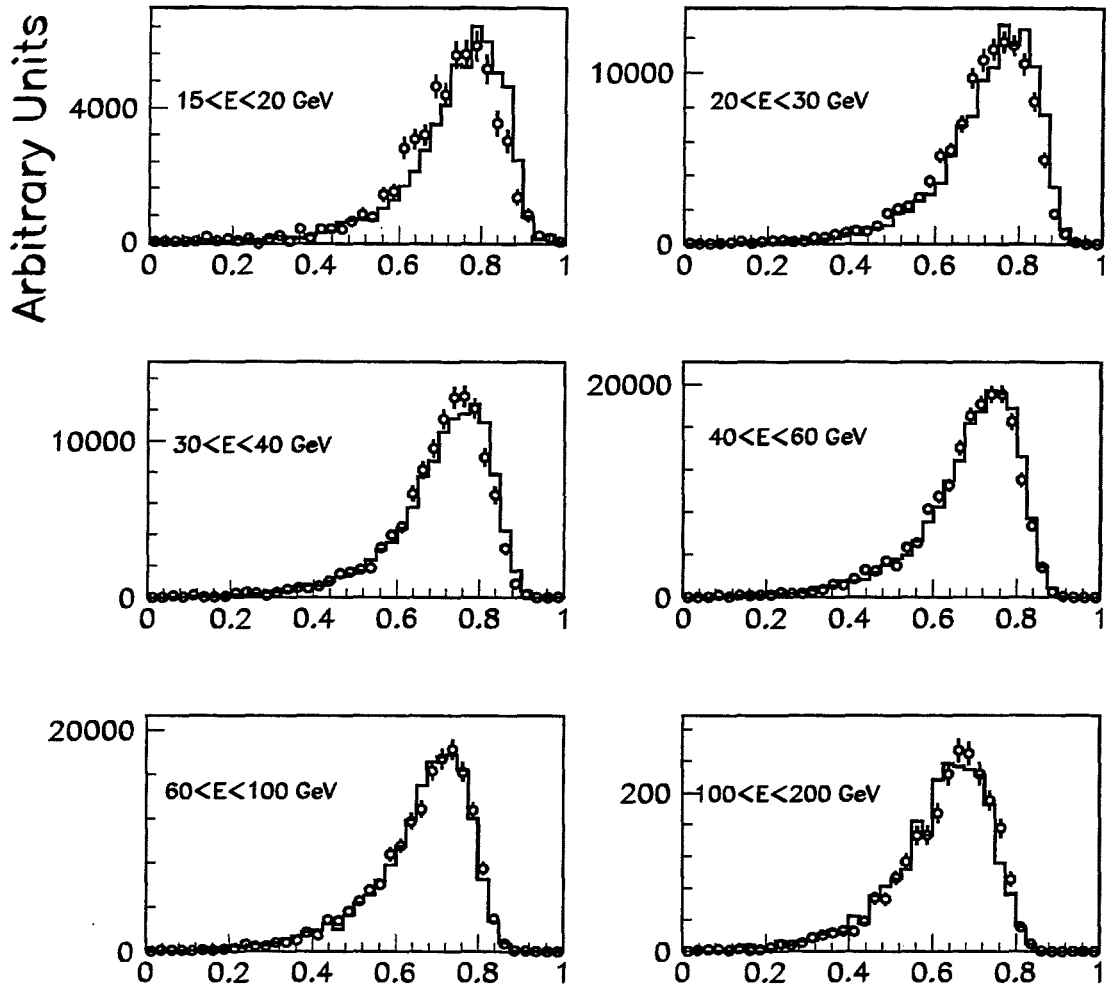


Figure 6.5: Comparison of the E_{front}/E_{total} distributions produced by the E706 Monte Carlo simulation with reconstructed EMLAC data. Data are presented in several photon energy ranges.

efficiency.

6.2.7 Muon Rejection

Beam halo muons were capable of mimicking showers of interest in the EMLAC. Four requirements were applied to eliminate events triggered by muon initiated showers which escaped the on-line veto. Corrections, based on the E706 Monte Carlo simulations, were applied to account for actual π^0 candidates which might be rejected by the muon requirements.

Off-line Veto Wall Requirement

The Minnesota Latch data for the veto wall was used to involve an off-line version of the on-line quadrant based muon veto. This off-line version of the veto wall veto was sensitive to longer time scale around the in-time bucket to provide enhanced muon protection.

Balanced p_T Requirement

High p_T interactions produced in the target were expected to produce showers on the *away-side*¹ of the detector whose net transverse momentum, p_T^b , effectively balanced that of the triggering high p_T particle. Events which triggered on accidental coincidences of interactions and beam halo muons would not generally exhibit such a p_T balance. The p_T^b/p_T distributions for both photons and muons showering in the EMLAC is shown in Figure 6.6. Pairs of showers with $p_T < 3.0$ GeV/c were excluded if $p_T^b/p_T < 0.3$.

¹The away-side of the EMLAC was defined as the azimuthal range from 120 to 240° with respect to the direction of the triggering shower in the plane transverse to the beam direction.

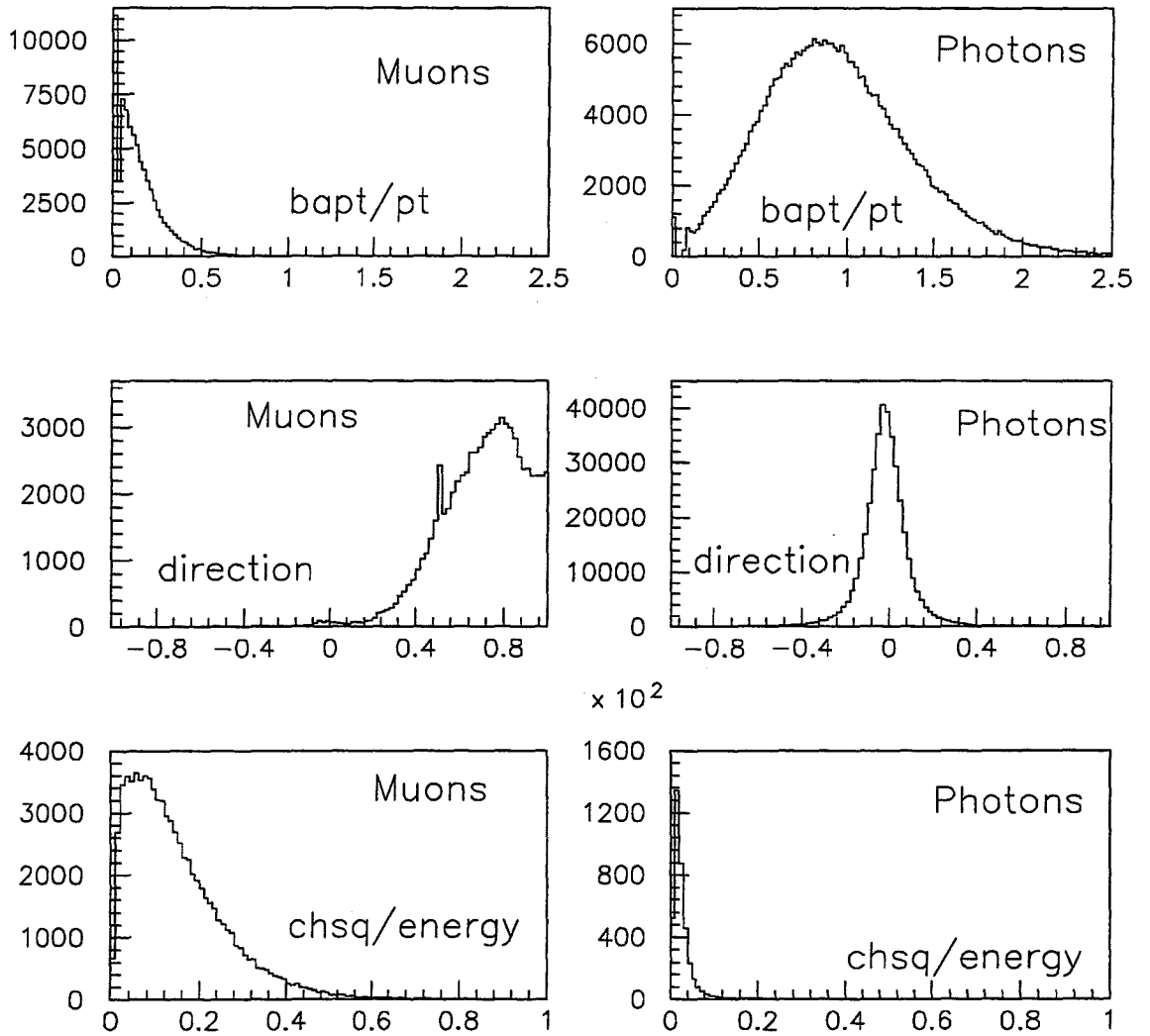


Figure 6.6: p_T^b/p_T (bap/pt), Directionality (direction) and χ^2/E (chsq/energy) distributions for both muons and photons producing showers in the EMLAC.

Directionality Requirement

Photons originating from the vicinity of the target will be incident on the EMLAC at larger angles relative to the beam direction than muons in the beam halo. The directionality of the shower, defined by

$$D = R_{front} - \frac{Z_{front}}{Z_{back}} R_{back}, \quad (6.2)$$

can be used to discriminate between beam halo muon showers and showers generated by photons from the target. Here R_{front} and R_{back} are the radial positions of the shower as measured in the front and back sections of the EMLAC respectively and Z_{front} and Z_{back} are the corresponding longitudinal positions of the front and back sections of the EMLAC. Photons resulting from the decay of mesons produced in the target are expected to have $D \approx 0$ while muons travelling nearly parallel to the beam generally have larger positive values for directionality. The directionality distributions for the both muons and photons showering in the EMLAC are shown in Figure 6.6. A requirement was applied to the directionality of the highest p_T photon in the two photon pair. Two shower combinations were rejected if the higher p_T shower had $p_T > 3.0$ GeV/c and directionality $D > D_{cut}$ where $D_{cut} = 0.193$ for $R < 40.175$ cm and $D_{cut} = 0.0048R$ (cm) at larger radii.

Chi-square Requirement

Fits to muon initiated showers in the EMLAC tend to have larger values of χ^2 than the fits to the photon initiated shower. As differences in shower shape vary with energy, the ratio χ^2/E was used to select the data sample. The χ^2/E distributions are shown in Figure 6.6 for both muon and photon initiated showers in the EMLAC. Two shower combinations were rejected if the higher p_T shower had $p_T > 3.0$ GeV/c and $\chi^2/E > 0.1$.

6.2.8 Trigger Selection

As discussed in Chapter 3, data selection was based on the implementation of various experimental triggers. The data used in this analysis of high p_T π^0 production were selected by the **SLH** and **SLL** triggers.

Each trigger had a characteristic p_T dependent efficiency for each group of 16 strips. Sample trigger p_T turn-on efficiency curves are shown in Figure 6.7 for both the **SLH** and **SLL** triggers. Here the *trigger* p_T scale has not been corrected for the EMLAC energy scale calibration and, so, does not correspond strictly to the same *physics* p_T as presented in the final cross-sections. The trigger thresholds were defined as the p_T for which the trigger became 50% efficient. The **SLH** and **SLL** triggers become efficient at physics p_T of ≈ 3.5 to 4.0 GeV/c and ≈ 3.0 GeV/c respectively. However, actual thresholds varied from local to local and octant to octant. The data from the **SLL** trigger is used to populate the lower p_T regions of the meson spectra while the higher p_T data is from the **SLH** trigger.

Curves such as these were used to evaluate the trigger efficiency corrections for each event. The trigger probability for each trigger for a given energy configuration in a given octant is defined as

$$P = 1 - \prod_i (1 - p_i) \quad (6.3)$$

where p_i is the trigger probability for the i th group in the octant and the product is taken over all groups in the octant. Contributions from individual octants with trigger probabilities less than 10% were excluded to eliminate large weights. Corrections for these losses are accommodated in the reconstruction efficiency.

6.2.9 Octant Correction

In order to maximize the available statistics of the data sample it was desirable to use the higher luminosity high threshold trigger to populate the lowest p_T possible

Local Trigger Turnons

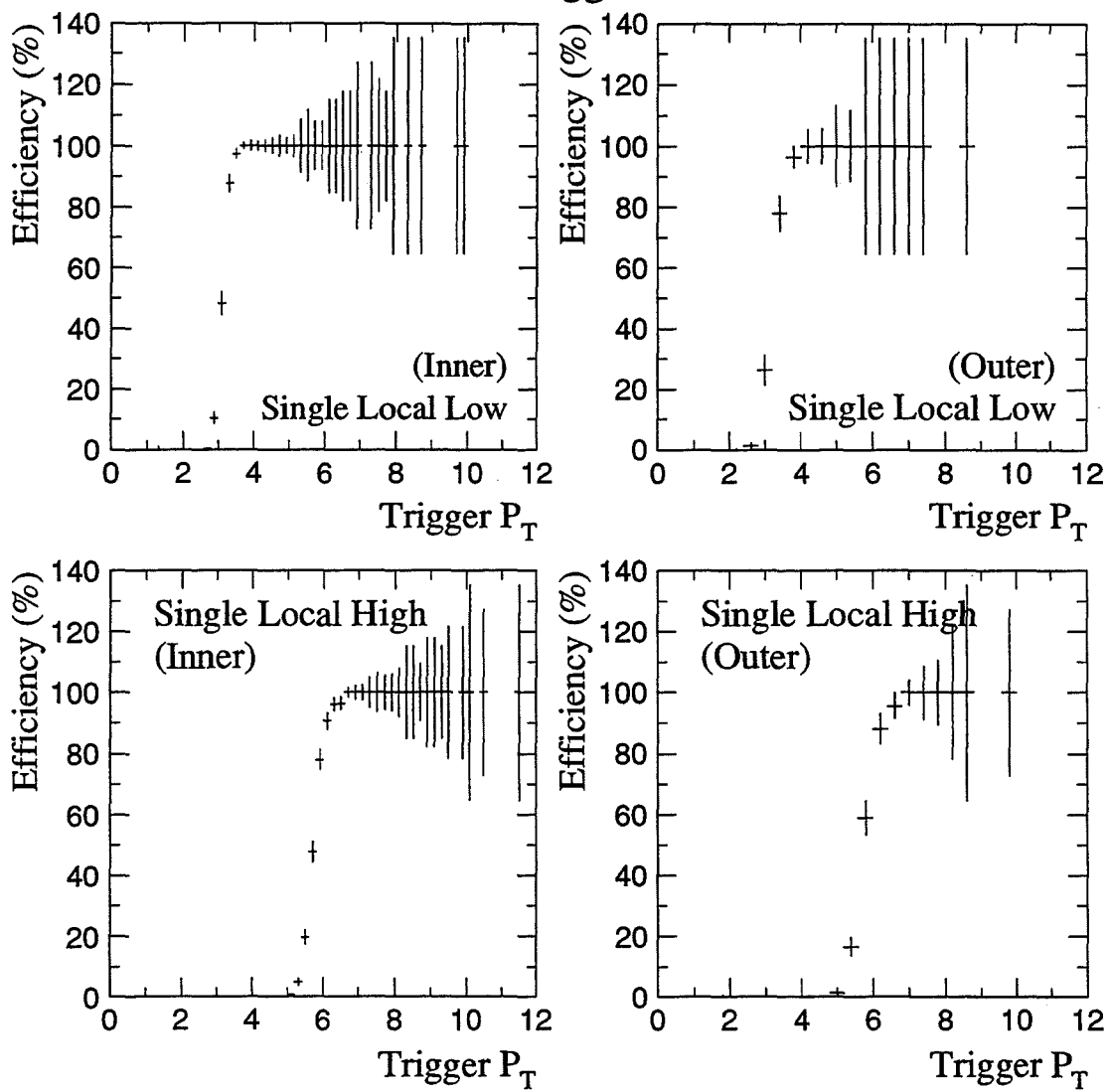


Figure 6.7: Sample trigger p_T turn-on efficiency curves for the SLH and SLL triggers for both the inner and outer sections of the EMLAC.

without unduly compromising the quality of the measurements. Since the thresholds of individual local groups were not identical, it was found for some octants in restricted p_T and rapidity ranges that the data would require large corrections. Instead these effects were corrected in the appropriate rapidity and p_T range by weighting each event by 8 over the number of octants which had reliable corrections for that specific trigger region.

6.2.10 Rapidity Requirement

The rapidity of a particle is given by

$$y = \frac{1}{2} \ln \left(\frac{E + p_{\parallel}}{E - p_{\parallel}} \right). \quad (6.4)$$

Here p_{\parallel} is the longitudinal component of the particle's momentum in the chosen frame of reference and E is the energy of the particle. Boosts along the longitudinal direction results in the transformation

$$y^* = y - \frac{1}{2} \ln \left(\frac{1 + \beta}{1 - \beta} \right). \quad (6.5)$$

Thus the shape of the rapidity distribution is invariant under a boost in the direction of the incident beam. The rapidity range for the two photon data sample was restricted to $-0.75 < y < 0.75$, and the reported cross-sections are averaged over that rapidity interval.

6.2.11 Signal Definition

Requirements were applied to the full data sample to select only those candidates whose mass was reasonably close to the accepted nominal value. The *signal region* was defined as the region between $0.10 \text{ GeV}/c^2 < M < 0.18 \text{ GeV}/c^2$ for π^0 candidates.

Sideband Subtraction

Backgrounds were subtracted from both the π^0 and η mass distributions as follows. *Sideband* regions with the same total mass range as the signal region were defined and a count of the total number of two photon weighted combinations in the sidebands was then subtracted from the corresponding signal region to provide a measure of the number of meson candidates.

6.2.12 Reconstruction Efficiencies

The E706 Monte Carlo was used to determine the two photon reconstruction efficiencies. The Monte Carlo generated events were analyzed using the same reconstruction software as the data, and the number of reconstructed mesons was compared to the number of generated mesons as a function of rapidity and p_T .

6.2.13 Branching Ratios

The measured yields must also be corrected to account for the fact that the π^0 decays into final states other than the $\gamma\gamma$ mode. For the $\pi^0 \rightarrow \gamma\gamma$ mode, the branching ratio [1] is 98.798%.

6.2.14 Beam Normalization

Determination of the beam count for the cross-section normalization involved several factors. The number of live triggerable tagged beam particles,² N_{TB} , is defined as

$$N_{TB} = N_B \cdot LiveFraction \cdot FractionTagged \quad (6.6)$$

where N_B is the scaler count of the number of incident particles satisfying **BEAM1***
BH. The *LiveFraction* term accounts for the fraction of the beam for which the

²I.e. Beam particles incident on the target while the data acquisition system was ready to trigger and readout data.

spectrometer was in the ready state as well as for the losses due to **CLEAN**, **SCRKILL**, **VW** and **EARLY_PT** trigger requirements described in Chapter 3. The *FractionTagged* accounts for the fraction of the incident beam which satisfies the particle tag. The fraction of the beam satisfying any particular tag, shown in Tables 5.4 and 5.5, were measured separately for the **HIGH** and **LOW** Čerenkov pressure samples from the Minnesota Latch data for low bias data by normalizing the number of low bias buckets which which satisfied **BEAM1 * BH** and each Čerenkov tag to the total number of low bias buckets which satisfied **BEAM1 * BH**.

6.3 Production Cross-Section Measurements

The invariant inclusive π^0 cross-section per nucleon was calculated using the equation

$$E \frac{d^3\sigma}{dp^3} = \frac{1}{2\pi p_T \Delta p_T \Delta y_{cm}} \frac{1}{\rho \ell N_a} \frac{N^{corr}}{N_{TB}}. \quad (6.7)$$

The phase space is expressed here in terms of p_T and the center-of-momentum rapidity (y_{cm}). ρ is the density of the target material, ℓ is the length of the target and N_a is Avogadro's number. N_{TB} is the live triggerable tagged beam count. N^{corr} is the number of reconstructed π^0 mesons in the p_T and rapidity interval $\Delta p_T \Delta y_{cm}$ weighted by factors to account for efficiency, geometrical acceptance, reconstruction efficiency, photon conversions, beam absorption in the target material, branching ratios, vertex efficiency, energy asymmetry and muon requirements.

6.4 Čerenkov Contamination Corrections

The resulting cross-sections at this point represented the production cross-sections for each incident particle type uncorrected for incident beam tag contaminations. The cross-sections were then corrected to account for these contaminations.

In general, the cross-section resulting from the application of Čerenkov tag requirements will include contamination due to mis-identified particles and background. Neglecting muons, the tagged (contaminated) cross-section, Σ_p , for incident protons may be expressed as a linear combination of the decontaminated cross-sections, σ_i , of all incident particle types where i represents π , K or p . Thus, neglecting contributions from the Čerenkov pressure curve backgrounds,

$$\Sigma_p = f_p \sigma_p + f_K \sigma_K + f_\pi \sigma_\pi, \quad (6.8)$$

where f_i are the fractional contributions of each particle type to the selected p tag at the operating pressure of the Čerenkov detector as measured from the comparison of Čerenkov Monte Carlo simulation to the measured pressure curves at that operating pressure. These values were presented in Tables 5.4 and 5.5. The background to the corresponding tag pressure curve will yield a fractional contribution given by f_b . The backgrounds represent instances for which any Čerenkov phototube signal above threshold was due entirely to spurious electronic noise. However, the Čerenkov tag logic required that a beam particle be present. These beam particles will contribute to the measured cross-sections and, so, the fractional contribution from the backgrounds should be taken into consideration in correcting the measured cross-sections for tag contaminations. For a given tag, the backgrounds will contribute to the cross-section measurement in proportion to particle fractions, x_i , in the beam. Thus the above equation is modified to reflect this contribution from the tag backgrounds.

$$\Sigma_p = f_p \sigma_p + f_K \sigma_K + f_\pi \sigma_\pi + f_b(x_p \sigma_p + x_K \sigma_K + x_\pi \sigma_\pi), \quad (6.9)$$

where f_b represents the net fractional contribution of the pressure curve background at the operating pressure for the chosen tag. Similarly, the tagged cross-sections for incident K^+ and π^+ mesons may be parameterized as

$$\Sigma_K = g_p \sigma_p + g_K \sigma_K + g_\pi \sigma_\pi + g_b(x_p \sigma_p + x_K \sigma_K + x_\pi \sigma_\pi), \quad (6.10)$$

and

$$\Sigma_{\pi} = h_p \sigma_p + h_K \sigma_K + h_{\pi} \sigma_{\pi} + h_b (x_p \sigma_p + x_K \sigma_K + x_{\pi} \sigma_{\pi}). \quad (6.11)$$

The coefficients x_i , f_i , g_i and h_i are determined by the comparison of the Čerenkov Monte Carlo simulation with the measured pressure curves (as discussed in Chapter 5). These values were presented in Tables 5.3 through 5.5. It should be noted that all measured contributions from incident π^+ mesons will include any contributions from incident beam muons since the Čerenkov detector does not discriminate between μ and π . Contributions from muons were judged negligible based on the upper limit on muon content of the beam provided by the measurements quoted in Table 5.2.

The cross-sections measured in each p_T bin were corrected to obtain the cross-sections for each incident beam particle. The corrected cross-sections result from a direct solution to the above linear equations 6.9 through 6.11. Resulting statistical uncertainties are propagated in quadrature.

Chapter 7

Results and Conclusions

7.1 Inclusive π^0 Cross-Section Results

7.1.1 Inclusive π^0 Cross-Section for Incident -515 GeV/c Beam

The inclusive cross-section for the production of π^0 mesons was measured for -515 GeV/c beam particles incident on a beryllium target. The majority particle in the -515 GeV/c beam was the π^- . The net contamination due to the minority K^- and \bar{p} was estimated [41] to be $\approx 3.5\%$, and that contamination was predominantly K^- . The resulting untagged cross-section is shown in Figure 7.1. The cross-section presented here includes all cuts and corrections discussed in Chapter 6 except that no Čerenkov cuts have been applied. This cross-section for incident 515 GeV/c π^- mesons was measured from data acquired during the 1990 data acquisition period.

7.1.2 Inclusive π^0 Cross-Section for Incident $+530$ GeV/c Beam

The inclusive cross-section for the production of high transverse momentum π^0 mesons was measured for $+530$ GeV/c beam particles incident on a beryllium target during the 1991 data acquisition period. The resulting untagged cross-section

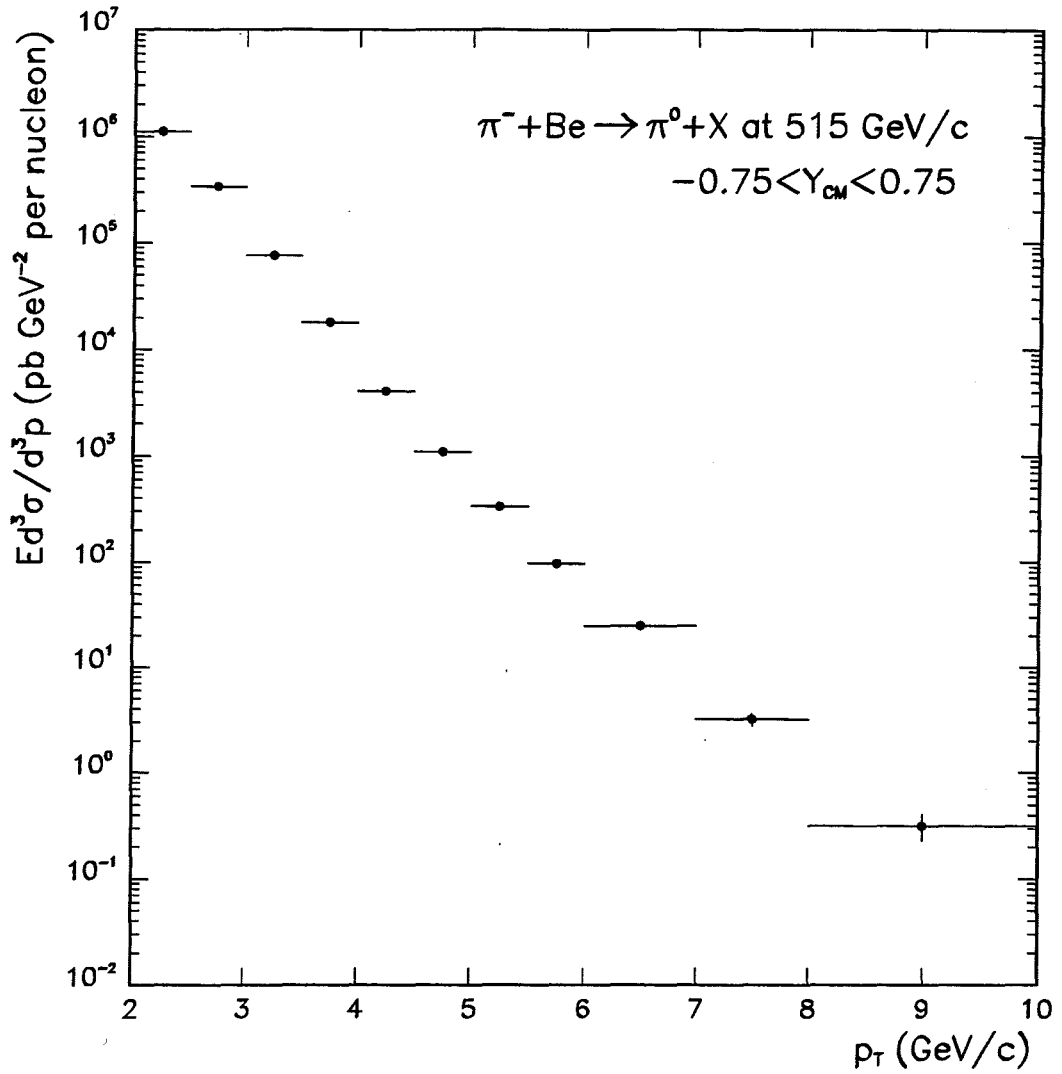


Figure 7.1: Inclusive cross-section as a function of π^0 p_T for the production of π^0 mesons by π^- mesons incident on the beryllium target. This cross-section is untagged and uncorrected for the negligible K^- and \bar{p} contamination. Data are plotted on a semi-logarithmic scale. Data were acquired during the 1990 data acquisition period.

is shown in Figure 7.2 for the higher sensitivity HIGH Čerenkov operating pressure. (The integrated luminosity of the high pressure sample is approximately twice that of the LOW pressure sample.) The cross-section presented here includes all cuts and corrections discussed in Chapter 6 except that Čerenkov tag requirements and associated contamination corrections have not been applied.

7.1.3 Tagged Versus Untagged Inclusive π^0 Cross-Sections for Incident +530 GeV/c Beam Particles

The cross-section data sample generated by the incident +530 GeV/c beam was separated using Čerenkov tags as discussed in Chapters 5 and 6. Figure 7.3 shows the ratio of the $p2\overline{K}3\pi2$ tagged π^0 inclusive cross-section to the untagged π^0 inclusive cross-section as a function of the $\pi^0 p_T$. This ratio decreases as the $\pi^0 p_T$ increases indicating that this tagged beam may have different characteristics than the untagged sample.

The ratio of the measured inclusive π^0 cross-sections for the $\pi3\overline{p}2$ tagged sample to the untagged sample is shown in Figure 7.4. This ratio increases significantly as the $\pi^0 p_T$ increases illustrating the fact that the $\pi3\overline{p}2$ tagged sample has substantially different characteristics than the untagged sample which is predominantly (> 96%) due to incident protons.

Figure 7.5 shows the ratio of the $K4\overline{\pi}2\overline{p}2$ tagged π^0 inclusive cross-section to the untagged inclusive π^0 cross-section for incident +530 GeV/c beam as a function of $\pi^0 p_T$. This tagged sample also appears to generate a different π^0 cross-section than the incident proton dominated untagged sample.

These results clearly illustrate that the Čerenkov tags are effective in tagging different beam particle types.

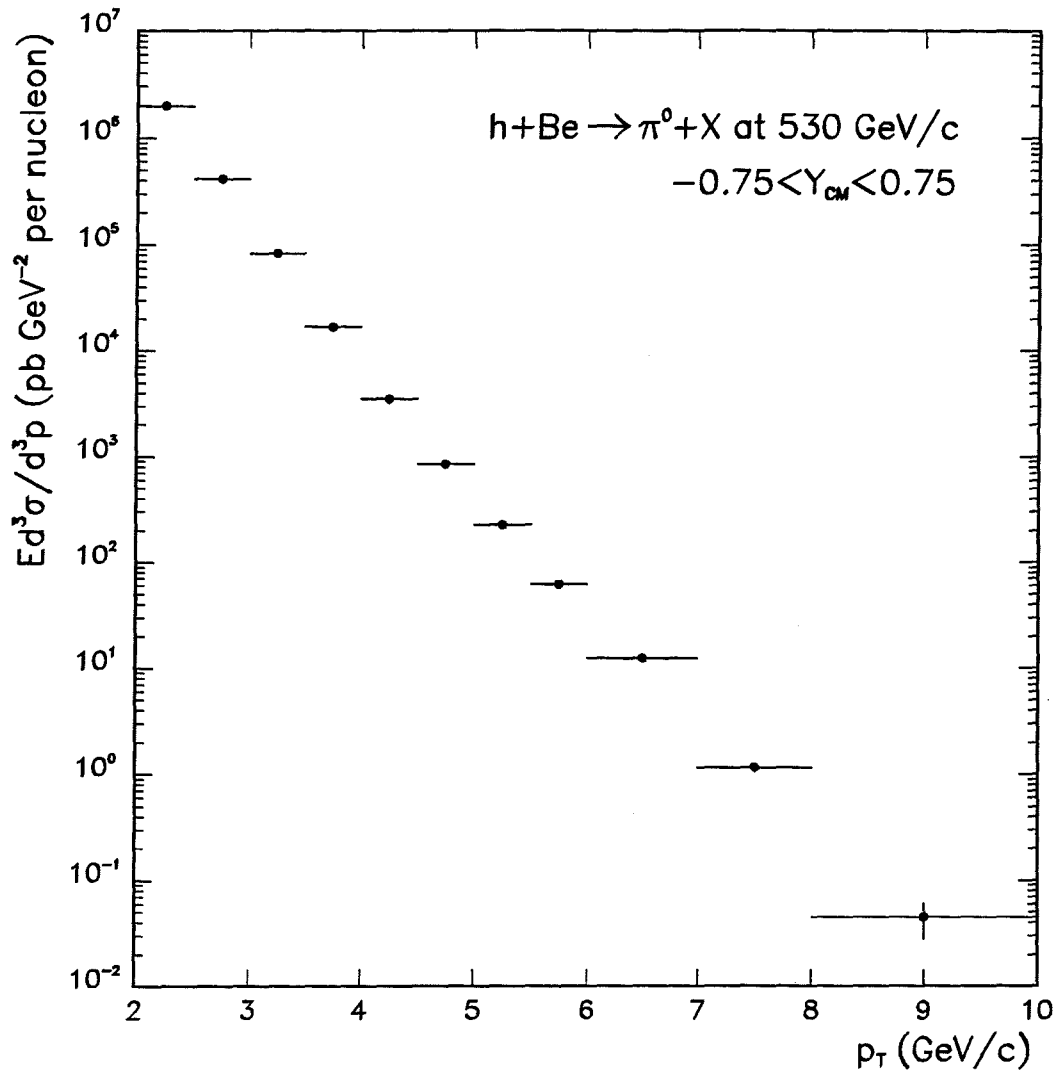


Figure 7.2: Inclusive cross-section as a function of π^0 p_T for the production of π^0 mesons by the unseparated and untagged +530 GeV/c beam particles incident on the beryllium target. Data represent the HIGH Čerenkov pressure sample only. Data are plotted on a semi-logarithmic scale.

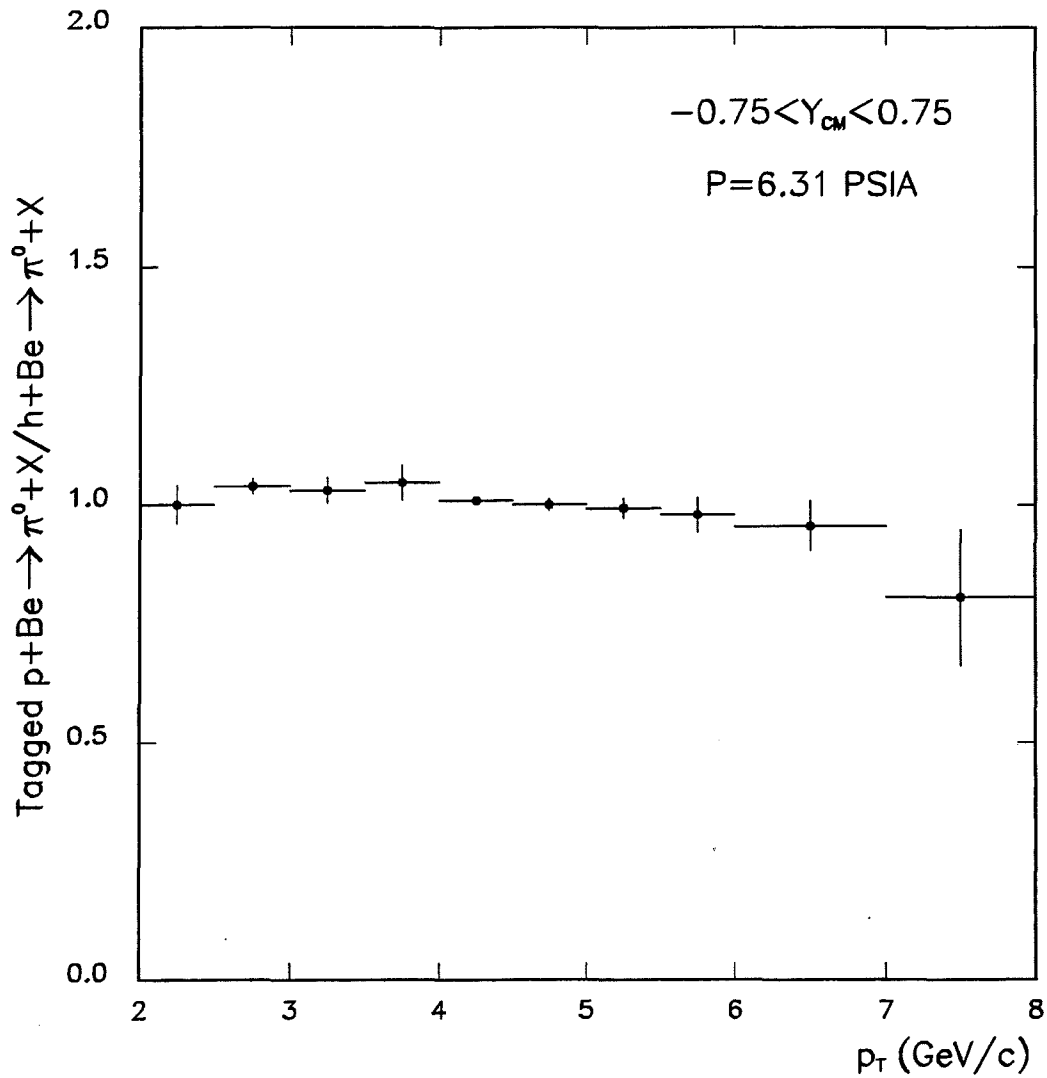


Figure 7.3: Ratio of the inclusive π^0 production cross-section for +530 GeV/c beam particles incident on the beryllium target which satisfy a $p2\overline{K}3\pi2$ tag to the corresponding untagged cross-section as a function of π^0 p_T . The tagged data are uncorrected for particle contaminations. Data are from the HIGH Čerenkov pressure sample only.

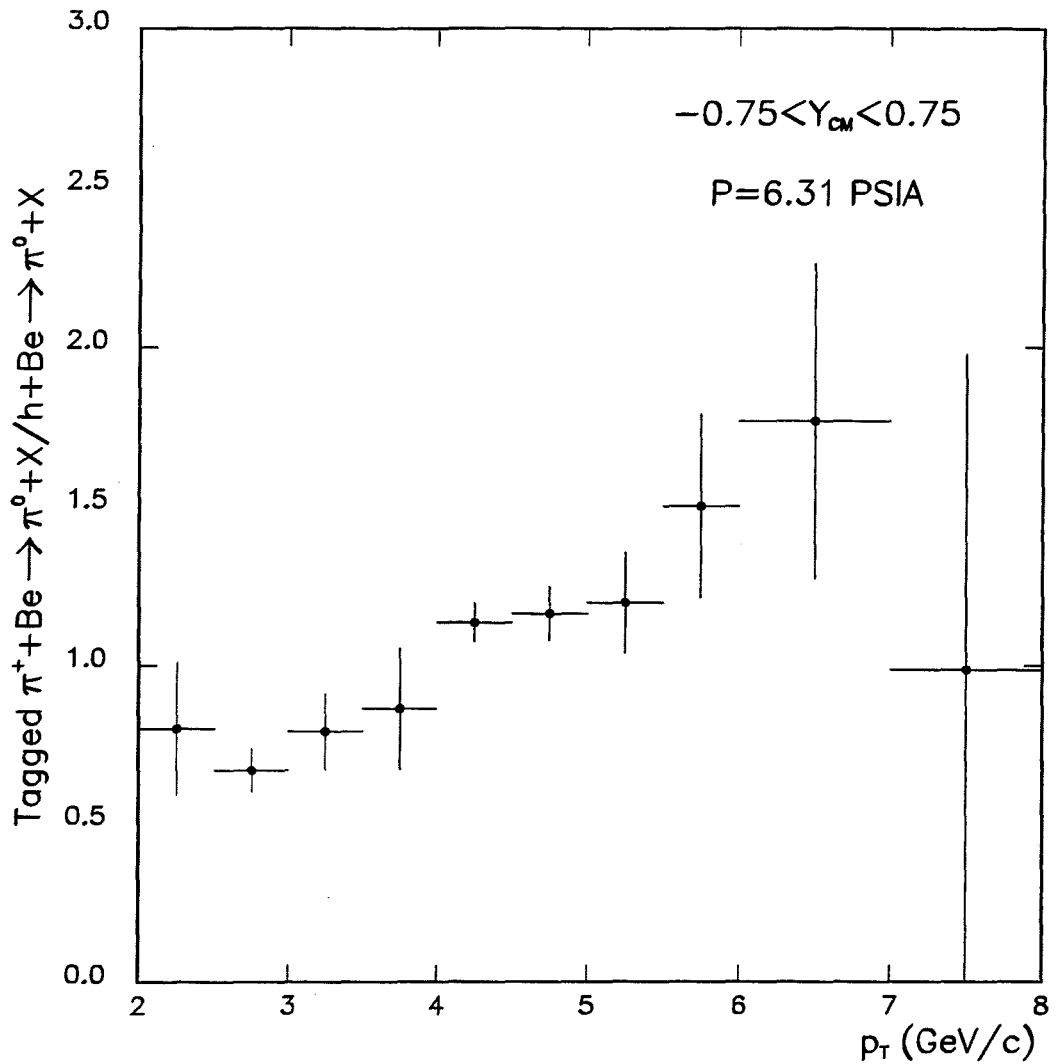


Figure 7.4: Ratio of the inclusive π^0 production cross-section for +530 GeV/c beam particles incident on the beryllium target which satisfy a π^0 tag to the corresponding untagged cross-section as a function of π^0 p_T . The tagged data are uncorrected for particle contaminations. Data are from the HIGH Čerenkov pressure sample only.

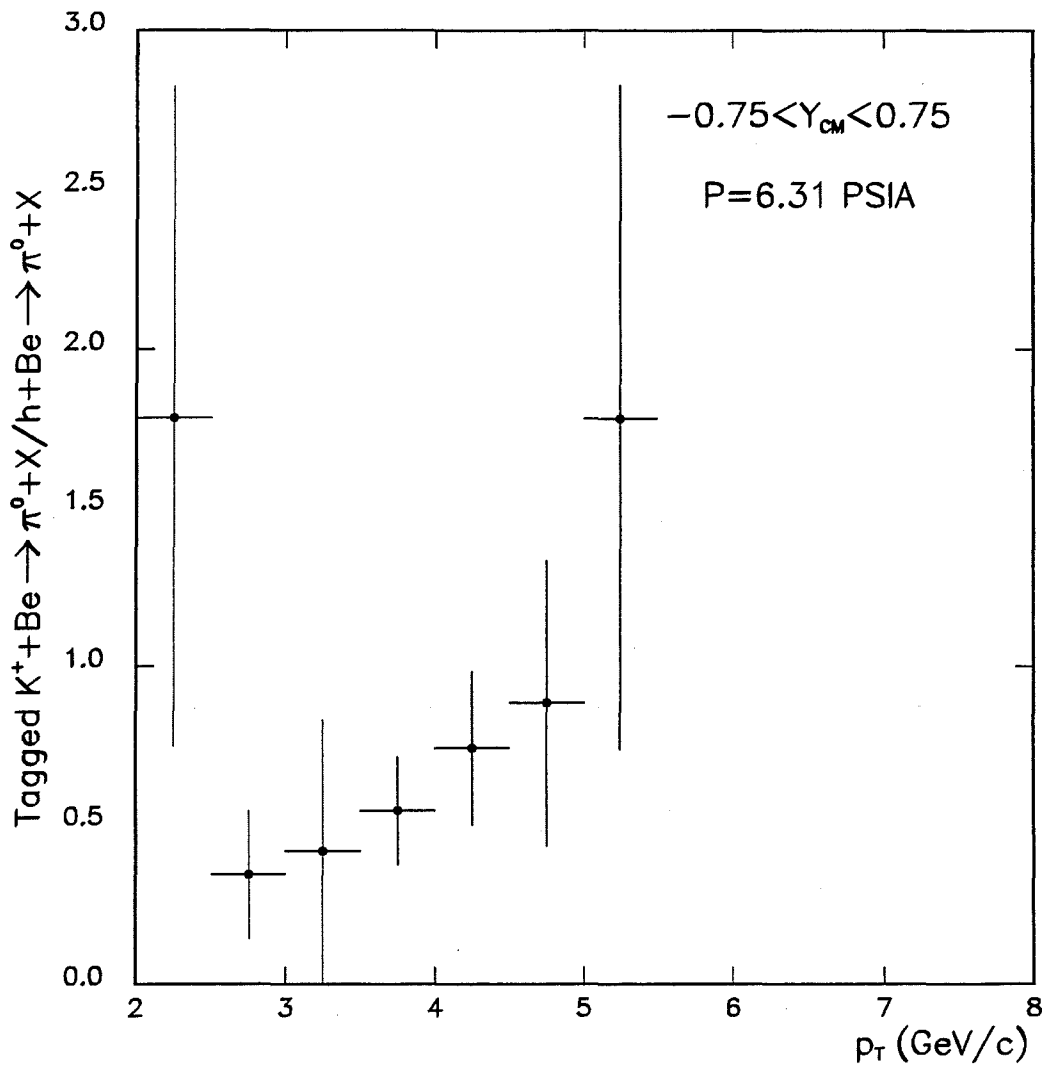


Figure 7.5: Ratio of the inclusive π^0 production cross-section for +530 GeV/c beam particles incident on the beryllium target which satisfy a $K4\pi^2p^2$ tag to the corresponding untagged cross-section as a function of $\pi^0 p_T$. The tagged data are uncorrected for particle contaminations. Data are from the HIGH Čerenkov pressure sample only.

7.1.4 Cross-Section Sensitivity to Operating Pressure

As discussed in previous chapters, the Čerenkov data were acquired at two standard operating pressures. This necessarily resulted in differences in the tag contaminations. Thus the contamination corrections to the measured cross-sections varied with operating pressure.

In order to investigate the sensitivity of the measured cross-section results to the different contamination corrections associated with the HIGH and LOW Čerenkov operating pressure samples, the ratio of fully corrected inclusive π^0 cross-sections for the HIGH and LOW Čerenkov pressures were calculated. Figure 7.6 shows the ratio of the cross-section results for the HIGH pressure relative to the LOW pressure sample for incident p tagged via the $p2\overline{K}3\pi2$ tag using the $\pi3\overline{p}2$ and $K4\pi2\overline{p}2$ tagged cross-sections to evaluate the contamination correction. Figure 7.7 shows the cross-section ratio for incident π^+ tagged via the $\pi3\overline{p}2$ tag with contamination corrections based on the $p2\overline{K}3\pi2$ and $K4\pi2\overline{p}2$ tagged cross-sections. (These ratios have been adjusted to account for the 10% untagged normalization difference between the HIGH and LOW pressure samples.) These figures show that the Čerenkov contamination corrected results from the HIGH and LOW pressure samples are consistent.

7.1.5 Inclusive π^0 Cross-Sections for Incident +530 GeV/c p , K^+ and π^+

The appropriate contamination corrected HIGH and LOW cross-sections were combined to obtain the weighted mean resultant cross-sections. The resulting π^0 inclusive cross-section for incident protons from the entire data sample is shown in Figure 7.8. The resulting corrected inclusive π^0 cross-section for incident +516 GeV/c π^+ is shown in Figure 7.9. The corresponding corrected inclusive π^0 cross-section for incident 0.5 TeV/c K^+ is shown in Figure 7.10.

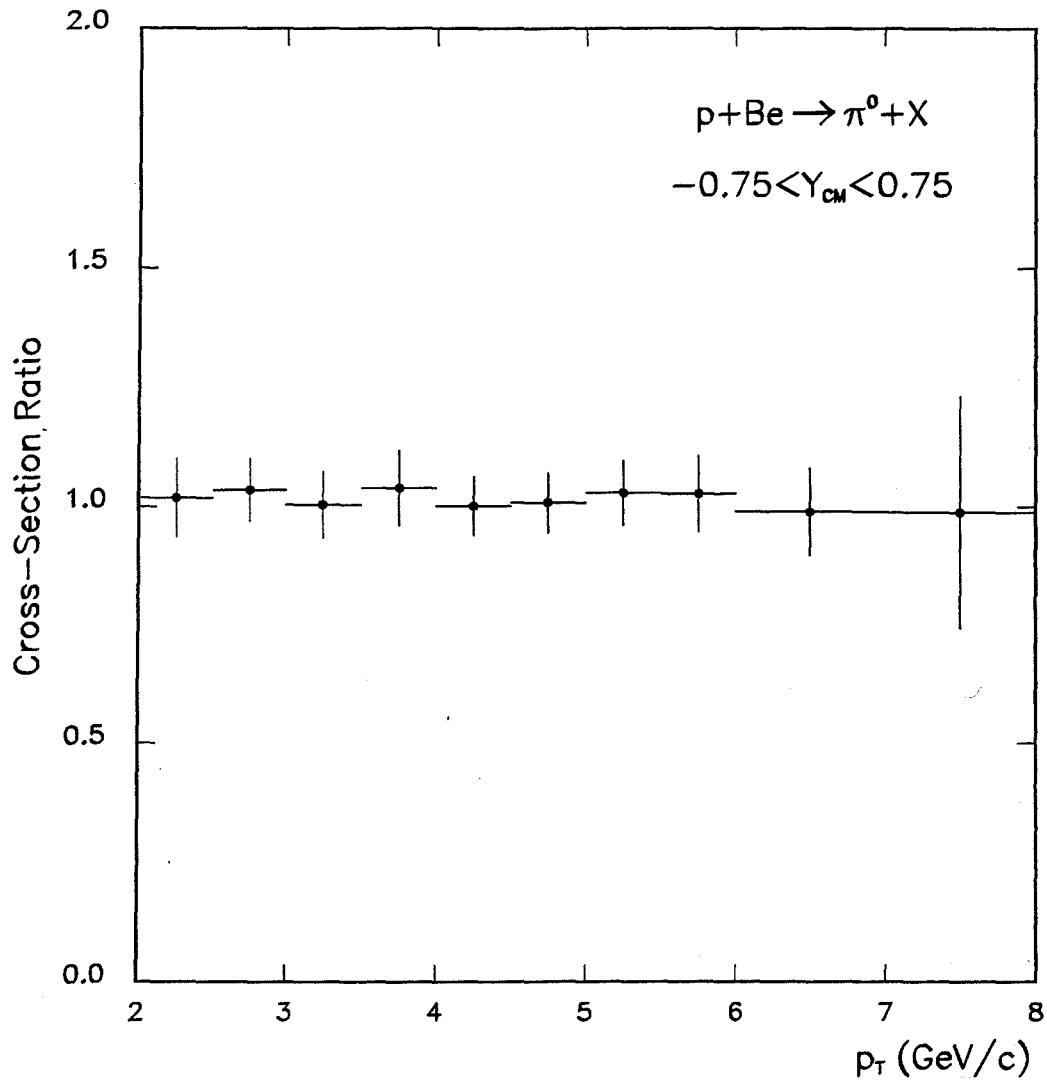


Figure 7.6: Ratio of the inclusive π^0 production cross-section measured at Čerenkov operating pressures of 6.31 psia and 6.24 psia for incident p as a function of $\pi^0 p_T$. The p tag employed in this measurement is $p2\overline{K}3\pi2$ while the $\pi3p2$ and $K4\pi2p2$ tagged cross-sections were also used in the contamination corrections.

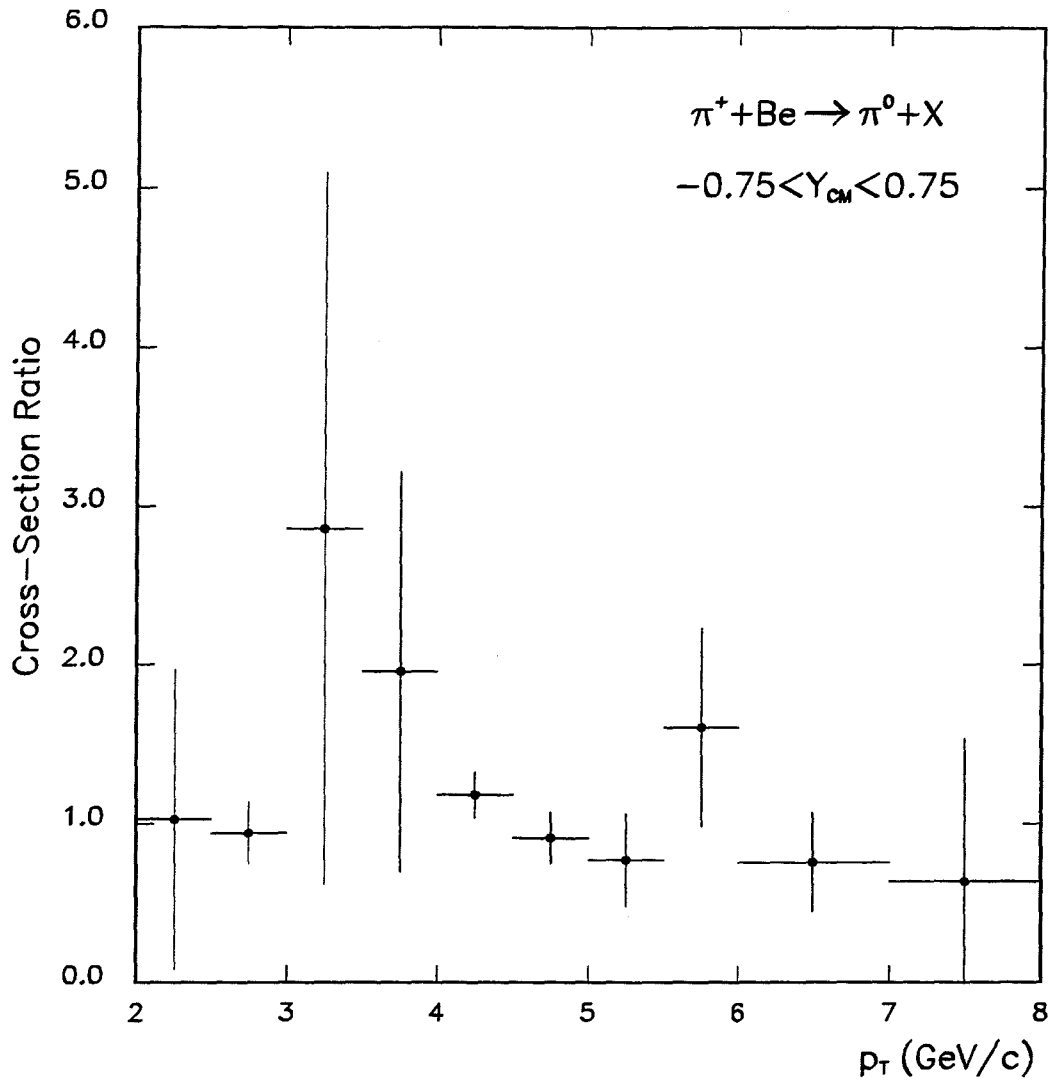


Figure 7.7: Ratio of the inclusive π^0 production cross-section measured at Čerenkov operating pressures of 6.31 psia and 6.24 psia for incident π^+ as a function of π^0 p_T . The π^+ tag employed in this measurement is $\pi 3 p \bar{2}$ while the $p 2 \bar{K} 3 \pi \bar{2}$ and $K 4 \pi \bar{2} p \bar{2}$ tagged cross-sections were also used in the contamination corrections.

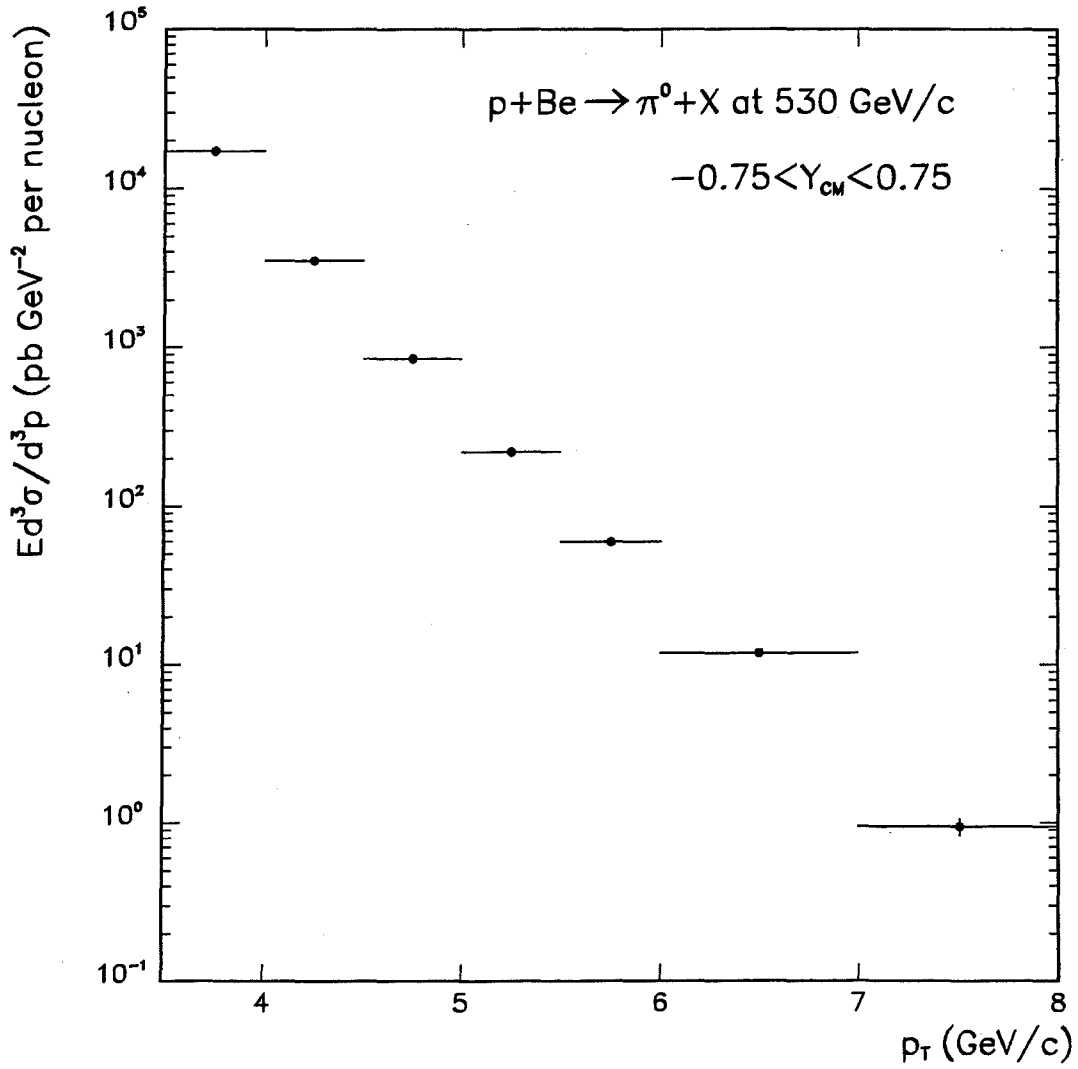


Figure 7.8: Inclusive π^0 cross-section per nucleon for 530 GeV/c p incident on beryllium as a function of π^0 p_T .

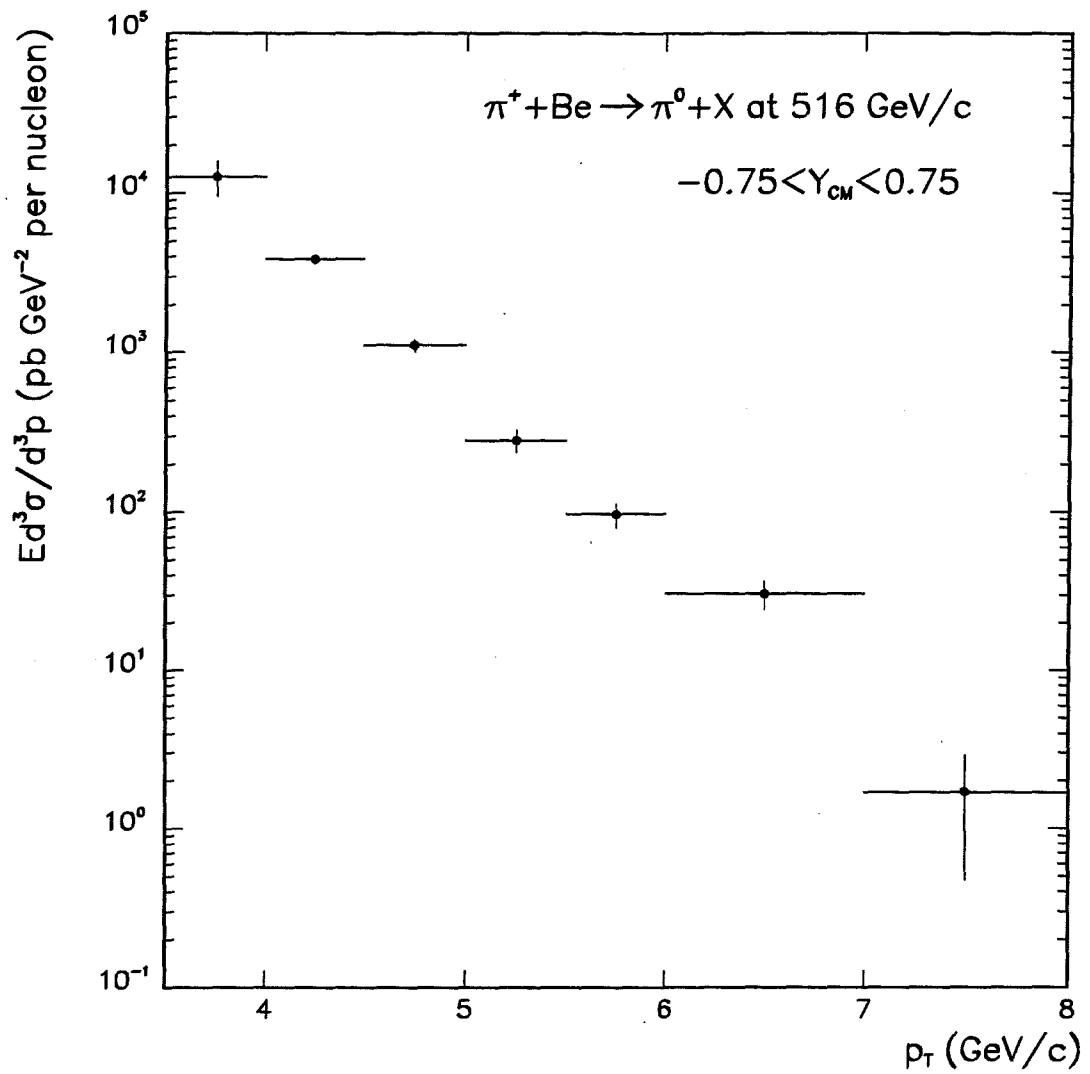


Figure 7.9: Inclusive π^0 cross-section per nucleon for 516 GeV/c π^+ incident on beryllium as a function of π^0 p_T .

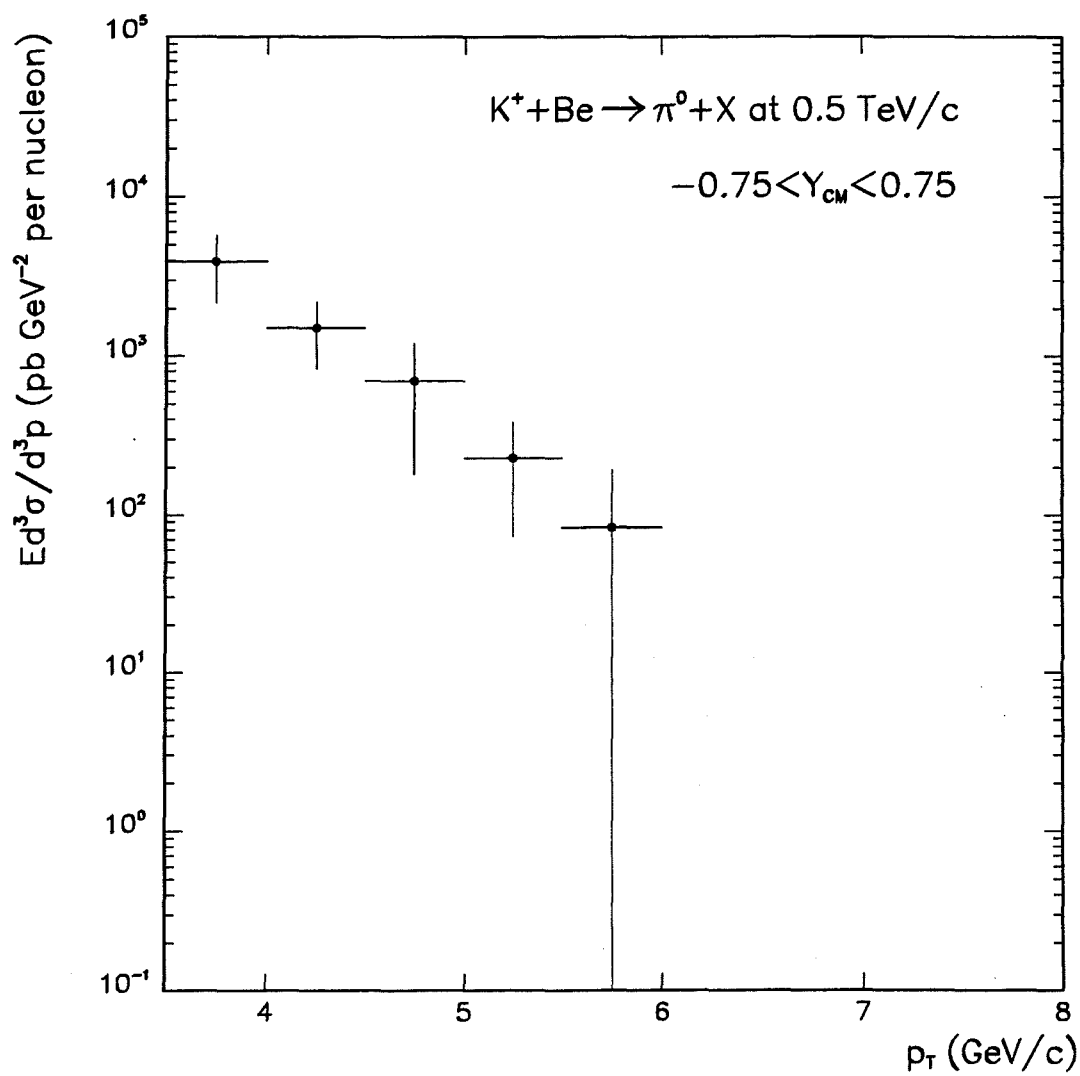


Figure 7.10: Inclusive π^0 cross-section per nucleon for 0.5 TeV/c K^+ incident on beryllium as a function of π^0 p_T .

7.1.6 Comparison of Cross-Sections from Different Incident Particle Types

Figure 7.11 shows the ratio of the inclusive π^0 cross-section for incident 516 GeV/c π^+ mesons to the corresponding cross-section for incident 515 GeV/c π^- mesons.

Figure 7.12 shows the comparison between the inclusive π^0 cross-sections for incident +516 GeV/c π^+ mesons versus incident +530 GeV/c p . The ratio of the rapidity distributions for incident +516 GeV/c π^+ to incident +530 GeV/c p is shown in Figure 7.13 for π^0 s in the range $4.0 \text{ GeV}/c < p_T < 4.5 \text{ GeV}/c$.

7.1.7 Comparison of Cross-Sections with QCD Calculations

The inclusive π^0 cross-section for incident +530 GeV/c p is compared in Figure 7.14 with Next-to-Leading-Logarithm (NLL) QCD calculations for the two choices of scale $Q = p_T$ and $Q = p_T/2$. Data are plotted as a function of $\pi^0 p_T$. Figure 7.15 illustrates the effect of k_T smearing on the QCD comparison to the measured cross-section for the scale $Q = p_T/2$. The calculation for $k_T = 1.4 \text{ GeV}/c$ is quite good.

The resulting corrected inclusive π^0 cross-section for incident +516 GeV/c π^+ is compared with the NLL QCD predictions in Figure 7.16. This cross-section is compared in Figure 7.17 to the NLL QCD calculations (for the scale $Q = p_T/2$) with k_T smearing included and once again, our measurement is consistent with the NLL QCD calculation when a k_T of order 1.4 GeV/c is included. QCD calculations are currently unavailable for the incident K^+ .

7.2 Conclusions

The foregoing analysis demonstrates the ability of the Meson West Čerenkov detector to simultaneously identify different incident charged beam particles even

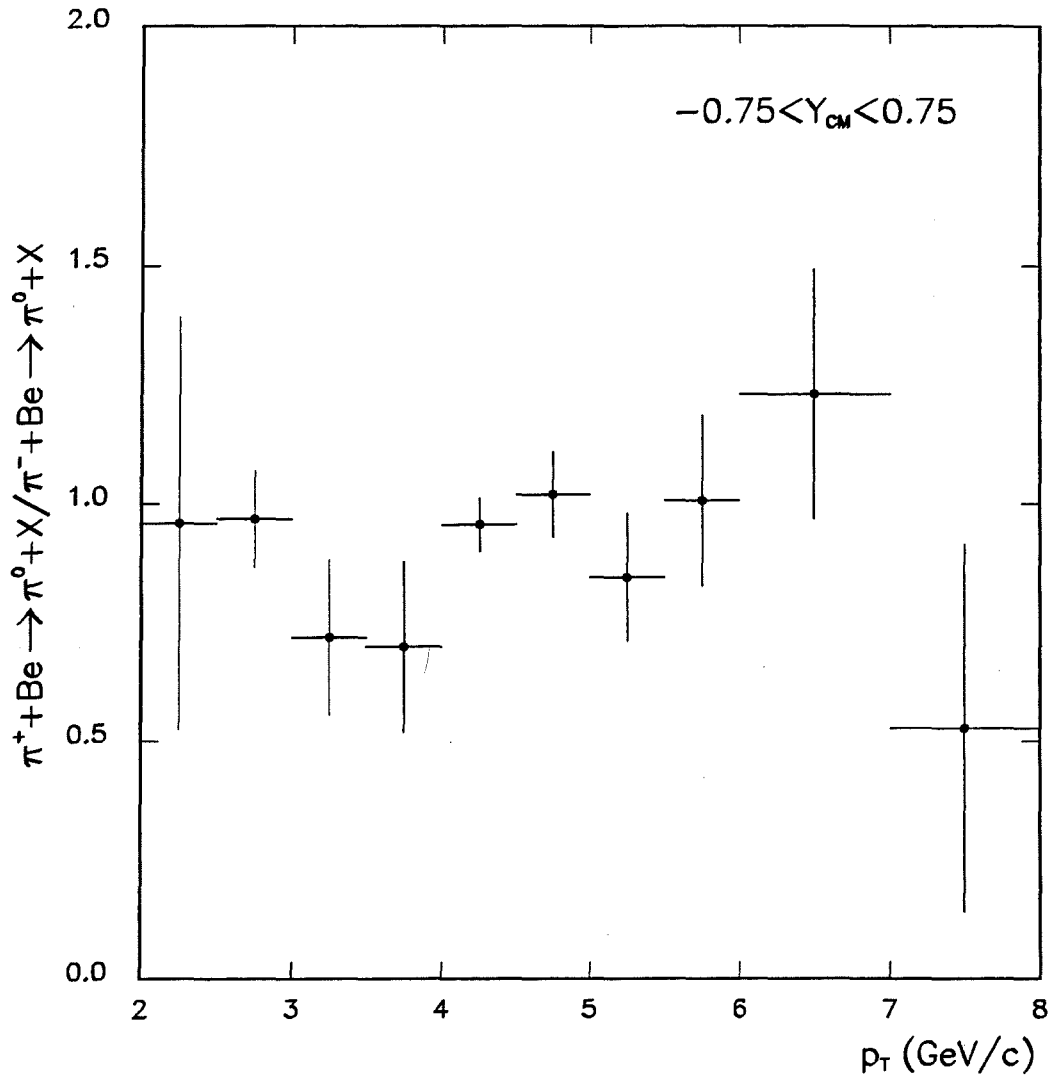


Figure 7.11: Ratio of the inclusive π^0 cross-section for 516 GeV/c π^+ incident on beryllium to the cross-section for incident 515 GeV/c π^- as a function of π^0 p_T .

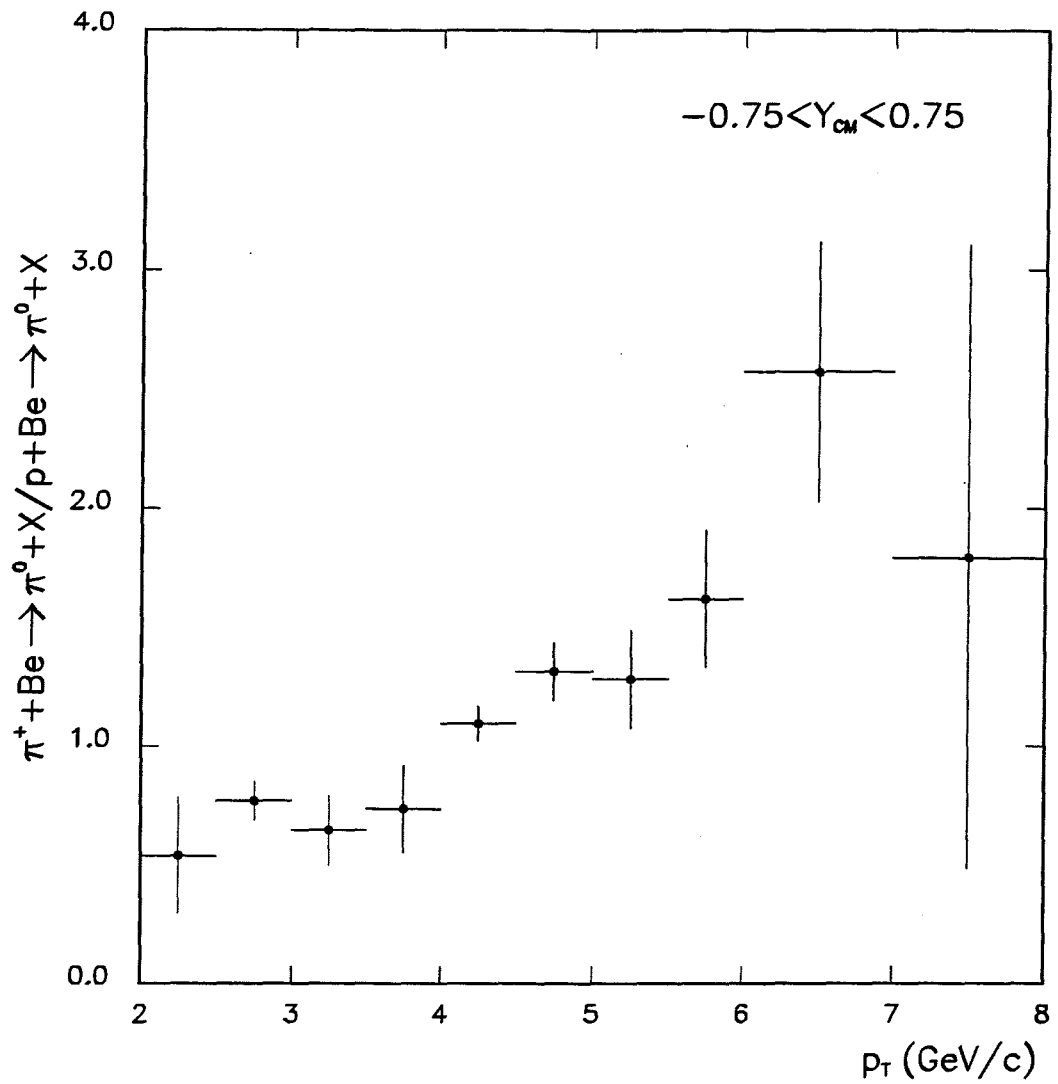


Figure 7.12: Ratio of the inclusive π^0 cross-section for 516 GeV/c π^+ incident on beryllium to the cross-section for incident 530 GeV/c p as a function of $\pi^0 p_T$.

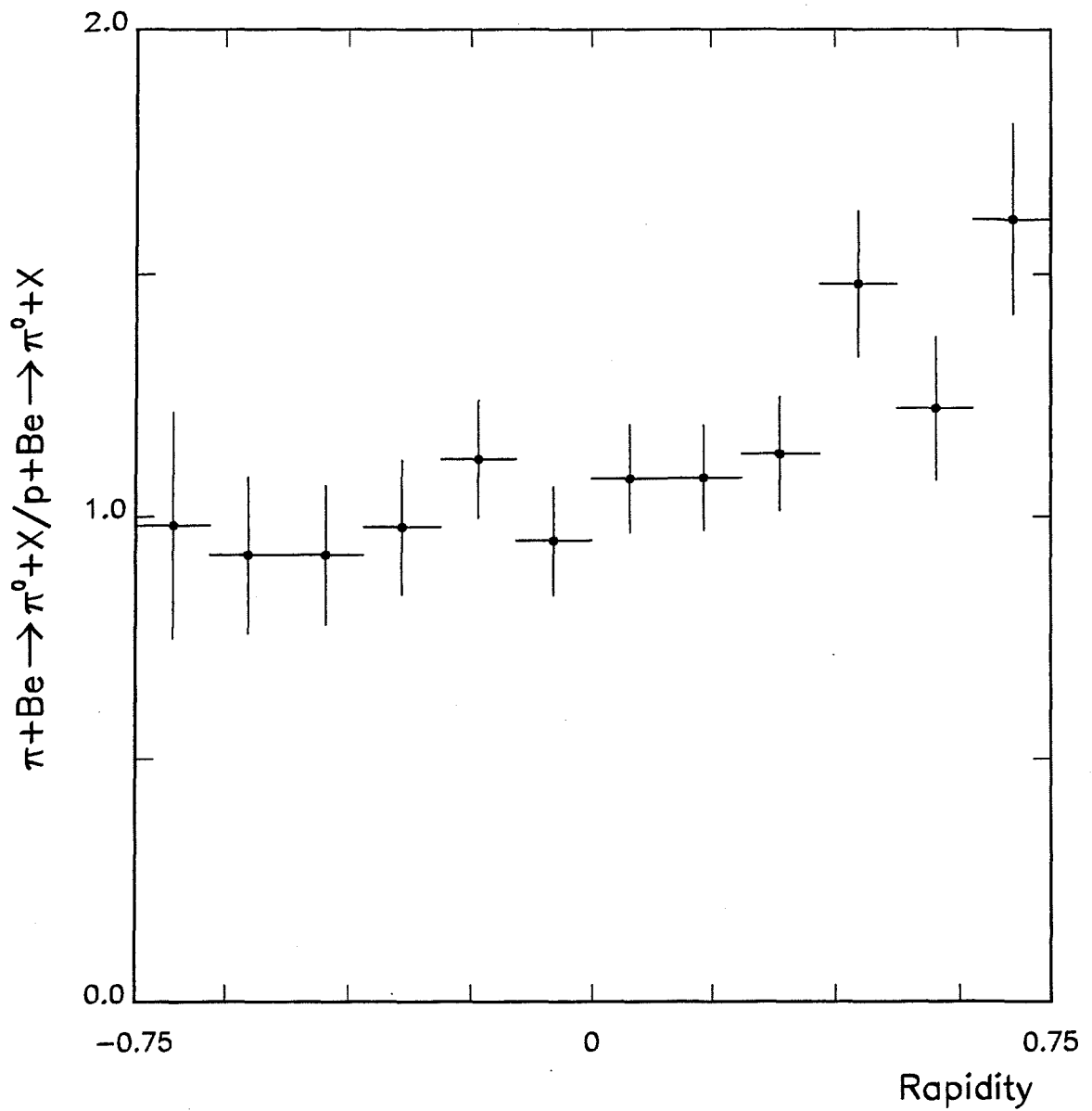


Figure 7.13: Ratio of the π^0 cross-section for incident 516 GeV/c π^+ to that generated by incident 530 GeV/c p as a function of π^0 rapidity for $4.0 \text{ GeV}/c < p_T < 4.5 \text{ GeV}/c$. The distribution generated by the incident π^+ is characteristically shifted towards more forward rapidities than the p distribution. Data are selected from the LOW Čerenkov pressure sample only.

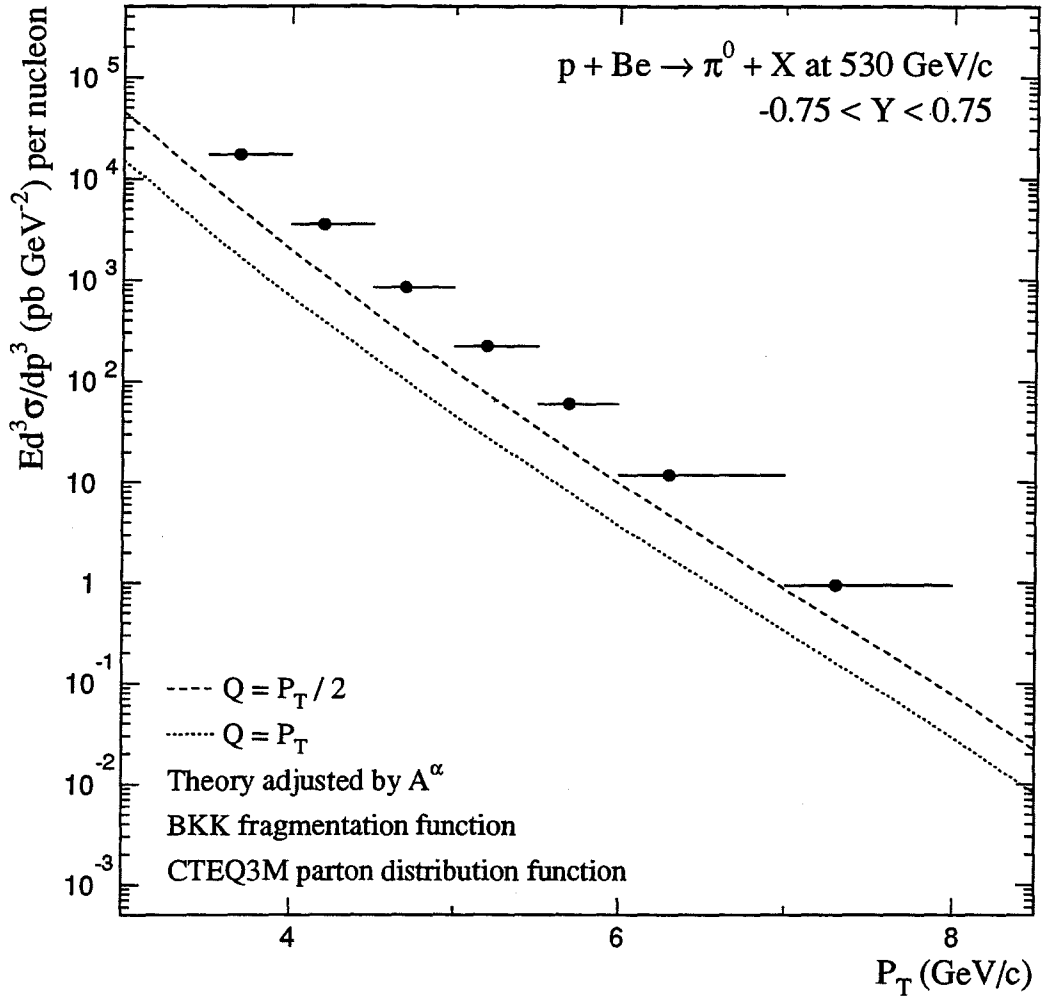


Figure 7.14: Inclusive π^0 cross-section per nucleon for 530 GeV/c p incident on beryllium as a function of π^0 p_T . The data are compared to the NLL QCD predictions for two choices of scale $Q = p_T$ and $Q = p_T/2$.

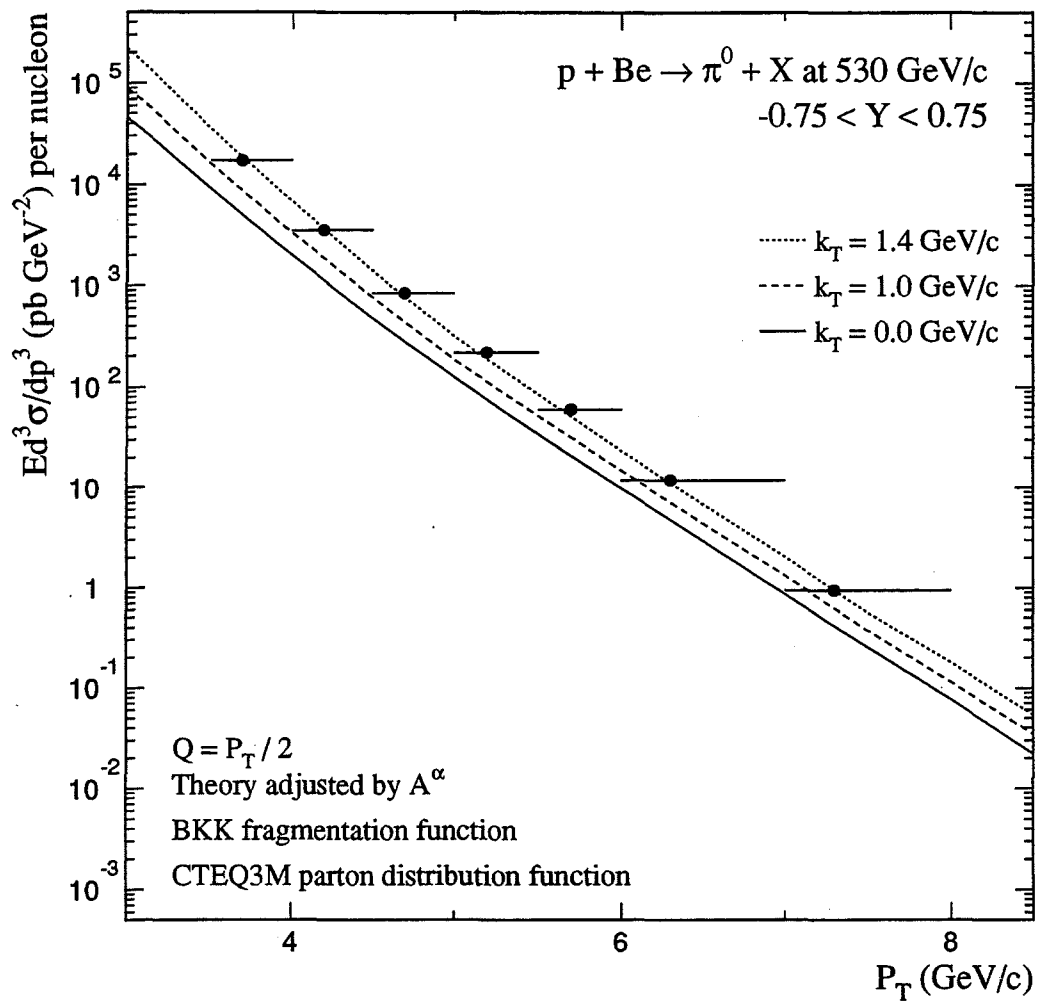


Figure 7.15: Inclusive π^0 cross-section per nucleon for 530 GeV/c p incident on beryllium as a function of π^0 p_T . Data are compared to NLL QCD predictions with k_T smearing included. The scale $Q = p_T/2$ has been employed.

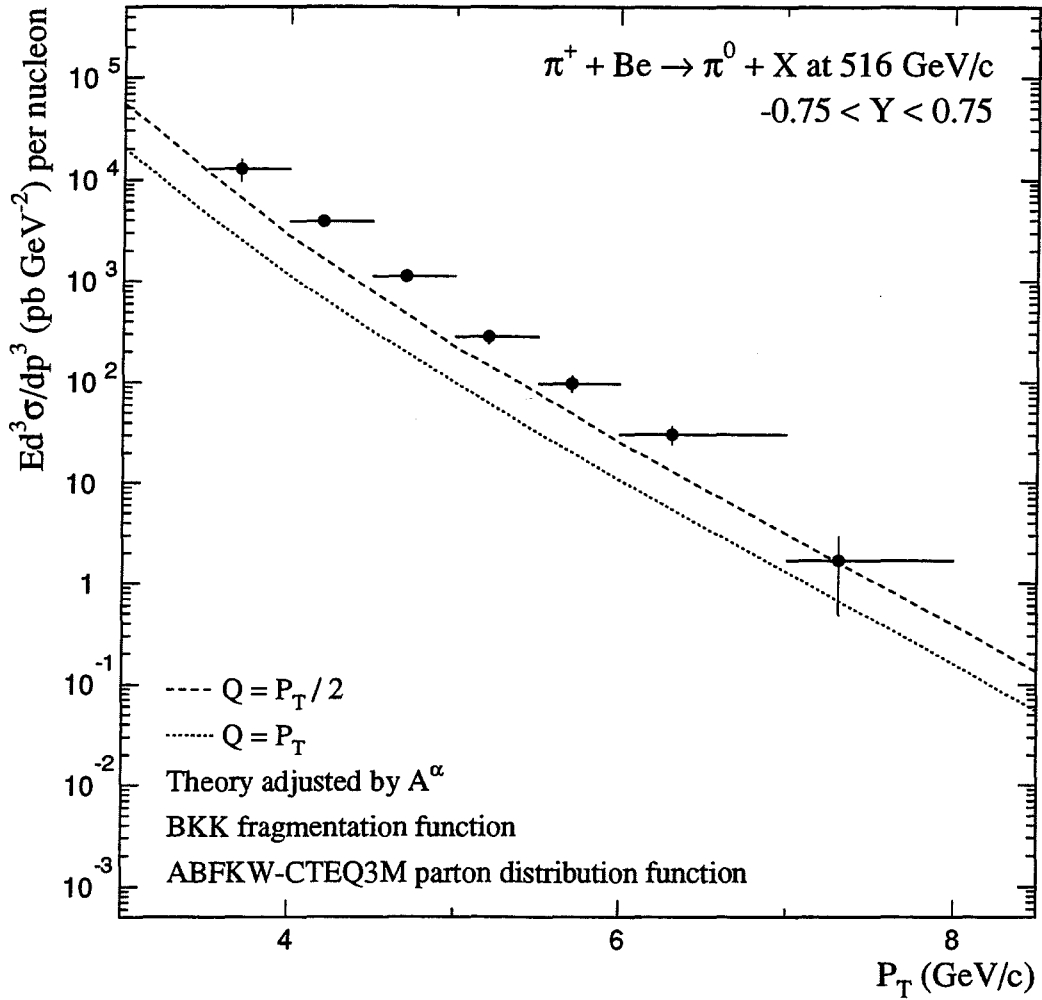


Figure 7.16: Inclusive π^0 cross-section per nucleon for 516 GeV/c π^+ incident on beryllium as a function of π^0 p_T . The data are compared to the NLL QCD predictions for the two choices of scale $Q = p_T$ and $Q = p_T/2$.

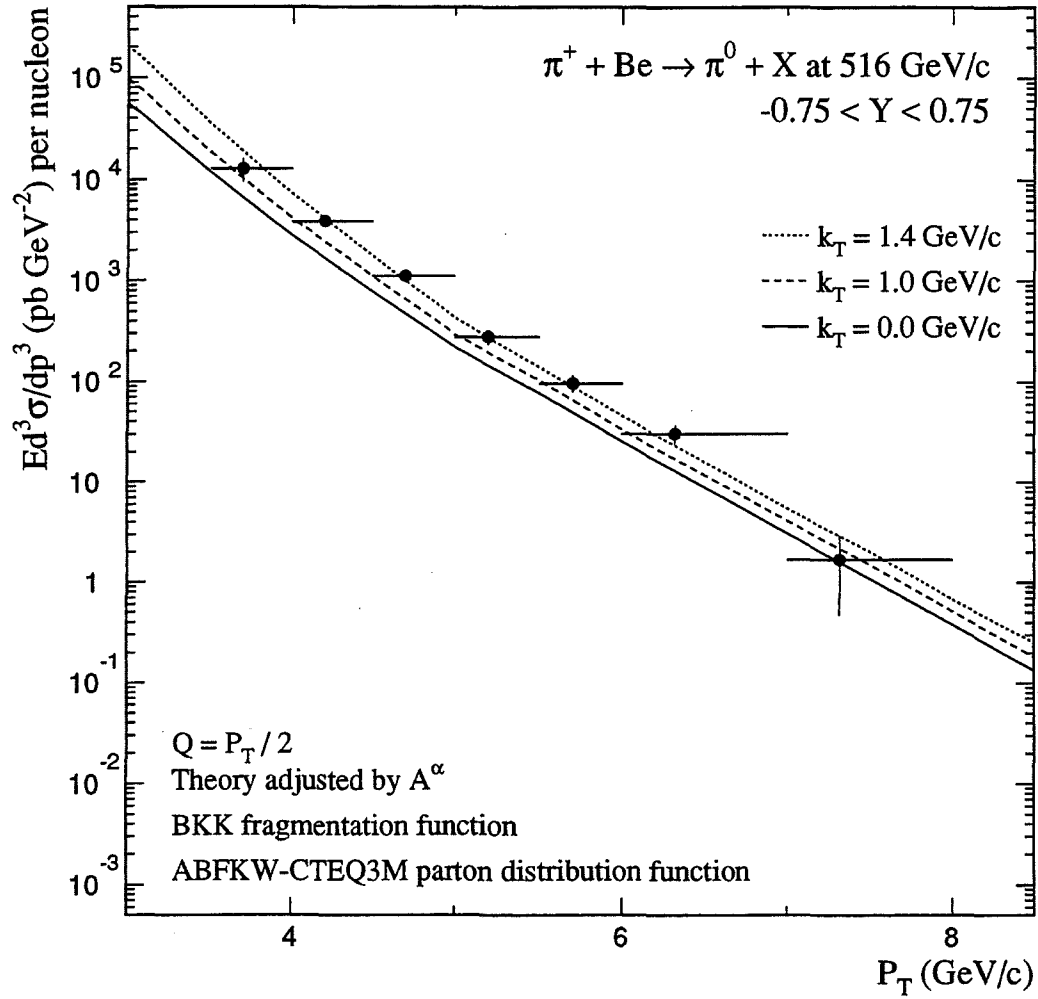


Figure 7.17: Inclusive π^0 cross-section per nucleon for 516 GeV/c π^+ incident on beryllium as a function of π^0 p_T . Data are compared to NLL QCD predictions with k_T smearing effects included. The scale $Q = p_T/2$ has been employed.

with low production yields. This conclusion is supported both by the Čerenkov Monte Carlo analysis as well as measurements of absorption cross-section ratios. The analysis also shows that the counter is capable of measuring the relative population fraction of each particle type in the incident beam.

Within statistical uncertainties, the ratio of inclusive π^0 production cross-sections for incident π^+ to incident π^- is consistent with unity. This observation is consistent with expectations based upon results from previous experiments at lower energies.

The ratio of the inclusive π^0 cross-sections for incident π^+ to incident p is found to increase with increasing $\pi^0 p_T$. This is consistent with expectations that, since the valence quarks in the π^+ ($|u\bar{d}\rangle$) each individually carry a larger fraction of the parent 516 GeV/c π^+ 's momentum than does each valence quark in the incident p ($|uud\rangle$) at 530 GeV/c, higher p_T particles may be more readily produced in interactions among the higher energy constituents.

The measured cross-sections for the incident charged particles in the +530 GeV/c beam were presented. Comparison of the results with NLL QCD predictions were most consistent with the NLL calculations using the scale $Q = p_T/2$ and a k_T smearing of 1.4 GeV/c.

Bibliography

- [1] R. M. Barnett et al., *Review of Particle Properties*, Phys. Rev. D **54**, 1 (1996).
- [2] F. Halzen and A. D. Martin, *Quarks and Leptons*, (Wiley, New York, 1984).
- [3] C. Quigg, *Gauge Theories of the Strong, Weak and Electromagnetic Interactions*, (Benjamin/Cumming, Reading, 1983).
- [4] D. H. Perkins, *Introduction to High Energy Physics*, 3rd ed., (Addison-Wesley, Menlo Park, 1987).
- [5] D. Griffiths, *Introduction to Elementary Particles*, (Harper and Row, New York, 1987).
- [6] D. J. Gross and F. Wilczek, Phys. Rev. Lett. **30**, 3143 (1973).
- [7] D. J. Gross and F. Wilczek, Phys. Rev. D **8**, 3633 (1973).
- [8] H. D. Politzer, Phys. Rev. Lett. **30**, 1346 (1973).
- [9] G. Altarelli and G. Parisi, Nucl. Phys. **B126**, 298 (1977).
- [10] W. M. Geist et al., *Phys. Rep.* **197**, 263 (1990).
- [11] N. A. McCubbin, Rep. Prog. Phys. **44**, 1027 (1981).
- [12] R. D. Field and R. P. Feynman, Nucl. Phys. **B136**, 1 (1978).
- [13] E. Fischback and G. W. Look, Phys. Rev. D **15**, 2576 (1977).

- [14] R. D. Field and R. P. Feynman, *Phys. Rev. D* **15**, 2590 (1977).
- [15] R. P. Feynman et al., *Nucl. Phys.* **B128**, 1 (1977).
- [16] J. F. Owens, *Rev. Mod. Phys.* **59**, 465 (1987).
- [17] J. F. Owens et al., *Parton Distribution Functions of Hadrons*, FERMILAB-PUB-92/59-T, March 1992.
- [18] P. Aurenche et al., *Nucl. Phys.* **B297**, 661 (1988).
- [19] J. F. Owens in *Quantum Chromodynamics: Theory and Experiment*, Proc. 3rd Lake Louise Winter Institute, Chateau Lake Louise, Canada, B. A. Campbell et al., ed., World Scientific (1988).
- [20] P. Aurenche et al., *Nucl. Phys.* **B286**, 509 (1987).
- [21] M. Glück et al., *Z. Phys.* **C53**, 127 (1992).
- [22] M. Glück et al., *Z. Phys.* **C53**, 651 (1992).
- [23] P. J. Sutton et al., *Phys. Rev. D* **45**, 2349 (1992).
- [24] P. N. Harriman et al., *Phys. Rev. D* **42**, 798 (1990).
- [25] P. Aurenche et al., *Phys. Lett.* **B233**, 517 (1989).
- [26] D. W. Duke and J. F. Owens, *Phys. Rev. D* **30**, 49 (1984).
- [27] J. F. Owens, *Phys. Rev. D* **30**, 943 (1984).
- [28] D. W. Duke et al., *Nucl. Phys.* **B195**, 285 (1982).
- [29] J. Kubar et al., *Nucl. Phys.* **B175**, 251 (1980).
- [30] M. Glück and E. Reya, *Nucl. Phys.* **B130**, 76 (1977).

- [31] H. Deden et al., Nucl. Phys. **B85**, 269 (1975).
- [32] J. F. Owens, Phys. Lett. **B266**, 126 (1991).
- [33] Win Baker. Private communication.
- [34] R. Tokarek, private communications.
- [35] W. Higgins, et al., *EPICURE User's Guide*, vol. 1—3, Fermilab Research Division Controls Software Release Note 37.2 (1989).
- [36] T. Toohig, *Fermilab Magnets, Power Supplies, and Auxiliary Devices: Technical Data*, TM-632, 2200.00, Fermilab (1975) and M. Bodnarczuk, *Experimental Areas Beam Line Transport Systems* (1983).
- [37] D. C. Carey, *The Optics of Charged Particle Beams*, Harwood (1987).
- [38] G. Tassotto, *Beam Profile Monitors Used in the Fermilab Fixed Target Beamlines*, FERMILAB-TM-1853 (1993).
- [39] Modification of the MWEST Čerenkov detector for simultaneous identification of three particle types was designed by C.J. Johnstone.
- [40] For more on the design and operation of differential Čerenkov counters see M. Benot, et al., NIM, **105**, 431 (1972).
- [41] I. Kourbanis, *The A Dependence of Leading Particle Production by 800 GeV/c Protons*, Ph.D. Dissertation, Northeastern University (1989).
- [42] P. A. Čerenkov, Docl. Akad. Nauk. SSSR, 2.451 (1934); S. I. Vavilov, Docl. Akad. Nauk. SSSR, 2.457 (1934); I. E. Tamm and I. M. Frank, Dokl. Akad. Nauk. SSSR, 14.107 (1937).

- [43] D. Dalgarno and A. E. Kingston, Proc. Phys. Soc. (London), **259A**, 424 (1960).
- [44] P. L. Smith, et al., Phys. Rev. A **13**, 1422 (1976).
- [45] J. V. Jelley, *Čerenkov Radiation and its Applications*, Pergamon (1958); J. D. Jackson, *Classical Electrodynamics*, 2nd ed., Wiley (1975).
- [46] A. Bodek, et al., Z. Phys. **C18**, 289 (1983).
- [47] 1990 Research Instrumentation Catalog, LeCroy Corporation.
- [48] S. D. Fantone, Appl. Opt., **30**, 4682 (1991).
- [49] Schematic figures courtesy of the Fermi National Accelerator Laboratory, Physics Department, Mechanical Engineering Division.
- [50] J. Tweed, private communication.
- [51] C. M. Yosef, *Production of High Transverse Momentum π^0 Mesons in Interactions at 530 GeV/c Proton and π^- Beams on Beryllium and Copper Targets*, Ph.D. Dissertation, Northeastern University (1990).
- [52] S. R. Blusk, *Measurement of the Production Cross-Section of Charm Mesons at High Transverse Momentum in 515 GeV/c π^- -Nucleon Collisions*, Ph.D. Dissertation, University of Pittsburgh (1995).
- [53] E. Engels et al., Nucl. Instr. Meth. **A279**, 272 (1989).
- [54] K. Hartman, *Hadronic Production of π^0 Pairs and Associated Event Structure*, Ph.D. Dissertation, Pennsylvania State University (1990).
- [55] C. Bromberg et al., Nucl. Instr. Meth **A307**, 292 (1991).

- [56] P. Chang, *Massive $\pi^0\pi^0$, $\pi^0\pi^-$, and $\pi^0\pi^+$ Production from 515 GeV/c π^- Collisions with Beryllium and Copper Targets*, Ph.D. Dissertation, Northeastern University (1994).
- [57] F. Lobkowicz et al., *Nucl. Instr. Meth.* **A235**, 332 (1985).
- [58] W. E. DeSoi, *Construction and Performance of a Liquid Argon Calorimeter for Use in Experiment E-706 at the Fermi National Accelerator Laboratory*, Ph.D. Dissertation, University of Rochester (1990).
- [59] C. Lirakis, *A Study of High Transverse Momentum η Production in 530 GeV/c Hadronic Interactions*, Ph.D. Dissertation, Northeastern University (1990).
- [60] R. Benson, *Characteristics of Forward Energy Production in Proton - Nucleus and Pion - Nucleus Collisions at $\sqrt{s} = 31.5$ GeV*, Ph.D. Dissertation, University of Minnesota (1990).
- [61] G. B. Osborne III, *A Measurement of the Muon Content of the 1991 MWest Beam*, E706 Note 197 (1992).
- [62] N. Varelas, *π^0 Production at High Transverse Momenta from π^- Collisions at 520 GeV/c on Be and Cu Targets*, Ph.D. Dissertation, University of Rochester (1994).
- [63] VAXONLINE System, FNAL Computer Department PN-252.
- [64] IEEE Standard FASTBUS, ISBN 471-84472-1 (1985).
- [65] CAMAC Instrumentation and Interface Standards, IEEE 1982, ISBN 0-471-89737.
- [66] Designed by P. Lukens of the University of Minnesota.

- [67] D. D. Skow, *A Study of High Transverse Momentum Eta Meson Production*, Ph.D. Dissertation, University of Rochester (1990).
- [68] L. Sorrell, *The E706 Trigger System*, E706 Internal Note 201, (1994).
- [69] L. R. Sorrell, *Measurement of the Nuclear Dependence of Direct Photon and Neutral Meson Production at High Transverse Momentum by Negative 515 GeV/c Pions Incident on Beryllium and Copper Targets*, Ph.D. Dissertation, Michigan State University (1995).
- [70] G. O. Alverson and E. L. Pothier, E706 Internal Note 139 (1985).
- [71] R. M. Roser, *Eta Production at High Transverse Momentum by Negative 520 GeV/c Pions Incident on Beryllium and Copper Targets*, Ph.D. Dissertation, University of Rochester (1994).
- [72] W. Dlugosz, *The Production of High p_T π^0 Mesons in 515 GeV π^- - Nucleus Collisions*, Ph.D. Dissertation, Northeastern University (1994) and private communication.
- [73] H. J. Klein and J. Zoll, *PATCHY Reference Manual*, CERN (1983).
- [74] J. P. Mansour, *High Transverse Momentum π^0 Production from π^- and p Beams at 530 GeV/c on Be and Cu*, Ph.D. Dissertation, University of Rochester (1989).
- [75] N. Varelas et al, *Calibration of the Fermilab E706 Liquid Argon Electromagnetic Calorimeter*, ICATPP-4, Proceedings of the 4th International Conference on Advanced Technology and Particle Physics, Como, Italy, 3-7 Oct 1994, E. Borchi et al., ed.; Nucl. Phys. B (Proc. Suppl.) 44, 153 (1995).

- [76] D. C. Carey, TURTLE (*Trace Unlimited Rays Through Lumped Elements*) A Computer Program For Simulating Charged Particle Beam Transport Systems, NAL-64, 2041.000, PM 9 (1978); K. L. Brown, et al., TRANSPORT, A Computer Program for Designing Charged Particle Beam Transport Systems, CERN 80-04, Super Proton Synchrotron Division (1980); D. C. Carey, *Third Order TRANSPORT with MADD Input*, TM-1546 (1988) and D. C. Carey, private communication.
- [77] A. J. Malensek, *Empirical Formula for Thick Target Particle Production*, FN-341, 2941.000 (1981) and private communication.
- [78] H. W. Atherton et al., CERN 80:07 (1980).
- [79] D. C. Carey, private communication.
- [80] T. Massam, *A General Program for Evaluating the Properties of Scintillation and Čerenkov Counter Optical Systems*, PM-47 (1976).
- [81] I. Kourbanis, private communication.
- [82] W. H. Press, *Numerical Recipes: The Art of Scientific Computing*, (Cambridge, New York, 1989).
- [83] S. E. Koonin, *Computational Physics, (Basic Version)*, (Benjamin/Cummings, Menlo Park, 1986).
- [84] A. Carroll et al., *Phys. Lett.* B80 (1979), 319.
- [85] W. Dlugosz, L. Apanasevich, G. Ginther and M. Zieliński, private communication.
- [86] G. Marchesini et al., HERWIG V5.6, CERN (1993).

[87] R. Brun et al., GEANT3 User's Guide, CERN DD/EE/84-1.

(1987), 43.

